Regulating curvature and mechanics of membranes in endocytosis by BAR domain proteins

Mijo Simunovic

Université Paris.Diderot (Paris 7)

Ecole doctorale 518: Matière Condensée et Interfaces

Physique en Ile de France

DOCTORAT

Physique

MIJO SIMUNOVIC

Regulating curvature and mechanics of membranes in endocytosis by BAR domain proteins

Thèse dirigée par Patricia BASSEREAU/Gregory A. VOTH

Soutenue le 5 Juin 2015

JURY

Jean-Baptiste FOURNIER	Président
Laurence SALOME	Rapporteuse
Daan FRENKEL	Rapporteur
Harvey MCMAHON	Examinateur

Acknowledgements

Many people contributed in meaningful ways to make this transatlantic and transdisciplinary undertaking possible. First, I have to thank my advisors, Patricia Bassereau and Greg Voth. I am thankful to Patricia for taking a chance on a theorist in her group despite highly unfavorable odds of success. Her continuous support, relentless enthusiasm, and creativity fueled my desire to learn complicated experimental techniques and to continue even at times when all my efforts seemed hopeless. I thoroughly enjoyed our stimulating discussions, which I will remember for many years. Greg thankfully assuaged my initial doubts of pursuing a scientific career and inspired me to seek a research path that I am now deeply passionate about. He offered just enough freedom and direction to make me feel confident but still very curious about the "next question". I am extremely grateful for continuously trusting me with challenging tasks over the past five years, for the patience in following a complicated route toward my degree, and for his incredible generosity. I thank my committee members, Laurence Salomé, Daan Frenkel, Jean-Baptiste Fournier, Harvey McMahon, Ka Yee Lee, and Suri Vaikuntanathan for their helpful advice and valuable input.

The members of the Bassereau team were extremely patient and supportive of me during my stay in Paris. I am forever grateful to Coline Prévost for teaching me how to be an experimental biophysicist and for giving me a roof over my head. I am very thankful to Marta Bally and Matthias Garten in the group and to Laura Picas at Curie for teaching me many useful experimental skills. I am thankful to all the members of the Voth group for their helpful and interesting conversations we had both around the office and at happy hours. In particular, I must point out Anand Srivastava whose model made my research possible, and James Dama, John Savage, Marissa Saunders, and Glen Hocky with whom I had many fruitful and fun discussions. I thank my friend Andela Šarić who has given me plenty of advice and encouragement in my scientific efforts for many years.

During the past five years, I had the privilege to collaborate with many talented people. I am grateful to our cell biology experts in Curie, Henri-François Renard and Ludger Johannes who inspired our project on fission and with whom we had a very fruitful and exciting collaboration. I very much enjoyed our interesting discussions. I am immensely thankful to Emma Evergren and Harvey McMahon without whose expertise this project would never fly off the ground. I also thank Anne Schmidt who kindly gave us the initial batch of proteins, which we used to build and shape our project. In my last days at Curie, Jean-Baptiste Manneville taught me a very interesting but complicated assay and I am grateful for his time and effort upon my departure, which have greatly elevated my project. I have had many insightful

and inspiring conversations with Jacques Prost and Andrew Callan-Jones, who constantly challenged me and showed me how to think analytically about biological problems. I am grateful to Ka Yee Lee for the support while I worked in her lab and to Michael Henderson for teaching me new techniques and patiently working with me on my project. I am thankful to Jen Martinez, Jim Werner, and Peter Goodwin at the Los Alamos National Lab for investing their valuable time and expertise in tackling a very challenging experiment with me. I must thank Carsten Mim and Vinzenz Unger with whom we had a successful collaboration over many years. I thank the Biophysics Program at University of Chicago for letting me store my proteins in their facilities.

I owe my gratitude to Branka Zorc and Tomislav Cvitaš, whose mentorship over the course of seven years was directly responsible for choosing to pursue a career in scientific research. The two of them, together with my undergraduate research advisors, Sanja Tomić, Bojan Žagrović, and Tomica Hrenar were key in shaping my research skills.

Finally, I am deeply thankful to my family, especially my mother, and my friends for their unconditional support and putting up with my not-so-infrequent whining. I am thankful to my dear friend Kathleen Cao with whom I have explored the culture and entertainment of Chicago and to all of my Croatian friends: Maja Deke, Sandra Koroljević, Ivana Ristovski, Željka Salinger, Andela Šarić, Marina Uzelac. I am thankful for the memorable times au bord de la Seine and many other places in Paris that I spent with Maryam Alqabandi, Senthil Arumugam, Marta Bally, Mohamed El Beheiry, Alice Berthaud, Thomas Bornschlögl, Fahima Faqir, Matthias Garten, Coline Prévost, Feng Tsai, and many others.

Preface

This thesis is prepared under the joint supervision between Patricia Bassereau at Institut Curie and Gregory A. Voth at the University of Chicago. I started a Ph.D. in Chemistry at the University of Chicago in August 2010. In September 2012, I enrolled in the Ph.D. program in Physics (Ecole doctorale: Matière Condensée et Interfaces, later renamed to Physique en Ile de France) at University of Paris Diderot (Paris 7). The two universities signed a dual sponsorship agreement (fr. *co-tutelle*), granting me a Ph.D. degree from each institution upon completion of the program. Due to the volume of the thesis, we split it into two tomes, wherein this tome presents the work predominately carried out at Institut Curie. Each of the two manuscripts has an extended summary of the accompanying manuscript. Considering that the biological systems are the same, there is an unavoidable resemblance in the introductions of the two theses. Analogously, the text of both theses will resemble articles we published or those currently in preparation. In particular, there are two published articles and one review paper that report the results of this thesis (Renard et al., 2015; Simunovic and Bassereau, 2014; Simunovic et al., 2015). There are two other research articles and two reviews currently in preparation. From the work of the accompanying thesis, there are four published articles (Simunovic et al., 2013a; Simunovic et al., 2013b; Simunovic and Voth, 2012, 2015). In addition, two research articles and one book chapter are currently in preparation.

1. Introduction

Membranes are ubiquitous in living systems. They function to compartmentalize the cell and its organelles, but also serve as mechanical support for proteins that control cellular trafficking and signal transduction (Alberts et al., 2014). Owing to the way membranes are assembled into lipid bilayers spanning microns in length and molecular width, they behave as elastic and highly dynamic molecular sheets (Goetz et al., 1999). Membrane's innate multiscale nature is further evident in the local interplay between proteins and lipids that drives the large-scale membrane remodeling characterized by an impressive array of morphologies (Lipowsky, 1991). These properties allow biological membranes to take part in several important cellular processes, as their restructuring is key to enabling communication between cells, formation of organelles, trafficking, division, and cell migration (McMahon and Gallop, 2005). The most notable sculptors of membranes in the cell are members of the Bin/Amphiphysin/Rvs (BAR) protein family (Dawson et al., 2006; Mim and Unger, 2012; Qualmann et al., 2011; Rao and Haucke, 2011). The characteristic structural feature of these proteins is an intrinsically curved domain that peripherally adheres to the membrane surface. Based on the shape of this domain, they are subdivided into classic BAR (or N-BAR if they also contain an N-terminal amphipathic helix), F-BAR, and I-BAR proteins. The spectrum of their abilities is highly diverse and it can most broadly be split into sensing and generating membrane curvature. As sensors, they get recruited to curved compartments in the cell where they stabilize highly curved surfaces. Additionally, they contain domains that target specific lipids and proteins, so their supplementary role is to recruit other proteins to the active site. As remodelers, they directly alter the architecture of the membrane, which serves to activate a variety of cellular process.

Recent studies have demonstrated that BAR domain proteins may even promote a change in the topology of the bilayer (Boucrot et al., 2012; Simunovic et al., 2013a), hence implicating them in membrane fission. For these reasons, the interaction between BAR proteins and the membrane can be described with a rich configurational phase diagram (Simunovic and Bassereau, 2014). Despite the tremendous research efforts, it is still unclear precisely when and to what extent the cell uses these various capabilities of BAR proteins to perform cellular functions. In fact, their role in endocytosis, an intensely studied membrane-remodeling process, has for a long time been controversial (Kirchhausen, 2012). This fact, together with the incredibly complex and multiscale behavior of membranes, makes the research on protein-mediated membrane-reshaping phenomena extremely challenging.

The aim of this thesis is to explore the configurational space of membrane remodeling, with an emphasis on BAR proteins. Chapter 1 gives a background and the

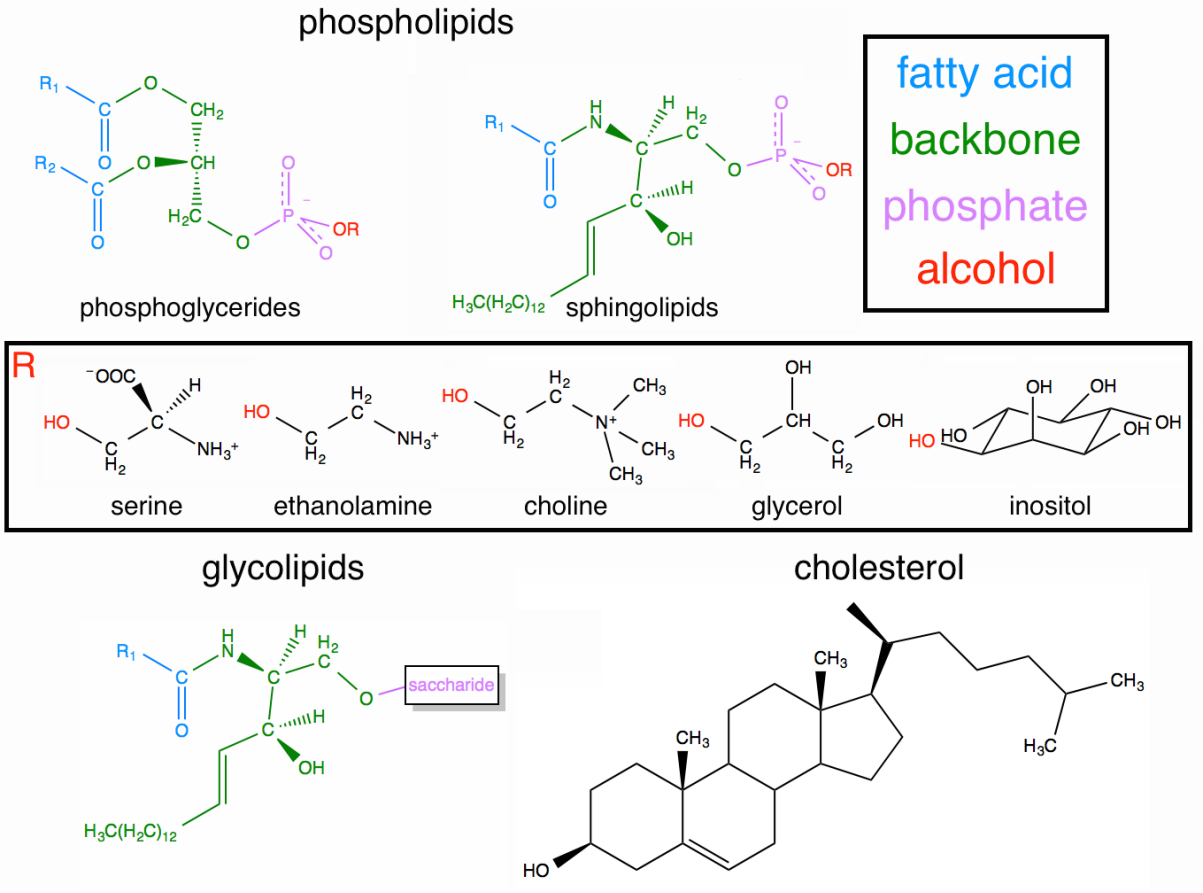

Figure 1.1.1: Structure of membrane lipids. Shown are three main groups of lipids that make up the cell membrane: phospholipids, glycolipids, and cholesterol.

biological context of the problem of membrane remodeling in cells. Chapter 2 describes the particular aims of the thesis and shows in detail the applied methodology. Chapter 3 is an extended summary of the work from the accompanying thesis. In Chapters 4–6, I will present our efforts in understanding the full range of capabilities of BAR proteins and elucidate the mechanism by which they carry out specific steps in a newly discovered endocytic pathway. In particular, in Chapter 4, I will show our work on understanding how curvature-generating proteins form polymeric scaffolds around membrane tubules and the role of protein's subdomains in this process, namely the amphipathic helices. In Chapter 5, I will discuss the mechanism of fission of scaffolded membrane tubules, induced by external pulling force, a mechanism we believe to be key in endophilin-mediated endocytosis. In Chapter 6, I will present the experimental evidence that shows that BAR domain itself can very efficiently sense membrane curvature, rebutting published research on this question. Finally, in Appendix I, I will show that membrane morphology can be affected by isotropic particles of vastly different sizes (namely, calcium ions), demonstrating that curvature can be induced by a much more general mechanism than typically considered in the literature.

1.1. Chemistry of lipid membranes

1.1.1) Molecular structure of lipids. Lipids are naturally occurring macromolecules that serve three principal purposes in organisms (Alberts et al., 2014). First, due to their reduced state, lipids are very efficient at storing energy. For example, the complete oxidation of a fatty acid lipid produces double the amount of energy than burning the same mass of carbohydrates or proteins. Secondly, several lipids have been identified as primary or secondary messengers in many signal transduction and molecular recognition processes. Some of these signaling events include the activation of G-protein-coupled receptors or nuclear receptors. Finally, and likely the most recognized role of lipids is forming membranes, a microscopic structure that separates the cell from the environment and compartmentalizes its organelles (Alberts et al., 2014; van Meer et al., 2008).

Lipids comprise a myriad of diverse molecules. There are three major groups of lipids in membranes: phospholipids, glycolipids, and cholesterol. Many other molecules are categorizes as lipids, such as fats, waxes, sterols, vitamins, etc. (Berg et al., 2002). **Phospholipids** are composed of an alcohol backbone, either glycerol or sphingosine, which make phosphoglycerides and sphingolipids, respectively. This backbone binds fatty acids and a phosphate that is typically derivatized with other alcohols (Fig. 1.1.1). The source of diversity of lipids comes from the length and saturation of the fatty acid chains and the composition of the alcohol on the phosphate. Most common alcohol moieties of phospholipids include choline, ethanolamine, serine, glycerol, and inositol, which then form phosphatidylcholine (PC), phosphatidylethanolamine (PE), phosphatidylserine (PS), diphosphatidylglycerol (PG), and phosphatidylinositol (PI) (Fig. 1.1.1). At neutral pH, this moiety determines the molecule's net charge. PS, PG, and PI have a single negative charge, whereas PE and PC are zwitterionic, meaning that they contain the same amount of positive and negative charge, making them net neutral. In phosphoglycerides, there are two saturated or cis-unsaturated fatty acid chains attached to the glycerol, forming diacylglycerol. In sphingolipids, sphingosine is attached to a single saturated or trans-unsaturated fatty acid, making ceramide. Most common sphingolipids are sphingomyelins (SM) that contain either choline or ethanolamine attached to the phosphate. **Glycolipids** contain sugars in their structure. In animal cells, glycolipids are similar in structure to sphingolipids, except that instead of the phosphate group, they have a saccharide moiety directly attached to the ceramide backbone. Finally, **cholesterol** belongs to a group of steroids, structurally very different from other lipids. Its rigid backbone comprises four hydrocarbon chains, derivatized on the one end with a short hydrocarbon chain, and a hydroxyl group on the other. The molecule is oriented such that its hydroxyl group is aligned with the phosphate group of other lipids (Berg et al., 2002; van Meer et al., 2008) (Fig. 1.1.1).

1.1.2) Self-assembly of lipids. From the chemical point of view, lipids are either hydrophobic (e.g. cholesterol, fatty acids) or amphipathic molecules (e.g. phospholipids and glycolipids). **Hydrophobicity** is the propensity to repel water. Despite its name (Greek ὕδωρ = water and φόβος = fear), hydrophobic interactions are not explicit repulsions between a hydrophobic moiety and water molecules. During solvation, water molecules surround the solute because they are attracted to it, thus lowering enthalpy. Considering that water molecules also readily form hydrogen bonds, an ordered network will form around the solute, hence unfavorably lower the entropy. When in contact with an apolar molecule, on the other hand, there are two options: water can either solvate the molecules thus separate the solutes, or it can get excluded from the space between two solutes, in which case the solute molecules will be attracted to one another (Fig. 1.1.2, A). Either way, enthalpy is unchanged as water does not interact with apolar molecules. Hence, the resulting configuration is determined by entropy, which favors the case in which water molecules are more disordered. Hydrophobic interactions are therefore the effective attractions between apolar molecules that result from this entropically-driven effect (Atkins and de Paula, 2010). **Amphipathic** molecules possess both a polar and an apolar moiety in their structure. A major consequence of such chemistry is that amphiphiles can parti-

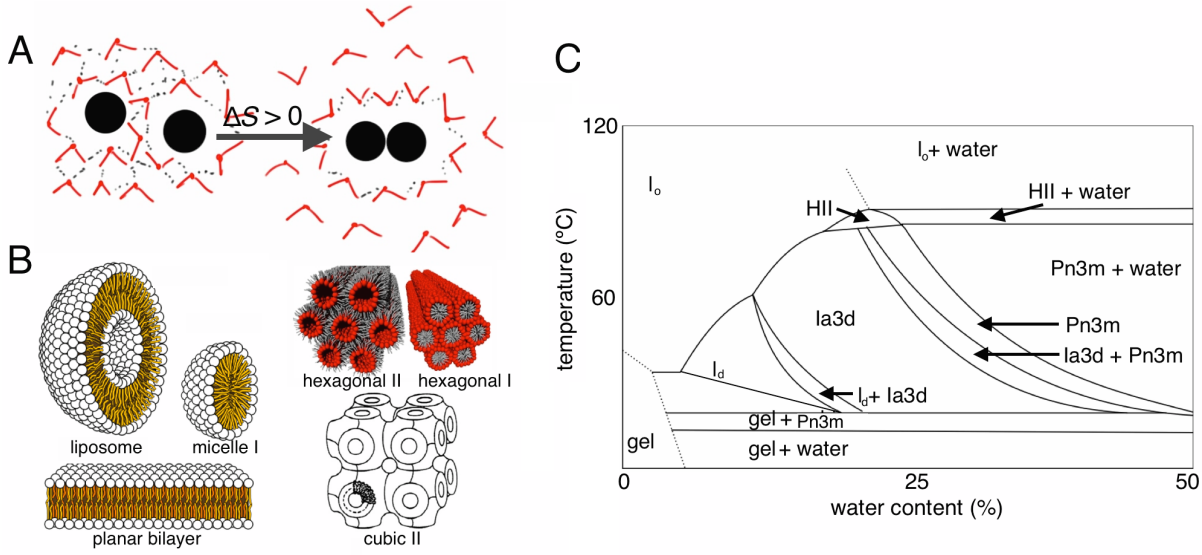

Figure 1.1.2: Structure of lipid assemblies. (A) Illustration of the hydrophobic effect. The exclusion of water molecules from the interface of two apolar molecules increases the entropy, ΔS, while keeping the enthalpy the same. Red lines represent water molecules, grey dotted lines hydrogen-bonds, black dots are apolar molecules. (B) Structure of lipid phases. Red and white spheres represent hydrophilic head groups, grey and yellow cylinders represent hydrophobic tails. Adapted from wikipedia and (Tresset, 2009) (C) Phase diagram of monooleil/water system. Redrawn from (Qiu and Caffrey, 2000). HII represents hexagonal II phase, Ia3d and Pn3m are cubic phases, l_o and l_d are, respectively, liquid ordered and liquid disordered phases.

tion organic molecules from water, essentially enabling the molecular complexity of life (Atkins and de Paula, 2010).

When phospholipids are mixed with water, their hydrophobic parts will stick to one another, whereas the hydrophilic moieties will be solvated by water. There are several geometries that can accommodate such chemistry (Ashrafuzzaman and Tuszynski, 2012). The most relevant to biology is a **lipid bilayer**. In this configuration, lipids either form planar or spherical surfaces (vesicles, liposomes) (Fig. 1.1.2, B). The bilayers can form a regular stack with a smectic order, called **lamellar phase**. The way lipids are organized in the plane can affect their fluidity. We distinguish three phases of bilayer membranes (in the decreased order of fluidity): liquid disordered (l_d), liquid ordered (l_o), and gel or solid phase (van Meer et al., 2008). Among non-lamellar phases, most common ones are: **micelle** (a spherical monolayer), **hexagonal** (a micellar tubule), and **cubic** phases (a complex three-dimensional lipid array interlaced with water tunnels) (Seddon, 1990; Tresset, 2009). The non-lamellar phases are further subdivided into two types based on the orientation of the hydrophobic tail of lipids. Type I phases are characterized by having an oil-in-water topology. In this configuration, the hydrophobic tails are oriented toward the center of the lipid structure, with the hydrophilic ends facing the bulk of the solution. Type II phases, also known as inverted phases, have the opposite, i.e. water-in-oil topology and are typically arranged into stacks (Fig. 1.1.2, B) (Seddon, 1990). Figure 1.1.2, C shows an experimentally determined phase diagram of a monooleil/water mixture, which has a particularly rich phase diagram, where we can see how phases depend on water content and temperature (Qiu and Caffrey, 2000).

1.1.3) Phase separation. Some lipids have a propensity to form certain phases as a result of their shape. For example, the hydrophilic head group in PE is much smaller compared to the lipid chain, resembling a cone. Conical lipids will be more likely to form a type II micellar or hexagonal phase than cylindrical lipids (Israelachvili et al., 1980). Moreover, an enrichment of conically shaped lipids in one leaflet of the membrane will impose a curvature stress in the bilayer. We will discuss this topic in much greater detail later (van Meer et al., 2008). The composition of the lipid chain may determine the fluidity of the lamellar phase. Most phospholipids will have at least one cis-unsaturated chain, rendering them more difficult to vertically stack in a bilayer and will typically form l_d domains. Single-chain lipids and lipids with unsaturated or long chains, such as sphingolipids will more easily stack against one another and form l_o domains. Single-chain lipids are also more prone to forming micelles, because single-chain lipids will repel each other less at the center of the micelle than double-chain lipids. In reality, predicting the steady-state assembly of lipids is not straightforward, especially for complex lipid mixtures. The practical consequence is that reconstituting membrane systems *in vitro* may often lead to unforeseen structures, such as multilamellar vesicles, gel phase bilayers, and other morphologies.

All known lipid bilayers can transition into gels at sufficiently low temperatures, known as the lipid melting temperature. At certain conditions, complex mixtures can separate their lipid components into different phases. The simplest system with coexisting **micron-sized domains** are ternary composition membranes, composed of: 1), lipids with a high melting temperature, 2), lipids with a low melting temperature, and 3), cholesterol (Baumgart et al., 2003; Dietrich et al., 2001; Samsonov et al., 2001; Veatch and Keller, 2003). Examples of low-melting-point lipids are dioleoylphosphatidylcholine (DOPC), with two 18-carbon-long cis-unsaturated lipid chains, and dilauroylphosphatidylcholine (DLPC), with two short saturated 12-carbon-long chains, both of which have a stronger preference for an l_d phase. Lipids such as dipalmitoylphosphatidylcholine (DPPC), with two saturated 16-carbon-long chains, distearoylphosphatidylcholine (DSPC), with two saturated 18-carbon-long chains, and SM, with a long single-chain ceramide, all prefer the l_o phase (Fig. 1.1.3). Cholesterol partitions into the l_o phase and enhances the formation of micron-sized domains because its rigid structure likely restricts the diffusion of lipids.

Domains in ternary giant unilamellar vesicles (GUVs) can be readily visualized with fluorescence microscopy. Such experiments revealed that micron-sized domains persist on time scales of minutes (Baumgart et al., 2003; Veatch and Keller, 2003). Binary mixtures can also phase separate, but into much smaller domains, 80–200 nm in size. These smaller domains are detected with molecular-level techniques, such as NMR, and they are especially stable near the miscibility critical point (Feigenson, 2006; Ipsen et al., 1987; Veatch et al., 2004). The coupling between the

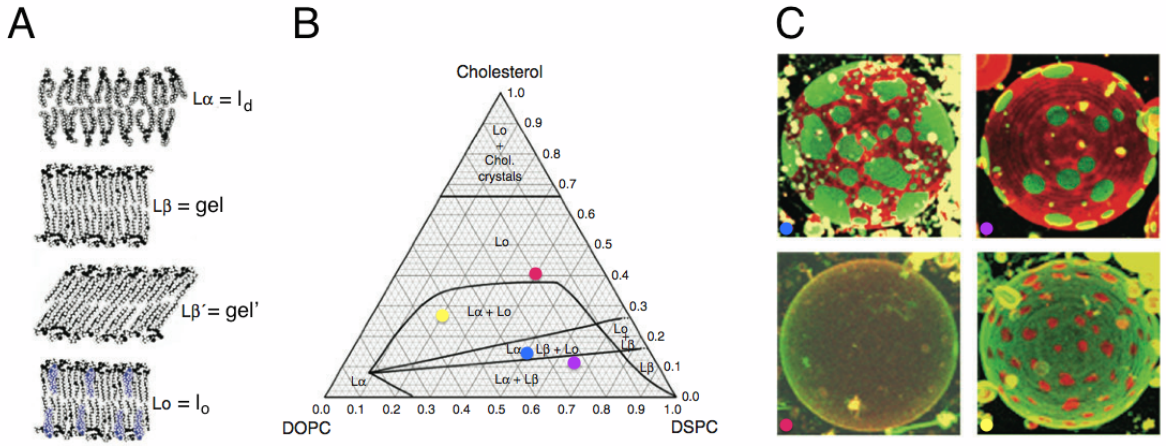

Figure 1.1.3: Phase separation. (A) Illustration of some lamellar phases: Lα = l_d, Lβ = gel, Lβ' = gel with tilted acyl chains; Lo = l_o. (B) Phase diagram of the ternary DOPC/DSPC/cholesterol mixture. (C) Fluorescence images of ternary mixtures GUVs color-coded by their corresponding places in the phase diagram in *B*. The mixture also contains a small percentage of lipid dyes that preferentially partition into the l_o (green) and l_d (red) phase. Adapted from (Feigenson, 2006).

scales in domain formation is unclear. Considering that the temperature at phase separation is close to physiological, it has been largely hypothesized that domain phase separation could have a significant functional role in the cell. Given the large research efforts in elucidating this problem, the literature has given these domains a special term: **lipid rafts**. I will return to this topic as part of biological context in section 1.3.

1.1.4) Lipid mobility. Lipid diffuse laterally in the bilayer, making the membrane fluid. The lateral diffusion coefficient is on the order of ~ 1 $\mu m^2/s$, thus we can estimate that it only takes a second for a lipid to traverse the entire surface of a micron-sized cell, such as bacteria. Lipids also freely rotate within the bilayer. On the other hand, migration from one leaflet to another, known as flip-flop, is extremely slow, on the order of days. The exception is cholesterol that rapidly translocates. Cells have developed specialized proteins, namely flippases, that mediate the ATP-dependent lipid flip-flop in the cell (Alberts et al., 2014; Lodish, 2008). The structure of lipids affects their lateral mobility in the same way it controls their phase behavior. For example, it has been found that lipids in the phase-separated ternary bilayers—composed of DOPC, SM, and cholesterol—have a ~ 3-fold slower diffusion coefficient in the l_o than in the l_d phase (Dietrich et al., 2001; Filippov et al., 2004). Again, the easier lateral packing of l_o lipids increases the van der Waals interactions among the surrounding lipids (Atkins and de Paula, 2010), slowing down the mobility. Another study has shown that adding cholesterol to DOPC bilayers (a low-melting-point lipid) decreases the diffusion coefficient linearly with cholesterol content, however no effect was observed when adding cholesterol to SM bilayers (high-melting-point lipid) (Filippov et al., 2003). Cholesterol does not influence lipid diffusion in l_d or l_o phases in ternary mixtures (DOPC/SM/cholesterol) (Filippov et al., 2004). These results again point to the likelihood of lipid rafts and their potential role in biology as regulators of cellular function. Membrane curvature also modules the lateral diffusion of lipids. In particular, the mobility of lipids decreases approximately twice in highly curved tubular membranes compared to planar membranes (Domanov et al., 2011) and ~ 2.5 times slower in membrane junctions (Simunovic et al., 2013a).

1.2. Physics of lipid membranes

Structural features of lipid bilayers are observable at multiple scales. They can span microns in lateral dimensions to form elastic sheets governed by macroscopic mechanics. At the same time, the cross-section of a lipid bilayer is orders of magnitude smaller, with only two molecules making up its thickness. This aspect demands a molecular point of view when studying any interactions with the membrane. The hydrophobic repulsion at the water-lipid tail interface gives rise to line tension that minimizes the edge of a bilayer, whereas the surface tension tends to minimize its

area. This process competes with elastic energy induced by bending the membrane. As a result of these opposing forces, biological membranes form a remarkable range of geometries. From the physical point of view, the behavior of the membrane is often explained by considering it to be a thin elastic sheet, without accounting for the molecular structure or the local composition inhomogeneities (Brown, 2008; Lipowsky, 1991). However, biological membranes are far more complex. First, they are fluid, which makes them much more flexible than solid elastic objects. Second, membranes contain hundreds of different components, so predicting its actual phase behavior is nearly impossible. Finally, cell membrane is not at equilibrium, making the thermodynamic treatment all the more difficult. Surprisingly however, the elastic description of the cell membrane has been remarkably successful in explaining the physical basis of large-scale membrane behavior and it has provided a very useful analytical framework for analyzing and understanding the experimental data (Brown, 2008).

1.2.1) Elastic energy of the membrane. Pioneering theoretical description of the membrane came in the 1970s, when Canham and Helfrich explained the shape of red blood cells by calculating the bending energy (F_{bend}) of a thin elastic sheet (Canham, 1970; Helfrich, 1973). We now call this equation the Canham-Helfrich Hamiltonian and it can be written as:

$$F_{\text{bend}} = \int dA \left[\frac{\kappa_{\text{m}}}{2} \left(c_1 + c_2 - c_0 \right)^2 + \kappa_{\text{G}} c_1 c_2 \right]. \qquad \text{(Eq. 1.2.1)}$$

In this expression, c_1 and c_2 are the principal curvatures of the membrane having the surface area A. The principal curvatures of a plane are the minimum and the maximum curvatures of an intersection between the surface and a perpendicular plane at a point of observation. The first summation term in Eq. 1.2.1 represents the elastic response of a bent surface from its equilibrium mean curvature, called the spontaneous curvature, c_0. The second summation term is the elastic response from generating Gaussian curvature in the surface. The resistance to bending is measured with the bending and the saddle splay modulus, κ_{m} and κ_{G}, respectively. See Fig. 1.2.1 for illustration of bending versus other types of strains, further discussed below.

The two types of curvatures are mathematically different in so that mean curvature is the linear component of curvature whereas Gaussian curvature is its quadratic component. As such, with small deformations, the linear term will be more dominant. Precisely, they are defined as:

$$H_{\text{m}} = \frac{1}{2} \left(c_1 + c_2 \right), \qquad \text{(Eq. 1.2.2)}$$

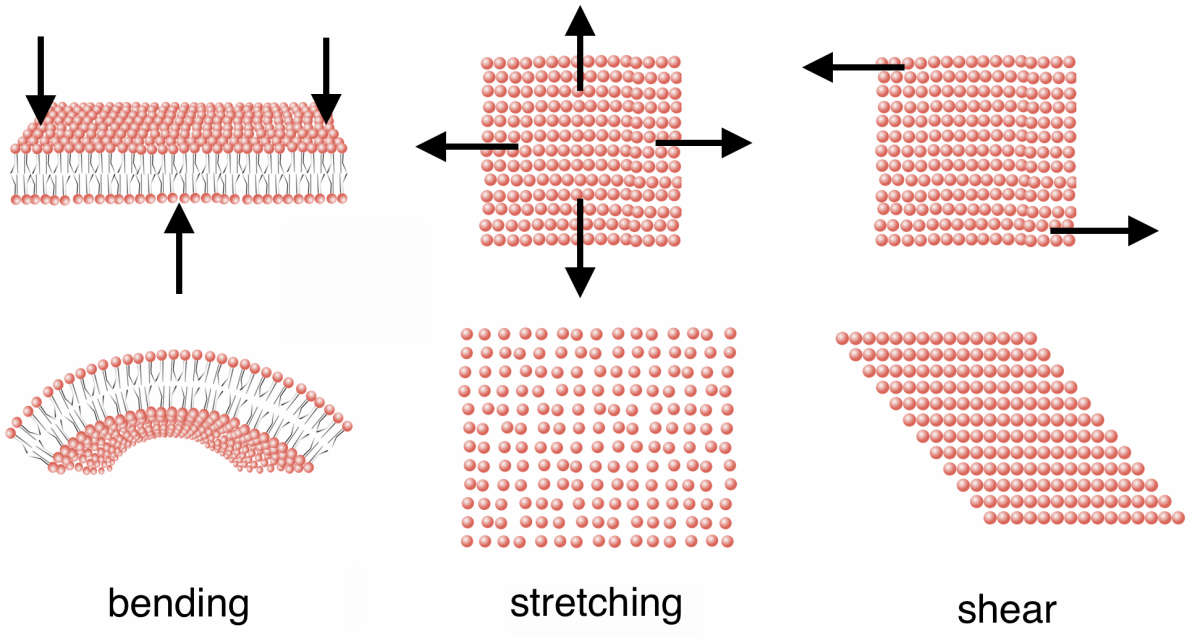

Figure 1.2.1: Elastic deformations of the membrane. The arrows represent the direction of the stress, resulting in different strain responses: bending, stretching, and shear.

$$K = c_1 c_2 \qquad \text{(Eq. 1.2.3)}$$

where H_m and K are, respectively, mean and Gaussian curvatures. Practically, the two curvatures can be distinguished based on the way they are perceived and measured. **Mean curvature** is defined by external observation of a surface embedded in some space and its sign is assigned by convention. **Gaussian curvature** is an intrinsic measure of curvature and may be perceived if sitting on the object itself. Hence, its value depends on the distances measured on the surface, independent of how they are embedded in space (Kühnel, 2002).

We define positive mean curvature if the membrane curves toward the binding object (e.g. a protein) and negative otherwise (Fig. 1.2.2). The sign of Gaussian curvature depends on the shape of the object itself. A sphere is characterized by having both principal curvatures positive (and equal), therefore $K > 0$. Conversely, a saddle will have one positive and one negative principal curvature, therefore $K < 0$. Finally, cylinders have one positive curvature, while the other is zero, making $K = 0$ (Fig. 1.2.2). Evidently, we need both curvatures to describe the geometry of a membrane and determine the energy required to deform a membrane from its spontaneous shape. For example, if a membrane is shaped into a saddle of equal magnitudes of principal curvatures, its mean curvature will be zero, while its Gaussian curvature will not. Such shape is found, for example, at the base of membrane buds formed in clathrin-mediated endocytosis. The inverse case is for a cylinder, a ubiqui-

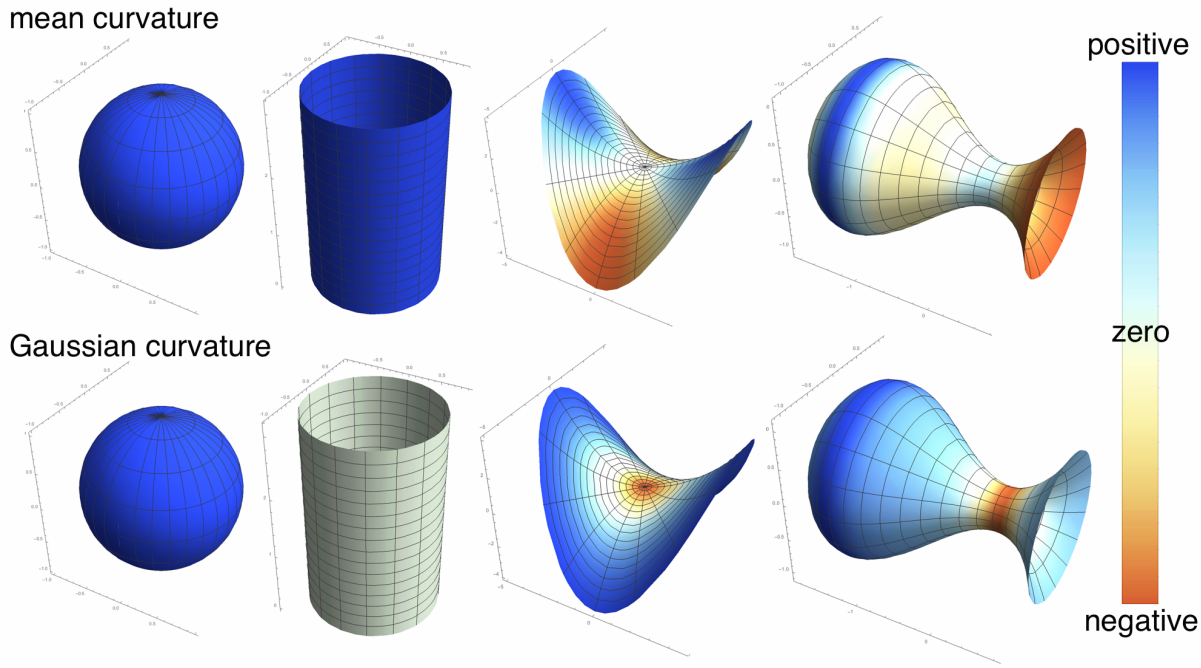

Figure 1.2.2: Membrane curvature. From left to right: sphere, cylinder, saddle, spherocylinder (may represent a step in endocytosis). Surfaces are color-coded based on mean (top row) and Gaussian (bottom row) curvatures. Note, mean curvature of a saddle is zero only if both principal curvatures have the same magnitude (not the case in this figure).

tous membrane shape in the cell, where Gaussian curvature is zero and mean curvature is positive (McMahon and Gallop, 2005). Figure 1.2.2 shows three basic membrane shapes, including a complex shape resembling a vesicle budding off a surface, color-coded based on both types of curvatures. Of note, Gauss-Bonnet theorem states that if in the course of shape changes the topology or the boundaries of the membrane patch remain unchanged, the integral accounting for the Gaussian curvature is constant. Therefore, we frequently omit the Gaussian curvature contribution from the Helfrich Hamiltonian.

Bending modulus of lipid membranes is in the range from 1 to 100 k_BT, where k_B is the Boltzmann constant and T the thermodynamic temperature. To illustrate the high bending elasticity of lipid membranes, consider polyethylene (e.g. a plastic bag), which has a hundred times higher bending modulus. Bending modulus of very stiff materials, such as brass, is another hundred times higher (Sackmann, 1994). For membranes, the bending modulus is dependent largely on the lipid composition. In the case of PC lipids, increasing the length of a saturated or a monounsaturated chain from 13 to 22 carbon atoms increases the bending modulus from 13 to 30 k_BT. The value significantly drops to 10 k_BT for cis-polyunsaturated PC lipids (18–20 carbon atoms) (Rawicz et al., 2000). Cholesterol has for a very long time been thought to stiffen the membrane by ordering the lipid chains, however recent work has shown

Table 1.2.1: Elastic constants for some bilayer membranes.

composition	DOPC	DOPC/chol	SOPC	SOPC/chol (1:1)	red blood cell
κ_m	16	15 (for 2:1 mix)	22	60	44
κ_A	310	890 (for 1:1 mix)	290	1985	

that cholesterol has an effect only on lipids with fully saturated chains (Pan et al., 2008).

We can determine the membrane bending modulus by observing the macroscopic fluctuations of lipid vesicles, using flickering spectroscopy (Brochard and Lennon, 1975; Pecreaux et al., 2004) or the microscopic fluctuations of supported bilayers with X-ray and neutron scattering (Daillant et al., 2005; Salditt, 2005). Another way of measuring the elasticity of membranes is by observing the response of lipid vesicles to deformation, using micropipette aspiration (Evans and Rawicz, 1990), extrusion of a membrane tether (Derenyi et al., 2002; Hochmuth and Evans, 1982; Hochmuth et al., 1982), or by applying an external electric field (Kummrow and Helfrich, 1991). Bending modulus can be deduced from computational simulations of lipid membranes, by applying the same relations as used in flicker spectroscopy (Boek et al., 2005; Lindahl and Edholm, 2000) or by calculating the strain response upon external stress (den Otter and Briels, 2003; Farago and Pincus, 2004; Harmandaris and Deserno, 2006). Table 1.2.1 lists mean bending moduli, that show typical values for lipid bilayers, along with trends of adding cholesterol. The values presented were measured by vesicle-aspiration techniques and are taken from (Evans, 1983; Marsh, 2006).

Saddle splay modulus, κ_G, is notoriously difficult to determine (Marsh, 2006). The measurement would need to involve monitoring a shape transition in which both the topology and the boundaries of the bilayer change, such as membrane fission or fusion, which are typically highly dynamic processes. For this reason, there are only a few measurements of this elastic parameter on lipid bilayers (Baumgart et al., 2005; Hu et al., 2012; Lorenzen et al., 1986). Deserno and coworkers recently developed an interesting simulation approach, in which they let a circular cap spontaneously close into a sphere (Hu et al., 2012). The dynamics of this process depends on the interplay of the two elastic parameters and, knowing κ_m, κ_G can accurately be extracted. In their work, they found that κ_G is negative and has a magnitude very similar to κ_m ($-\kappa_G/\kappa_m = 0.90–1.05$).

Spontaneous curvature, c_0, is another intrinsic mechanical measure of the membrane and it represents its resting mean curvature. Strictly, a bilayer with symmetric and laterally homogenous composition in both leaflets, in the absence of ex-

ternal influence, will have c_0 = 0. To generate curvature in a resting membrane, an asymmetry needs to be brought into the system. The asymmetry may be supplied by 1), the difference in lipid composition between the two leaflets, 2), by introducing an asymmetrically shaped object into the membrane, and 3), by exposing the bilayer on each side to solutions containing different compositions of a), ions, b), particles, or c), proteins (Lipowsky and Dobereiner, 1998). There are other ways of generating membrane curvature, such as with external pulling force or by crowding. We will discuss the mechanism of generating membrane curvature in more detail in Section 1.3.

There are two additional parameters in the elastic energy of the membrane that come as Lagrange multipliers when constraining the area and the volume (Miao et al., 1994).

$$F_{\text{area}} = \sigma \int dA \,, \qquad \text{(Eq. 1.2.4)}$$

$$F_{\text{volume}} = \Delta p \int dV \,, \qquad \text{(Eq. 1.2.5)}$$

where σ and $\Delta p = p_{\text{out}} - p_{\text{in}}$ are the **membrane tension** and the **pressure difference** across the bilayer, respectively. They both represent the resistance to deformation either in the area or in the volume. While surface tension plays a very important role in membrane-remodeling phenomena, the pressure difference is typically considered vanishing and so Eq. 1.2.5 is rarely included in the total energy of the membrane. Membrane tension is related to the stretching modulus of the membrane, an intrinsic elastic parameter, via:

$$\sigma = \kappa_A \frac{A - A_0}{A_0} \,, \qquad \text{(Eq. 1.2.6)}$$

where κ_A is the stretching or the area compressibility modulus, A and A_0 are the current and the equilibrium area, respectively. This mechanical parameter may be obtained by monitoring the expansion of lipid vesicles with micropipette aspiration at high tension. The values obtained were around 240 mN/m and, unlike the bending modulus, they did not significantly depend on the length or the saturation of lipid chains (Rawicz et al., 2000). See Table 1.2.1 for some representative values, taken from (Rawicz et al., 2008). The maximum a bilayer membrane can be stretched before it undergoes lysis—or break—is ~ 1–3%, corresponding to tensions between 1 and 30 mN/m, depending on composition (Olbrich et al., 2000; Rawicz et al., 2008).

Bending and stretching moduli are related through membrane thickness (h) as (Rawicz et al., 2000):

$$\kappa_m = \kappa_A \frac{h^2}{24}. \qquad \text{(Eq. 1.2.7)}$$

Due to their fluidity, membranes do not have a static **shear** strain and so shearing—applying a force parallel to a surface (Fig. 1.2.2)—does not contribute to the total free energy. Shear strain is important in the case of gel-phase bilayers or in biological membranes in contact with the cytoskeleton. Membranes have a shear viscosity, which is a dynamic property measuring the stress as a response to a difference in shear rate. Shear viscosity is a result of the friction between the two layers (den Otter and Shkulipa, 2007).

Finally, by combining the contributions from bending, stretching, and pressure, **Helfrich Hamiltonian** of a vesicle (F_H) becomes:

$$F_\mathrm{H} = \int dA \left[\frac{\kappa_\mathrm{m}}{2} \left(c_1 + c_2 - c_0 \right)^2 + \kappa_\mathrm{G} c_1 c_2 \right] + \sigma \int dA + \Delta p \int dV \,. \qquad \text{(Eq. 1.2.8)}$$

1.2.2) Thermal fluctuations. According to (Brochard and Lennon, 1975), as early as 1890 the researchers observed a breathing or flickering motion of red blood cells under a light microscope. Interestingly, in later years, this observation was often attributed to active enzymatic processes on the cell membrane. We understand today that the phenomenon is purely physical and is a consequence of random thermal fluctuations which give rise to undulatory motions of the membrane. Brochard & Lennon have measured this motion in red blood cells and theoretically predicted near-micron fluctuation wavelengths in the limit of negligible tension, which is why we are able to observe flickering of tensionless red blood cells or GUVs with light microscopy (Fig. 1.2.3, A) (Brochard and Lennon, 1975; Pecreaux et al., 2004).

To describe these motions it is easier to reformulate the Helfrich Hamiltonian by using the Monge gauge parameterization that simplifies the calculation of curvature (Fig. 1.2.3, B). In this representation, the membrane surface is written in terms of a height function ($h(x,y)$) from a reference plane (typically the midplane of the membrane), parameterized by x and y, i.e., $u(x,y,h(x,y))$. It is important that the surface has no overhangs, meaning that the projection on the surface is unique. Alternatively, one can use a rotated base plane or, for example, parameterize the surface with spherical coordinates. Using Monge gauge, we can calculate the surface element as (Brown, 2008; Chaikin and Lubensky, 2000):

$$dA = dxdy\sqrt{1 + \left(\partial h / \partial x\right)^2 + \left(\partial h / \partial y\right)^2} \,. \qquad \text{(Eq. 1.2.9)}$$

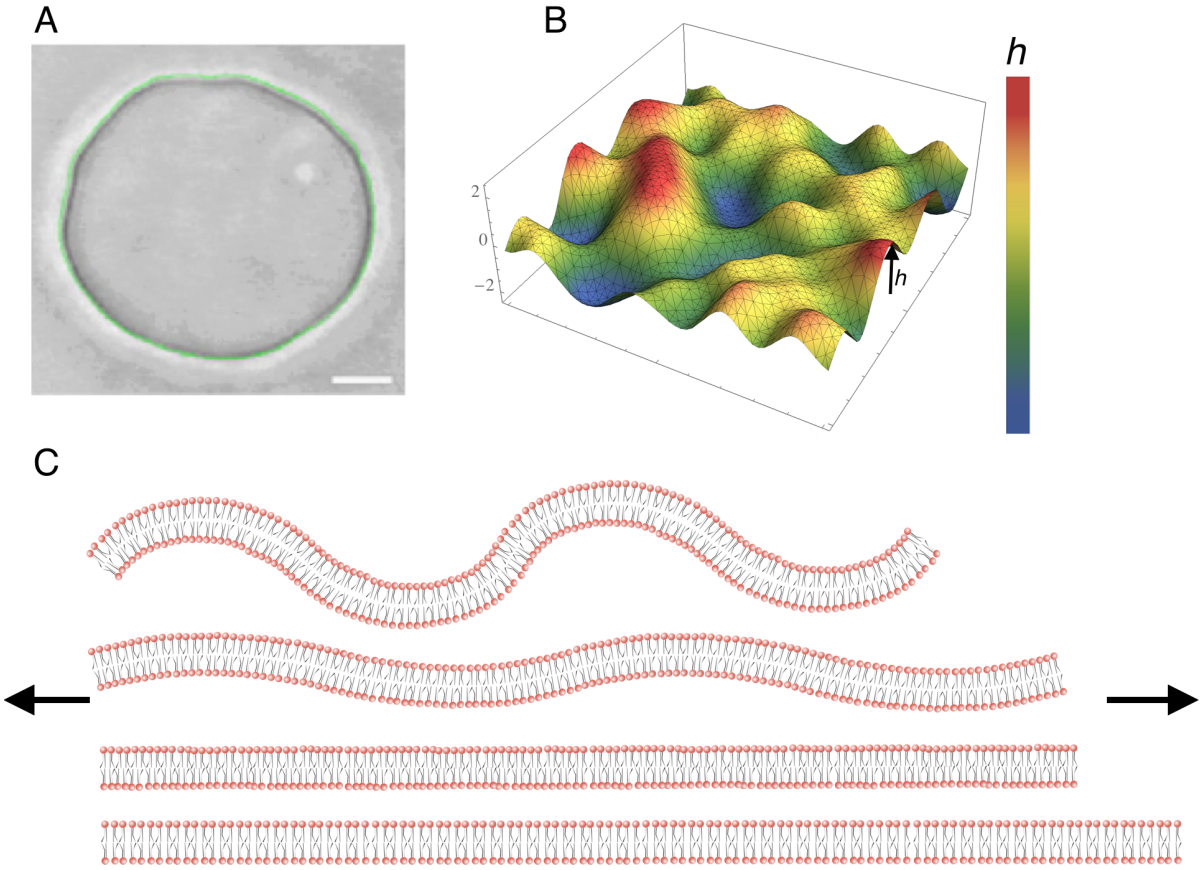

Figure 1.2.3: Thermal fluctuations. (A) Left: A fluctuating GUV with its contour highlighted in green. Scale bar is 5 μm. Adapted from (Pecreaux et al., 2004). (B) A fluctuating surface, color-coded based on the height from the surface midplane, as in the Monge representation of the membrane. (C) Applying tension on a fluctuating membrane (arrows represent the direction of the stress). Initially membrane tension is in the entropic regime (top two cartoons). Additional stress shifts the membrane in the enthalpic regime (bottom two cartoons). All membrane cartoons contain the same number of lipids.

From this expression it turns out that the local mean curvature at any point in the low-gradient approximation, i.e. $\nabla h \ll 1$, is simply:

$$H_{\mathrm{m}} = \frac{1}{2}\left(\frac{\partial^2 h}{\partial x^2} + \frac{\partial^2 h}{\partial y^2}\right) = \frac{1}{2}\nabla^2 h\,. \qquad \text{(Eq. 1.2.10)}$$

By analyzing the geometry of the surface compared to its projection, we can rewrite the tension in the Monge representation as:

$$\frac{A - A_0}{A_0} = 1 - \cos\varphi \approx \frac{\varphi^2}{2} = \frac{1}{2}(\nabla h)^2\,, \qquad \text{(Eq. 1.2.11)}$$

where φ is the angle between the surface element and the base plane. Neglecting Gaussian and spontaneous curvatures, we write the **Helfrich Hamiltonian**, F_{H}, as:

$$F_{\mathrm{H}} = \frac{1}{2}\int_A \left[\kappa_{\mathrm{m}} \left(\nabla^2 h \right)^2 + \sigma \left(\nabla h \right)^2 \right], \qquad \text{(Eq. 1.2.12)}$$

where A, again, is the area, although strictly it is the projected membrane area onto the base plane. For simplicity in calculation, we turn to reciprocal space by carrying out a Fourier expansion:

$$h(\mathbf{r}) = \sum_{\mathbf{q}} h(\mathbf{q})\, e^{i\mathbf{q}\mathbf{r}}, \qquad \text{(Eq. 1.2.13)}$$

where $\mathbf{r} = (x, y)$ and $\mathbf{q} = (q_x, q_y)$ are the real-space and reciprocal-space vectors, respectively, q being the wave number. The Helfrich Hamiltonian becomes:

$$F_{\mathrm{H}} = \frac{1}{2A} \sum_{\mathbf{k}} \left(\kappa_{\mathrm{m}} q^4 + \sigma q^2 \right) \left| h(\mathbf{q}) \right|^2, \qquad \text{(Eq. 1.2.14)}$$

where,

$$h(\mathbf{q}) = \int_A d\mathbf{r}\, h(\mathbf{r}) e^{-i\mathbf{q}\mathbf{r}}. \qquad \text{(Eq. 1.2.15)}$$

Now, we calculate the thermal average of $h(\mathbf{q})^2$, by applying the equipartition theorem, $\langle F \rangle = \frac{1}{2} k_{\mathrm{B}} T$, on individual Fourier amplitudes (so-called q-modes), yielding a **fluctuation spectrum**:

$$\left\langle \left| h(\mathbf{q}) \right|^2 \right\rangle = \frac{L^2 k_{\mathrm{B}} T}{\kappa_{\mathrm{m}} q^4 + \sigma q^2}, \qquad \text{(Eq. 1.2.16)}$$

where L is the length of a square membrane patch and the angular brackets represent ensemble average.

Based on Eq. 1.2.16 we can distinguish two q-regimes. In the case of low surface tension ($q \gg \sqrt{\sigma/\kappa_{\mathrm{m}}}$), the fluctuation spectrum is in the q^{-4} regime and so the long wavelengths are dominant. We can estimate the root-mean-square amplitude (h_{RMS}) in this regime by summing over q, which gives (Lindahl and Edholm, 2000):

$$h_{\mathrm{RMS}} \approx \sqrt{\frac{L^2 k_{\mathrm{B}} T}{8.3 \pi^3 \kappa_{\mathrm{m}}}}. \qquad \text{(Eq. 1.2.17)}$$

Evidently, increasing the stiffness of the membrane decreases its undulation amplitude. We can therefore estimate for a membrane patch with 20 μm length (typical membrane size in experimental systems) the amplitude of fluctuations to be 0.3 μm, a wavelength accessible to light microscopy. Taking a much smaller membrane patch, such as one used in simulations, significantly decreases this amplitude. In particular, a 100 nm by 100 nm membrane patch will yield an amplitude of only 1.6 nm.

In the case of a high surface tension ($q \ll \sqrt{\sigma/\kappa_m}$), the q^{-2} term dominates, and we can estimate:

$$h_{RMS} \sim \sqrt{\frac{k_B T}{\sigma} \ln \frac{L}{a}}, \qquad \text{(Eq. 1.2.18)}$$

where a is the diameter of a lipid molecule. Plugging in the same values for the hypothetical large-scale experimental system above (L = 20 μm, a = 0.5 μm, σ = 0.1 mN/m), the amplitude becomes only 12 nm.

Analogously, we can sum over q in Eq. 1.2.16 to describe the fluctuations in the membrane area (Brown, 2008):

$$\frac{\langle A - A_0 \rangle}{A_0} = k_B T \sum_{\mathbf{q}} \frac{q^2}{\kappa_m q^4 + \sigma q^2}, \qquad \text{(Eq. 1.2.19)}$$

$$\frac{\langle A - A_0 \rangle}{A_0} \approx \frac{k_B T}{8\pi\kappa_m} \ln\left(\frac{\pi^2 / a^2 + \sigma / \kappa_m{}^2}{\pi^2 / A + \sigma / \kappa_m{}^2} \right), \qquad \text{(Eq. 1.2.20)}$$

Again, we can distinguish two regimes. In the limit of vanishing tension, the excess area reduces to:

$$\frac{\langle A - A_0 \rangle}{A_0} \approx \frac{k_B T}{8\pi\kappa_m} \ln\left(\frac{L}{a} \right). \qquad \text{(Eq. 1.2.21)}$$

Under low tension, i.e. when we stretch the membrane on the scale much larger than molecular, but still smaller then the system size ($\kappa_m \pi^2 / L^2 << \sigma << \kappa_m \pi^2 / a^2$), the formulation becomes:

$$\frac{\langle A - A_0 \rangle}{A_0} \approx \frac{k_B T}{8\pi\kappa_m} \ln\left(\frac{\kappa_m \pi^2}{\sigma a^2} \right), \qquad \text{(Eq. 1.2.22)}$$

and so as fluctuations are suppressed, the projected area logarithmically increases with tension (Evans and Rawicz, 1990). At high tension, we can apply elastic theory

as in Eq. 1.2.6 to calculate the excess area. The low-tension regime is also called the **entropic** regime, because with applying tension we are unfolding the membrane without inducing any in-plane stretching. The latter regime is the **enthalpic** regime where we indeed stretch the membrane and affect the non-bonded interactions among lipids (Fig. 1.2.3, C) (Evans and Rawicz, 1990). Combining the two regimes, we obtain the expression:

$$\frac{\langle A - A_0 \rangle}{A_0} \approx \frac{k_B T}{8\pi\kappa_m} \ln\left(\frac{\kappa_m \pi^2}{\sigma a^2}\right) + \frac{\sigma}{\kappa_A}. \qquad \text{(Eq. 1.2.23)}$$

The presented formulation accounts for the total area of the membrane, which, in one part, is stored in the optically resolved fluctuations and, in other part, in short scale fluctuations not visible with optical microscopy. Fournier and coworkers proposed an effective Hamiltonian that integrates out these short scale fluctuations, therefore defining an effective membrane tension related to the optically resolved area. This measure is more appropriate for interpreting micropipette aspiration experiments (Fournier et al., 2001).

Strong undulations affect the mechanical properties of the membrane. We can write the general expression for the effective modulus ($\kappa_{m,eff}$) as (Helfrich, 1998; Peliti and Leibler, 1985):

$$\kappa_{m,\,eff} = \kappa_m \left(1 - \alpha \frac{A - A_0}{A_0}\right), \qquad \text{(Eq. 1.2.24)}$$

where α is a numerical factor. Interestingly, different theoretical treatment of the membrane led to qualitatively different consequences for the effective bending modulus. Peliti and Leibler demonstrated that thermal fluctuations decrease the effective bending modulus (with $\alpha = 3$), reasoning that fluctuations make the membrane more crumpled and corrugated, thus easier to bend (Peliti and Leibler, 1985). Conversely, Helfrich finds the opposite effect of thermal fluctuations (with $\alpha = -1$), arguing that fluctuations induce the crinkling of the membrane, which stiffens it (Helfrich, 1998).

1.2.3) Non-thermal fluctuations. To end this subchapter, it is worth mentioning that cellular processes at the macroscopic level can also be governed by stochastic forces that are not thermal in origin. An example are stochastic forces coming from the cytoskeleton, as a collective motion of molecular motors. These forces induce non-thermal, directed motion in the cell and are thought to enhance the transport of various components in the cytoplasm, such as vesicles, mitochondria, and signaling proteins (Guo et al., 2014). It is important to note that the pulling and pushing action of actin filaments on the membrane are most prevalent form of active fluctuations. Typ-

ically, it is assumed that thermal fluctuations dominate all other random forces on the membrane, and this assumption seems valid in many cases. However, Prost and Bruinsma have shown that in membranes coupled to an active process, at larger length scales, the fluctuations are actually dominated by the non-equilibrium noise (Prost and Bruinsma, 1996). The activity of ion channels, for instance, can give rise to non-equilibrium fluctuations, as shown experimentally (Girard et al., 2005; Manneville et al., 1999).

1.3. Remodeling biological membranes

1.3.1) The "real" cell membrane. The theoretical modeling outlined in the previous section treats the membrane as a thin elastic sheet, subjected to thermal fluctuations, and ignores any in-plane inhomogeneities. It provides an excellent understanding of the equilibrium shapes and phase behavior of membranes, which makes them flexible barriers between the cell or its organelles and the surrounding medium. However, biological membranes are not at equilibrium. They house active processes such as the translocation of molecules across the bilayer or the redox reactions in oxidative phosphorylation, the key metabolic pathway in the cell (Berg et al., 2002). Another source of complexity of cell membranes is their composition, as illustrated in Fig. 1.3.1, A.

Lipids are not evenly distributed among organelles and the composition even differs between the leaflets of the same bilayer (except in the endoplasmic reticulum) (Holthuis and Levine, 2005; van Meer et al., 2008). The asymmetry in composition is crucial to achieve specific functions localized to the particular segment of the cell. Lipids are initially synthesized primarily in the endoplasmic reticulum, Golgi apparatus and the lipid droplets. Then, they are selectively transported to their designated leaflet, primarily via vesicular trafficking, although new hypotheses are emerging in the field of lipid transport (van Meer et al., 2008). The outer leaflet of the plasma membrane is primarily composed of PC and SM lipids, whereas the inner leaflet contains mostly PE and PS lipids (Fig. 1.3.1, B) (Cooper, 2000). Another constituent of the inner leaflet is a family of PI lipids, notably phosphatidylinositol 4,5-bisphosphate (PIP_2), a lipid used in this study. Chemically, PIP_2 is doubly phosphorylated on the inositol ring, giving it high charge density (Fig. 1.3.1, C). This lipid participates in a number of signaling events, binding to G-protein-coupled receptors. It also specifically binds to some protein domains, promoting the recruitment of proteins to the membrane, for example in endocytosis (see Section 1.4) (Alberts et al., 2014; Cooper, 2000; McLaughlin and Murray, 2005).

So far, we only discussed lipids as membrane constituents. In fact, cell membranes on average contain only 50% lipids by mass, the rest mostly being made up of

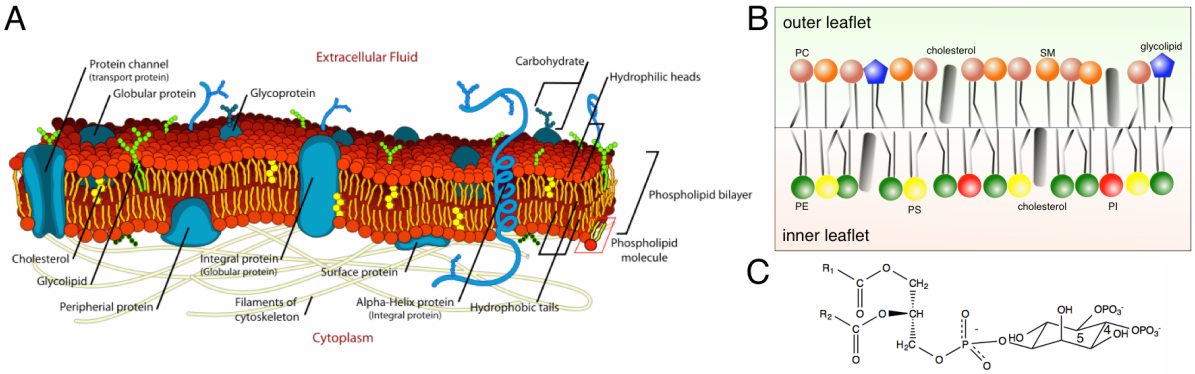

Figure 1.3.1: Cell membrane. (A) A cartoon of a cell membrane depicted with various types of lipids, proteins and the cytoskeleton. Taken from wikipedia. (B) The asymmetry in composition of the plasma membrane. The number fraction of individual lipid species is exaggerated. (C) Molecular structure of PIP_2.

proteins (Alberts et al., 2014). The two extreme examples are the inner mitochondrial membrane, which contains ~ 80% proteins, while the myelin membrane contains only ~ 20% proteins. The high protein content in mitochondria is a result of the oxidative phosphorylation machinery that takes place in this organelle, whereas the high lipid amount in myelin serves to electrically isolate the nerves from their environment (Lodish, 2008). Cell membrane is also in contact with the cytoskeleton, which imparts mechanical properties and may influence the behavior of the membrane.

A highly celebrated view of the cell membrane is the fluid mosaic model, proposed by Singer and Nicolson in 1972 (Singer and Nicolson, 1972). The model sees the membrane as a liquid two-dimensional bilayer with proteins embedded among lipids at low concentrations (Fig. 1.3.1, A). The fundamental aspects of the model are correct, but over the years it has been elucidated that the membrane is structurally much more complex and it is far from being a static macromolecular assembly (Goni, 2014). The novel view of the membrane includes many more transmembrane and peripherally bound proteins and it accounts for those that only temporarily bind (such as BAR proteins). It is also suspected that other lipid phases, besides the l_d phase, exist in the cell. Furthermore, the existence of phase separation *in vitro* has stimulated numerous studies trying to capture the aforementioned lipid rafts in the cell. Lipid rafts remain a very attractive notion, since phase separation in the cell could potentially segregate certain lipids from others (Simons and Ikonen, 1997; Simons and van Meer, 1988). This process would potentially form active domains, enhancing signaling, endocytosis, exocytosis, fusion, etc. Although their existence, size, lifetime, and role in biology are continuously being unveiled (Lingwood and Simons, 2010; Simons and Sampaio, 2011), it is not entirely clear whether they are formed by equilibrium thermodynamics or by active processes (Feigenson, 2006;

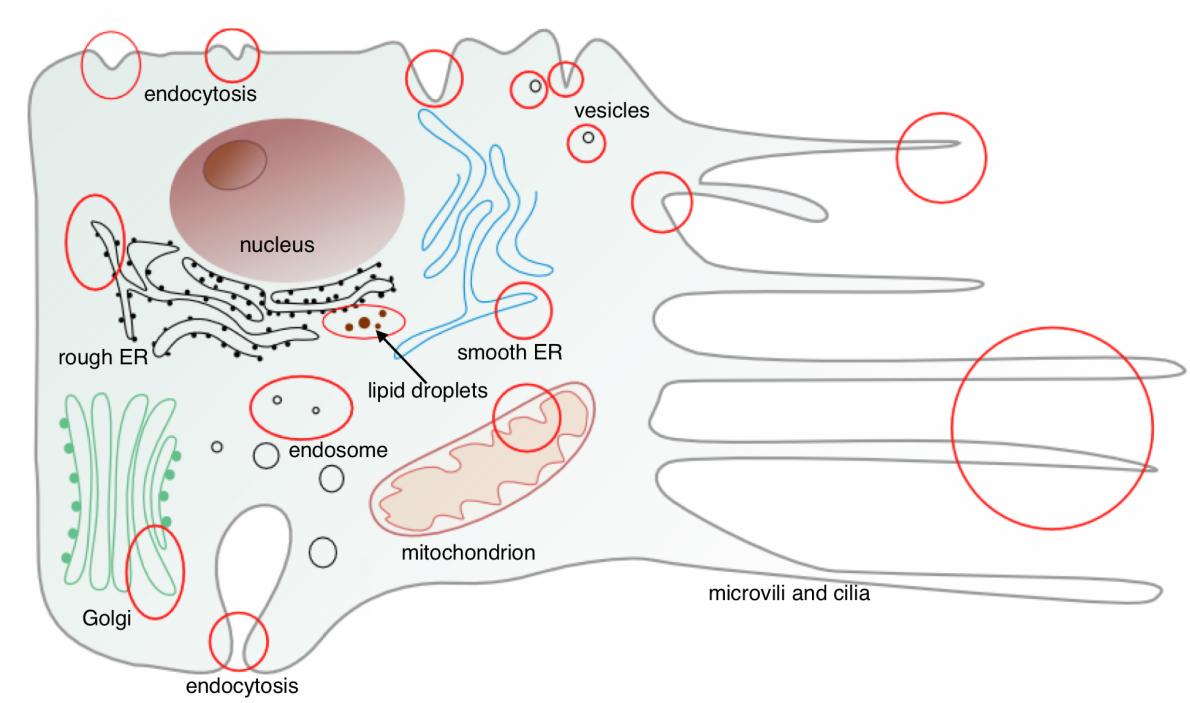

Figure 1.3.2: Curvature in the cell. A simplified cell model, highlighting various cellular membranes that are highly curved and where active processes occur due to curvature (red circles). Scale is exaggerated for clarity. ER - endoplasmic reticulum.

Jacobson et al., 2007; Munro, 2003; Sens and Turner, 2011; Turner et al., 2005; van Meer et al., 2008).

1.3.2) Generating membrane curvature — theory. The fluid mosaic model is concerned mostly with membrane composition at small scales and it neglects a very important aspect of cell membranes — presence of highly curved geometries. Figure 1.3.2 illustrates the morphological complexity of various cellular membranes. Membrane curvature has been widely accepted to play significant roles in the cell and it is, in fact, the central topic of this thesis. Some cellular junctions, such as microvili, are permanently curved. Another example is the endoplasmic reticulum, which has a particularly complex shape, composed of a three-dimensional network of tubules. On the other hand, some parts of cell membranes only temporarily adopt curvature. Transiently generating curvature is key to carrying out many important functions, such as endocytosis, vesicular trafficking, or in the formation of dynamic filopodia (McMahon and Gallop, 2005).

Thermal fluctuations have the energy of the order of 1 $k_B T$. Considering that the bending modulus of the membrane is usually an order of magnitude higher, fluctuations are insufficient to induce permanent curvature in the membrane. There are multiple ways to generate curvature and the resulting geometry is likely a combination of several of these mechanisms. Originally, Helfrich and Canham explained different membrane morphologies solely by varying the spontaneous curvature

term, and so their model is often referred to as the **spontaneous-curvature model** (Canham, 1970; Helfrich, 1973). Another theory, called the **bilayer-couple model**, was subsequently proposed, where the shapes are calculated by fixing the difference in areas between the two leaflet (Heinrich et al., 1993). Both of these theories yield many of the experimentally observed shapes of vesicles, however neither of the two approaches explains correctly the transition pathways or some more complex membrane geometries. A way to unite the two theories into a more flexible model is by including the spontaneous curvature and allowing the tensile forces to asymmetrically dilate the two leaflets. The free energy contribution from the change in the difference in area between the two leaflets, F_{ed}, can be described as elastic (Miao et al., 1994), therefore:

$$F_{\mathrm{ad}} = \frac{\kappa_{\mathrm{ad}}}{2}\frac{\pi}{Ad^2}\left(A^{\text{in-out}} - A_0^{\text{in-out}}\right)^2 \qquad \text{(Eq. 1.3.1)}$$

where $A^{\text{in-out}}$ and $A_0^{\text{in-out}}$ are the differences in areas of the two leaflets at a given step and at equilibrium, respectively, κ_{ad} is the area difference modulus (theoretically estimated to be comparable in magnitude to κ_{m}), d is the separation between the monolayers modeled as thin sheets, and A, as before, is the area of the membrane. The area difference between the two layers can be related to the total mean curvature (i.e. local curvature multiplied by the total area) of the membrane by geometric considerations:

$$A^{\text{in-out}} = Ad\left(c_1 + c_2\right). \qquad \text{(Eq. 1.3.2)}$$

The total energy for a vesicle experiencing shape changes is then given by adding Eq. 1.3.1 to Eq. 1.2.8 (and omitting the Gaussian curvature contribution), which gives the **area-difference elasticity model** (Kralj-Iglic et al., 1996; Svetina and Zeks, 1989):

$$F_{\mathrm{H}} = \int dA\left[\frac{\kappa_{\mathrm{m}}}{2}\left(c_1 + c_2 - c_0\right)^2\right] + \frac{\kappa_{\mathrm{ad}}}{2}\frac{\pi}{Ad^2}\left(A^{\text{in-out}} - A_0^{\text{in-out}}\right)^2 + \sigma\int dA + \Delta p\int dV\,. \qquad \text{(Eq. 1.3.3)}$$

Moreover, spontaneous curvature is not a constant; rather, it is affected by the asymmetric binding of particles, ions, or proteins. At the molecular level, we can visualize that particles tilt the surrounding lipid head groups and this way induce curvature. When the density of particles is low—therefore they do not interact with one another—we assume that the spontaneous curvature is linearly dependent on the amount of bound particles:

$$c_{0,\,\mathrm{eff}} = \sum_i^N \phi_i \overline{c}_i\,, \qquad \text{(Eq. 1.3.4)}$$

where ϕ is the area density of bound particle i, N the total number of particles, and $\bar{c}$ the intrinsic spontaneous curvature of the bound particles (Callan-Jones and Bassereau, 2013; Leibler, 1986). This intrinsic curvature is the effective curvature a single particle would impart on the membrane at equilibrium and does not necessarily reflect the actual shape of the bound particle. In Eq. 1.3.4 we added a subscript to the total spontaneous curvature to distinguish particle-imposed curvature from the spontaneous curvature of a bare membrane, c_0. Leibler included the contribution from this interaction into the Helfrich Hamiltonian as a linear contribution to the total free energy, according to:

$$F_{\mathrm{H}} = \int dA \left\{ \left[\frac{\kappa_{\mathrm{m}}}{2} \left(c_1 + c_2 - c_0 \right)^2 \right] - \Lambda \phi \left(c_1 + c_2 \right) + \frac{1}{2} b |\nabla \phi|^2 + f[\phi] \right\}. \qquad \text{(Eq. 1.3.5)}$$

In Eq. 1.3.5 the first term is the elastic bending energy as before, where c_0 is often taken as zero, considering that studied membranes typically have equal lipid composition in the two layers. Second term is the curvature-coupling term, where Λ is the coupling strength. The last two terms account for the diffusion of bound particles, with b being a phenomenological parameter and $f[\phi]$ has the shape of a Landau mean-field energy. Again, we can minimize this Hamiltonian by constraining the surface and the volume (and the difference in leaflet areas), which will add membrane tension and pressure difference in the calculation.

A different expression for the spontaneous curvature, which only depends on the bound densities of particles, is given by Lipowsky and Dobereiner:

$$c_0 = \frac{k_{\mathrm{B}} T}{4 \kappa_{\mathrm{m}}} d \left(\phi_{\mathrm{out}} - \phi_{\mathrm{in}} \right), \qquad \text{(Eq. 1.3.6)}$$

where d, as before, is the separation between two monolayers, ϕ_{out} and ϕ_{in} are the respective concentrations on the outer and the inner layer. By applying the Langmuir adsorption isotherm, which relates the bulk concentration (C) to the bound concentration (ϕ) of particles via the equilibrium coefficient K_{d}, we obtain:

$$c_0 = \frac{k_{\mathrm{B}} T}{4 \kappa_{\mathrm{m}}} d \phi_{\max} \frac{C_{\mathrm{out}} - C_{\mathrm{in}}}{K_{\mathrm{d}}}, \qquad \text{(Eq. 1.3.7)}$$

where $\phi_{\max}$ is the maximum bound density of particles (Lipowsky, 2013; Lipowsky and Dobereiner, 1998).

1.3.3) Generating membrane curvature — examples. Let us now examine the most important mechanisms of generating curvature in the cell.

A) Lipid composition. We already discussed that the three-dimensional shapes of some lipids may induce curvature. For example, cylindrical lipids will repel one another due to their large head groups (Fig. 1.3.3, left). To alleviate steric stresses, the layer containing these lipids will expand, which in turn results in positive spontaneous curvature. In a cell membrane, it is possible to enrich one layer with cylindrical lipids by way of protein-mediated flip-flop or by chemically modifying lipids by enzymes. For example, sphingomyelinase cuts off the phosphate head group from SM, enriching the ceramide content in the leaflet exposed to this enzyme. Ceramide is shaped like an inverted cone, with tail groups bulkier than the head group. Therefore, ceramide dilates the opposite layer, inducing negative spontaneous curvature and tubulation, which has been experimentally demonstrated (Holopainen et al., 2000).

Another way of generating curvature with lipid composition is by phase separation, as illustrated in Fig. 1.3.3, left. Each phase will have an edge energy, proportional to the length of the phase boundary. This energy and its conjugate, line tension, is the one-dimensional equivalent of the surface energy and its conjugate, surface tension. To minimize the total length of edges, domains will coarsen and ultimately coalesce into two distinct domains (Baumgart et al., 2003). At this point, there is a competition between bending, line tension, and surface tension. For instance, if line tension dominates, the edge will tend to be as small as possible, which can be achieved by budding out one of the domains. Budding, on the other hand, is opposed by the bending energy. Numerous free-energy minimization and Monte Carlo simulation efforts have been carried out to understand the morphological consequences of phase-separated vesicles. They have resulted in a very rich shape behav-

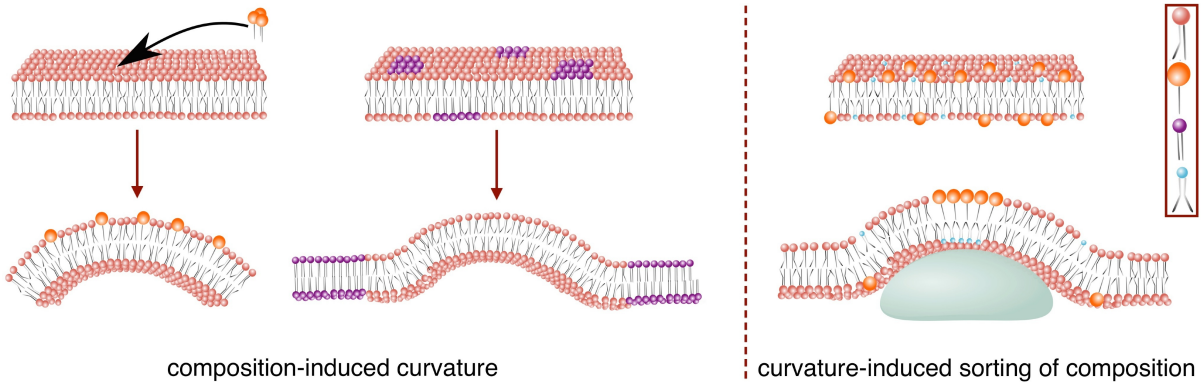

Figure 1.3.3: Coupling of lipid composition and membrane curvature. Mechanisms of generating membrane curvature: by asymmetrically introducing lipids (left) and phase separation (center). Lipid sorting of a membrane with mixed and symmetric composition. Curvature is induced by depositing a membrane on a curved substrate. Top right shows the shapes of individual lipids, from top to bottom: lipid typically in l_d phase, lipid with large head group, lipid typically in l_o phase, lipid with small head group.

ior of such systems. The ultimate consequence, i.e., the stabilization of finite-size domains, budding transitions, or the number of buds per vesicle seems dependent on the size of domains, the elastic properties of the membrane (namely, the bending moduli of individual domains), as well as surface and line tension (Funkhouser et al., 2010; Hu et al., 2011; Li et al., 2013; Rim et al., 2011; Semrau et al., 2009; Sens and Turner, 2006; Taniguchi, 1996; Taniguchi et al., 2011; Ursell et al., 2009).

B) Transmembrane inclusion. Proteins that span both leaflets of the membrane are called transmembrane proteins. Transmembrane proteins are expected to induce spontaneous curvature if they perturb one layer more than the other, which is the case for conically shaped proteins, like the blue protein in the cartoon in Figure 1.3.4. Examples of proteins with conical transmembrane domains are the nicotinic acetyl receptor (Unwin, 2005) and voltage-gated potassium channel (Mackinnon,

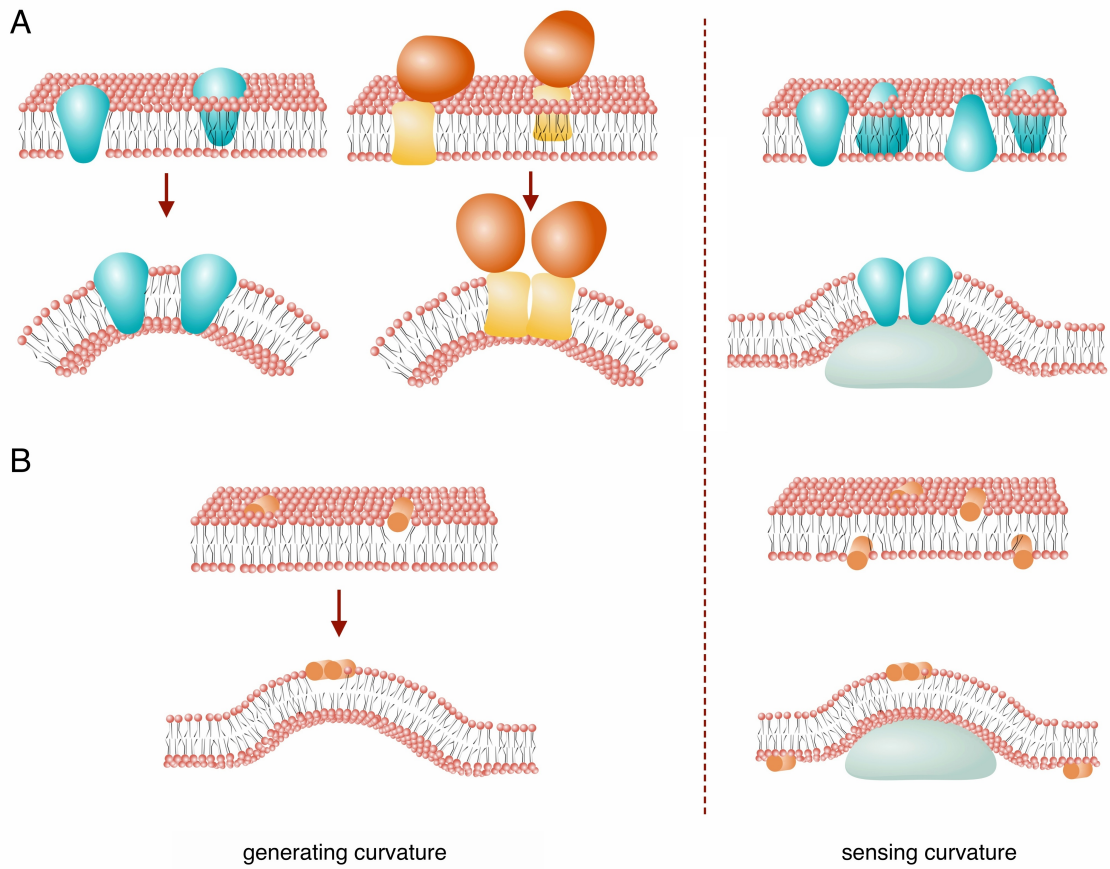

Figure 1.3.4: Coupling of membrane inclusions and curvature. Left: generating membrane curvature by (A) transmembrane proteins and (B) amphipathic helices. Conical transmembrane proteins and amphipathic helices induce curvature by asymmetrically tilting the neighboring lipids. Cylindrical transmembrane proteins may hypothetically induce curvature by steric clashes of bulky ligands. Right: sensing membrane curvature by (A) transmembrane proteins and (B) amphipathic helices. In both cases, the membrane contains symmetric composition therefore spon-

2004). Theoretically, we can treat the inclusion of proteins via the spontaneous curvature term as before, although it may be necessary to include structural and mechanical parameters of the protein itself, such as rigidity (Aimon et al., 2014). Hypothetically, cylindrical transmembrane proteins can be expected to induce curvature if they are attached to bulky ligands. Such ligands would tend to separate the proteins, easily achieved by budding or tubulation, illustrated by the yellow protein in Figure 1.3.4 (Johannes et al., 2014; McMahon and Gallop, 2005). The interaction among ligands can also be explained in terms of entropic pressure, which is described below.

C) Shallow insertion. Some proteins and their domains partially penetrate into the bilayer, which can induce significant stress on the binding leaflet (Fig. 1.3.4, B, left). Chemically speaking, in order not to get absorbed by the hydrophobic core of the bilayer, domains that shallowly insert into the bilayer need to be amphipathic, so that one side of the molecule attracts hydrophobic lipid tails, whereas the other is bound to the hydrophilic head group. Many cytosolic and peripherally binding proteins contain amphipathic helices. Apolipoproteins, for example, solubilize lipids, including cholesterol, for their transport through blood (Walther and Farese, 2009; Wilson et al., 1991). Another large group of proteins that insert into the lipid bilayer is a family of antimicrobial peptides. Their insertion into the lipid core can reduce line tension, promoting the formation of pores. Antimicrobial peptides have an important immunological role as they attack bacteria (Brogden, 2005). Many proteins involved in endocytosis contain amphipathic helices, implicated in various forms of membrane remodeling (Boucrot et al., 2012). The curvature-coupling of amphipathic helices is one of the research topics of this thesis and will be detailed later.

Theoretical investigation has shown that the degree of insertion is the key parameter in determining the effective spontaneous curvature of the membrane (Campelo et al., 2008; Zemel et al., 2008). Moreover, the relationship between spontaneous curvature and insertion depth is not trivial. Insertion at a depth of approximately one third of the thickness of one layer induces maximum curvature. With further insertion, the magnitude of spontaneous curvatures decreases and reverses sign at two thirds layer thickness (Zemel et al., 2008). According to these calculations, shallow insertions markedly increase the effective bending modulus for very thin bilayers to as much as 150 $k_{\mathrm{B}}T$. The elasticity of bilayers structurally similar to cell membrane is much less sensitive to insertion, although it is affected, especially at the insertion depth that produces maximum curvature (Zemel et al., 2008). Importantly, these predictions have not yet been quantified experimentally.

D) Adhesion. Membrane deformation by peripherally bound objects is likely the most difficult mechanism to rigorously explain from the theoretical point of view. It is also the mechanism that has received significant attention from the biologists and physicists in different contexts. Early experiments with nanoparticles

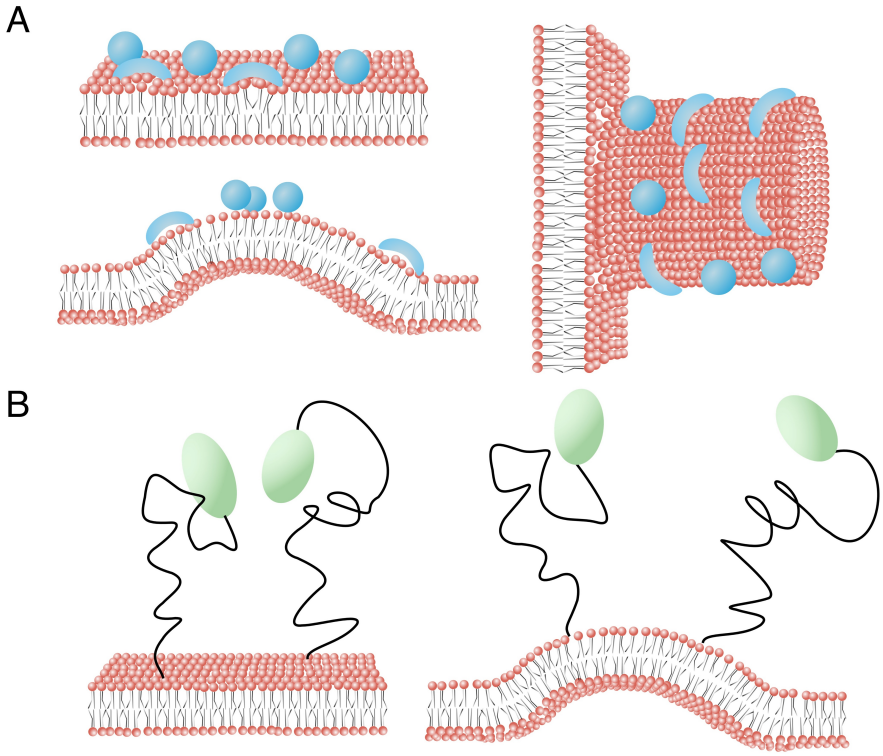

Figure 1.3.5: Membrane adhesion and entropic pressure. (A) Left: Generating membrane curvature by adhesive interactions of spherical particles (that include ions) and BAR proteins. Note, how BAR proteins were purposely placed close to the neck of the induced bud based on results from molecular dynamics simulations (Simunovic et al., 2013b). Right: Sensing positive mean curvature by BAR proteins and hypothetically by adhesive particles (the latter has not been demonstrated yet). The cylindrical curvature was depicted on purpose, as BAR proteins did not show preference for curvature of small tethered liposomes (see text). (B) Generating curvature by entropic pressure created by a two-dimensional gas of tethered particles (green).

bound to GUVs have demonstrated that few particles on the membrane will associate and induce moderate curvature (Koltover et al., 1999). A myriad of theoretical studies followed, which have shown that nanoparticles may induce both small and very large deformations. The magnitude of deformation as well as curvature-induced aggregation of particles depends on a number of parameters, but mostly on the particle-membrane interaction strength, bending modulus, and membrane tension (Saric and Cacciuto, 2013). Although rarely viewed this way in literature, binding of proteins can in fact be examined similarly to binding of nanoparticles. Proteins are certainly more complex, 1), because they are comparable in size to membrane thickness, 2), their shape is not simple, 3), the way they interact with the membrane is typically multimodular, and 4), proteins may undergo conformational changes. That said, experimental studies combined with analytical theory have been able to condense these complexities into generic parameters, such as spontaneous curvature, and successfully relate the experimental observations with physical models (Callan-

Jones and Bassereau, 2013). BAR proteins are especially challenging to theorists, as they often have both the shallow insertion domains and the adhesive component, therefore it is difficult to succinctly describe all these interactions. Recent computational studies were successful in accounting for this complexity by the anisotropic modeling of the protein, demonstrating the remodeling prowess of BAR proteins (Kabaso et al., 2012; Ramakrishnan et al., 2013; Simunovic et al., 2013a; Simunovic et al., 2013b). Figure 1.3.5, A illustrates the generation of membrane curvature by adhesive particles and molecules.

E) Entropic pressure and crowding. We discussed that transmembrane proteins may recruit bulky molecules to the surface that form steric repulsions, which will drive positive curvature to alleviate the stress. In a similar way, it has been proposed that curvature may be generated by entropic pressure created by crowding. This hypothesis was first computationally demonstrated by calculating the morphological effect of grafted polymers on the membrane. Binding of such chains does not fall into any of the aforementioned categories of inducing curvature. Therefore, a new mechanism was proposed in which the loss of conformational entropy creates a heterogeneous pressure field that can deform the underlying soft surface (Fig. 1.3.5, B) (Bickel et al., 2001; Breidenich et al., 2000). The calculations were later experimentally demonstrated by tethering DNA and proteins on the membrane (Nikolov et al., 2007; Stachowiak et al., 2012). In the latter experiment, the authors hypothesize that molecules tethered to the membrane collide with one another, thus forming a two-dimensional gas-like phase above the membrane plane. Thus created pressure can impart a bending moment across the separation distance and generate curvature (Stachowiak et al., 2012). The authors claim that crowding is especially relevant in the context of the insertion mechanism. According to theoretical predictions, a complete membrane coverage by amphipathic helices is required for the insertion mechanism to have a large-scale effect (Campelo et al., 2008). Such concentrations are unlikely realizable in cells, therefore crowding is an attractive alternative explanation how proteins containing such modules induce curvature at lower densities. Kozlov, McMahon and coworkers disagree with this assessment. They provide experimental evidence where the same concentration of bound proteins induced a large-scale shape change only in the case of the protein that shallowly inserted into the membrane. Furthermore, they cast doubt on the physiological relevance of the lipid composition in the work by Stachowiak *et al*, as this composition had been previously shown to readily undergo remodeling. They also hypothesize that in cells the entropic pressures would cancel out, since both sides of the cell are likely equally crowded. Hypothetically, if by virtue of an active mechanism certain proteins would get locally crowded, they would cease to freely diffuse and hence could not behave like a two-dimensional gas above the surface (Kozlov et al., 2014). As will be shown in this thesis, increased concentrations of BAR proteins inhibit the movement of both

the proteins and the lipids underneath, therefore generating the entropic pressure does not seem very likely in the case of BAR proteins.

F) Coating and scaffolding. Some proteins form a three-dimensional network that can impart its shape, like a mold, on the membrane. For example, BAR proteins and dynamin constrain the membrane in the tubular form (Fig. 1.3.6 A, right), whereas COPI, COPII, and clathrin constrain the membrane in the spherical form (Fig. 1.3.6, A left) (Johannes et al., 2014; McMahon and Gallop, 2005). It is important to note that BAR proteins are often described to generate curvature either via amphipathic helices or as tubular scaffolds. Tubular scaffolds stabilize curved geometries and can even fix the radius of the tubule, but such structures form *post facto*, they do not generate initial curvature. Therefore, neglecting the fact that BAR proteins act as adhesive particles on the membrane is incorrect. In other words, BAR proteins induce curvature of flat membranes by adhesive interactions, whereas after if forms a coat, it remodels the membrane by way of altering the radius of membrane tubules, which resist the rigid scaffold. I will further discuss the molecular details of dynamin, clathrin, and BAR-mediated curvature in the Section 1.4.

G) Molecular motors. Membrane curvature can be induced by external pulling force (Fig. 1.3.6, B). Such forces are generated by the cytoskeleton machinery and molecular motors. For example, the polymerization of actin filaments gives rise to many curved cellular geometries, such as filopodia, pseudopodia, and axonal growth cones (Sheetz, 2001). *In vitro* reconstitution has demonstrated that molecular motors, such as kinesins and myosins, can attach to the membrane and extrude a nanotube, by moving along the cytoskeletal filaments (Koster et al., 2003; Roux et al., 2002). Considering that the force generated by single molecular motor proteins is on the order of 1 pN, it seems that the collective action of multiple motors is responsible for generating membrane tubules (Leduc et al., 2004). It has been speculated that

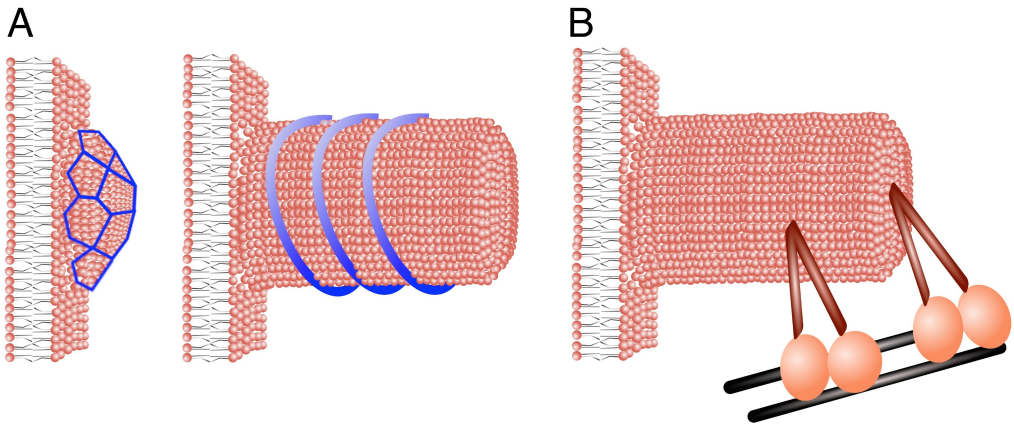

Figure 1.3.6: Shaping the membrane by molds and external force. (A) Molding the membrane by external structures, such as coats (left) and scaffolds (right). (B) Creating membrane tubes with external force, such as with molecular motors.

actin polymerization has a role in endocytic events (McMahon and Gallop, 2005) and we will show here the role of actin and molecular motors in generating external force that directly contributes to fission of membrane nanotubes (see Chapter 5).

1.3.4) Sensing membrane curvature — lipid and protein sorting. In the previous section, we discussed how asymmetric binding generates membrane curvature. Now, we reverse the argument, i.e. we explore how curvature affects the lateral organization of the membrane. If certain lipids or proteins, due to their shape, induce curvature instabilities in the membrane, it seems likely that they would prefer to assemble in curved regions, even if curvature was formed by some other means. Consider a curved membrane composed of conical and cylindrical lipids, homogeneously distributed between both layers. In the absence of external forces, the bilayer will not have spontaneous curvature and so it will, competing with surface tension, remain as flat as possible. If we externally induce positive curvature in the region of the membrane, cylindrical lipids in that region will no longer pack ideally as their contact surface will reduce compare to a flat membrane. As a result, we may expect the cylindrical lipids to migrate to the flat areas of the membrane, whereas the conical lipids will move to the curved regions. This process is termed **lipid sorting** and is illustrated in Fig. 1.3.3, right. Another way to minimize bending energy is by recruiting lipids with a lower bending modulus in the regions of higher membrane curvature (Callan-Jones and Bassereau, 2013).

Interestingly, theoretical calculations have demonstrated that any enthalpic gain by lipid sorting is insufficient to overcome the benefit of mixing entropy, therefore lipid sorting mechanism seemed irrelevant in cells (Derganc, 2007). That said, it has been experimentally demonstrated on membranes comprising SM, DOPC, and cholesterol that this barrier can in fact be overcome, albeit when the composition is close to a demixing point. In this regime of the phase diagram, there are short-range interactions among different lipid species that enhance the enthalpic attraction (Sorre et al., 2009; Tian et al., 2009). A recent study using a bilayer deposited over a nanoparticle-covered flat surface, has demonstrated that single-chained lipids enrich in regions of high curvature even at low percentage (i.e. far from demixing) (Black et al., 2014). The authors suggest that the additional contribution to demixing in their case is provided by the high concentration of lipid packing defects on spherically curved membranes, which recruit single-chained lipids. Lipid sorting has been discovered in bacterial cells by identifying an enrichment of cardiolipin, a lipid with nonzero spontaneous curvature, at the highly curved bacterial poles. The authors also show that the organization of individual lipids at low percentage was unaffected by curvature, implicating again the importance of short-range interactions in offsetting the high cost of mixing entropy (Renner and Weibel, 2011).

Analogously, we may expect that proteins that induce curvature will get sorted in curved membrane regions (Fig. 1.3.4, right). Indeed, ample experimental evidence has demonstrated the enrichment of BAR proteins on membrane nanotubes formed by external force. Curvature sorting has been confirmed with quantitative experiments for a range of proteins, which we group according to the way they interact with the membrane: 1) dynamin — interacts with the membrane as a coat (Roux et al., 2010); 2) syndapin and CIP4 (F-BAR proteins) — interact with the membrane via adhesive interactions and also form a coat on membrane tubule (Frost et al., 2008; Ramesh et al., 2013); 3) amphiphysin and endophilin (N-BAR proteins) — interact with the membrane via adhesive interactions, shallow insertions, and scaffolds (Heinrich et al., 2010; Mim et al., 2012; Sorre et al., 2012; Zhu et al., 2012); 4) epsin — interacts with the membrane via a shallow insertion (Capraro et al., 2010); and 5) KvAP — conically shaped transmembrane protein (Aimon et al., 2014). Here, I have only highlighted proteins that have been studied on membrane nanotubes.

Some proteins (e.g. endophilin) have been shown to preferentially bind to smaller vesicles. In fact, conflicting evidence was found using an assay with tethered small vesicles by Stamou and coworkers. Their finding is that amphipathic helix motifs are solely responsible for sensing membrane curvature, unlike the adhesive and coating BAR domains that in their assay were not enriched on small vesicles (Bhatia et al., 2010). The role of adhesive and coating protein domains in curvature sensing therefore remains and open question and we explore this issue quantitatively in Chapters 4 and 6.

As we just discussed, analytical theory and numerical simulations predict that nanoparticles may induce membrane curvature at large scales, despite not being anisotropic or forming large-scale assemblies that can mold membrane shape. Analogously to proteins, we may expect that membrane-adhered particles would also preferentially bind to curved surfaces (Fig. 1.3.5, A). The most generic explanation is that the repulsive interactions between particles (e.g. due to charge or excluded volume) would drive them to regions that have a higher surface area to volume, such as cylinders. To the best of my knowledge, this hypothesis has not been tested.

It is generally difficult to separate the discussion of generating curvature and curvature-based sorting of lipids and bound proteins. Any particle present in the membrane in the regime that induces curvature, will at the same time attract other curvature-sensing components and the two effects (generating *vs.* sensing) will enhance each other. Moreover, if we create curvature externally, curvature-sensing particles will be enriched in curved regions even in the low-density regime (where the particles do not induce curvature) or if they are symmetrically bound to both leaflets. This way, locally the particles will reach the curvature-generating regime and again the system gains both effects.

1.3.5) Membrane tension. We already discussed surface tension in the context of membrane theory. Membrane tension is a difficult concept to define in simple and generic terms. Nevertheless, it is a very important mechanical effector of membrane remodeling in the cell and we briefly revisit it here. Most broadly, membrane tension relates to the lateral stress imposed on the membrane, resulting in a strain characterized by the change in membrane area. If we minimize the Helfrich bending energy by constraining the total membrane area and the total volume, membrane tension comes out as the Lagrange multiplier of the fixed area. More often, we treat membranes as (moderately) compressible, where the contribution to the free energy from area expansion is considered to be elastic, as thoroughly discussed above. Lipowsky has recently demonstrated that no matter if we consider the membrane as compressible or not, we obtain the same expression. More precisely, membrane tension derived as a Lagrange multiplier by minimizing the bending free energy at constant volume and constant area is identical to the tension derived by minimizing the combined bending and stretching free energy at constant vesicle volume (Lipowsky, 2014), i.e.:

$$\sigma = -\left(\frac{\partial F(A,V)}{\partial A} \right)_V = \kappa_A \frac{A - A_0}{A_0} \qquad \text{(Eq. 1.3.8)}$$

As a side note, Lipowsky also proposed an intrinsic tension scale of curvature elasticity, termed the spontaneous membrane tension, σ_0. This measure arrises in the cases where the membrane has a high spontaneous curvature, but experiences external constraints (e.g. large volume of GUVs) that preclude it to attain this curvature. Spontaneous tension seems to provide the scale of actual membrane tension in some vesicle morphologies and possibly account for spontaneous tubulation of supported bilayers exposed to adsorbing particles. Its expression has been estimated as:

$$\sigma_0 = 2\kappa_m c_0^2 \qquad \text{(Eq. 1.3.9)}$$

Understanding membrane tension is further complicated by the ambiguity in the **definition of surface area**. Lipid membranes undergo thermal fluctuations and so their apparent, or macroscopically observed area is smaller than their actual, microscopic area. We already discussed how applying lateral stress on the low-wavelength fluctuating membrane initially flattens out the undulations (the so-called entropic regime) before stretching the membrane (the so-called enthalpic regime). Based on this fact, we can define tension as conjugate to the actual area, and separately, tension as conjugate to the projected area. There is another parameter with the dimension of membrane tension in the denominator of the fluctuation spectrum. Fournier & Barbetta have carefully derived the relationship between the three measures of membrane tension and concluded that they are in fact all different, within the thermodynamic limit and in the entropic regime (Fournier and Barbetta, 2008).

Understanding this distinction is crucial when measuring tension. Flickering spectroscopy measures the tension-like coefficient in the fluctuation spectrum, micropipette aspiration experiments measure the projected-area tension, whereas the stress tensor calculated in computational simulations measures the total-area tension.

Let us first consider two more complications relevant to the cellular environment. First, the theoretical treatment that we have so far reported neglected the possibility of lipids leaving or entering the bilayer in a non-steady state manner (Rao and Sarasij, 2001). Brown, in his review, reflects on this issue and states that changes in membrane area are unlikely in the cells, as they can withstand stretching of only a few percent before rupture. Instead, the change in area is likely due to the change in the lipid amount and so "we should interpret σ as a **chemical potential** rather than a true surface tension" (Brown, 2008). While I disagree with this statement, considering that Brown neglected the important entropic regime and the fact that cells have plenty of membrane reservoir in folds (Gauthier et al., 2012), nonequilibrium processes surely can affect effective membrane tension. For example, Bassereau and coworkers have demonstrated that a fusion-triggered uptake of lipids into GUVs reduces their effective tension, even leading to negative values (Fig. 1.3.7) (Solon et al., 2006). This type of process may be very relevant in phenomena that involve the changing of the bilayer topology, such as membrane fusion and fission.

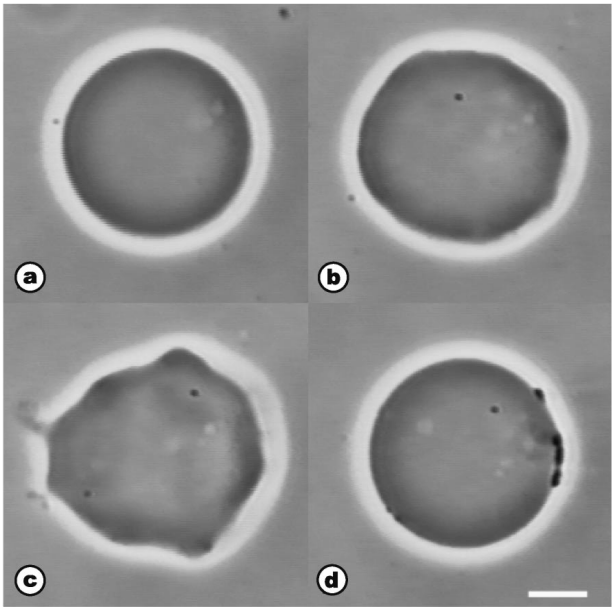

Figure 1.3.7: Curvature instabilities induced by lipid uptake. Shown is a time lapse of a negatively charged GUV in contact with positively charged small vesicles, t = 0 s (a), 10 s (b), 15 s (c), 45 s (d). The vesicle transforms from tense, via large fluctuations and tubulations (see panel c, left), and equilibrates again into a tense state. Scale bar: 10 μm. Taken from (Solon et al., 2006)

The second complication is when membranes are in contact with a surface. **Adhesion** gives rise to another tension term which scales as the adhesion energy per area (Gauthier et al., 2012). Such cases are actually quite relevant in cells. The cytoskeleton acts as an adhesive wall that provides additional tension to the membrane and can even control the fate and dynamics of membrane-remodeling processes, such as endocytosis and exocytosis (Auth et al., 2007; Fournier et al., 2004; Gauthier et al., 2012; Sheetz et al., 2006). When measuring the tension of cell membranes, it is difficult to separate the adhesive tension from the in-plane tension, defined earlier. By measuring membrane tension in cells lacking the cytoskeleton, Sheetz calculated that the contribution to tension from adhesion in cells can be as much as 75% (Sheetz, 2001).

To summarize, we can attempt to answer the main question of this section: what is membrane tension in cells? Effective tension in the cell membrane is a combination of 1), in-plane tension (or the bilayer tension), effectively induced by the osmotic difference across the bilayer and the fluctuations, and 2), adhesion to the cytoskeleton (Fig. 1.3.8). The highest measured tension in cells is 0.45 mN/m in motile keratocytes (Lieber et al., 2013). To gain some reference, compare this value to the limit of the entropic regime (~ 0.1 mN/m) and the aforementioned lysis tension (~ 10 mN/m). Generally, membrane tension in cells is considered to be low, which is attributed mostly 1), to the presence of membrane folds (Raucher and Sheetz, 1999) and 2), to caveolae, 60–80 nm wide membrane invaginations replete with SM, cholesterol, and caveolin proteins (Sinha et al., 2011). Both of these membranous structures basically act as tension-stats of the cell, since frequent membrane-remodeling phenomena in which microscopic chunks of membrane are cut out (e.g. endocytosis) would otherwise create deadly fluctuations in the tension (Gauthier et al., 2012). Of note, caveolae also mediate an endocytic pathway, outlined in the next subchapter.

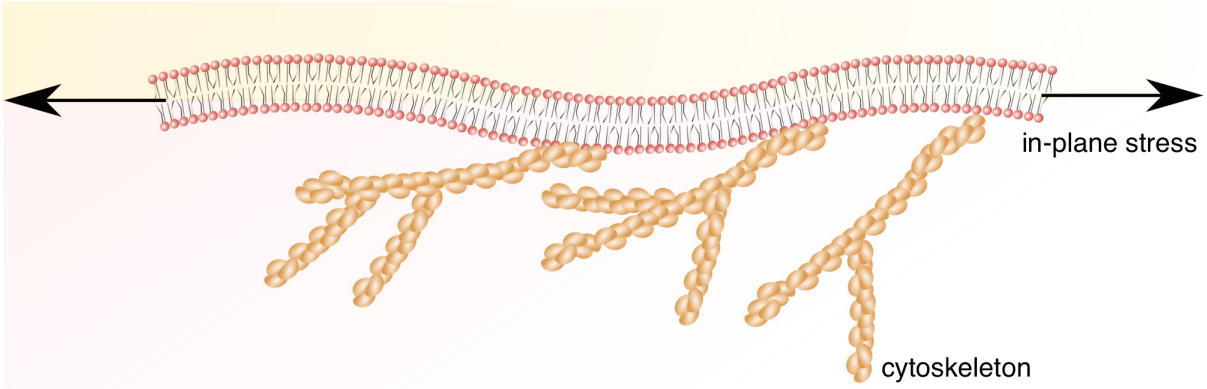

Figure 1.3.8: Sources of membrane tension in the cell. Apparent membrane tension is a sum of the in-plane tension generated by the difference in osmotic pressures across the bilayer and the adhesion energy per area provided by the cytoskeleton.

Despite these works, there is evidence that membrane tension could vary across different areas of the cell, due to tight junctions and diffusion barriers (Li et al., 2002). One may also conceive that diffusion barriers or interleaflet frictional forces would create a sufficient timescale at which local membrane tension could be temporarily induced to affect cellular phenomena. It is known that high membrane tension inhibits endocytosis and tubulation (Dai and Sheetz, 1995; Shi and Baumgart, 2015). In the accompanying thesis, we discovered that surface tension has a much deeper effect, altering the geometry and the strength of protein-protein interactions and the geometry of protein association.

1.3.6) Cytoskeleton and molecular motors. Cytoskeleton refers to different types of filamentous networks of proteins that span the cytoplasm. They provide the mechanical support for cells and are responsible for their shape and deformation. There are three types of protein filaments that make up the cytoskeleton: 1), actin-based filaments (or microfilaments), composed of polymers of actin subunits and of many associated proteins that influence their organization and dynamics, 2), intermediate filaments, comprising dozens of different types of proteins, and 3), microtubules, composed of polymerized tubulin. Numerous molecular motors interact with the cytoskeleton. The forces they produce drive active processes at different length scales. At very large scales, the cytoskeleton is responsible for the motility of cells and is crucial in cell division. As discussed above, cytoskeleton also interacts with the membrane, modulating membrane tension but also generating specialized membranous shapes, namely cilia, flagella, filopodia, lamellipodia, and podosomes (Alberts et al., 2014). At the more molecular scale, cytoskeleton takes part in generating membrane tubules, essential for the traffic of vesicular transport intermediates between organelles. Dynamic tubular networks are also part of the structure of the endoplasmic reticulum, Golgi apparatus and endosomoes (Leduc et al., 2010).

Microtubule filaments are polarized, meaning that they posses a plus end, which grows toward the cell periphery, and a minus end, situated near the center of the microtubular assembly. In general, molecular motors move along microtubules directionally. For example, in intracellular transport, kinesins are plus-end directed motors, whereas dyneins operate toward the minus end (Granger et al., 2014). Actin polymerization also produces a directed force, by adding monomers and growing toward the extremity in contact with membrane, and its activity is indispensable in clathrin-dependent endocytosis in yeast and it is a major factor in endophilin-mediated endocytosis in mammalian cells. The latter mechanism is part of the results of this thesis and will be discussed in Chapter 5.

1.4. Endocytosis & BAR proteins

Endocytosis is cell's way of internalizing nutrients and various functional molecules. This mechanism is quite different from diffusion through the bilayer, which takes place either passively, where molecules freely migrate between the lipids or actively, mediated by transmembrane protein channels. In endocytosis, the membrane engulfs the incoming cargo in a vesicle that subsequently pinches off toward the cytoplasm. Thus encapsulated material enters the endosomal pathway where it is taken to various parts of the cell. Textbooks usually distinguish two types of endocytosis based on the size and type of the incoming cargo. **Phagocytosis** is the internalization of microorganisms and dead cells, usually carried out by specialized cells, such as macrophages as part of the immune response. **Pinocytosis** is the uptake of much smaller cargo, typically proteins, and this process is carried out by virtually every eukaryotic cell (Alberts et al., 2014). Sometimes, pinocytosis is separated from classic endocytosis as the process by which only liquids and cargo not connected to the membrane get internalized in the cell. We focus on the classical endocytosis, a mechanism by which cargo that initially gets recruited to the membrane is taken into the cell and discuss mechanisms involved in this pathway.

Evidently, endocytosis requires efficient way of generating membrane curvature, which is achieved by a machinery of proteins. Among these proteins are the aforementioned clathrin, BAR proteins, and epsins. Molecular motors and other proteins that generate force, such as actin and dynamin, also take important parts, especially in the final stages of endocytosis. Clathrin-mediated endocytosis has for a long time been considered the major pathway of entering into the cell. However other, often much faster, clathrin-independent routes have recently begun to emerge, such as the endocytic pathway studied in this thesis.

1.4.1) Clathrin-mediated endocytosis. The highly recognizable image associated with clathrin-mediated endocytosis is a membrane vesicle enclosed by a cage-like polymeric assembly of clathrin. The basic unit of the cage is the so-called clathrin triskelion (Fig. 1.4.1, A) (Kirchhausen, 2000). Clathrin does not interact directly with the membrane; instead, it requires adaptor proteins, such as AP2, to link them to the endocytic site. Many other proteins were identified to participate in endocytosis, such as epsin and BAR proteins, which couple with membrane curvature, and dynamin, which cuts off the endocytic vesicle from the underlying membrane. Determining the precise role of each protein is very challenging due to the dynamic and highly variable variable nature of this process (Johannes et al., 2014; Kirchhausen, 2009; Lundmark and Carlsson, 2010; McMahon and Boucrot, 2011; Saheki and De Camilli, 2012; Taylor et al., 2011).

One of major controversies surrounding clathrin-mediated endocytosis is the mechanism of generating membrane curvature. Most prominent candidates are BAR

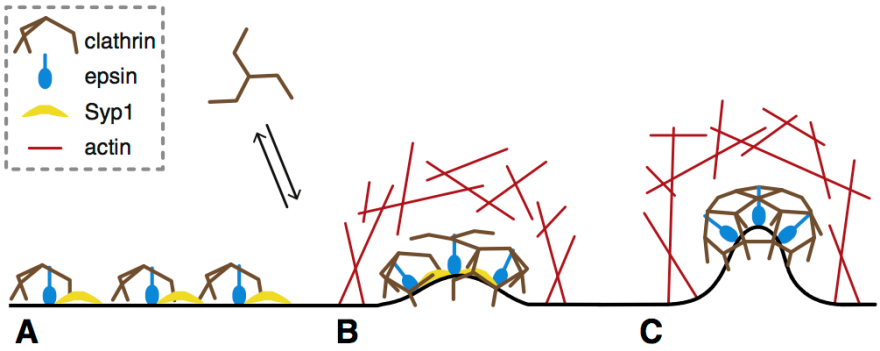

Figure 1.4.1: Scheme of events in clathrin-mediated endocytosis in yeast. (A) All proteins are present at the endocytic site, but actin. Clathrin binds to the flat membrane, but does not form a lattice. (B) Actin polymerization triggers membrane bending. (C) Clathrin forms a lattice. Taken from (Kukulski et al., 2012).

proteins and epsins, because they possess strong curvature-generating capabilities, much stronger than one would expect of a clathrin coat. Indeed, many studies identified F-BAR proteins at the early endocytic sites and for this reason they are described as initial curvature generators (Henne et al., 2010; McMahon and Gallop, 2005). However, according to a recent study, clathrin polymerization alone is sufficient to induce budding of liposomes, although the physics driving this process was not explained (Dannhauser and Ungewickell, 2012). The role of other BAR proteins in endocytosis has also been recently brought into question, in light of a variety of generic ways one can induce membrane curvature (Kirchhausen, 2012). Another argument against the importance of BAR proteins is evidence that synaptic vesicle endocytosis is only mildly affected after knocking out endophilin or amphiphysin (Saheki and De Camilli, 2012). Other studies have shown contrasting results, where deleting endophilin or disrupting its ability to bend the membrane had a much more detrimental impact on functionality of synaptic vesicles (Bai et al., 2010; Verstreken et al., 2002). Therefore, challenging the importance of BAR proteins in clathrin-mediated endocytosis is premature. Actin is another variable effector in this process. It is indispensable in yeast, which lacks dynamin, whereas mammalian cells only recruit actin polymerization when membrane tension is high (Boulant et al., 2011).

Recent development of the correlative fluorescence and electron microscopies has allowed to probe clathrin-mediated endocytosis at very high spatial and temporal resolutions. Using this method, Briggs, Kaksonen and coworkers have identified the sequence of events in clathrin-mediated endocytosis in yeast (Kukulski et al., 2012). They found that F-BAR, epsin, and a fully assembled clathrin coat initially bind to a flat membrane, but do not curve it. Bending takes place only after the onset of actin polymerization. Budding is presumably followed by the rearrangement of the clathrin coat (Fig. 1.4.1). Finally, ~ 9 s after the the initiation, fission takes place. The mechanism of fission has not been elucidated, although actin and two am-

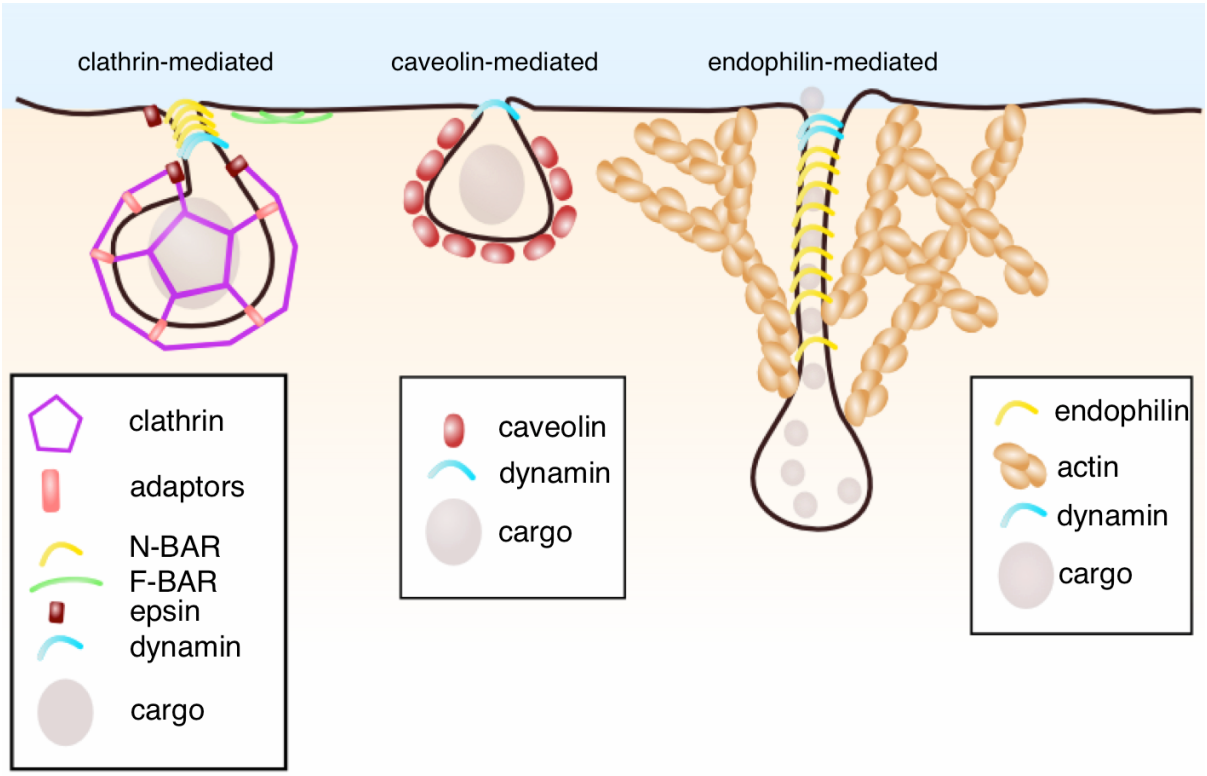

Figure 1.4.2: Endocytosis. Depicted are three endocytic pathways with key ingredients. The list of proteins involved is by no means comprehensive.

phiphysin proteins, Rvs161 and Rvs167 were found to be key (Kukulski et al., 2012). Another study has also implicated Rvs161, Rvs167, together with an F-BAR protein Bzz1 in fission in clathrin-mediated endocytosis in yeast (Kishimoto et al., 2011). This fact will be important in Chapter 5, where we demonstrate how BAR-protein scaffolds can promote fission of membrane tubes.

1.4.2) Clathrin-independent endocytosis. There are two key challenges in elucidating clathrin-independent mechanisms. First, usual method of identifying novel clathrin-independent pathways is by perturbing the function of clathrin, which may have unexpected consequences on the homeostasis of proteins and lipids in the cell. Second, there are no clear biochemical markers or conserved membrane morphologies in these pathways for straightforward identification (Doherty and McMahon, 2009). For these reasons, clathrin-independent endocytosis is much less understood.

Proteins of the caveolin family mediate **caveolar endocytosis** (Fig. 1.4.2). This process internalizes diverse cargo, such as lipids, albumin, and pathogens, however it is often redundant to other mechanisms. The morphology of the membrane is a 60–90 nm flask, called caveola, that detaches from the underlying membrane in a dynamin-dependent manner (Mayor et al., 2014). As mentioned in the previous section, endophilin, an N-BAR protein, has been implicated in clathrin-dependent pathway but its role has been controversial. A recent work has elucidated that endophilin in fact controls a distinct pathway, independent of clathrin, but dependent

on dynamin and actin (Fig. 1.4.2) (Boucrot et al., 2015; Renard et al., 2015). This pathway takes place at the leading edge of cells and is very fast (~ 1 s), which is why it is termed **fast endophilin-mediated endocytosis**. Moreover, it drives the internalization of several G-protein-coupled receptors, various receptor tyrosine kinases, and it is hijacked by Shiga and cholera bacterial toxins (Renard et al., 2015). The molecular and physical mechanism of fission in fast endophilin-mediated endocytosis has been studied in Chapter 5 of this thesis.

1.4.3) BAR proteins: structure, assembly, and curvature coupling. The superfamily of BAR-domain proteins has been implicated in many important cellular tasks, from generating membrane curvature and maintaining complex membranous geometries, to helping assemble multiprotein machineries in a number of membrane-remodeling phenomena (Qualmann et al., 2011). These proteins contain variable modules, wherein the crescent-shaped BAR domain is present in all members. The membrane-binding region of this domain is lined with positively charged residues, so they are highly reliant on negatively charged lipids, such as PS or PIP_2. Most BAR proteins also contain amphipathic helices that enhance their curvature-sensing and generating capabilities. The first high-resolution structure was determined for amphiphysin, which showed that the functional form of BAR proteins is a dimer and that its binding to the membrane of cells or vesicles induces large-scale tubulation (Peter et al., 2004). Recently, by specific recruitment of BAR proteins to cellular compartments, Inoue and coworkers demonstrated that BAR proteins indeed are active curvature generators of plasma and organelle membranes (Suarez et al., 2014).

Based on the shape of the BAR domain, we divide them into: classical BAR/N-BAR, F-BAR, and I-BAR proteins (Figure 1.4.3). N-BAR proteins are classical BAR proteins with an amphipathic helix at each of their N-termini in the dimer. Virtually all classical BARs are N-BAR proteins, except for a few, such as arfaptin and centaurin. Notable N-BAR proteins include amphiphysin and endophilin. They are structurally very similar, except that endophilin contains two additional small amphipathic helices, termed insert helices. A recent study has shown that every known member of the sorting nexin (SNX) family, involved in the endosomal sorting of proteins, is an N-BAR domain protein (van Weering et al., 2012). All BAR/N-BAR proteins induce and stabilize positive membrane curvature, generating tubules with diameters ranging from 20 to 60 nm (Qualmann et al., 2011). F-BAR proteins, such as FCHo2 implicated in early stages of clathrin-mediated endocytosis (Section 1.4.1), are characterized by longer and typically shallow BAR domains. They also interact with positive membrane curvature, inducing tubules with diameters from 60 to 100 nm. F-BARs do not contain amphipathic helices, although some members, like syndapin, display short loops that can wedge into the bilayer. Syndapin, like endophilin and amphiphysin, has been found in later stages of clathrin-mediated endocytosis indicating that it couples with higher curvature, unlike other F-BAR proteins (Qual-

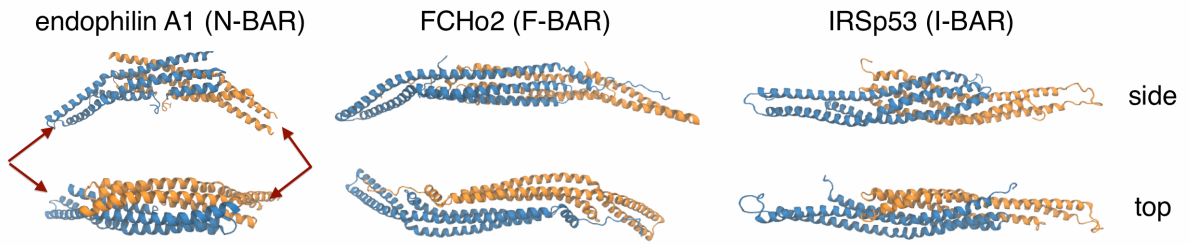

Figure 1.4.3: BAR proteins. Ribbon representation of selected BAR proteins. From left to right: endophilin A1 (PDB ID: 1ZZW), FCHo2 (2V0O), IRSp53 (2YKT). Structures are color-coded by monomer. Maroon arrows represent N-termini of each monomer, i.e. the sites of amphipathic helices that were not resolved with X-ray diffraction.

mann et al., 2011; Rao and Haucke, 2011). Conversely, I-BAR proteins induce negative curvature, therefore resulting in membrane invaginations. Some members contain amphipathic helices, like ABBA, although others, e.g. missing-in-metastasis (MIM), and IRSp53, do not (Mattila et al., 2007). There are other minor classifications, such as PH-BAR and PX-BAR, typically subclassified under classical BAR domain, and pinkBAR which displays a straight BAR domain (Mim and Unger, 2012). Figure 1.4.3 displays representative BAR proteins.

The curved shape of BAR proteins provides an intuitive understanding of why they couple with membrane curvature, although the mechanism of generating and sensing curvature is much more complex than simple shape arguments. The way they interact with the membrane is a combination of shallow insertion, adhesion, and in some cases, scaffolding. A recent study by Bassereau and coworkers, using membrane nanotubes tethered to GUVs, has revealed that the way N-BAR proteins interact with membranes depends on their surface density. In the low-density regime (up to a few percent surface coverage), proteins do not reshape the membrane, but they are readily recruited to membrane nanotubes. Conversely, at higher densities, they impart a strong morphological effect on the membrane. Therefore, N-BAR proteins predominantly act as curvature sensors at low protein densities and as curvature manipulators at high densities (Sorre et al., 2012). Chapter 3 will outline the results from the accompanying thesis where we will discuss the assembly of N-BAR proteins at the molecular resolution and how it is affected by protein density and mechanical properties of the membrane.

BAR proteins also contain modules involved in the recruitment of other proteins or specific lipids. Src homology 3 (SH3) domain, present in endophilin and amphiphysin, specifically binds to the proline-rich domain in dynamin, helping to recruit it to the endocytic site (Meinecke et al., 2013). Pleckstrin homology (PH) domain specifically binds to PI lipids and can thus participate in various signaling events. This domain is part of a plethora of different proteins, including some BAR

proteins, namely centaurins. Phox homology (PX) domain targets phosphatidylinositol 3-phosphate (PI3P), a singly phosphorylated PI, and it is part of many proteins, including the SNX family (Teasdale and Collins, 2012).

1.4.4) Amphipathic helices in BAR proteins. We discussed that a shallow insertion into the membrane is theoretically predicted to induce appreciable spontaneous curvature, attaining a maximum effect at the insertion depth of approximately one third of a lipid layer (Section 1.3.3). In proteins, this mechanism is achieved by an amphipathic helix that is thought to exist as a random coil in solution. Upon interacting with lipids, it folds and aligns its long axis parallel to the plane of the membrane (Drin and Antonny, 2010). To understand their role in curvature-related phenomena, we ask two important questions.

First, are amphipathic helices able to induce large-scale membrane remodeling? It has been demonstrated *in vitro* that epsin, that binds to PIP_2-containing membranes via an amphipathic helix, drives the formation of tubules with a diameter of ~ 20 nm (Ford et al., 2002). By contrast, a different *in vitro* study has shown that the amphipathic helix from an N-BAR protein BRAP, that as wild type readily generates membrane tubules, efficiently binds to the membrane but cannot remodel it (Fernandes et al., 2008). The authors categorically excluded amphipathic helices to contribute to membrane bending in BAR proteins. This conclusion may be overly simplified, as multiple curvature-generators could enhance each other's activity in non trivial ways. For example, a recent study employing electron paramagnetic resonance demonstrated that the amphipathic helices of endophilin insert deeper into tubular membranes than small vesicles, promoted by tighter packing of the crescent BAR domain on membrane tubules (Ambroso et al., 2014). This study did not explain the curvature-generating role of amphipathic helices, but it showed that cooperative binding of different modules can alter their combined activity in a way different than the sum of its parts.

Second, can amphipathic helices sense membrane curvature? It turns out that many amphipathic helices indeed bind better to membranes with higher curvature. For example, it has been shown in bacterial cells that an amphipathic helix protein SpoVM localizes to membranes with higher curvature (Ramamurthi et al., 2009). Antonny and coworkers showed that the amphipathic helical domain ArfGAP1, called APLS motif, has a higher affinity to smaller liposomes. Their work demonstrated that curvature-sensing by amphipathic helices is key in regulating the transport of vesicles from the Golgi to the endoplasmic reticulum. Moreover, they proposed that APLS motif prefers curvature by way of sensing lipid packing defects, parts of the membrane where the hydrophobic core of the bilayer is exposed to the solvent (Bigay et al., 2003; Pranke et al., 2011). The same curvature-sensing mechanism was attributed to alpha-synuclein, an amphipathic helix protein whose aggre-

gation has been linked to Parkinson's disease (Nuscher et al., 2004). Based on all-atom computer simulations, Voth and coworkers have shown that highly curved membranes promote the coarsening of packing defects that facilitate the folding of an amphipathic helix (Cui et al., 2011). More recent computer simulations have demonstrated the dynamics of packing defects sensing by amphipathic helices (Vanni et al., 2014; Vanni et al., 2013). As mentioned previously, epsin also binds to the membrane via an amphipathic helix and its preference to curvature has been demonstrated in tether-pulling experiments *in vitro* (Capraro et al., 2010). By contrast, magainin 2, which is an antimicrobial peptide and an amphipathic helix, does not strongly sense membrane curvature (Wieprecht et al., 2000).

Stamou and coworkers developed an assay in which vesicles of different size were tethered to an inert substrate via streptavidin-biotin bonds. By incubating BAR proteins with small vesicles and measuring the relative fluorescence signal of proteins compared to lipids, they found that BAR proteins cease to sense curvature when their amphipathic helices are mutated or deleted. They categorically conclude that BAR domain in BAR proteins cannot sense curvature; instead, this task is solely carried out by the amphipathic helices. While their findings show unexpected coupling of BAR domains with curved membranes, their conclusion will be shown to be partially fallacious in this thesis. Chapters 4 & 6 will highlight these results as well as a possible explanation for the observed discrepancies among different experimental systems. Taken together, it seems that the multimodular interaction of BAR proteins with membranes makes it incredibly challenging to isolate the contribution of each effect. For these reasons, the particular roles of BAR proteins and epsins in endocytosis has remained a mystery for a number of years.

1.4.5) Endophilin. Endophilins were originally discovered as SH3-containing proteins (Chen and Antonarakis, 1997). Based on their colocalization with endocytic proteins, they were renamed to endophilins (Micheva et al., 1997). The functional unit, like in the great majority of BAR proteins, is a homodimer, wherein each monomer contains an N-BAR domain and a C-terminal SH3 domain. There is a short variable domain between the N-BAR and the SH3 domains. In addition to two N-terminal helices per dimer, unlike amphiphysin, there are two short helices underneath the concave surface of the protein dimer, termed insert helices (Gallop et al., 2006; Masuda et al., 2006; Weissenhorn, 2005).

There are several known isoforms of endophilin: A1, A2, A3, B1, and B2. A1 is specifically localized in the brain, whereas other A variants are found across the organism. As previously discussed, endophilins have been implicated in clathrin-mediated endocytosis. In particular, A variants are active in synaptic vesicle endocytosis, contributing to various stages of the process, such as the formation of clathrin-coated pits, recruitment of dynamin, and narrowing of the tubular neck, although its

precise role remains unclear (Kjaerulff et al., 2011). Endophilin A2 drives the aforementioned distinct endocytic pathway (Boucrot et al., 2015; Renard et al., 2015). Endophilins B are more prominently recruited to membranes of organelles, rather than the plasma membrane. Endophilin B1 was found to be crucial in triggering apoptosis and its role has been linked to the formation of autophagosomes, an organelle that translocates cellular components for degradation (Kjaerulff et al., 2011). In healthy cells, it was found to stabilize the mitochondrial tubular network (Karbowski et al., 2004).

To recapitulate from previous sections, in terms of its interactions with the membrane, endophilin has been found to: **1), sense tubular and spherical curvature, 2), generate tubules from vesicles and various cellular membranes, 3), promote the vesiculation of small vesicles.**

1.4.6) Centaurin. There are six genes encoding centaurin proteins in mammals, which have four domains in common: a BAR domain, a PH domain, Arf-GAP (ADP-ribosylation factor GTPase-activating protein) and Ank (ankyrin repeat) domains (Jackson et al., 2000). Their BAR domain comes without amphipathic helices.

Recently, a structure of β1-centaurin (also known as ACAP1) was determined by X-ray diffraction and it showed a BAR domain with a ~ 40 nm intrinsic radius of curvature (compare to ~ 20 nm for endophilin and 60 nm for F-BAR protein FBP17) (Pang et al., 2014). It has been previously shown that the binding of β2-centaurin (ACAP2) is sensitive to the liposome size and that it tubulates liposomes and membranes in overexpressing cells. Importantly, deleting the PH domain strongly affected the binding of β2-centaurin, but did not completely abolish the curvature-sensing activity. Also, PH domain alone, despite binding to the membrane, did not induce tubulation (Peter et al., 2004).

A recent study on the structure of β1-centaurin showed an apparent contradiction. PH domain of β1-centaurin displays a short, 7-residue-long loop that, according to the authors, inserts into the membrane and is solely responsible for imparting curvature (Pang et al., 2014). While this finding possibly points to a more versatile role of PH domains, the authors' conclusion that BAR domain is irrelevant for membrane curvature is erroneous. In their study, they make conclusions based on the membrane phenotype after mutating either the PH or BAR domain, but fail to recognize that mutations that disrupt the tubulation activity, also disrupt the binding to the membrane itself, an obviously crucial step in affecting membrane curvature. They implicate the importance of BAR domain in helping the entire protein pack around the tubule based on cryo-electron microscopy imaging, however it is important to be very cautious when drawing conclusions from a crystal-like assembly that heavily exceed the physiologically attainable concentrations of proteins. The

conservative conclusion is that PH domain, as shown by McMahon and coworkers, is crucial for the recruitment of centaurins to the surface of the membrane, by interacting with PIP_2, and, possibly, it attributes to membrane curvature. We will assess the curvature-generating capabilities of β2-centaurin in Chapter 4 and quantify its curvature sensing in Chapter 6.

Centaurins have been implicated in endosomal trafficking and in regulating the remodeling of the actin cytoskeleton (Jackson et al., 2000; Randazzo et al., 2000). Their Arf-Gap component helps regulating the ADP ribosylation factors and some centaurins have been linked to a variety of cellular signaling pathways. β1-centaurin was also implicated as a clathrin coat complex in endocytic recycling (Li et al., 2007), whereas the Arf-GAP and Ank domains of β2-centaurin are essential in the neurite outgrowth (Kobayashi and Fukuda, 2012). Whether centaurins participate in membrane-remodeling phenomena is yet to be revealed.

1.4.7) Epsin. Epsins have several domains: an epsin N-terminal homology (ENTH) domain, which binds to the membrane, and a C-terminal domain that binds clathrin and clathrin adaptors (Chen et al., 1998; Ford et al., 2002). The 17 N-terminal residues of epsin become folded into an amphipathic helix when in contact with PIP_2. Epsin contains clathrin-adaptor-binding domains and so it recruits the clathrin machinery to the endocytic sites, although unlike clathrin adaptors, it is thought to drive the initial curvature in clathrin-mediated endocytosis (Ford et al., 2002). The remodeling power of epsin has been proven *in vitro.* It is still unclear how these proteins associate on the membrane, despite some evidence that they aggregate prior to inducing tubulation (Yoon et al., 2010). A recent study in mouse cells has revealed that epsin helps recruit actin to clathrin-coated pits, which generates force for the formation of vesicles. Additionally, knocking out epsin precludes these cells from dividing correctly, which could indicate an important link between epsin and the actin cytoskeleton (Messa et al., 2014). Finally, a study showed that epsin, just like endophilin, due to the insertion into the bilayer, promotes the fragmentation of small vesicles, hence implicating their role in membrane fission. We will study the fissiogenic capabilities of epsin 1 in Chapter 5 and its interaction with tubular membranes in Chapter 4.

1.5. Membrane fission

The final step in endocytosis is the complete detachment of the endocytic vesicle from its underlying membrane, termed membrane fission. In fission, the membrane bilayer is cut into two distinct membranes, therefore, unlike in budding and tubulation, the topology of the bilayer changes. Fission is a very important biological process, as it underlies all trafficking events that involve the membrane. However,

due to its highly dynamic nature, it is not understood as well as curvature-instability phenomena. Many proteins have been implicated in fission. Most notable example is dynamin, which terminates clathrin-dependent endocytosis. The model in which dynamin takes the energy from GTP-hydrolysis to induce a strong constriction is very attractive as it provides an intuitive understanding how fission may occur at the molecular level: the stability of the bilayer structure is compromised by squeezing. However, fission is a more complicated mechanism and cells likely have various different fission pathways. Yeast cells, for example, do not use dynamin, so a power stroke mechanism cannot be used to explain how tubules are cut in their case. Instead, as mentioned previously, yeast cells use actin and likely BAR proteins. As will be demonstrated in this thesis, although dynamin improves the efficiency of endophilin-mediated endocytosis, the fission step can in principle occur with any protein that produces an external force, such as actin polymerization or molecular motor dynein. Let us first consider the theoretical requirements for membrane fission then list ways membrane fission could be achieved in the cell.

1.5.1) Hemifission intermediate. Membrane fission, just like budding and tubulation, is driven by the opposing mechanical and chemical forces. Fission produces two membrane components, each having a smaller area and a different curvature than the original membrane. For example, if starting from a planar membrane and producing a vesicle or starting from a vesicle and producing two smaller vesicles, the curvature of the resulting membranes is higher. Therefore, fission pays the price of mean bending energy and, hence **higher κ_m disfavors fission**. At the same time, the lipid interconnectivity is rearranged, which will affect the contribution to the free energy from Gaussian curvature. The total integral of the Gaussian bending energy yields: $F_G = 2\pi\kappa_G\chi$, where $\chi = 2\big(N(\text{compartments}) - N(\text{holes})\big)$. In the case of endocytic fission, $\chi = 2$, therefore, more negative values of κ_G will favor fission. Strictly, fission will affect the enthalpic contribution to the free energy due to the change in lipid-lipid interactions and also the entropy, as lipids upon fission have a smaller diffusion space. Finally, membrane and line tension will affect the likelihood and timescale of fission, and whether it is favored or disfavored will depend on the shape of the intermediate state.

The so-called hemifusion or hemifission intermediate, in which the two bilayers fuse together in the course of fission, is preferred as it does not involve the opening of large pores that would leak out the vesicle material (Fig. 1.5.1) (Kozlov et al., 2010). Kozlovsky and Kozlov proposed a model in which they calculated the total bending energy of 1), the membrane consisting of a constricted neck connected to a vesicle of radius r_{ves}, 2), the hemifission intermediate, and 3), the two separated membranes. They found that the first energy strongly depends on the radius of the aperture between the neck and the vesicle r_{ap} and jumps to ~ 100 k_BT at $r_{ap} < 5$ nm (r_{ap} is measured from the bilayer midplane). The hemifission energy shows a critical be-

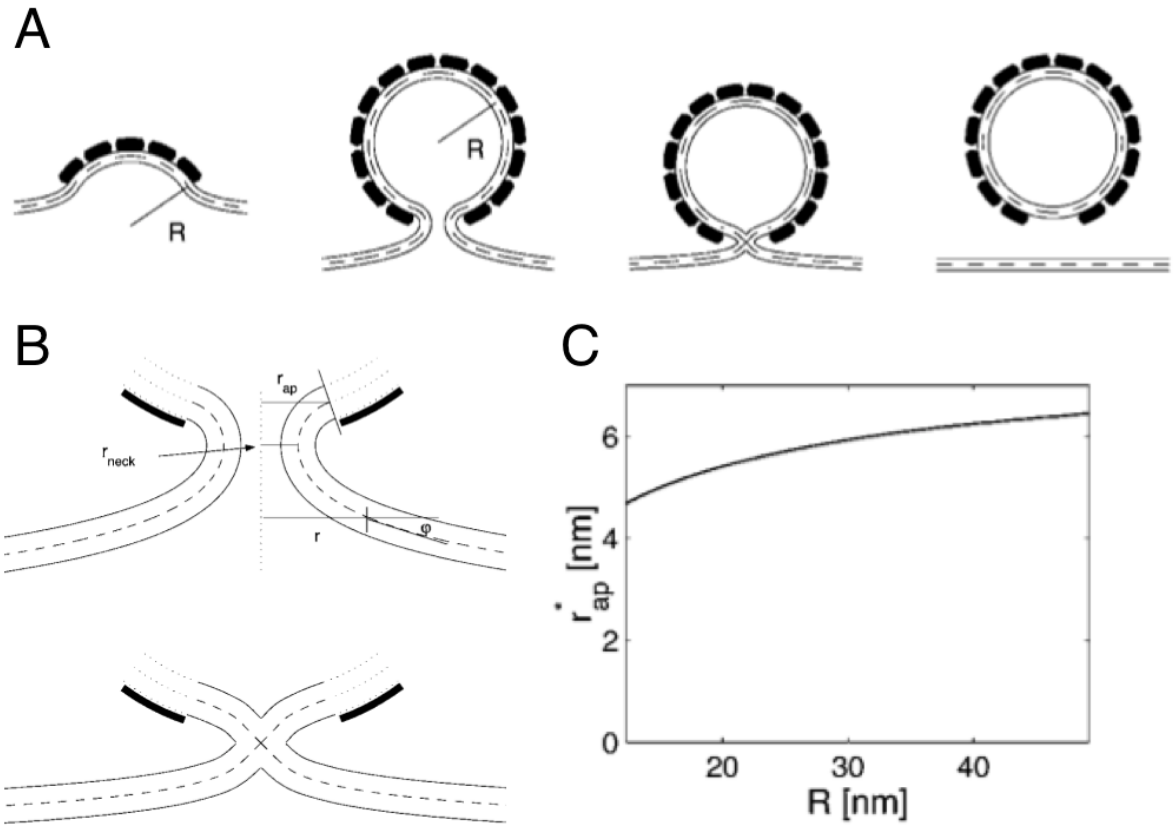

Figure 1.5.1: Fission via hemifission intermediate. (A) Time sequence (from left to right): bud of radius R, vesicle connected to the surface via a neck, hemifission state, separated vesicle. (B) The detailed geometry of the constricted neck (with aperture radius, r_{ap}, and neck radius, r_{neck} (top) and the hemifission state (bottom). (C) The critical aperture radius, r_{ap}*, as a function of the vesicle radius, R. Adapted from (Kozlovsky and Kozlov, 2003).

havior, where at the critical neck radius, r_{ap}*, the membrane will form the hemifission state. The energy of the separated membranes is always lower than the hemifission energy, therefore, as long as the hemifission state is attained, fission will spontaneously occur. They found that r_{ap}* increases with r_{ves}, with approximately 5 nm for a 20-nm vesicle (Kozlovsky and Kozlov, 2003). Interestingly, the authors find that even a small magnitude of positive spontaneous curvature increases the critical aperture radius, hence favors fission.

While, this model provides an excellent quantitative understanding of energies leading to membrane fission, the authors neglected key parameters such as the effect of the proteins on the elastic moduli. Furthermore, in many cases, the initial shape of the membrane may not necessarily be a catenoid with a zero mean curvature; rather, it could be a tubule. The tubular morphology is extremely important for the endocytosis mechanism studied in this thesis, where BAR proteins form a scaffold stabilizing the cylindrical membrane geometry. Finally, it is very important to

point out that literature frequently quotes the article by Kozlovsky and Kozlov, stating that the neck radius needs to collapse to 3 nm to reach the hemifission state (for example: (Cocucci et al., 2014; Morlot et al., 2012; Morlot and Roux, 2013)). As I have explained above, Kozlovsky and Kozlov calculate the aperture radius to be ~ 5 nm for the vesicle radius of ~ 20 nm, which yields a neck radius of r_{ap}^2/r_{ves} = 1.3 nm, instead of the quoted 3 nm (Fig. 1.5.1). Furthermore, this result is sensitive to the bilayer thickness, spontaneous curvature, and the bending moduli of the membrane, which depend on the lipid composition and the bound protein. It is also likely that including membrane tension would alter this result, which is especially important for the mechanism of tension-sensitive dynamin-induced fission (see more below).

1.5.2) Defect nucleation. Although we expect that endocytic fission proceeds through a hemifission state to prevent leakage, it is worth mentioning the lysis mechanism, in which fission is induced by open an unhealable hole in the membrane. As we mentioned in Section 1.3, the stretching of the membrane is counteracted by the membrane tension. It has been shown that the tension at which the membrane ruptures is between 1 and 30 mN/m and it largely depends on composition (Evans et al., 2003; Olbrich et al., 2000). Evans and coworkers found that the tension, at which most vesicles burst, slowly rises with how fast the membrane was brought to lysis tension. This behavior is consistent with the cavitation theory in which the membrane ruptures at tension above the cavitation barrier. However, if tension is increased very rapidly, the lysis tension grows exponentially with the tension increase rate. Under this regime, the limiting step of rupture is the creation of a defect (Fig. 1.5.2, A). In sum, tensile fission occurs in two steps: 1), nucleation of normally present membrane defects, 2), nucleated defects become an unstable hole. The nucleation of defects requires a nonzero membrane tension and the defect density increases with increased membrane tension. In addition, the experiments predict very small size of rupture pores (~ 1 nm width) with lifetimes of ~ 0.1 s to 10 s (Evans et al., 2003; Evans and Smith, 2011). Therefore, it is possible that endocytic fission, especially when dealing with morphologies more complex than a spherical vesicle connected via a short cylindrical neck, involves several molecular mechanisms, including defect nucleation.

1.5.3) Line tension. We discussed in Section 1.1.3 that mixed lipid can membranes undergo phase separation, which gives rise to line tension at the domain boundary. Thus created edge energy generates a budding instability and can even lead to fission provided sufficiently narrow bud neck. It has been demonstrated that phase-separated GUVs may, at a high surface to volume ratio, spontaneously separate into two vesicles of distinct phases (Baumgart et al., 2003). Analogously, Bassereau, Goud and their coworkers experimentally demonstrated that, after triggering phase separation in membrane tubules extruded by external force, the tubules rapidly break at the interface of the two phases (Fig. 1.5.2, B) (Roux et al., 2005). Allain and coworkers

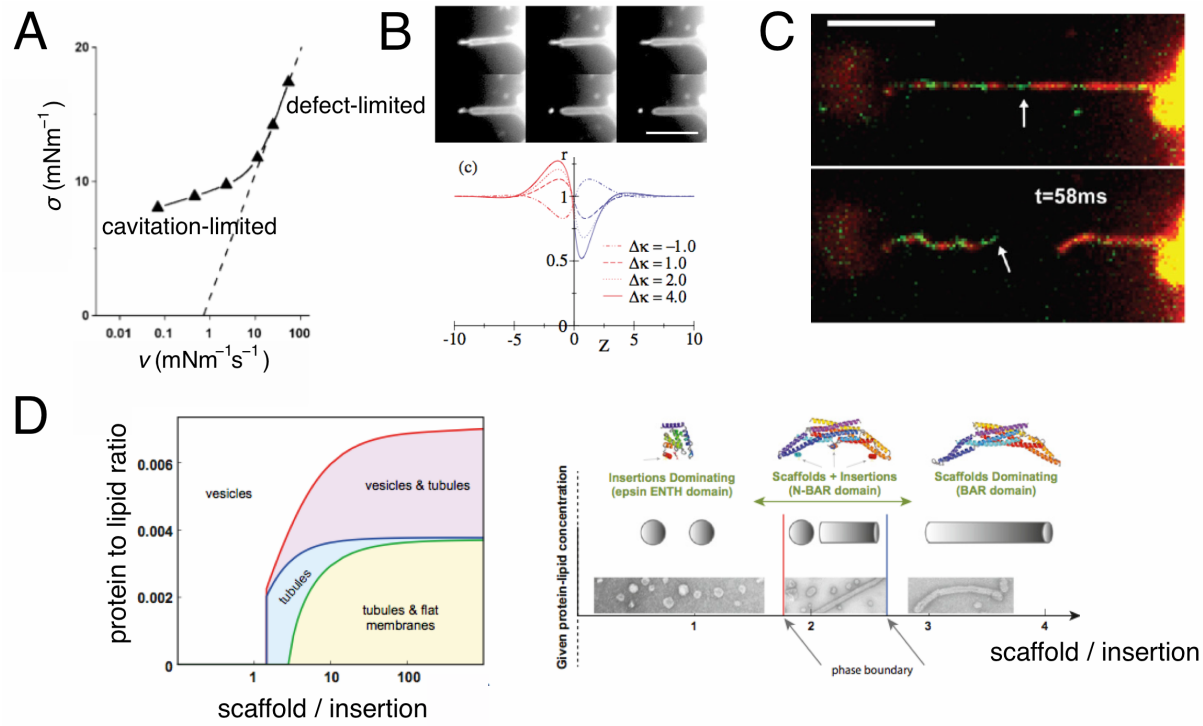

Figure 1.5.2: Mechanisms of membrane fission. (A) Two regimes of membrane lysis due to tension. Adapted from (Evans et al., 2003). (B) Fluorescence time sequence of fission of phase-separated nanotubes (top). Tube radius as a function of its profile (bottom) at different bending moduli. Adapted from (Allain et al., 2004). (C) Fission of membrane nanotubes induced by dynamin upon GTP hydrolysis. Adapted from (Morlot et al., 2012). (D) Fragmentation of small vesicles by shallow insertions of amphipathic helices. Left: phase diagram as a function of protein concentration and the ratio of scaffolding (BAR) domains *versus* amphipathic helices. Right: Representative proteins (top) and the morphological consequences of their binding to the membrane (bottom).

calculated the shape at the interface of a phase-separated tube, by employing a Hamiltonian that contained separate bending and surface tension terms for the two phases, plus line tension at the interface, and an external force that keeps the membrane tubular. They found that in the absence of line tension, the radius between the phases increases almost smoothly from the phase with a higher to the phase with a lower mean bending modulus. Line tension squeezes the interface down to vanishing radius for very high line tension. Interestingly, the difference in Gaussian bending rigidities of the two phases creates an instability for a nonzero neck radius (Fig. 1.5.2, B) (Allain et al., 2004). A similar result was obtained years before by MacKintosh and coworkers, where they calculated the stability of a tubule bridging two vesicles, i.e. a membrane dumbbell (Chen et al., 1997). They evaluated the contribution of the Gaussian curvature. The important difference is that they considered the membrane had a perfectly miscible binary composition, hence there is no line tension, but the two components had different Gaussian moduli. By applying the elastic energy and including a coupling between the local lipid composition and the Gauss-

ian curvature, the tubule may become unstable and spontaneously lead to fission if the minor lipid component favors positive Gaussian curvature (Chen et al., 1997). Both results demonstrate that the minimum requirements for fission is a two-component system with different elastic properties that may—but do not need to—phase separate.

1.5.4) Tubule constriction. Dynamin is the most notable protein to modulate fission in endocytosis. It is a relatively small GTPase that assembles into a helical oligomer and forms a coat around a tubular membrane. The stiffness of the dynamin coat induces membrane curvature by way of imposing a 10-nm radius of the tubule, independently of its equilibrium radius set by tension equilibrium (Morlot and Roux, 2013). It is widely believed that GTP hydrolysis induces a conformational change in dynamin, which significantly constricts the membrane tubule, to radii small enough to induce fission via a hemifission state (Roux et al., 2006; Sweitzer and Hinshaw, 1998). The constriction hypothesis has been challenged on multiple occasions, especially since high-resolution imaging showed that maximum constriction by dynamin is ~ 5 nm (Zhang and Hinshaw, 2001), most likely insufficient to cross the hemifission barrier. Recent experimental work by Roux and coworkers has shown that fission takes place at the edge of the dynamin polymer (Fig. 1.5.2, C). Based on this result, the authors propose that the mismatch in the mechanical properties of the coated and the bare tubular segments accumulates significant stress at the dynamin edge, which reduces the hemifission barrier, and not the constriction underneath the coat *per se*. They also find that increased membrane tension contributes to the lowering of the energy barrier (Morlot et al., 2012). Kirchhausen and coworkers have imaged clathrin-mediated endocytosis in live cells and identified that dynamin preferentially assembles into dimers counting 13 or 14 dimers typically involved in fission (Cocucci et al., 2014).

The model proposed by Roux and coworkers is compatible with the theoretical models derived for multicomponent membranes (Allain et al., 2004; Chen et al., 1997), as the lipids underneath the rigid dynamin coat can effectively be thought of as a membrane component with different elastic properties than the uncoated lipids. As a reminder, these models explain fission as an interplay of mismatch in Gaussian bending moduli of the two components, surface tension and, in the case of phase separation, line tension. They do not include an intermediate hemifission state. Thus, it is important to note that fission can be explained and modeled without this hemifission step.

1.5.5) Shallow insertion. McMahon, Kozlov and coworkers have shown that N-BAR proteins or epsin induce the fragmentation of small vesicles (200 nm in diameter) (Boucrot et al., 2012). The vesiculation positively correlates with the number of amphipathic helices per protein and is inhibited by the scaffolding BAR domain. They

developed an analytical model in which they differentiate the scaffolding mechanism from shallow insertions by amphipathic helices and analyze their effect on the funnel shape of the membrane that is predicted to precede fission. Such morphology is characterized by having a large membrane midplane area, compared to the outer areas of the membrane. Shallow insertion expands the outer area, therefore destabilizes the shape of the funnel, leading to fission. Scaffolding by BAR proteins, on the other hand, do not alter the area of the outer membrane surface and inhibit fission. This mechanism could be extended to the observation of why the insertion of a hydrophobic loop of a PH domain critically impacts dynamin-mediated fission (Kozlov et al., 2010; Ramachandran et al., 2009).

2. Aims and Approaches

Broadly, the main aim of this thesis is understanding the way peripheral membrane proteins interact with membrane curvature and elucidate their function in cellular processes. We have already mentioned specific aims in Introduction, when discussing the background of a particular cellular phenomenon. Let us recapitulate all the specific aims here.

1) We will study the way endocytic proteins, namely BAR proteins and epsin, modulate membrane curvature. We will explore the dynamics by which they assemble into tubular coats, and the way they affect the mechanical properties of the membrane (Chapter 4).

2) We will investigate if BAR proteins and epsin can induce fission of membrane tubules in the context of a newly discovered clathrin-independent endocytic mechanism and explore the potential cooperative action of BAR proteins and molecular motors (Chapter 5).

3) We will explore the specific contribution of the scaffolding BAR domain *versus* amphipathic helices in: scaffolding (Chapter 4), fission (Chapter 5), and sensing membrane curvature (Chapter 6).

4) Finally, we will expand our study of membrane modulators to explore the more generic mechanism of inducing spontaneous curvature by studying the interaction of lipid membranes with calcium ions (Appendix I).

The main scientific method of this study is reconstituting biological systems *in vitro*, by building minimal systems that reproduce a measurable effect. In other words, we study a cell phenomenon (e.g. endocytosis) by isolating a desired aspect of this phenomenon (e.g. membrane fission) and constructing a simple and controllable system. The disadvantage of such approach is that we neglect the important collective effect of numerous components and the complex modulation achieved by an interplay of various components. However, the significant advantage of this approach is that we carefully control many important parameters; namely, protein concentration, lipid composition, surface tension, membrane geometry. By systematically varying these parameters, we investigate the full range of protein-membrane interactions, which would otherwise be masked in complex and noisy systems (e.g., a cell).

GUVs are particularly attractive membrane models since they are big enough (5–50 μm in diameter) to be resolved by optical microscopy. They are also amenable to micropipette-aspiration techniques and manipulation by optical tweezers which can be used to modulate the mechanics and geometry of the membrane. Further-

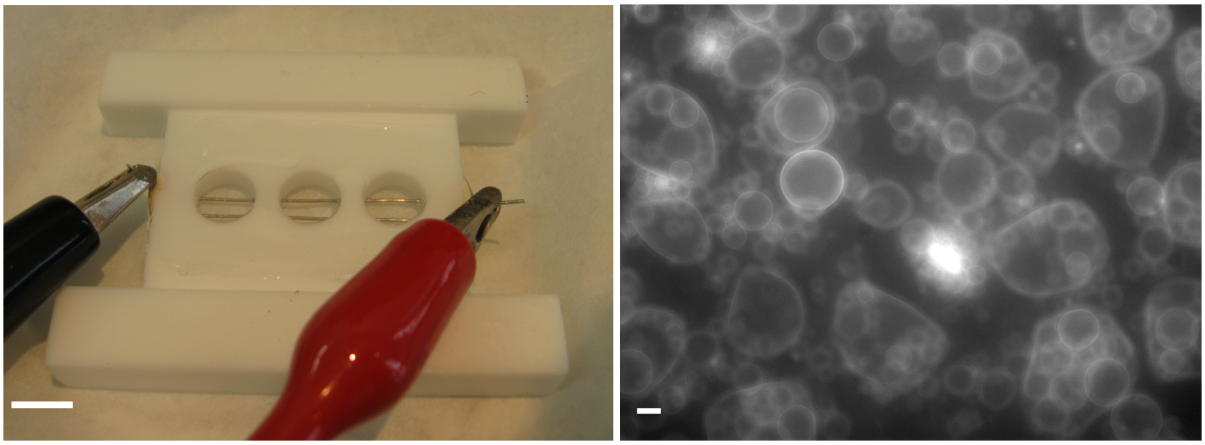

Figure 2.1.1: Preparation of GUVs. Left: Teflon electroformation chamber for preparing GUVs on Pt-wires. Image taken from (Sophie Aimon, PhD thesis, 2012). Scale bar: ~ 2 cm. Right: Epifluorescence image of GUVs composed of 80% egg-PC and 20% cholesterol prepared with electroformation on ITO plates. Scale bar: 5 μm.

more, observing single vesicles at a time lets us correlate the amount of bound proteins or particles with the morphological or mechanical effect on the membrane.

2.1. Experimental membrane models

2.1.1) Reagents. Total brain extract (131101P), L-α-phosphatidylinositol-4,5-bisphosphate (PI(4,5)P2, 840046P), 1,2-dioleoyl-sn-glycero-3-phosphatidylcholine (DOPC), 1,2-dioleoyl-sn-glycero-3-phosphatidylserine (DOPS), 1,2-dioleoyl-sn-glycero-3-phosphatidylethanolamine (DOPE), 1,2-distearoyl-sn-glycero-3-phosphoethanolamine-N-[biotinyl(polyethyleneglycol)-2000] (DSPE-PEG(2000)-biotin), and 1,2-dioleoyl-sn-glycero-3-phospho-L-serine-N-(7-nitro-2-1,3-benzoxadiazol-4-yl) (NBD-PS) were purchased from Avanti Polar Lipids. BODIPY-TR-C5-ceramide, BODIPY-FLC5-hexadecanoyl-phosphatidylcholine (HPC*), TR-1,2-dihexadecanoyl-sn-glycero-3-phosphatidylethanolamine (DHPE*), BODIPY-FL C5-ganglioside GM1 (GM1*) were purchased from Molecular Probes. All reagents used to make buffers and β-casein from bovine milk (>99%) were purchased from Sigma-Aldrich. Polystyrene streptavidin-coated beads (diameter 3.2 μm) were purchased from Bangs Laboratories. We obtained the proteins from our collaborators Harvey McMahon (Cambridge) and Ludger Johannes (Institut Curie), further specified in Chapter 4.

2.1.2) Preparation of GUVs. Electroformation is the most common way of preparing GUVs (Angelova et al., 1992). The method has gained considerable traction since it only takes 1–3 h to produce vesicles, much faster than ~ one day required to produce GUVs by spontaneous swelling of a rehydrated lipid film (Reeves and Dowben, 1969). The method accelerates the swelling of vesicles using an alternating current (AC), however the theory behind the process is not well understood (Meleard et al.,

2009). For some time, the key disadvantage of the method was the inability to grow GUVs in buffers that contain physiological ionic strength. This obstacle was overcome by applying a weaker current at higher frequency (Montes et al., 2007). Furthermore, it has been shown that growing GUVs at higher frequency works much better on Pt-wires (Fig. 2.1.1., A) than on semi-conductive plates coated with indium titanium oxide (ITO) (Mathivet et al., 1996).

We used both ITO plates and Pt-wires to prepare GUVs. When using ITO plates, first, lipid mix dissolved in chloroform at 1 g/L was deposited on the conductive side of two ITO plates (PGO, Iserlohn, Germany). The lipids were deposited in a snake-like pattern to make the film as thin and unilamellar as possible. In our case, we spent approximately 10 μL of the lipid mix per ITO plate of dimensions 4 cm by 10 cm. The ITO plates were dried under vacuum for about an hour. Then, they were fixed at a distance of ~ 1–2 mm, sealed by a putty sealant (Vitrex), hydrated with 200 mM sucrose, and finally attached to a function generator under a sine AC current, at 1 V (peak to peak) and 10 Hz. We grew vesicles containing up to 20% net charge for one hour, whereas those containing 30% net charge for 45 min. Importantly, we could not use ITO plates to grow DOPC-containing GUVs that had more than 20% DOPS unless we added DOPE at a fraction matching DOPS (e.g. DOPC:DOPS:DOPE = 1:1:1 molar ratio). In addition, we could not grow vesicles composed of the total brain extract and PIP_2 on ITO plates. After growth, the GUVs were identified under a phase-contrast light microscope (Fig. 2.1.1, B) and ~ 10 μL was collected from GUV-rich regions.

GUVs with a composition of ~ 95% total brain extract and 5% PIP_2 (molar ratios, molar mass of the extract approximated at 800 g/mol) were grown on Pt-wires at near-physiological salt conditions. The lipid mix was deposited onto a pair of Pt-wires, in drops separated by 0.5 cm (total ~ 4 μL). The wires were dried under vacuum for 30–60 min then hydrated in a solution of 70 mM NaCl, 100 mM sucrose, and 10 mM tris, at pH = 7.4. We then applied a sine AC current through the Pt-wires at 500 Hz and 280 mV. The GUVs were grown overnight in the fridge (4 °C). While, the composition of the solution inside GUVs could be different, deviations from these optimized conditions typically resulted in: low GUV yield or too many small, multilamellar, non-fluid, and tense vesicles, etc. In addition, these conditions produce GUVs that gain excess surface area within 15 min of being collected, ideal for micropipette-aspiration experiments. Importantly, we disconnected the wires just prior to each experiment, collected GUVs directly from the wires using a pipette (~ 10 μL of final solution per droplet of the lipid mix), transferred them on ice and used as soon as possible. We did not use GUVs for more than 4 h.

2.1.3) Preparation of SUVs. SUVs, or small unilamellar vesicles, were used for ζ-potential measurements and for the subsequent preparation of supported lipid bilay-

ers. First, a lipid mix (at 1 g/L) was completely dried under nitrogen in a glass vial, by rapidly rotating the vial to evenly spread the lipids on the bottom and the walls. The total mass of dried lipids was ~ 1 mg. The mix was hydrated in 1 mL of 200 mM sucrose then shaken for an hour at 37 °C. The hydrated lipids (in a reinforced glass vial) were subjected to five rounds of flash freezing in a cold bath (prepared by dropping a block of dry ice in ethanol) then rethawing. Then, the thawed lipids were extruded through a 100-nm polycarbonate filter 21 times. We expect that hydrating in solutions of low ionic strength inhibits the formation of multilamellar charged vesicles due to lower screening.

2.1.4) Making supported bilayers. SUVs formed in Section 2.1.3 were deposited onto a plasma-cleaned coverslip at ~ 0.5 g/L then washed with buffer (100 mM NaCl and 10 mM tris buffer, pH = 7.4), making sure the surface does not get exposed to air. The principle of the method is the following: cleaning the coverslips in the plasma oven under vacuum makes the glass surface very hydrophilic due to ionization. SUVs adhere extremely well to the glass which causes them to burst and turn into a planar bilayer.

2.1.5) Making tensionless tubules from multilamellar sheets. We deposited a drop of a lipid mix containing 95 % total brain extract and 5 % PIP_2 onto an acid-cleaned glass slide. The deposit was dried for an hour under vacuum then rapidly hydrated with a solution of 100 mM NaCl and 10 mM tris buffer (pH = 7.4). This process creates multilamellar sheets with many tensionless tubules emanating from the edges. We observed the edges of the sheet with differential interference contrast microscopy before and after adding the protein (to a bulk concentration of 5 μM) for up to 30 min.

2.2. Microscopy and optical tweezers

2.2.1) Optical microscopy. An optical microscope relies on lenses to magnify an illuminated sample (Mertz, 2010). Lenses are typically housed in an objective, characterized by two parameters: numerical aperture and magnification. The maximum resolution of optical microscopy (R_{max}) is given by the Abbe criterion:

$$R_{\max} = \frac{0.61\lambda}{N_a}, \qquad \text{(Eq. 2.1)}$$

where N_a is the numerical aperture, given by $N_a = n\sin\theta$, n being the index of refraction, θ half the maximum angle at which light can enter or exit the objective, and λ the wavelength of light. R_{max} of a fluorescence microscope is ~ 250 nm. This value is often termed the **diffraction limit**, representing the minimum distance at which two

objects should emit light in order to be separately resolved. Therefore, resolution can be improved (i.e. R_{max} is low) by making λ low, while making n and θ high (Mertz, 2010).

Bright field microscopy is the simplest optical microscopy technique in which light is transmitted through the sample and collected at the objective. Denser or stained areas of the system will absorb more light, providing a contrast that allows us to observe the sample. **Phase contrast microscopy** takes advantage of that fact that transparent objects with different thickness or refractive indices alter the phase of diffracted light. The optics is set up so that it manipulates the diffracted and non-diffracted light, increasing the contrast of transparent objects. In **differential interference contrast microscopy** the optics is assembled in a way to be sensitive to refractive index gradients of different areas of a specimen. It works by, first, passing the light through a polarizing filter, which orients the electromagnetic waves in one plane. Next, the light is bifurcated and separated by a distance equal to objective resolution. After passing through the sample, the light beams coalesce, however due to the differences in refractive indices within the sample, there are amplitude variations between the two beams that cause a strong contrast.

2.2.2) Fluorescence microscopy. Fluorescence microscopy is a type of optical microscopy where, instead of magnifying objects based on different absorptions of reflections of visible light, it excites fluorescent molecules and captures their emitted fluorescence. The basic setup is an **epifluorescence or a wide-field microscope**. Here, a filter is placed after a high-intensity illumination lamp (e.g. mercury arc lamp) that selectively lets pass only a narrow range of wavelengths. The light is then directed toward a dichroic mirror that reflects beams of certain wavelengths, while letting others pass through. In this case, the mirror reflects the excitation light, which then irradiates the sample. Fluorescence molecules absorb excitation light and, through the phenomenon of fluorescence, emit light of lower energy, hence higher wavelength. The emitted light passes through a dichroic mirror, which can filter out any non-absorbed excitation light (same as above), and then goes through the emission filter, which eliminates any other background light, not coming from fluorescent molecules. The caveat of this setup is that the entire visual field of the sample is illuminated creating a lot of noise in imaging. In **confocal microscopy**, spatial filtering eliminates the light outside the thickness of the focal plane (~ 100 nm) which effectively increases the resolution and the contrast. The basic configuration comprises a point illumination and a pinhole placed in front of the detector, in an optically conjugated plane. The depth of the image can be changed by altering the focus, which gives a three-dimensional image of the sample.

Super-resolution microscopy is a technique that makes use of different timing of emission of two fluorophores so to separately localize them even if they are

within the diffraction limit (Gould and Hess, 2008; Hell and Wichmann, 1994). The two most common variations of this method are the photo-activated localization microscopy (PALM) (Betzig et al., 2006; Hess et al., 2006) and stochastic optical reconstruction microscopy (STORM) (Rust et al., 2006). Both techniques are based on applying an activation laser at low power, which stochastically triggers the emission of a small percentage of molecules. Ideally, the fluorohpores remain in the active state for one to three imaging frames then either get bleached (used in PALM) or deactivated (used in STORM). The sample is observed over time then the image is reconstructed by combining all the localization points.

2.2.3) Optical tweezers. Optical or laser tweezers (also referred to as optical trap) are a microscopic manipulation technique that can be used to exert and measure molecular forces in the range from 0.1 to 100 pN (Ashkin et al., 1986; Neuman and Nagy, 2008). Tweezing objects with light works in the following way: a laser beam is focused so that its center is brighter than its edges. In contact with object that reflects or refracts light, it gains momentum, but due to the conservation of motion, the object receives equal and opposite momentum. The total force on the object can be decomposed into two orthogonal components: the attractive component which is a result of the strong electric field gradient toward the center of the beam, polarizing the molecules, and a scattering force that acts in the direction of the beam. If the gradient force is higher than the scattering force, the objects are stably trapped. Due to the scattering force, objects are trapped slightly outside the center of the beam. The trap acts like a spring, so in the limit of small displacements, the restoring force is linear with displacement.

2.3. Tether-pulling experiment[1]

2.3.1) The microscope. Tether-pulling experiments were carried out on a Nikon TE2000 inverted microscope equipped with an eC1 confocal system (Nikon). There were two laser lines operating at λ = 488 nm and λ = 543 nm (Fig. 2.3.1, A). The optical path was supplemented with optical tweezers, induced by a 5 W ytterbium fiber continuous wave laser emitting infrared light (λ > 1070 nm; IPG GmBH Germany) (Fig. 2.3.1, B). We used two high-aperture objectives: an oil-immersion (100 times magnification, N_a = 1.3) and a water-immersion (60 times magnification, N_a = 1.27) objective.

2.3.2) Micropipette aspiration. Aspiring GUVs with a micropipette achieves 1) immobilizing the membrane for confocal imaging, and 2) setting membrane tension by

[1] I am extremely grateful to Coline Prévost who taught me everything there is to know about tether-pulling experiments and their analysis.

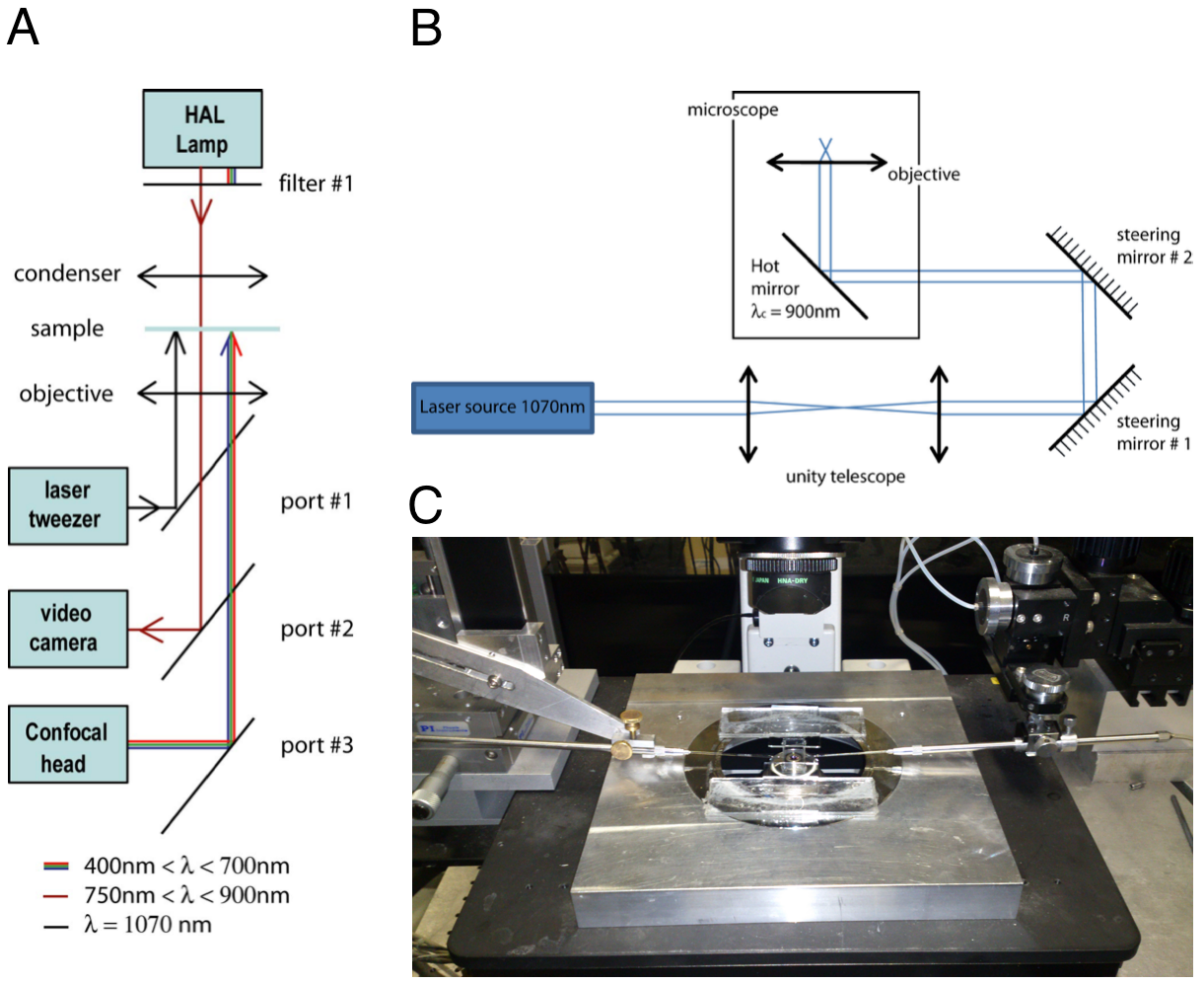

Figure 2.3.1: Experimental setup. (A) Optical path of the microscope. Optical trap (laser tweezer) is achieved with a 1070-nm continuous wave laser (port #1), bright field microscope uses near-infrared light (port #2), while confocal microscopy uses visible light (port #3). Taken from (Sorre et al, 2009), Fig. S1. (B) Scheme of the optical trap used in this thesis. Taken from Benoit Sorre, PhD thesis, 2010. (C) Photograph of the microscopy stage, showing the experimental chamber mounted on an objective (center), with the aspiration pipette on the left and the injection pipette on the right.

varying the aspiration pressure. We can calculate the membrane tension via the Laplace equation (Kwok and Evans, 1981):

$$\sigma = \Delta p \frac{r_p}{2\left(1 - r_p / r_{ves}\right)}, \qquad \text{(Eq. 2.2)}$$

where σ is membrane tension, Δp is the hydrostatic pressure, and r_p and r_{ves} are, respectively, radii of the aspiration pipette (at the exit) and the vesicle. Note that this formula requires that the length of the aspirated membrane be at least r_p (Kwok and

Evans, 1981), therefore in the analysis, we eliminated all data points that did not meet this requirement.

Micropipettes were prepared using a borosilicate glass capillary (with internal and external radii of 0.7 mm and 1 mm, respectively; Harvard Apparatus). The capillary was pulled using a pipette puller (Sutter instrument P-2000) then the shape of the pipette exit was refined with a microforge (MF-800, Narishige, Japan) so to set the pipette diameter at 5–7 μm. The aspiration pipette was filled with buffer containing 5 g/L β-casein, to passivate the glass capillary surface. The pipette was then connected to a water tank, which controls the aspiration pressure. To calculate the hydrostatic pressure, we first set a zero-pressure. To do that, we observed the pipette under the bright field microscope, set it next to a visible object (such as a colloidal bead) then adjusted the aspiration until there was no net movement of the colloidal bead at the pipette exit. With subsequent aspiration, we calculated Δp according to:

$$\Delta p = \rho(\mathrm{H_2O}) g \Delta h(\mathrm{H_2O}), \qquad \text{(Eq. 2.3)}$$

where $\rho(\mathrm{H_2O})$ is water density, g the Earth's gravitational acceleration, and $\Delta h(\mathrm{H_2O})$ the height of the water tank (compared to the zero position). The height difference was varied up to ~ 5 cm, corresponding to ~ 500 Pa.

2.3.3) Experimental protocol. The experimental chamber was constructed by attaching two coverslips onto a custom built metal frame (Fig. 2.3.1, C) so that the two coverslips are separated by ~ 2 mm. The experimental chamber and the aspiration pipette were filled with a 5 g/L solution of β-casein (dissolved in 100 mM NaCl, 10 mM tris, pH = 7.4) so to minimize the adhesion of lipids to the glass surface. The tip of the aspiration pipette (connected to a water tank as described above) was brought inside the experimental chamber with an x-y-z micromanipulator. In addition to the micromanipulator, the horizontal position of the aspiration pipette was controlled with a piezoelectric actuator (Physik Instrumente). Casein was incubated for 30 min. The chamber was then rinsed several times and filled with the experimental solution. In case of GUVs made out of lipid brain extract doped with 5% PIP_2, we used an experimental solution composed of 100 mM NaCl and 40 mM glucose (buffered with tris to pH = 7.4). Importantly, the ionic strength of solutions used to grow GUVs (inside GUVs) and for tether-pulling experiments (outside GUVs) was confirmed to be within 10 mOsm using an osmometer (Loser, Germany) to avoid osmotic shock. Then, we added a fractionate amount of polystyrene beads. Another pipette was filled with the solution of a curvature-active molecule (e.g. protein), as outlined in individual chapters. Usually, only the tip of the injection pipette was filled by suction, then the back of the pipette was filled with mineral oil, leaving no air inside. The vesicles were left to deflate for 10–30 min after which we sealed the chamber with mineral oil to prevent evaporation.

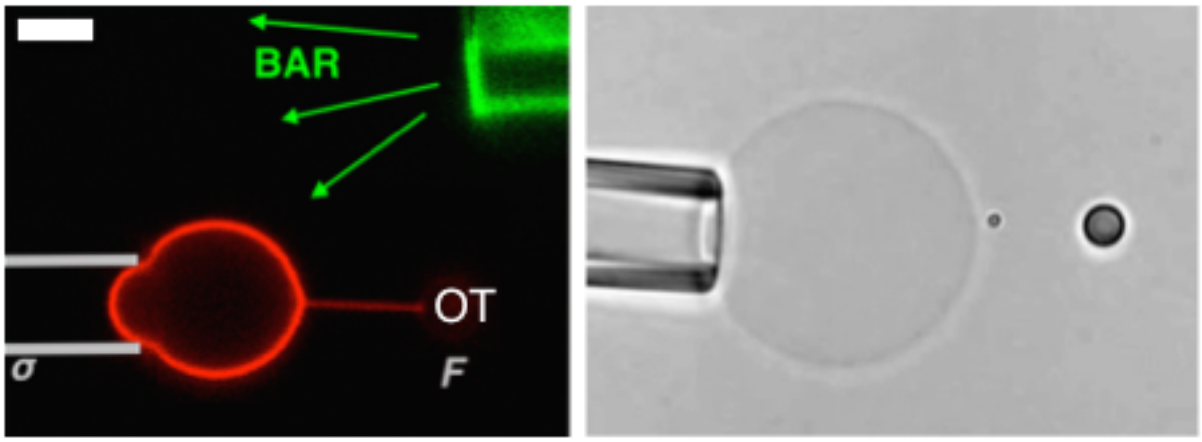

Figure 2.3.2: Tether-pulling experiment. Confocal fluorescence (left) and bright field (right) images of a tether pulled from an aspired GUV. F = force, σ = membrane tension, OT = optical trap. Scale bar = 5 μm.

GUVs with enough excess area (i.e., those with visible undulations) were aspired in a micropipette (Cuvelier et al., 2005; Kwok and Evans, 1981). Note, each time before aspiring a GUV, we re-adjusted the aspiration pressure to zero (as described above). Then, we trapped a bead in the optical trap. We gently tethered the GUV to the bead and pulled back, forming a tubular membrane between the GUV and the bead (Fig. 2.3.2). Subsequently, we injected the desired solution with another pipette in the close proximity of the tether (Fig. 2.3.2, left) at a pressure of 1–2 Pa. During the experiment, we would set the aspiration pressure, record the bright field microscopy image at 30 frames per second (Fig. 2.3.2, right) and take several images with the confocal microscope. After several minutes, we would change the aspiration pressure and repeat the procedure. Typically, we would do a set of measurements before and another set after injection to see the effects on the same vesicle. Of note, the direction of aspiration pressure (increase or decrease) is irrelevant (see the control experiment in Chapter 4).

2.3.4) Force measurement and calibration. We measured the force based on the movement of the trapped bead. Assuming that the trap behaves as a Hookean elastic spring, the force may be written as:

$$F = k_{\mathrm{OT}}\left(a - a_0\right), \qquad \text{(Eq. 2.4)}$$

where F is the force on the optical trap, k_{OT} is the trap stiffness, a and a_0 are the current and the equilibrium positions of the bead, respectively. We measured the bead position simply by monitoring the movement of the center of the bead from the bright field microscopy images. We used a camera to record the images, with pixel size of 0.1355 μm (before 1 May, 2013) and 0.154 μm (after 1 May, 2013).

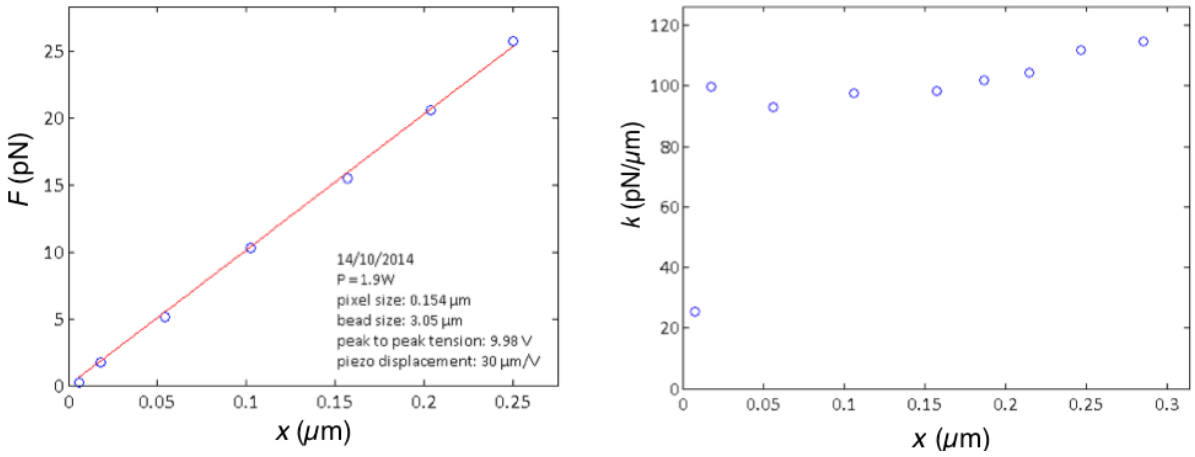

Figure 2.3.3: Calibration of the optical trap. Plots of force (F) and trap stiffness (k) as a function of the displacement of the bead (shown is a representative example). Linear fit of the force versus displacement yields the trap stiffness ~50 pN μm^{-1} W $^{-1}$. Power of the laser in both plots: 1.9 W. Measured 15 μm above the bottom coverslip.

We calibrated the stiffness of the trap by observing the displacement of the bead from its equilibrium position upon applying a viscous force.[2] According to the Stokes' law of viscous drag:

$$F_v = 6\pi\eta r v\,, \qquad \text{(Eq. 2.5)}$$

where F_v is the viscous force, η the viscosity of the solution, r the radius of the bead, and v the velocity of the bead relative to the fluid. We created a viscous force by applying a triangle wave of varying amplitude to the piezo actuator, which dragged the stage (i.e., the fluid inside the chamber). The measured output force was proportional to the applied velocity and the slope of the plot gives the stiffness of the trap (Neuman and Block, 2004) (Fig. 2.3.3, left). We confirmed that the stiffness does not appreciably change over a range of displacements up of 0.3 μm (Fig. 2.3.3, right). We repeated the measurement several times over the past three years, yielding (all in pN μm^{-1} W^{-1}): 50 (before January 2013), 45 (January 2013 - 18 March 2013), 53 (18 March 2013 - 1 May 2013), 47 (1 May 2013 - January 2015).

2.3.5) Fluorescence measurement. We used confocal microscopy to measure the fluorescence intensity of fluorescent dyes present in the GUV. We acquired images in the red and the green channels, with a ~ 1 s delay in acquisition time between the two channels. For the green channel, we excited the system using a 0.2 mW laser at 488 nm, whereas for the red channel, we used a 0.03 mW laser at 543 nm.

[2] Many thanks to Coline Prévost with whom I worked on calibrating the trap and to Feng Tsai and David Saletti who performed the final measurement.

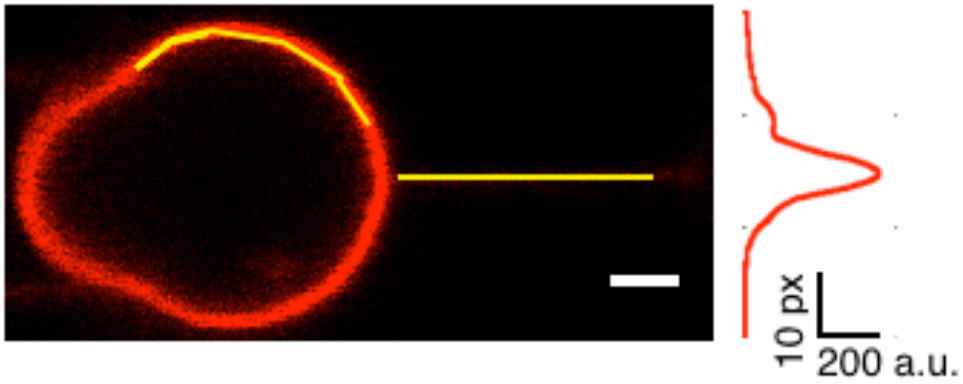

Figure 2.3.4: Fluorescence measurement. Yellow lines are the central lines in fluorescence measurements. Plot shows fluorescence intensity profile along the tubule line and 30 horizontal pixel lines above and below. The final fluorescence intensity is the maximum in shown plot minus the average in intensity of the top ten lines of the whole image. The yellow line in the vesicle was first flattened then the analysis was carried out as on the tubule.

To quantify the fluorescence on the tubule, we drew a line along the length of the tubule, then measured the intensity in pixels along the drawn line, plus thirty horizontal lines of pixels above and below. Next, we averaged the intensities in each horizontal line and selected the maximum of the average intensities (Fig. 2.3.4). The result was the maximum average intensity minus the background, calculated as the average intensity of the ten outermost horizontal lines of pixels in the original image. We measured the fluorescence intensity on the vesicle in the same way, except that we created the initial line by unwrapping the contour of half of the vesicle.[3]

2.3.6) Calibration of the tubule radius and protein areal density. The radius of the tubule (r) is set by the membrane tension and it can be derived from the Helfrich Hamiltonian (see the details in Chapter 4): $r = F/(4\pi\sigma)$. Force, F, represents the tether-retraction force, i.e. the point force experienced by the bead in the optical trap. Considering that curvature-active molecules likely affect the tether-retraction force (F), we require an independent measurement of the radius of the tubule. As the tubule radius is narrower than the confocal slice thickness, the total intensity of the tubule per unit length is proportional to the circumference, implicitly radius. The fluorescence intensity of the tubule can be calibrated against its radius by measuring the radius of the tubule of a reference membrane (i.e., in the absence of curvature generators) from the tether-retraction force. Then, we rescale the fluorescence intensity to match this radius at the same membrane tension, i.e:

[3] The indispensable Matlab code used to analyze the fluorescence was written by Gil Toombes and Coline Prévost.

$$r = C_{\mathrm{f}} \frac{I_{\mathrm{t}}}{I_{\mathrm{ves}}}, \qquad \text{(Eq. 2.5)}$$

where I_{t} and I_{ves} are the fluorescence intensity of the tubule and vesicle, respectively, and C_{f} is the calibration factor, previously determined as 200±50 (Sorre et al., 2012) and later a similar value was obtained by Sophie Aimon in the group (Aimon et al., 2014). Note, we normalize the fluorescence intensity of the tubule by the intensity of the vesicle, as the precise amount of labeled lipid in the membrane is not the same in each experiment.

To measure the density of proteins bound to the membrane, we applied a previously developed quantification protocol (Galush et al., 2008; Sorre et al., 2012). The method is based on calibrating the density of the protein by relating its fluorescent intensity to the intensity of another fluorescent molecule, for which we can easily quantify the amount. For the reference fluorophore, we used a fluorescent lipid HPC*. We can write the areal density of the desired fluorophore on the GUV ($\varphi_{i,\mathrm{ves}}$) in terms of HPC* as:

$$\varphi_{i,\mathrm{ves}} = \frac{\varphi_{\mathrm{HPC*,ves}}}{I_{i,\mathrm{b}} / I_{\mathrm{HPC*,b}}}. \qquad \text{(Eq. 2.6)}$$

We correct the areal density by the ratio of intensities of the measured fluorophore and HPC* in bulk, $I_{i,\mathrm{b}}/I_{\mathrm{HPC*,b}}$, considering that the two fluorophores do not necessarily emit the same intensity at the same concentration. Hence, first we determined the ratio of fluorescence intensities between Alexa488 (bound to a protein) and HPC* in bulk (dissolved in mineral oil), yielding $I_{i,\mathrm{b}}/I_{\mathrm{HPC*,b}} = 0.91\pm0.05$. Next, we measured the fluorescent intensity of GUVs composed of egg-PC and HPC* at mole fractions χ = 0.01%–1%. We assume that the incorporation of the fluorescent lipid into the GUV is stoichiometric. If we assume that the area per lipid is 0.7 nm^2, the number of HPC* per μm^2 per leaflet is 1.43 million multiplied by χ. As expected, fluorescence intensity linearly depended on the HPC* concentration (Fig. 2.3.5), i.e.,

$$\varphi_{\mathrm{HPC*,ves}} = A I_{\mathrm{HPC*,ves}}, \qquad \text{(Eq. 2.7)}$$

however the slope of intensity with respect to HPC* amount (A) depends on the selected detector sensitivity (i.e., gain) and the applied neutral density (ND) filter. Therefore, we repeated the experiment at various different gains and ND filters (see Fig. 2.3.5 for example and Table 2.3.1 for all measured values for A).

Finally, to calculate the areal density of proteins on the vesicle, we determined the number of Alexa488 fluorophores per molecule of the protein, by measuring the

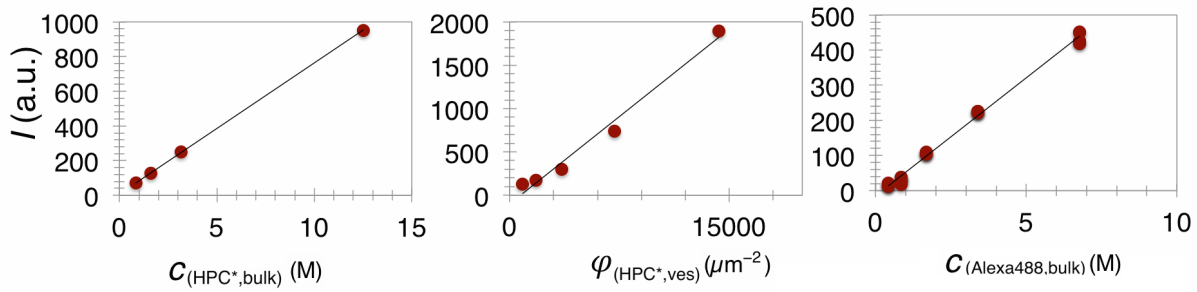

Figure 2.3.5: Surface density calibration. Relating fluorescence intensity to the concentration of HPC* in bulk (left), in GUVs, and of Alexa488 in bulk (right). Table 1 shows the reciprocal slope of the plot in the center. In shown experiments, we used a gain of 110 and ND8 and ND4 filters.

absorbance using a nanodrop. The number of fluorophores per protein (n_f) were calculated according to the formula suggested in the Molecular Probes manual:

$$n_f = \frac{A_{488}/\varepsilon_{488}}{\left(A_{280} - 0.11A_{488}\right)/\varepsilon_{280}}, \qquad \text{(Eq. 2.8)}$$

where A_{488} and A_{280} are the absorbance values per unit length at 488 nm and 280 nm, respectively, ε_{488} and ε_{280} are the molar absorption coefficients of Alexa488 and the protein, respectively. We calculated the molar absorption coefficients of the proteins by using an online server (http://web.expasy.org/protparam/), which gave 26 930 M^{-1} cm^{-1} for β2 centaurin (BAR and PH domains). We obtained n_f = 1.3 (per protein monomer). Note, considering there is only one cysteine per monomer, it appears that 30% of label molecules bound in non-specifically. Therefore, to calculate the areal density of BAR/N-BAR protein dimers, we used the following formula (where the factor 2 accounts for the dimer):

$$\varphi_{\mathrm{BAR,ves}} = \frac{AI_{\mathrm{BAR,ves}}}{0.91 \times 2 \times n_f}. \qquad \text{(Eq. 2.9)}$$

Table 2.3.1:* Calibration of HPC* density in the GUV. Shown are values of A (in μm^{-2}) for a given gain and ND filter filter. Values were obtained by taking a reciprocal slope of the center plot in Fig. 2.3.4.

	gain						
	80	90	100	110	120	130	140
ND4 & ND 8	103.7	38.2	17.5	8.1	4.8	3.4	1.1
ND 8	42.4	17.2	8.0	5.9	2.9	1.6	

Fluorescence intensities of HPC in bulk and GUVs were analyzed by Coline Prévost.

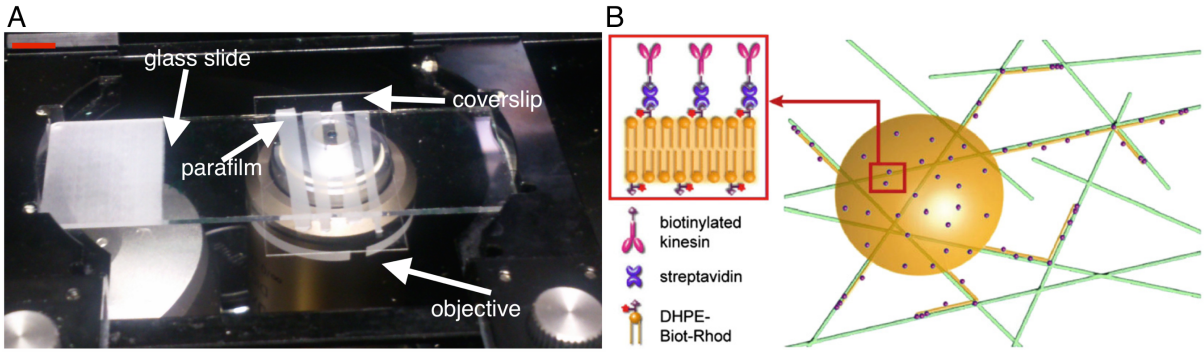

Figure 2.4.1: Pulling tethers with kinesin. (A) Photograph of the experimental chamber. Scale bar ~ 2 cm. (B) Scheme of the assay. Biotinylated kinesins bind streptavidin in solution, which serve as anchors to biotin in the GUV. Adding ATP initiates the walk of kinesin along microtubules polymerized on the glass surface (green lines), forming membrane tubules. Scheme taken from (Leduc et al 2010).

For the moment, we are unable to accurately measure the number of Alexa488 per endophilin A2 N-BAR domain, as it does not contain any tryptophan residues, necessary for efficient excitement at 280 nm. Considering that the labeling procedure was the same as with centaurin and that both constructs contain one cysteine per monomer, we can assume a comparable binding efficiency.

2.4. Pulling tethers with molecular motors

Proteins, kinesin and biotinylated tubulin, were previously prepared and kindly provided by Jean-Baptiste Manneville. All proteins were stored at −80 °C. We follow previously described protocols for the extrusion of tubules from GUVs (Leduc et al., 2010; Leduc et al., 2004).

2.4.1) Polymerization of microtubules. 50 µL of tubulin (~10 µM) was incubated at 37 °C for 15 min, which induces their polymerization. Then, we added 2 µL of 1 mM taxol (diluted in water) to 50 µL of tubulin. Taxol acts to stabilize the microtubules. We centrifuged the mix for 15 min at 37 °C, at a speed of 70 000 rpm (ultracentrifuge, rotor TLA-100). We removed the supernatant and resuspended the sediment in 50 µL BRB (25 µL of 4X BRB, 75 µL H_2O, 3 µL of 1 mM taxol). We let the microtubules incubate for at least one day and we used them no more than 3 days after preparation.

2.4.2) Coupling kinesin to microtubules. First, we washed a glass slide with ethanol and water. We cut small rectangular pieces of parafilm, adhered them to the glass slide edge-to-edge, spaced at ~ 0.5 cm. Then, we covered the glass slide with an unwashed coverslip (directly from the box). We placed the assembled chamber on the

hot plate (100 °C) for ~ 30 s, melting the parafilm that, after cooling, acted as a sealant (Fig. 2.4.1, A). Thus formed assembly has several small experimental chambers, of volume ~ 5 μL.

We filled the chamber with 5 μL polymerized microtubules and kept for 15 min at room temperature. Then, we incubated 5–10 μL of biotinylated kinesin (~ 10 μM) with 5 μL streptavidin (at comparable concentration as kinesin) for 15 min on ice. During incubation of kinesin, we first rinsed the experimental chamber (containing microtubules) with ~ 10 μL of buffer composed of: 97 μL of 50 mM imidazole (dissolved in 7 g/L casein) and 3 μL of 1 mM taxol, buffered to pH ~ 7. **Importantly, the rinsing was done as carefully as possible**, as fluxes in the chamber cause the polymerized microtubules to desorb from the glass. We incubated for 5 min at room temperature. Next, we rinsed (again, very carefully) with ~ 10 μL of buffer composed of: 96.5 μL of 50 mM imidazole, 0.5 μL of 1 M DTT, and 3 μL of 1 mM taxol, buffered to pH ~ 7. We incubated for another 5 min. Finally, we injected the chamber with 5 μL kinesin that has been incubating with streptavidin. We incubated for at least 10 min. Note, this incubation step can be prolonged for a couple of hours if desired.

2.4.3) Motor-induced tether-pulling assay. To initiate the motors, we rinse the chamber with 10–15 μL motility buffer, composed of: 89 μL experimental buffer (in our case, 40 mM glucose, 100 mM NaCl, and 10 mM tris, at pH = 7.4), 0.5 μL of 1 M DTT, 3 μL of 1 mM taxol, 2 μL of 100 mM ATP (freshly prepared), 3 μL of 4X oxygen scavenger (freshly prepared). In case the experimental buffer does not contain glucose, it needs to be added to the mix (2.5 μL of 1 M solution).

Immediately after rinsing, 1–2 μL of highly concentrated solution of GUVs (that need to contain a fractionate amount of biotinylated lipids) is added to the experimental chamber. The GUVs are directly collected from the GUV-rich areas in the Pt-wire chamber. It is possible to spin down the vesicles (at 1000 rpm, 90 s), however we did not notice a difference in yield. After introducing GUVs, we tilt the chamber at 45° for one minute to help sediment the vesicles then mount it on the objective (Fig 2.4.1, A). We imaged as soon as possible. Note, that excessive exposure to fluorescent excitation can abort the motors due to oxidation. Figure 2.4.1, B shows a scheme of the assay.

2.5. Molecular dynamics simulations

Theoretical approaches to studying biological phenomena have seen appreciable advancements in the past decade, allowing detailed structural and thermodynamic descriptions of fundamental cellular processes, such as protein folding, lipid vesicle formation, or large-scale structural rearrangements of macromolecules. The observa-

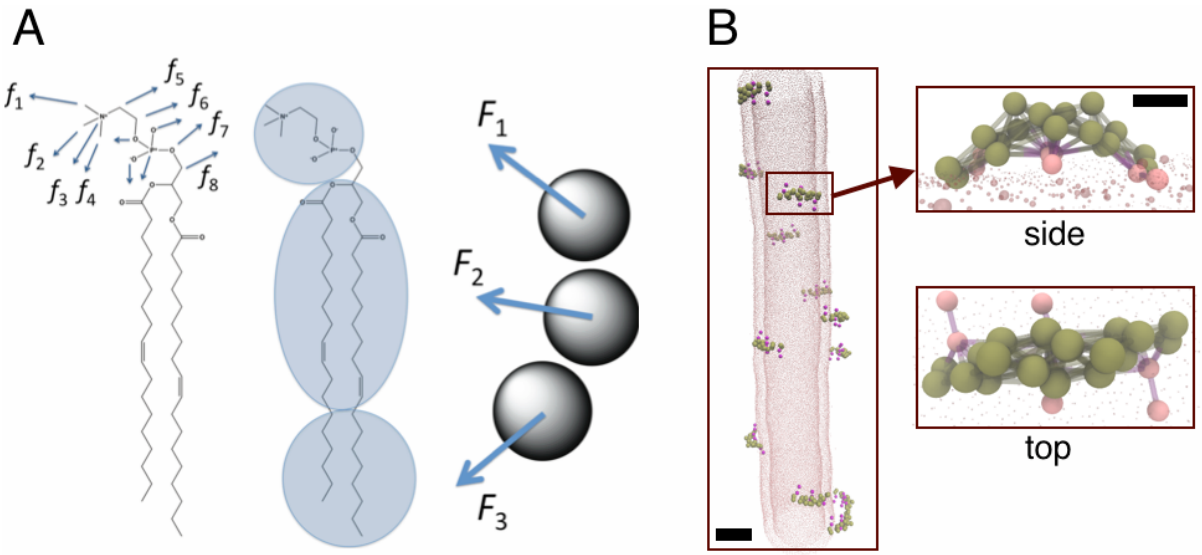

Figure 2.5.1: CG models. (A) Atomic (left) and the three-site CG (right) representation of the lipid. The circled atoms in the middle comprise the corresponding CG sites in the CG model. Lower-case *f* are forces on each atom, whereas upper-case *F* represent averaged forces on each CG site. (B) Membrane tubule constructed from the CG lipid coated with a 26-site CG N-BAR domain. Shown is the initial configuration of a simulation with 5% N-BAR coverage. N-BAR model is magnified on the right. Scale bars are 10 nm and 3 nm (inset).

tion of dynamics of biological systems at high resolution is still beyond the reach of most available experimental techniques, making computational methods irreplaceable in modern chemical and biophysical research. Such methods predict the behavior of atoms and molecules by making use of various theories that describe their interactions, such as quantum mechanics, Newtonian dynamics, or macroscopic mechanics. The choice of theory depends on the resolution we wish to simulate and the computational limitations. For example, in all-atom molecular dynamics (MD) simulations, each atom (or a small subset of atoms) is represented with a sphere of certain size, charge, etc. The total energy is calculated based on the interactions between each atom, usually derived from quantum mechanics or adapted from thermodynamic experiments. After calculating the total force experienced by each atom, their movement is simulated by using Newton's laws (van Gunsteren et al., 2006). However, at present, such simulation approach is very expensive if the system exceeds a million atoms, roughly corresponding to a large protein surrounded by a box of water.

Enhanced sampling and coarse-graining strategies provide a way of accessing larger time and length scales, while ensuring that the behavior of such processes is well described (Ayton and Voth, 2009). As we aimed to simulate the collective behavior of N-BAR proteins on the membrane, we required to simulate many protein molecules at longer time scales. Hence, we used **coarse-grained** (CG) MD simula-

tions. In CG models many atoms are clumped together into a single sphere (i.e., CG site), therefore significantly reducing the number of degrees of freedom. There are two opposite ways of obtaining such models: the bottom-up approach, in which forces are estimated from all-atom simulations, or *ad hoc*, where the interactions are approximated by matching some experimental observations (Ayton and Voth, 2009; van Gunsteren et al., 2006).

2.5.1) CG models. To model the lipid bilayer, we used a previously developed solvent-free three-site lipid model (Srivastava and Voth, 2013). One site represents the hydrophilic head group, whereas the other two represent the hydrophobic tails of a lipid, as depicted in Figure 2.5.1, A. The interaction among CG sites were calculated in a bottom-up way, by averaging forces from an all-atom simulation of a lipid bilayer, supplemented by analytical functions for regions of the configurational space poorly sampled in all-atom simulations (Izvekov and Voth, 2005; Srivastava and Voth, 2013). In CG simulations, we only accounted for the forces between lipid sites that were within 2 nm.

A previously developed model of an N-BAR domain of endophilin A1 was used. The model comprises 26 CG sites (Fig. 2.5.1, B), where the intraprotein interactions were modeled as harmonic bonds by using the elastic network model (Mim et al., 2012), whereas protein-protein and protein-lipid interactions were modeled with a Lennard-Jones potential (Ayton et al., 2010). The Lennard-Jones parameters used were 1.8 kcal/mol well depth at 1.5 nm between sites representing amphipathic helices and lipid head groups, 0.2 kcal/mol at 1.5 nm for other protein sites and the lipid head group, and 0.24 kcal/mol at 2 nm for all protein-protein interactions. These parameters were derived by combining previous free-energy simulations (Ayton et al., 2010) and by estimating the binding energy from a previously published Langmuir adsorption isotherm (Sorre et al., 2012).

2.5.2) Simulation parameters. We simulated lipid bilayer tubules coated with N-BAR domains at 5 to 40% surface coverage. A tubule, 150 nm in length and 20 nm in diameter of the outer layer, was created by patching a cylinder surface with a small equilibrated planar bilayer. This method was developed for reconstructing CG structures of membranes from the continuum-mechanics simulations (Lyman et al., 2011). Alternatively, initial membrane structure can be assembled by geometrically placing lipids with an estimated spacing based on the known area per lipid. The advantage of patching a cylindrical frame with small patches of bilayers is in shortening the equilibration time. We enclosed the tubule inside a simulation box in a way that it interacts with its periodic images in the z-directions, leaving at least 50 nm of space in the x- and y-directions (Fig. 2.5.1, B). The tubule interacted with itself across periodic boundaries in the z-direction, virtually making it infinite in length.

To equilibrate the structure, first, we ran energy minimization then several MD simulations with time steps increasing from 1 fs to 10 fs (total of ~ 600 000 time steps). We ran the simulations at constant *NVT* conditions (*V* being the volume of the box, *N* being the number of molecules in the box, and *T* the temperature of the thermostat, set at 300 K). Next, we placed a desired density of CG N-BAR domains on the surface of the tubule, either randomly or in a closely packed arrangement. We repeated the equilibration as above. Then, we carried out production run simulations for ~ 30 million time steps at a time step of 12 fs for all simulation systems (see Chapter 4). Note that in CG MD simulations, the unit of the time step corresponds to Newtonian dynamics, but not necessarily to the actual simulated time. Typically, the simulated time is much larger than the time set by the integrator.

3. Self-assembly of BAR proteins (summary of the University of Chicago Ph.D. work)

For completeness, let us briefly summarize the result of the accompanying thesis. There, we combined CG MD and continuum mechanics simulations with various microscopy imaging techniques to investigate the assembly of N-BAR proteins on the membrane and the mechanism by which they generate curvature. For a complete description of these results, please refer to the accompanying thesis or the papers references in this chapter.

Our simulation approach can be described as multiscale, as we employed a variety of different resolutions (implicitly levels of theory) where we used the information from one level to obtain crucial modeling parameters in the other. At the CG level, we used the same lipid and protein models as described in Section 2.5.1. Importantly, such highly coarse model allowed us to simulate very large scale systems. To the best of our knowledge, our work is the first to simulate protein assembly on a membrane systems of optically resolvable size. In particular, there were two membrane systems: a planar membrane, infinite via periodic boundary conditions, and a large vesicle (200–300 nm in diameter). We simulated the motion of particles using MD, as described in Section 2.5.2.

Even with CG MD simulations, we are still limited in the system size and the time scales we can simulate. To explore the dynamics at longer scales, we used continuum-mechanics simulations. In this model, the basic element is a particle containing information on lipid and protein compositions (i.e., a field variable). The total energy of each particle is a combination of the Helfrich Hamiltonian and the phenomenological Landau energy. The former contains bending and curvature-coupling terms, similar to theories outlined in the Introduction, whereas the latter depends on the variation in the lipid and protein compositions.

Finally, we used microscopy techniques to image large-scale protein organization on the membrane. In particular, we used super-resolution STORM microscopy to observe the assembly of various BAR proteins on LUVs tethered to an inert surface. On the other hand, we used atomic force microscopy to study the organization of various BAR proteins on supported lipid bilayers. Please, refer to the accompanying manuscript for experimental details.

3.1.1) Self assembly of N-BAR proteins. We ran CG MD simulations of N-BAR domains on planar bilayers and on vesicles at surface densities of 4–20%. We found that N-BARs readily aggregate on the membrane, forming long **linear chains and meshes** (Fig. 3.1.1, A). Considering that there are no strong explicit protein-protein attrac-

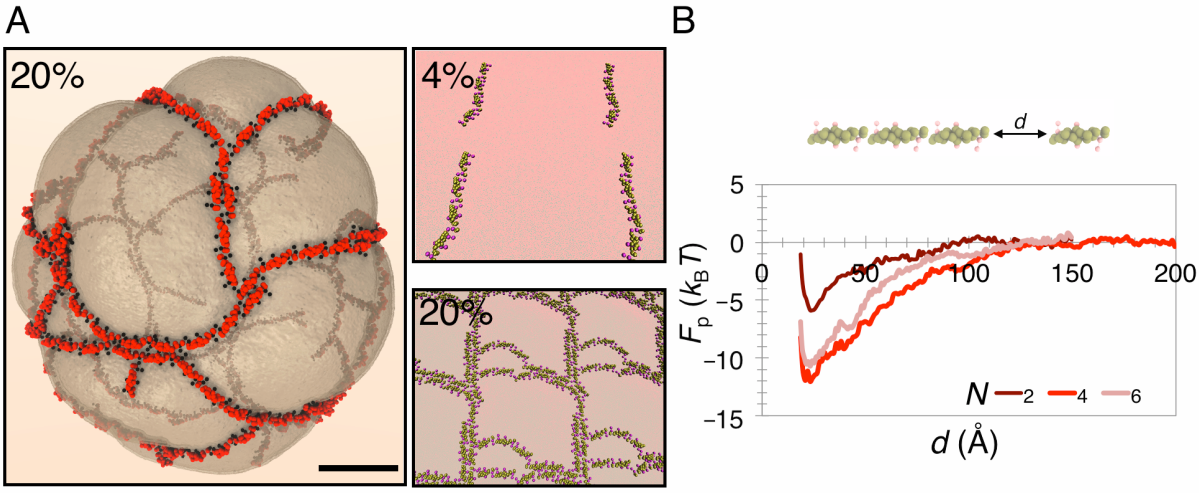

Figure 3.1.1: Linear aggregation and meshing N-BAR domains. (A) Final snapshots of CG MD simulations with N-BARs on a lipid vesicle (left) and planar bilayer (right). Percentages denote surface coverage of proteins. The two images on the right adapted from (Simunovic et al, 2013b). (B) Free energy of polymerization (F_p) as a function of the distance between the aggregate and the incoming protein (d), as depicted in the image above the plot. N denotes the number of N-BARs in the total aggregate (including the incoming N-BAR).

tions in the model, it appears that the interactions are mediated solely by membrane curvature. Indeed, using umbrella-sampling calculations, we found that there is a very high free energy gain of adding an N-BAR domain to an already formed linear aggregate, computed to be 12 k_BT. Moreover, the interaction length scale was very large, around 10 times that of the Debye length (Fig. 3.1.1, B). This work has been published in (Simunovic et al., 2013b)

Next, we assessed the existence of such aggregates by using atomic force microscopy. In particular, we imaged supported bilayers (composed of 30% DOPS and 70% DOPC), incubated with ~ 100 nM endophilin A1 or β2 centaurin. The proteins were kindly provided by Carsten Mim and Vinzenz Unger (endophilin A1) and Emma Evergren and Harvey McMahon (β2 centaurin). We observed very similar association behavior, resolving very long strands on the surface of the membrane upon adding the proteins (Fig. 3.1.2, A). Interestingly, the aggregates were spaced at a much larger distance in experiments, at 200–500 nm, compared to ~ 40 nm observed in simulations of vesicles. To better understand the interactions between lines of protein aggregates, we used CG MD simulations to calculate the free energy of interaction between two lines of N-BARs of varying length. We found that there is a very strong membrane-mediated repulsion of two linear protein polymers, acting at a striking distance of ~ 50 nm, and even higher in the case of longer polymers (Fig. 3.1.2, B). These calculations help explain the much larger separation between lines that we observe in experiments on supported bilayers.

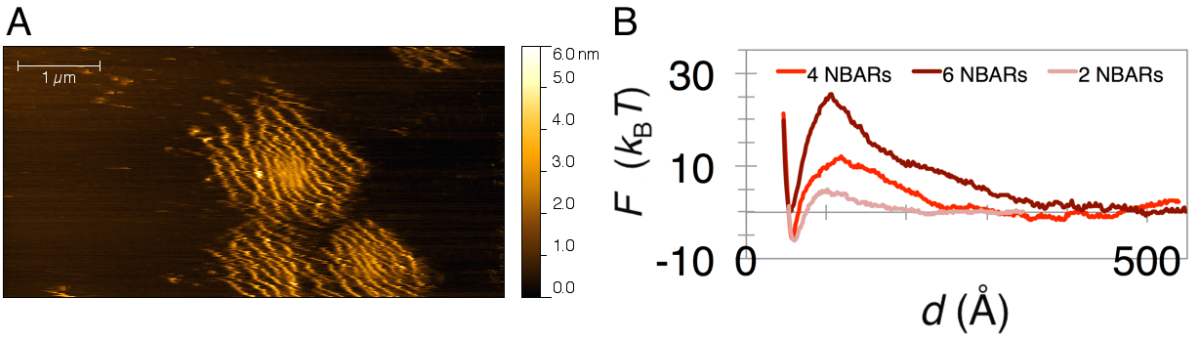

Figure 3.1.2: The repulsion of N-BAR lines. (A) Atomic force microscope image of a supported lipid bilayer (70% DOPC, 30% DOPS) incubated with 140 nM N-BAR domain of endophilin A1. Color scheme on the right represents the height from the surface. (B) Free energy (F) as a function of the distance between two lines of N-BAR aggregates (d). Clearly, with increased aggregate length, the repulsion is sensed at much larger distance. Legend shows the number of N-BARs in each line.

Linear aggregation could have important biological implications. By aggregating this way, as opposed to forming isotropic aggregates, proteins can get recruited to membrane-remodeling sites much more rapidly and from long distances. Moreover, protein meshing could serve to immobilize the membrane-remodeling sites and control the size of the forming endocytic bud (Simunovic et al., 2013a; Simunovic et al., 2013b).

3.1.2) Self-assembly and membrane mechanics. In addition to inducing significant local curvature, proteins also induce strong stress variation in their vicinity (Fig. 3.1.3, A). Therefore, we asked the opposite question: do mechanical properties of the membrane change the way proteins associate? To test this hypothesis, we conducted CG MD simulations on planar bilayers at varying membrane tensions. It turns out that membrane mechanics strongly affects the protein association. In particular, increased membrane tension 1), changes the geometry of assembly of N-BAR domains, and 2), inhibits protein-protein interactions (Fig. 3.1.3, B). We quantified these changes by carrying out free-energy calculations, which showed that increased tension permits a wider angle of dimerization (Fig. 3.1.3, C). These results indicate that any variations in local membrane tension could quantitatively, but also qualitatively, affect membrane-remodeling phenomena. For example, rapid endocytic or exocytic events could transiently alter membrane tension, faster than it can be recovered with membrane folds. Moreover, in endophilin-mediated endocytosis, actin polymerization can also locally increase tension, thus affecting the way endophilin associates on the membrane. This work has been published in (Simunovic and Voth, 2015).

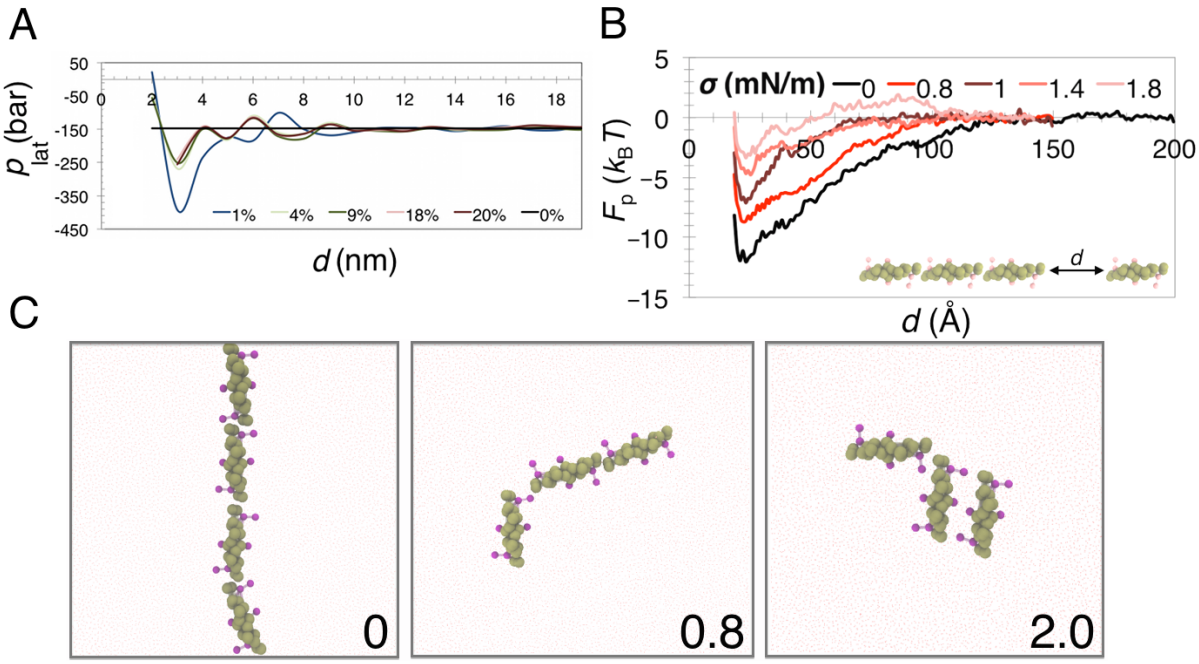

Figure 3.1.3: Membrane tension affects protein assembly. (A) Lateral pressure profile (p_{lat}), averaged around each protein (d - distance from the center of mass of the protein). (B) Free energy of polymerization (F_p) as a function of the distance (d) between the incoming protein and the linear chain, at different membrane tensions (σ). (C) Snapshots from CG MD simulations at different tensions, indicated in each panel. Top left image adapted from (Simunovic et al, 2013b), the rest adapted from (Simunovic and Voth, 2015).

3.1.3) The formation of reticular membranes. Cryo-electron imaging of small vesicles incubated with large amounts of endophilin[4] indicated that vesicles undergo complex transitions. To study the morphological consequences of vesicles at higher protein densities, we combined continuum-mechanics with CG MD simulations of 300-nm-wide vesicles, coated with > 50% N-BAR domains. Indeed, these simulations revealed an entirely different molecular mechanism on the membrane, marked by a transformation of the entire vesicle into a network of tubules (Fig. 3.1.4, A). It appears that the strong in-plane stress variations causes the bilayer structure to break. CG MD simulations showed that the proteins arrange into a nematic assembly and drive the folding of the membrane into tubules (Fig. 3.1.4, B). Our collaborators, Carsten Mim and Vinzenz Unger (Northwestern University) reconstructed a 3D tomogram from electron microscopy imaging of vesicles incubated with a high density of N-BAR domains, which confirmed the existence of a tubular network (Fig. 3.1.4, B, top left). These results point to a potential important role of N-BAR proteins in forming and stabilizing reticular membrane structures (Simunovic et al., 2013a). This mechanism—although likely not used by endocytosis—could be very important in the formation of reticular structures that have been shown to rely on BAR proteins,

[4]Cryo-electron microscopy was done by Carsten Mim in the lab of Vinzenz Unger, Northwestern University.

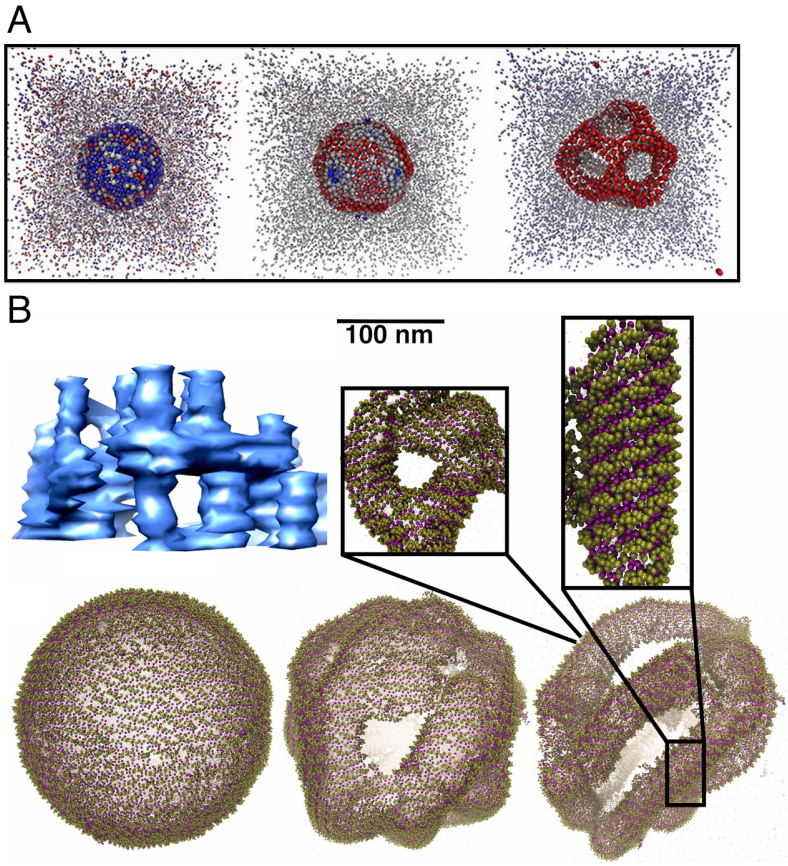

Figure 3.1.4: The formation of tubular networks. (A) Time lapse of a continuum-mechanics simulations of a vesicle immersed in a quasi-particle solvent. Particles are colored based on the density of proteins, from low (blue) to high (red). Adapted from (Simunovic et al, 2013a) (B) Top left: cryo- electron tomography of the N-BAR-coated tubular network (segmentation of the cryo-EM tomogram). Bottom: time lapse of a CG MD simulation of N-BARs on lipid vesicle at 90% density. The scale bar corresponds to CG MD simulations and the tomogram (not the magnified inset). Adapted from (Simunovic et al, 2013a).

such as T-tubules (requiring amphiphysin) and mitochondrial tubular networks (requiring endophilin B). At the same time, this study has also confirmed that N-BAR domains have the capability to induce a topological change in the membrane (i.e., membrane fission), setting an important precedent for the study of fission induced by endophilin in Chapter 5. This work has been published in (Simunovic et al., 2013a)

4. Scaffolding membrane tubules by proteins

The crescent shape of BAR proteins lets intuit that they interact with curved membranes (see Section 1.4). Indeed, many studies have revealed that BAR proteins are enriched on curved membranes and that they induce spontaneous tubulation of the membrane if recruited at sufficiently high areal density (Callan-Jones and Bassereau, 2013; Peter et al., 2004). Cryo-electron microscopy imaging has suggested that a densely packed assembly of BAR proteins (~ 100% surface coverage) on the membrane may help stabilize tubular geometry (Frost et al., 2008; Mim et al., 2012). Fluorescence microscopy, on the other hand, has shown that tubules may be stabilized at much lower densities (~ 30%) (Sorre et al., 2012), however the dynamics of formation of protein scaffolds has not been shown. Therefore, our aim was to elucidate the mechanism by which proteins form scaffolds on membrane tubules. In particular our goal is to explore how the binding of proteins couples to the morphological and mechanical properties of the membrane and shed light on the molecular aspects of this process.

4.1. *In vitro* reconstitution

4.1.1) The composition of the membrane. One of major issues when reconstituting protein-membrane system is finding a membrane composition that will 1), faithfully represent a cell membrane, and 2), consistently recruit proteins on the surface. BAR domain does not have a preference for specific lipids, however its membrane-binding surface is lined with positively charged residues. Therefore, it requires negatively-charged lipids to bind to the membrane (Mim and Unger, 2012; Qualmann et al., 2011). As mentioned in the introduction, some BAR proteins have a PH domain, and so these proteins need PIP_2 lipids as well. We chose to work with a lipid composition derived from the total brain extract, commonly known as the Folch extract. This composition, being a natural extract and not a synthetic composition, more faithfully represents a cell membrane and it is very commonly used in biology (Bhatia et al., 2009; Boucrot et al., 2012; Peter et al., 2004; Takei et al., 1999). Furthermore, our experience showed that this composition (doped with 5% PIP_2) recruited every membrane-binding protein that we tested (endophilin, centaurin, sorting nexin 9, M1 protein of the influenza virus). I remind the reader that we could not produce these GUVs using electroformation on ITO plates (see Section 2.1.2), however growing them on Pt-wires overnight in the fridge and in ~ 100 mM NaCl buffer yielded a good amount of vesicles.

The actual composition of the brain extract is variable and it contains over eighty different types of lipids. A study using high accuracy mass spectrometry has

shown that the porcine brain extract contains mostly PC lipids (approximately 40 types), then various amounts of PE, PS, SM, and lysophosphatidylcholine (Yu et al., 2006). They did not report the presence of PI or cholesterol, possibly because the amount was below the chosen detection limit. Therefore, we doped the lipid extract with 5% PIP_2, as often done in membrane studies using Folch liposomes (Boucrot et al., 2012).

4.1.2. The mechanics of the membrane. Considering the complicated nature of the composition, we first examined the viability of these GUVs. First, we tested the mechanical properties of the membrane by carrying out tether-pulling experiments in the experimental buffer and in the absence of any curvature-generating molecules (for details of the setup see Section 2.3). Figure 4.1.1. shows an experiment on a GUV where we initially stepwise increased membrane tension, then repeated the measurements by decreasing membrane tension, all while injecting a (non-curvature-active) buffer solution. As expected, with increased membrane tension, the tether-retraction force increases while the radius of the tubule decreased (Fig. 4.1.1). Moreover, we confirmed that the values of force and radius are not appreciably affected by the direction of change of membrane tension (Fig. 4.1.1, black versus grey dots). This measurement implies that the bilayer is fluid, as any change in tension prompts the lipids to flow between the vesicle and the tubule, otherwise the force and the radius would remain unaltered.

To calculate the bending rigidity, we start with the Helfrich Hamiltonian:

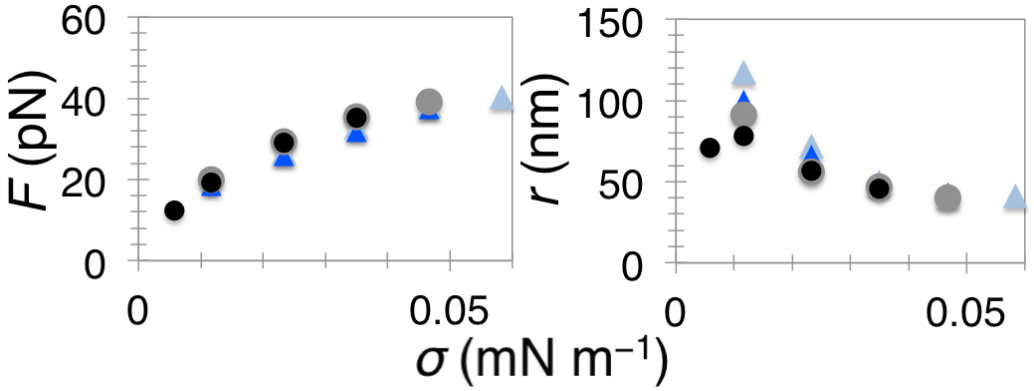

Figure 4.1.1: The fluidity of the membrane. Shown are tether-retraction force, F (left) and tubule radius, r (right) as a function of membrane tension for a single GUV composed of the total brain extract and 5% PIP_2. The experiment was performed by, first, stepwise increasing membrane tension, σ, (black dots) then stepwise decreasing it (grey dots). Then, we injected the experimental buffer with 0.15 μM inactive protein (i.e. did not bind to the membrane), first stepwise increasing σ (blue triangles) then again decreasing it (light blue triangles). There is almost complete superposition. Note, in the first measurement (black dot that deviates), the tubule was not in focus.

$$H_t = \frac{\kappa}{2}\left(\frac{1}{r} - \frac{1}{R_0}\right)^2 A + \sigma A - fL \qquad \text{(Eq. 4.1)}$$

where H_t is the total free energy of the tubule, κ is the membrane bending rigidity, r and R_0 are, respectively, the mean and the spontaneous radii of curvature, i.e. the reciprocal mean and spontaneous curvature. A and L are, respectively, the area and the length of the tubule, and f is the pulling force on the membrane (Derenyi et al., 2002; Kwok and Evans, 1981). At equilibrium, r becomes the tether radius (denoted r or R) and the force becomes the aforementioned tether retraction force (F). To compute R and F, we minimize H_t with respect to L and R (Derenyi et al., 2002), i.e. $\partial H_t / \partial R = 0$ and $\partial H_t / \partial L = 0$, yielding:

$$F = 2\pi\sqrt{2\sigma\kappa + \frac{\kappa^2}{R_0^2}} - 2\pi\kappa\frac{1}{R_0} \approx 2\pi\sqrt{2\sigma\kappa} - 2\pi\kappa\frac{1}{R_0} \qquad \text{(Eq. 4.2)}$$

$$\frac{1}{R^2} = \frac{2\sigma}{\kappa} + C_0^2 . \qquad \text{(Eq. 4.3)}$$

The equations reveal that the curvature and the retraction force of the tubule scale as square root of membrane tension. Fitting the model to our data gives κ. Considering that we measured the radius from the fluorescence intensity and not from the force (see Section 2.3.6), we have two independent measurements of κ (Fig. 4.1.2). Fitting the force equation (Eq. 4.2) to our data yields κ = 46.1±4.5 k_BT (mean±SD) (N = 45, N — number of experiments), whereas fitting to the tubule radius measurements yields κ = 57.4±3.4 kBT (N = 36). In both cases, k_B is the Boltzmann constant and T thermodynamic temperature (300 K). Although, these values are higher than typical values of synthetic phosphatidyl lipid vesicles (~ 20 k_BT), they are comparable to the rigidity of red blood cell (43 k_BT) (Evans, 1983). Moreover, it is not surprising to find

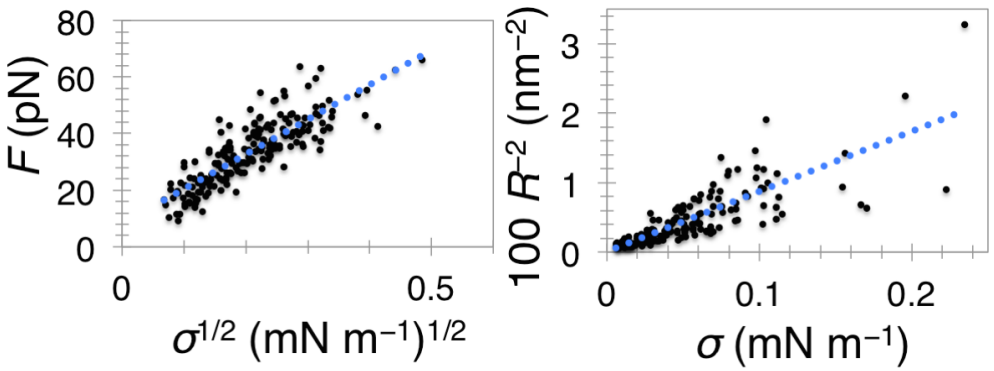

Figure 4.1.2: Mechanics of the membrane. Shown are fits of Eq. 4.2 (left) and Eq. 4.3 (right) to our data. Number of independent vesicles: 45 (left), 36 (right). Tubule radius was measured from the lipid fluorescence.

a higher κ value, considering that the mixture contains SM lipids and lipids with chains of varying lengths and saturation (Rawicz et al., 2000; Yu et al., 2006).

According to Eqs. 4.2 and 4.3, in the absence of spontaneous curvature, the offset of the force and the radius should be zero. Fitting yields offsets of $(6.8\pm1.7)\times10^{-3}$ nm^{-1} (Eq. 4.2) and $(3.9\pm4.1)\times10^{-3}$ nm^{-1} (Eq. 4.3), corresponding to spontaneous radii of curvature 150 nm and 250 nm, respectively. A positive offset in the force indicates a negative radius of spontaneous curvature. We note that we systematically observe a positive offset in the force, regardless of lipid composition (except for the case of an uncharged membrane, see Appendix I). We hypothesize two possible sources for the offset in force of the charged membranes. First, if there is a difference in salt concentration in the inner and the outer buffer, the repulsions of charged head groups are less screened in the leaflet exposed to a buffer of higher ionic strength. As a result, the membrane would tend to curve toward the leaflet with less screening to alleviate charge repulsions, hence generate spontaneous curvature. Indeed, in our case, the NaCl concentration inside the GUVs is generally ~ 30 mM lower than the experimental buffer, which is a result of optimization of conditions.

Other possible contributions to the offset are the insertion of Na^+ between the lipid head groups (see Appendix I), an asymmetry in composition between the two leaflets, and adhesion of the membrane to the glass surface. However, considering the size of a BAR protein like endophilin or centaurin (~ 12 nm), we can neglect the membrane spontaneous curvature of the membrane relatively to that of the protein.

4.1.3) Phase behavior of the membrane. Considering that the total brain extract contains many lipids of varying chains, it is possible that our GUVs could undergo phase separation (see Section 1.1.3.). We tested the phase behavior of our model membrane by using fluorescent lipids known to partition into different phases. In particular, we doped the membrane with GM1* (at 1% molar fraction), a lipid equally distributed between l_o and l_d phases, and DHPE* (at 0.5% molar fraction), a lipid that strongly favors the l_d phase. Of note, the same lipid dyes were previously used in studying the curvature sorting of lipids (Sorre et al., 2009).

Using confocal microscopy, we observed a homogenous distribution of the two fluorescent lipids in all imaged GUVs (N = 16) (Fig. 4.1.3, A). It appears that the membrane composed of the total lipid brain extract and 5% PIP_2 does not phase separate. Next, we tested if we can trigger the separation with curvature. We measured the fluorescent intensity of the two dyes in the tubule, relative to the vesicle, at different membrane tensions (implicitly curvatures). The relative ratios of the two dyes is termed the sorting ratio, s:

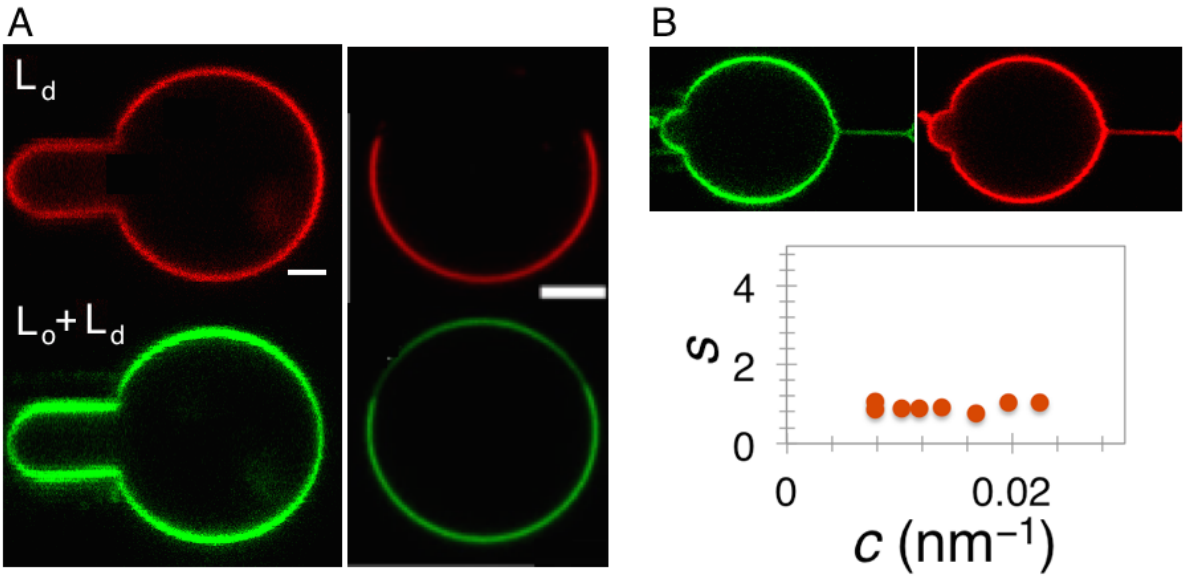

Figure 4.1.3: Phase behavior of the membrane. (A) Homogeneous distribution of the lipid dyes in total lipid brain extract vesicles (left) compared to the phase-separated ternary vesicle (right). The images of the phase-separated vesicles adapted from (Sorre et al, 2009). (B) The absence of lipid sorting of total lipid brain extract vesicles. Tubule radius calculated from the force and sorting is adjusted by the polarization factor. Shown is representative of four different experiments.

$$s = \frac{1}{P_f} \frac{I_t^{DHPE} / I_t^{GM1}}{I_{ves}^{DHPE} / I_{ves}^{GM1}} \qquad \text{(Eq. 4.4)}$$

where I_t and I_{ves} are the fluorescence intensities of individual dyes (as indicated in the superscript) in the tubule and vesicle, respectively. P_f is the polarization factor, which takes into account the polarization of the excitation light (Sorre et al., 2009). As shown in Figure 4.1.3, B, neither labeled lipid gets enriched in the tubule with increased curvature, which indicates that the membrane is not close to a demixing point (Sorre et al., 2009). We measured P_f as the relative ratio of intensity of one dye over the other (in the absence of sorting). P_f depends on lipid composition, and for the total brain extract it measures 2.1±0.3 (mean±SD, N = 4). This value is consistent with previous measurements for SM-containing ternary composition GUVs (Sorre et al., 2009).

Based on the observed mechanical and phase properties, **we conclude that our GUVs are viable model systems of a fluid membrane.**

4.1.4) Proteins. We used various curvature-generating proteins in this study, whose biological relevance is described in the Introduction (Section 1.4). Namely, we studied:

1) endophilin A2 (unlabeled mouse full length and labeled rat N-BAR domain)

2) endophilin A2 with truncated N-terminal helices (unlabeled mouse full length)

3) endophilin A2 E37K, D41K (labeled rat N-BAR domain)

4) β2 centaurin (labeled human BAR + PH domains)

5) epsin 1 (unlabeled full length)

Proteins 1, 3, 4, and 5 were synthesized and kindly provided by Emma Evergren and the lab of Harvey McMahon (Cambridge University), protein 2 was synthesized and kindly provided by Henri-François Renard and the lab of Ludger Johannes (Institut Curie). Alexa488 maleimide, which binds to the cysteines in the protein, was

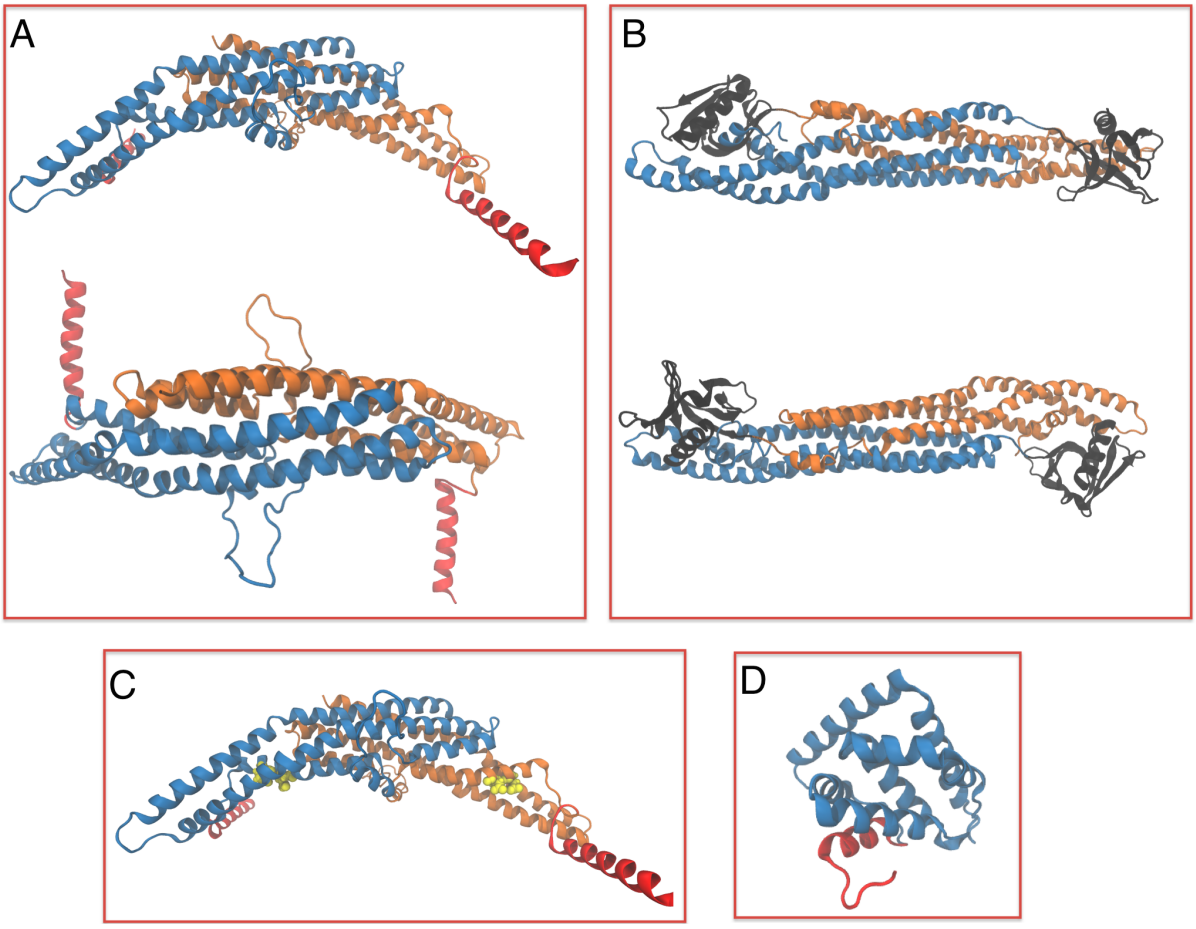

Figure 4.1.4: X-ray and homology modeling structures of proteins used in the study. (A) Homology modeling of N-BAR domain of endophilin A2. (B) Homology modeling of BAR and PH domains of β2 centaurin. For A and B: proteins viewed from the side (top) and above the membrane surface (bottom). (C) Endophilin A2 E37K, D41K (mutated residues colored yellow). (D) Crystal structure of the ENTH domain of epsin 1 (PDB ID: 1EDU). Blue and orange color-coding based on monomer; red: N-terminal helices; black: PH domain.

used as the fluorescent label. Please, refer to Section 2.3.6 for measurements of labeling efficiencies.

To gain a better understanding of the molecular structure of these proteins, we used Swiss-Model (swissmodel.expasy.org) to construct 3D models of our proteins based on X-ray structures of their closest homologues. To model the N-BAR domain of rat endophilin A2, we used rat endophilin A1 as the homologue (PDB ID: 2C0B), whereas for the modeling of human β2 centaurin (BAR + PH domains), we used the structure of β1 centaurin as the homologue (PBD ID: 4NSW). To remind the reader, endophilins belongs to N-BAR proteins, while centaurins belong to the classical BAR domain family. A noteworthy difference between the two proteins, besides lacking the N-terminal amphipathic helices, is that BAR domain of β2 centaurin displays a much shallower curvature than the BAR domain of endophilin A2 (Fig. 4.1.4).

4.2. Tubulation of the membrane

Let us start with simply observing the morphology of the membrane after binding of the protein. We incubated BAR proteins with GUVs at bulk protein concentrations of 0.5–3 μM. Note that all protein concentrations are expressed per monomer. By observing the labeled proteins with confocal microscopy, our first observation is that both endophilin and centaurin readily bind to brain extract vesicles (Fig. 4.2.1). After ~ 15 min of incubation, most vesicles displayed a dramatic morphological change, marked by large-scale tubulations of the vesicle surface (Fig. 4.2.1, A). Similar membrane remodeling has already been reported with other BAR proteins and epsin (Ambroso et al., 2014; Peter et al., 2004; Saarikangas et al., 2009; Sorre et al., 2012; Takei et al., 1999; Yoon et al., 2010).

We observed spontaneous tubulation of both the N-BAR domain and the full-length endophilin A2 (Fig. 4.2.1, A and C). Next, we observed the tubulation in time by directly injecting endophilin on 1), a supported lipid bilayer[5], and 2), in the vicinity of the aspired GUV. Seconds after injection, the tubules emerged homogeneously on the vesicle surface (Fig. 4.2.1, A and C). We then incubated β2 centaurin with giant liposomes. Interestingly, β2 centaurin also induced large-scale tubulation, just as observed with endophilin (Fig. 4.2.1, B). Of note, a prior study has shown that overexpression of this protein in cells leads to the massive tubulation of the plasma membrane (Peter et al., 2004). **Apparently, the insertion into the lipid bilayer by amphipathic helices is not a required part of the mechanism for large-scale membrane remodeling.**

5 Many thanks to Marta Bally who taught me how to make and image supported lipid bilayers and for doing most of the bilayer experiments in this thesis with me.

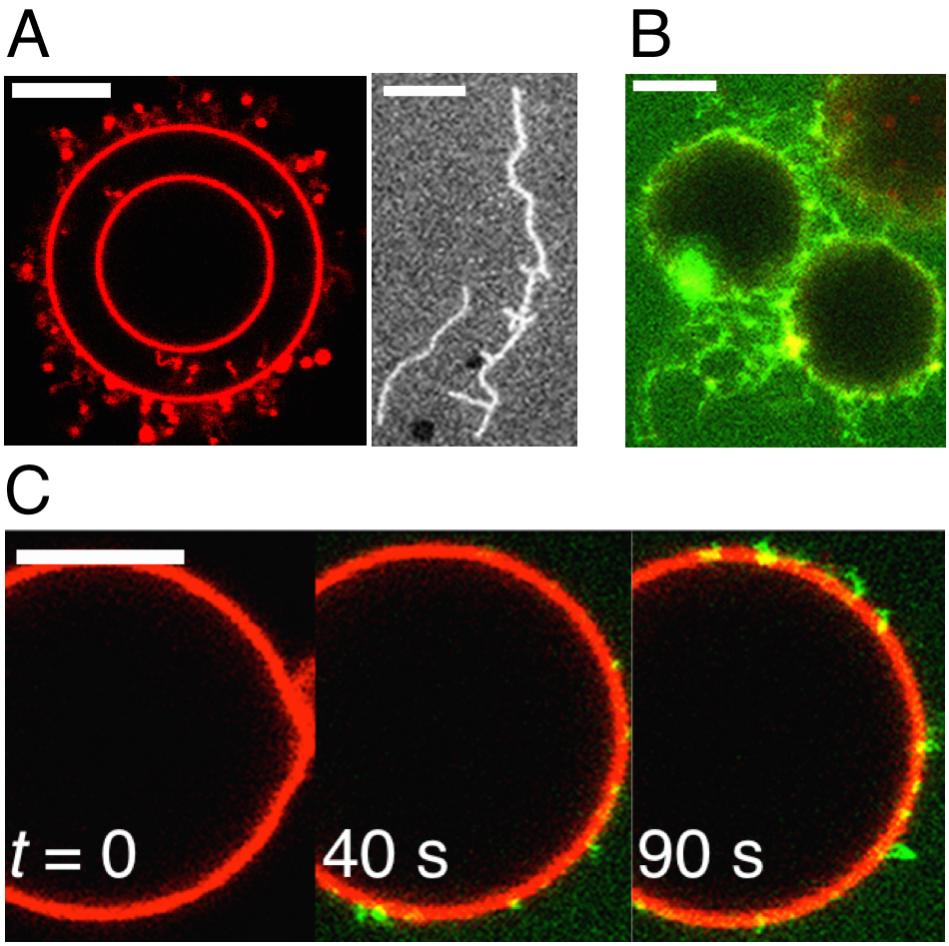

Figure 4.2.1: BAR proteins induce tubulation of the membrane. (A) Spontaneous tubulation induced by full-length endophilin A2 from the GUV (left) and the supported bilayer (right) at bulk protein concentration of 2 μM. The experiments with supported bilayers were done with Marta Bally. (B) Spontaneous tubulation induced by β2 centaurin (2 μM). (C) Spontaneous tubulation of an aspired GUV injected with N-BAR domain of endophilin A2 at 2 μM in the pipette. GUVs composed of the total lipid brain extract + 5% PIP_2, supported bilayer composed of 30% DOPS, 70% DOPC. In A, fluorescence comes from labeled lipids; in B and C, shown is the overlay of lipid (red) and protein fluorescence (green). Scale bar: 5 μm.

4.3. Dynamics of scaffolding

Next, we investigated the way proteins interact with curved membranes by injecting them in the vicinity of tubules pulled from GUVs at concentrations in the pipette of 1–5 μM (see Section 2.3 for the details of the experiment). The actual concentration of the protein in the vicinity of the GUV is lower than the pipette concentration due to dilution. We traced the fluorescence intensity of Alexa488 bound to a protein from the pipette exit to the base of the pulled tubule (Fig. 4.3.1) and found an average dilution factor of 2.0 (N = 3). Considering that, in most cases, we quantify the bound

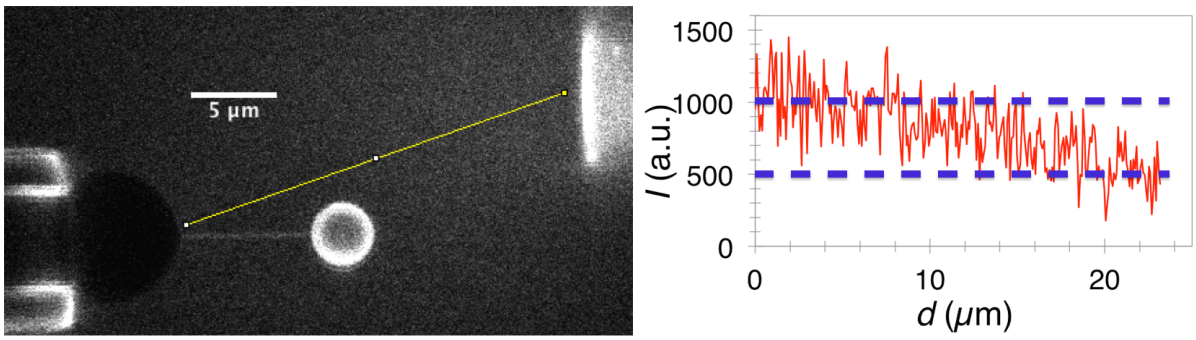

Figure 4.3.1: Dilution of injected proteins. Measuring the reduction in fluorescence intensity of Alexa488 (bound to β2 centaurin) from the injection pipette exit to the base of the tether (yellow line).

density of the protein on the membrane (as outlined in Section 2.3.6), knowing the precise effective bulk protein concentration is not important.

4.3.1) Decrease of force. We found that after the injection of the proteins, there is a marked decrease in the tether-retraction force. Furthermore, in many cases, endophilin A2 and β2 centaurin caused buckling of the tubule, whereby the tubule no longer exerted force on the trapped micron-sized particle (Fig. 4.3.2). This observation indicates that proteins take over for the optical trap in stabilizing the curved membrane. The formation of protein scaffolds was previously demonstrated for some N-BAR and F-BAR proteins by using the same setup as we use here, and also by using cryo-electron microscopy (Frost et al., 2008; Mim et al., 2012; Ramesh et al., 2013; Sorre et al., 2012).

Epsin 1 did not induce the buckling of tubules, however its binding markedly lowered the tether-retraction force (Fig. 4.3.2). In general, the reduction in the remodeling force indicates that it becomes less difficult to bend the bilayer toward the protein-binding leaflet. Therefore, it appears that all three proteins: endophilin A2, β2 centaurin, and epsin 1 induce **positive spontaneous curvature** and thus contribute to the stability of the cylindrical membrane geometry. This result is consistent with the observed outward spontaneous tubulation of membrane tubules (Section 4.2 and Fig. 4.3.2).

4.3.2) Endophilin scaffold initiates at the neck of a membrane tubule. Before examining the mechanical effect on the membrane by protein scaffolds, we took a closer look at the way endophilin proteins bind to a membrane tubule. Based on confocal imaging, endophilin initially binds to the neck of the pulled tether, either at the interface with the GUV or at the interface with the optically trapped bead (Fig. 4.3.3, A). To specify, endophilin first bound to the GUV interface in the great majority of cases (53 out of 59 experiments). Out of those 53 cases, it simultaneously also bound to the interface at the bead in 27 experiments. In the four out of six negative cases,

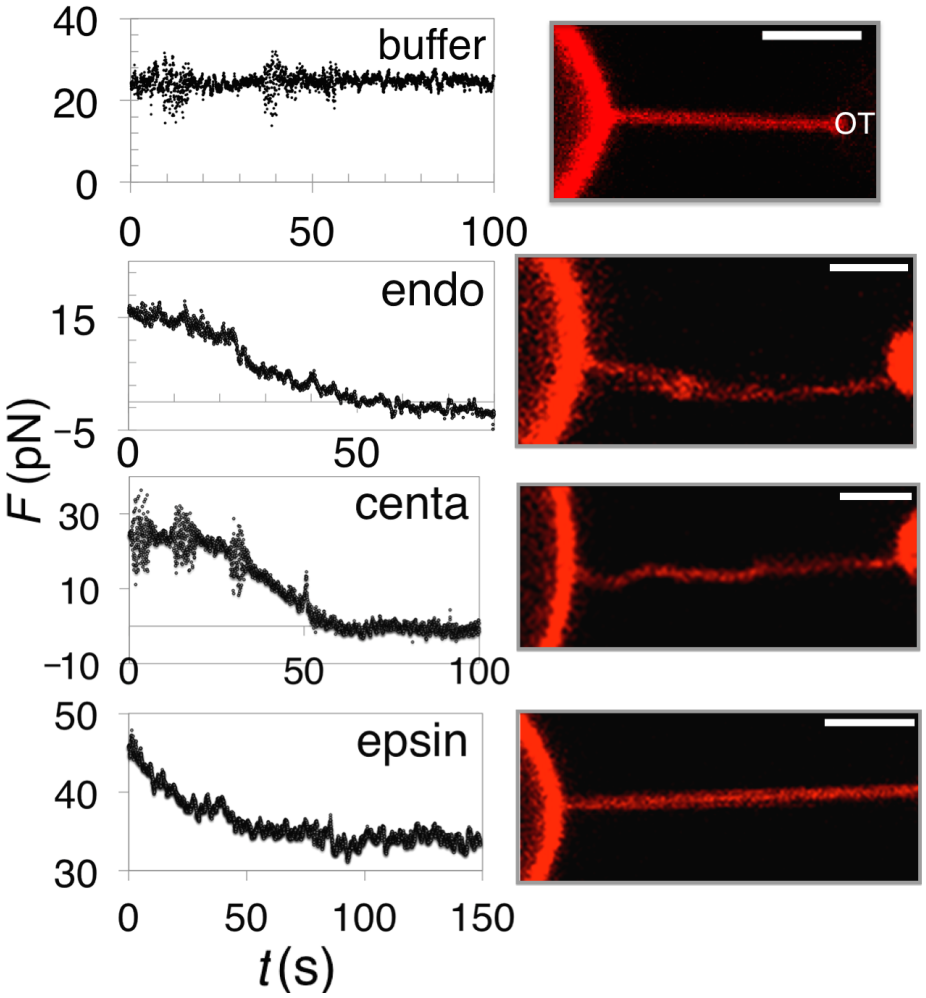

Figure 4.3.2: Curvature-generating proteins reduce the tether-retraction force. Measuring force (F) in time (t) after the injection of proteins at pipette concentrations of 1-5 μM on extruded membrane tubules (left) and final confocal microscopy snapshots (right). Tested proteins: endophilin A2 (endo), β2 centaurin (centa), and epsin. Buffer represents the control where the buffer was injected. Fluorescence comes from labeled lipids. Scale bar: 3 μm. OT = optical trap.

endophilin appeared to bind homogeneously along the tubule. Granted, in those cases the initial binding could have been recorded insufficiently fast. In the two remaining negative cases, the protein was observed to first bind in a region other than the interface.

Based on these observations, it appears that endophilin is selective toward highly negative Gaussian (or saddle-like) curvature, which is in agreement with the CG MD simulations described in Section 3.1.1 (Simunovic et al., 2013b). Endophilin immediately forms a scaffold, which elongates continuously along the tubule, until it covers it partially or fully (Fig. 4.3.3, A, B). The first sign that a scaffold has formed is a clear reduction of the lipid fluorescence intensity underneath the protein (Fig. 4.3.3, A, lipid channel). This observation implies a constriction of the tubule radius, which

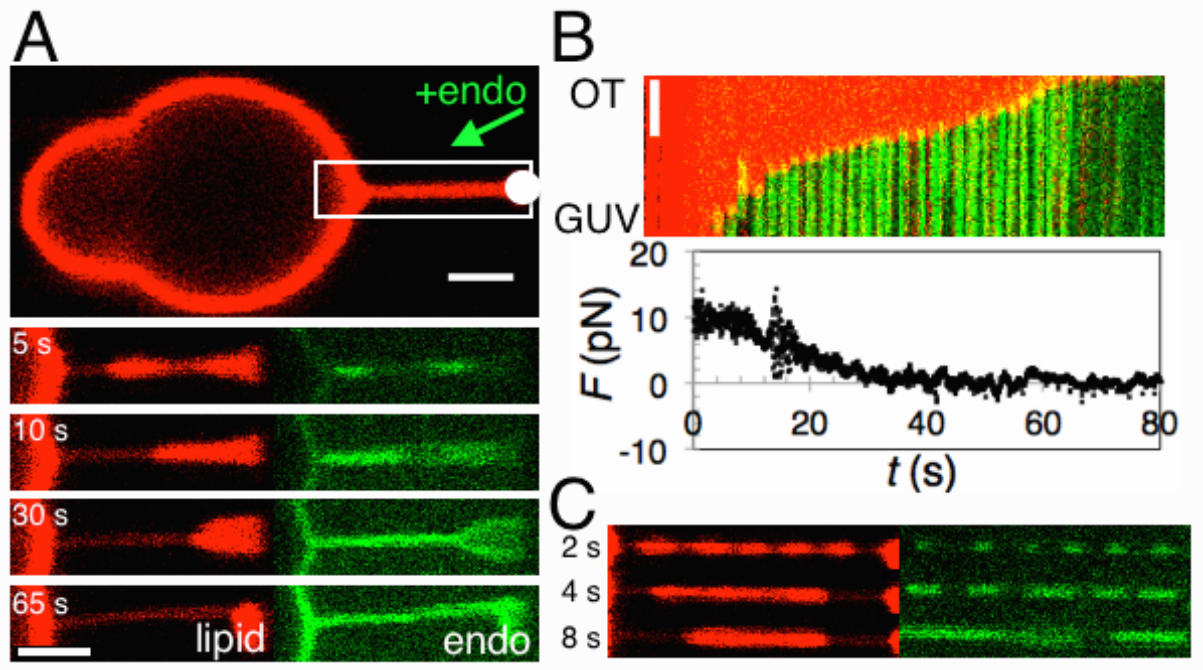

Figure 4.3.3: Scaffolding by endophilin A2. (A) Protein initially binds to the necks of the tube (at the GUV and at the bead). It forms a scaffold, constricting the tubule, then continuously elongates until completely covering the tubule. White circle = OT. (B) A kymogram, showing the scaffold growth from the GUV to the bead. Lipid and protein channels are overlaid. The plot shows tether-retraction force (F) as a function of time (t). The x-axis of the kymogram coincides with the x-axis of the plot. C) Time lapse of a striation pattern induced by endophilin. For all: scale bar is 2 μm, GUV = giant unilamellar vesicle, OT = optical trap, endo = endophilin A2 WT. In all, $t = 0$ marks the time when protein was detected on the tubule.

has previously been observed with BAR domain proteins, although never in a dynamic way (Renard et al., 2015; Sorre et al., 2012).

By comparing the force plot with the confocal images, we see that the binding and constriction are concurrent with the drop in the tether-retraction force (Fig. 4.3.3, B). A fully covered tubule imposes no force on the optical trap and undergoes buckling, as shown in Fig. 4.3.2. Similarly to experiments with the tubulation of the membrane, we observed no difference in the tubule-binding behavior between the full-length and the N-BAR domain of endophilin A2.

Interestingly, at higher injected concentrations (> 3 μM), endophilin initially formed a striated pattern on the tubule, marked by a brief (a few seconds) **beading instability** (Fig. 4.3.3, C, top row, observed in six experiments). The striation rapidly coarsened leading to an elongation of the scaffold from both necks of the tubule. This behavior is reminiscent of the way dynamin binds to membrane tubules, although with some differences (Morlot et al., 2012; Roux et al., 2010). Both endophilin and dynamin form a temporary striated pattern on the tubule, however endophilin

seems to form a somewhat more evenly spaced clusters than dynamin, based on our observations compared to figures in (Morlot et al., 2012; Roux et al., 2010). In both cases, however, the shape of the tubule underneath the striated protein resembles a beading instability (Fig. 4.3.3, C). Moreover, dynamin induces an appreciable effect on the force only when it fully covers the tubule, whereas in our case, the force is reduced as soon as endophilin initiates the scaffold.

Two theoretical works may help in understanding our observations. In the first, Gov and coworkers have developed a theory to explain the binding of dynamin. They used the standard Helfrich Hamiltonian, complemented with various terms describing the binding and mixing of the protein, as well as curvature coupling of dynamin oligomers (Shlomovitz et al., 2011). Interestingly, they showed that higher protein concentrations induce a uniformly unstable tubule, i.e. a bifurcation in the tubule radius at a given tension (Fig. 4.3.4, A blue and pink lines). In other words, the tubule can adopt two radii at the same tension: a wider tubule poorly bound by the protein and a narrow tubule, much closer to C_0, enriched with the protein. Apparently, this transient state leads to a dynamic instability that promotes a local condensation of the protein, which in our case is the step clearly evident in Fig. 4.3.3., A. The calculations also predict an energy barrier between two polymerized protein domains, which could explain the metastable striated pattern of binding, as seen in Fig. 4.3.3., C. The theory behind our case would be more complicated, as the non-polymerized BAR proteins also couple with curvature (see Chapter 6 and e.g. (Sorre et al., 2012)) and the fact that protein scaffolds inhibit the lipid flow (see Chapter 5), however it seems that our observations are aligned with their predictions.

Another theoretical study, conducted by Lorman, Parmeggiani and coworkers showed that if including the often neglected energy contribution due to a pressure difference across the membrane to Eq. 4.1, the shape of the tubule shows various structural instabilities (Fig. 4.3.4, B), including buckling and beading (Monnier et al., 2010). Furthermore, they showed that the instabilities of the bare membrane control protein adhesion to the tubule. Their model predicts that the most stable configuration of the tubule is that where the proteins are evenly spaced along the tubule. Although we do not observe resonance modes of bare tubules, adding the protein could either change the resonance wavelength, making them visible, or induce the required pressure difference to generate theoretically predicted instabilities. For example, compare the wave-like instability (Fig. 4.3.4, B, panel b) with Fig. 4.4.1, A, final snapshot. Also, compare their predicted beading instability (Fig. 4.3.4, B, panel d) with our observed instability in Fig. 4.3.3, C. It is not clear, however, if the wavelengths of instabilities from their calculations are sufficiently long to induce micron-sized separation between protein domains.

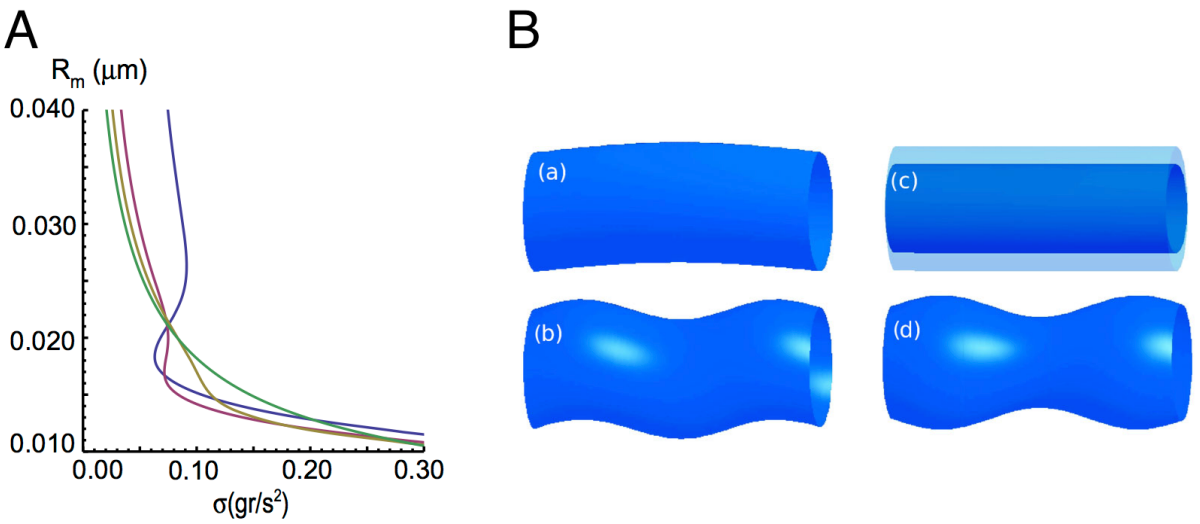

Figure 4.3.4: Tubular instabilities previously predicted by theory. (A) Uniform tubule radius, R_m, *versus* membrane tension, σ, for different bulk dynamin concentrations: high (blue), intermediate (purple), low (yellow), no protein (green). At high concentrations, there is a bifurcation of the tubule radius. Adapted from (Shlomovitz et al., 2011). (B) Low-energy modes of the tubule: buckling (a), wavy (b), stretched (c), beading (d). Taken from (Monnier et al., 2010).

Both of these theoretical works, the previous experimental works on dynamin, and the behavior of endophilin shown here, demonstrate that membrane fluctuations may appreciably affect the spatial localization of proteins on curved membranes, despite strong protein-membrane interactions (Shlomovitz et al., 2011).

4.4. The role of subdomains in scaffolding and mechanically affecting the membrane

BAR proteins are generally believed to induce curvature 1), by adhesive interactions via its positively charged BAR domain and 2), by shallow insertion of amphipathic helices (Bassereau et al., 2014). The relative contribution of these effects is still debated, especially when it comes to the mechanism of sensing curvature and scaffolding. Therefore, we aimed to examine how amphipathic helices affect the dynamics of scaffolding membrane tubules. β2 centaurin provides good testing ground as it is one of few BAR proteins that naturally comes without amphipathic helices (see Fig. 4.1.4 for the image of the protein's structure).

Contrary to endophilin, centaurin bound homogeneously along the length of the tubule, with no detectable preference to the neck (Fig. 4.4.1). Nevertheless, as shown before, there was reduction in the tether-retraction force during binding (Fig 4.3.2), often leading to a buckling instability (Fig. 4.4.1, A, top). Furthermore, binding of the protein changed the radius of the tubule, even though the aspiration pres-

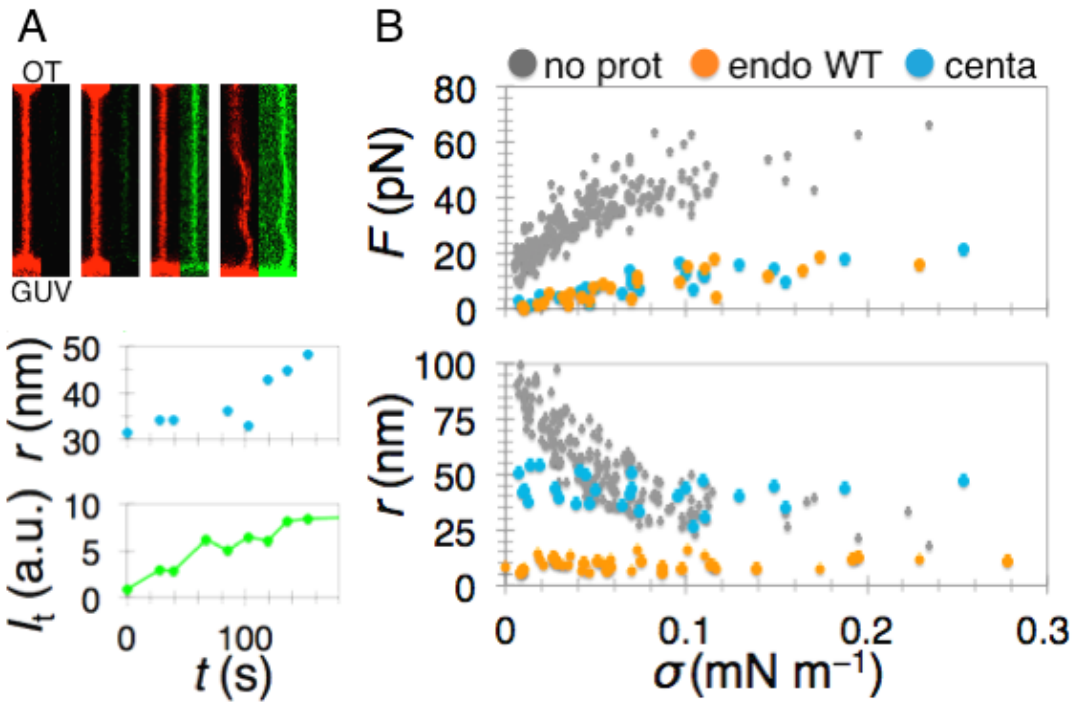

Figure 4.4.1: Scaffolding by endophilin *versus* centaurin. (A) β2 centaurin binds homogeneously along the tubule (red: lipids; green: protein). Plots show dilation of narrow tubules induced by a scaffold of β2 centaurin (top: fluorescence intensity, I_t, of β2 centaurin on the tubule; bottom: tubule radius, r, deduced from lipid fluorescence). (B) The mechanics of the reference membrane (composition: total brain extract doped with 5% PIP_2, $N = 45$) and after the formation of scaffold by endophilin A2 WT (endo WT, $N = 7$) and β2 centaurin (centa, $N = 5$). F measured from the optical trap, r from the lipid fluorescence.

sure—implicitly tension—remained the same. Figure 4.4.1 (bottom) shows an example where binding of β2 centaurin dilated a 30-nm tubule by ~ 20 nm. Clearly, β2 centaurin forms a supramolecular network that actively reshapes the membrane, just like N-BAR proteins.

Next, we measured the mechanical properties and compared them to the reference membrane. In the presence of the protein, the mechanics of the membrane is drastically changed, due to the imposed scaffold by both endophilin and centaurin. In particular, the tether-retraction force is significantly lowered for all tested membrane tensions (Fig. 4.4.1, B, top). At the same time, the tubule radius is fixed, regardless of membrane tension (Fig. 4.4.1, B, bottom). Interestingly, the tubule scaffolded by centaurin is approximately four times wider than the one scaffolded by endophilin (precisely, 42.5 nm and 10 nm, respectively, see Table 4.4.1).

At this point, let us revisit the mechanical properties of the membrane. As shown in Eq. 4.2, the force has a square-root dependence on membrane tension. How about in the presence of a protein scaffold? Based on a model that has previ-

Table 4.4.1: Radius (r) of scaffolded tubules deduced by fluorescence. Mean±SD (N measurements).

	endo WT	endo ΔH0	endo E37K, D41K	centa	epsin
r (nm)	9.8±2.8 (10)	21.4±11.6 (7)	19.9±3.0 (7)	42.5±7.0 (5)	*

*epsin did not display constant radius

ously been developed in our group (Sorre et al., 2012), it turns out that in case of a fixed tubule radius, the force linearly depends on the membrane tension:

$$F = 2\pi R_{sc}\left(\sigma - \sigma_0\right) \qquad \text{(Eq. 4.4)}$$

where R_{sc} is the scaffold radius and σ_0 is the tension where the tether-retraction force vanishes. First, we check the logarithmic dependence of force on tension. Indeed, the bare membrane shows a nearly square-root dependence on membrane tension, with the log-log slope of 0.4 (Fig. 4.4.2). As expected, the log-log slope for both endophilin A2 and β2 centaurin, in the case where their density is high, is nearly one (~ 0.9). Fitting our data for endophilin to Eq. 4.4 yields R_{sc} = 8.0±0.7 nm, which is in very good agreement with the scaffold radius measured from lipid label fluorescence. The fitted value for centaurin, 13.1±1.8 nm, is surprisingly small compared to the measured radius of the scaffold. We hypothesize that, while the scaling behaves according to previous predictions, the model developed for amphiphysin is unable to fully capture the behavior of centaurin. A more rigorous derivation, which will include explicit protein-protein interactions and the internal structural parameters of the protein and its scaffold, is currently underway by our collaborators, Andrew Callan-Jones (Paris 7) and Jacques Prost (Institut Curie). We also note that insufficient sampling could contribute to the error as well. **The most important conclusion is that**

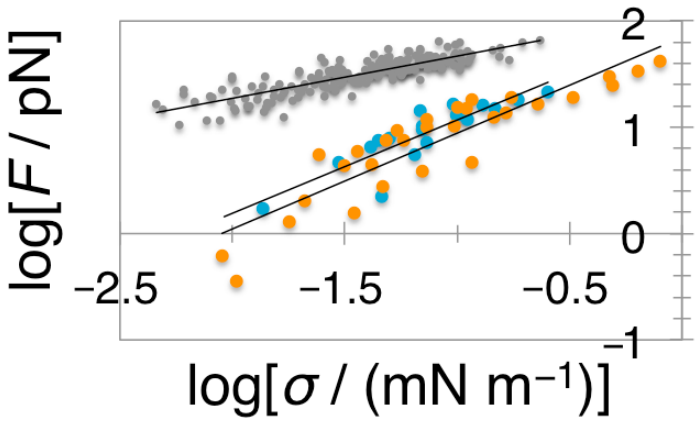

Figure 4.4.2: Scaling of force on membrane tension. Linear fit yields: for bare membrane (grey): 0.41±0.02 and 2.1±0.03 (slope and y-offset); for endophilin A2 scaffold (orange): 0.90±0.08 and 1.85±0.10; and for β2 centaurin scaffold (blue): 0.88±0.12.

BAR proteins without amphipathic helices can, just as N-BAR proteins, form rigid scaffolds that strongly determine the shape of the membrane.

The results shown in Fig. 4.4.1 represent data in which the tubule was constricted along the entire length and displayed a monotonous dependence of the force with membrane tension. I note that these results correspond to the high-density regime reported for amphiphysin (Sorre et al., 2012). To specify, there were a total of 72 experiments for endophilin and six cases of centaurin in which we observed the scaffold formation, evidenced by the clear change in tubule radius. We systematically measured F versus σ in 26 cases for endophilin and six cases for centaurin. Out of those cases, seven cases of endophilin and five cases of centaurin displayed the dependence as in Fig. 4.4.1.

We observed two other scaffolding regimes, primarily for endophilin. In one, there was an incomplete formation of the scaffold, characterized by a non-vanishing constant force, observed in 13 cases of endophilin. In the other case type, the entire tubule was covered by the scaffold and the tubule persistently buckled preventing the force to rise from zero, regardless of increased tension. This regime was observed in six cases of endophilin and one case of centaurin. Both case types are likely a consequence of kinetic trapping due to rapid squeezing of the water and the free membrane upon initial tubule constriction. Interestingly, such kinetic trapping has been predicted in passing in the theoretical work explaining dynamin binding (Shlomovitz et al., 2011). In fact, we often observed that the membrane tubule following the wave of the growing scaffold get significantly deformed (see e.g. Fig. 4.3.3., A) which can trap the protein growth to fully cover the tubule. Furthermore, as will be explained in Chapter 5, protein scaffolds inhibit lipid dynamics, which can significantly slow down the tension equilibrium. At present, we do not explore these regimes as they do not directly pertain to our aims or the conclusions that we draw in this chapter.

Despite observing centaurin to form scaffolds just as endophilin, we still cannot rule out amphipathic helices in endophilin to be the key contributor to scaffolding. To address this issue, the labs of Harvey McMahon and Ludger Johannes constructed two endophilin mutants. In the first, they truncated the N-terminal amphipathic helix of the full-length endophilin A2. In the second, they mutated one glutamate and one aspartate from the membrane-binding region of endophilin A2 N-BAR domain into lysines (E37K, D41K). This reversal of charge enhances the binding of the BAR domain to the membrane and it does not affect the N-terminal helices. This way, we can compare the influence of affecting both the amphipathic helix and the BAR modules in endophilin. Interestingly, both variants bound to the tubule starting from an interface, in the same manner as WT (Fig. 4.4.3). In the case of the charge reversal mutant, we observed the striated pattern binding as with the WT. Unfortu-

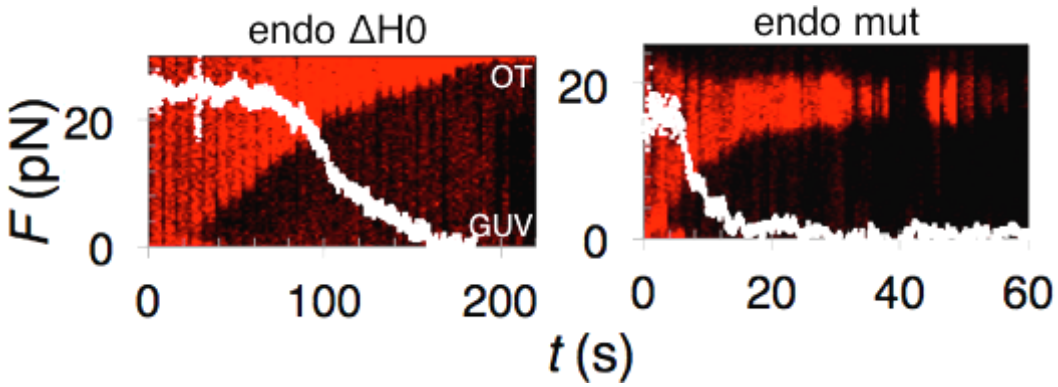

Figure 4.4.3: Amphipathic helices do not determine the location of binding in endophilin. Shown are force plots (white marker) overlaid on kymograms (red marker) of lipid fluorescence of a membrane tubule during the binding of endophilin variants. Endo ΔH0 = endophilin A2 with truncated N-terminal helices; endo mut = endophilin A2 E37K and D41K.

nately, labeling the the helix-deletion mutant was unsuccessful, therefore we do not know whether that protein also binds in a striated pattern or not. Nevertheless, we could observe that both variants formed a scaffold, evidenced by the total decrease in the force (Fig. 4.4.3, A).

It appears that, indeed, the **amphipathic helices are not necessary** for the formation of the scaffold nor for the preferential binding to the tubular neck. Nevertheless, the amphipathic helix is important. Truncating the N-terminal helices strongly impairs the protein's binding ability, requiring a seven-fold increase (compared to WT) in the bulk concentration to achieve the formation of the scaffold. The poor binding is also evident from the very long time scale at which we observed the force decrease during scaffold formation, compared to the wild type or the mutant (Fig. 4.4.3). Furthermore, both variants significantly changed the radius of the scaffolded tubule, where in the absence of N-terminal helices, the protein displays a much wider range of tubular radii. Precisely, we measured a scaffold radius of 21.4±11.6 nm (mean±SD) for the helix-deletion mutant and 19.9±3.0 nm for the charge-reversal mutant (Table 4.4.1).

Finally, we tested the full-length epsin 1, another important endocytic protein, believed to initiate membrane bending in clathrin-mediated endocytosis (see Section 1.4). To remind the reader, epsin does not contain a BAR domain; instead, it binds and bends the membrane via an amphipathic helix. Similarly to centaurin, we could not observe the constriction to start from the neck; rather it appeared homogenous along the tubule length. Unlike endophilin and centaurin, the force never reached zero and so we never observed buckling. However, there was a strong mechanical effect, characterized by a systematic reduction in both the force and the radius for a wide range of membrane tensions (Fig. 4.4.4). **These observations indicate that**

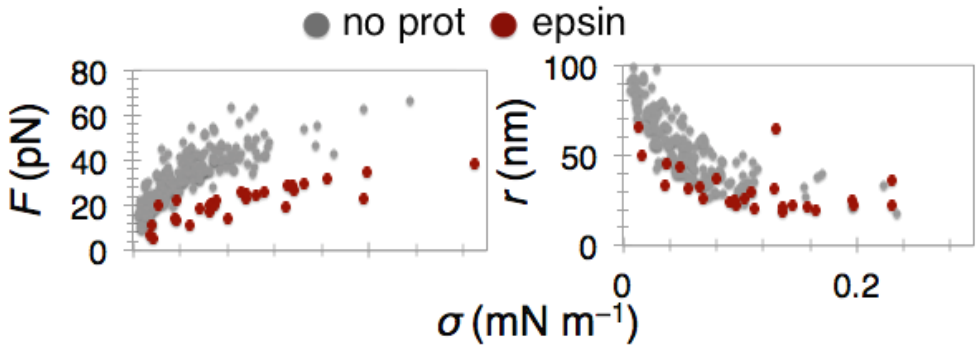

Figure 4.4.4: Epsin alters membrane curvature and mechanics. Shown are the dependence of force and tubule radius after injecting epsin 1. As there was no label on the protein, we only recorded cases where we observed the reduction in the force ($N = 5$).

epsin, hence implicitly amphipathic helices, may in fact remodel the membrane, albeit without forming a rigid scaffold.

We hypothesize, based on our observations, that a strong constriction induces a pressure perturbation across the bilayer, leading to tubular instabilities, as discussed in (Monnier et al., 2010; Shlomovitz et al., 2011). Considering that centaurin imposes a relatively wide tubular radius, it does not display a beading instability. It seems that the structure of endophilin has evolved to induce a very strong constriction and hence strong tubule perturbations. Amphipathic helices are not required to form a scaffold, although for endophilin, they are crucial in recruiting it to the membrane. They also enhance the spontaneous curvature and help rigidify the scaffold, as evidenced by the wide distribution of tubule radii in the absence of helices. This conclusion is aligned with previous electron microscopy imaging and CG MD simulations (Mim et al., 2012). On the other hand, BAR domain appears crucial in forming the scaffold itself, possibly as a combination of membrane-mediated curvature attraction and ordered packing on the surface.

4.5. Molecular structure of protein scaffolds

4.5.1) Areal density of proteins. Electron microscopy imaging and CG simulations (see Chapter 3) have revealed that at very high protein to lipid ratios, BAR proteins form highly ordered and densely packed assembly (Frost et al., 2008; Mim et al., 2012; Simunovic et al., 2013a). Fluorescence microscopy experiments, on the other hand, have shown that the density of the N-BAR protein amphiphysin in the regime where it forms a scaffold was ~ 5000 μm^{-2} on the tubule (Sorre et al., 2012). Following the same quantification protocol (see Section 2.3.6), we found a similar areal density of β2 centaurin dimer on the scaffolded tubule, 7400±1800 μm^{-2}. If approximating the area of a β2 centaurin dimer, based on homology modeling (see Section 4.1), to

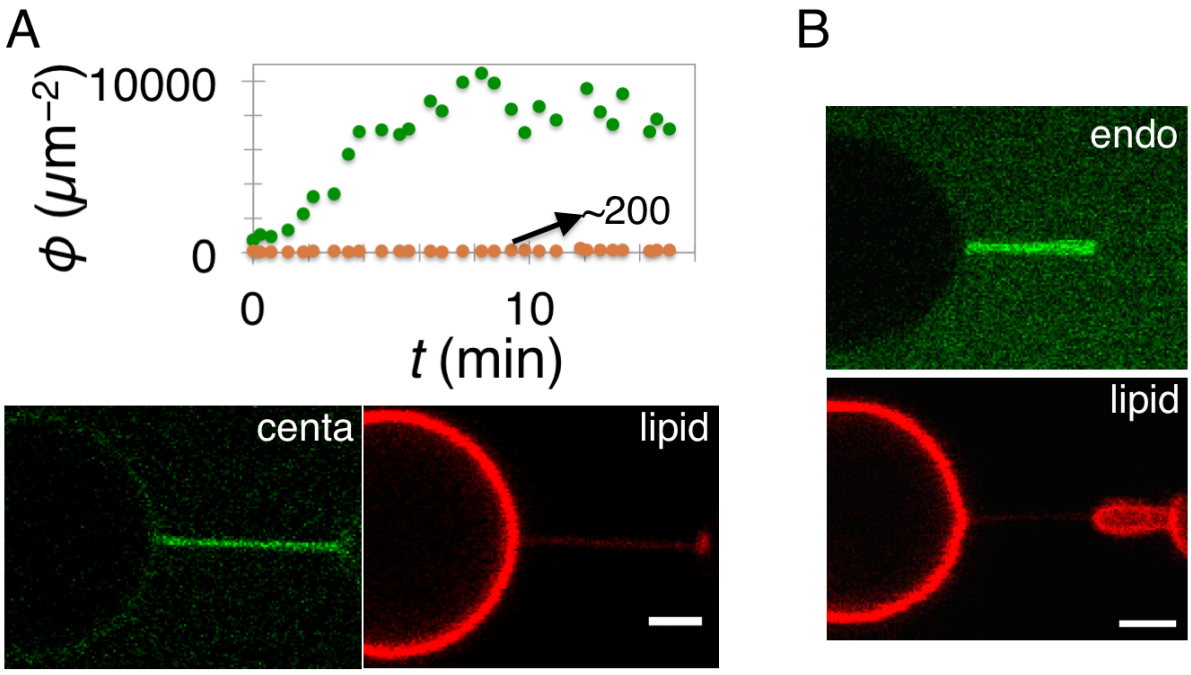

Figure 4.5.1: Molecular density of scaffolds. (A) Plot showing the recruitment of β2 centaurin (centa) on the membrane tubule (green), reaching ~35% surface coverage and on membrane vesicle (green), constant at ~ 1%. Confocal images show the strong enrichment of centa on the tubule, compared to the vesicle. (B) Formation of a scaffold of endophilin A2 (endo) on the tubule, with an undetectable amount of proteins on the vesicle.

be 50 nm^2, the fraction coverage of a scaffolded tubule is ~ 35%. This result indicates that proteins do not need to be tightly packed to mold the membrane. Furthermore, we found a wide range of areal densities on the vesicle that can give rise to the formation of a scaffold on the membrane, although if the density exceeds ~ 3000 μm^{-2}, it systematically leads to scaffolding. Precisely, in experiments depicted in Fig. 4.4.1, B, we measured areal density on the vesicle to be 3600±830 μm^{-2} (18% coverage) for β2 centaurin dimer. These observations are consistent with the density-dependent behavior of amphiphysin (Sorre et al., 2012). Based on our observations, it appears that BAR proteins do not need to be densely packed to induce remodeling. We remind the reader from Chapter 2 that we are presently unable to determine the labeling efficiency of the N-BAR domain of endophilin A2 as the protein lacks tryptophan residues needed for spectrophotometric measurement at 280 nm. Considering that it has been already demonstrated that the density of an N-BAR scaffold is ~ 25%, repeating this measurement for endophilin A2 is not crucial.

Strikingly, in some cases, we observed the formation of a scaffold at very low densities of the protein on the vesicle. Figure 4.5.1, A shows an example where β2 centaurin covered only 1% of the vesicle but as much as 40% of the tubule. To quantify, we only observed this behavior in two out of 16 cases in which there was low density binding on the vesicle (see Chapter 6). As the scaffold only formed near the

end of the experiment, we did not count those two cases in the data of Fig. 4.4.1. For endophilin, on the other hand, the effect was much stronger. We observed cases where the amount of endophilin on the vesicle was undetectable, yet it formed a scaffold on the tubule. The scaffold was evidenced by strong constriction, visible growth of the scaffold and the concurrent vanishing of the force, finally followed by buckling (Fig. 4.5.1, B). To specify, there were 21 out of 72 aforementioned cases of endophilin scaffolds in which we measured the protein fluorescence. Out of those 21 cases, a complete scaffold formed in four cases and an incomplete one in two cases, while keeping an extremely low or undetectable amount of protein on the vesicle. The reason why we emphasize these experiments is that very little protein on the underlying flat membrane can form scaffolds on tubules, which implies that they can have a much stronger membrane-remodeling role in low-concentration environments.

4.5.2) Simulations of N-BAR assembly on tubules. Fluorescence imaging provided insights into the density of proteins on scaffolded tubules, but it would still be valuable to understand the way proteins are assembled in this configuration at molecular resolution. We used CG MD simulations of the N-BAR domain of endophilin on a lipid bilayer tubule (see Section 2.4). To briefly recapitulate, in CG modeling, molecules are represented at a resolution much lower than atomistic, which makes it tractable to simulate mesoscopic biomembrane systems at long (i.e., microsecond) time scales. MD simulations integrate the motion of particles based on Newtonian dynamics, giving insights into time-dependent movement of proteins on the membrane. Each lipid was represented with three CG sites (hydrophilic head group and two hydrophobic chains) (Srivastava and Voth, 2013), while the N-BAR domain was represented with 26 sites using elastic-network modeling as described previously (Ayton et al., 2010). We have employed the same model in elucidating the self-assembly of N-BAR proteins of flat membranes and vesicles, described in the accompanying thesis (Simunovic et al., 2013a; Simunovic et al., 2013b; Simunovic and Voth, 2015). Here, we created a lipid bilayer cylinder, 20-nm in diameter and 150-nm in length, connected in z-direction with its periodic boundary images (thus virtually infinite in length). We placed N-BAR domains on the membrane surface at 5%, 10%, and 40% coverage, starting either from a random or tightly packed configuration. We carried out ~ 30 million simulation time steps, roughly equivalent to a microsecond time scale. We note that in CG simulations it is impossible to determine the actual time.

We observed that, regardless of the initial assembly of proteins and the protein density, N-BAR domains readily interacted with one another along their longitudinal axis (Fig. 4.5.2). Curiously, this arrangement resembles linear aggregation, as we demonstrated on flat membranes and vesicles (Simunovic et al., 2013b). On flat membranes and quasi-flat vesicles, linear aggregates interconnect into meshes. On

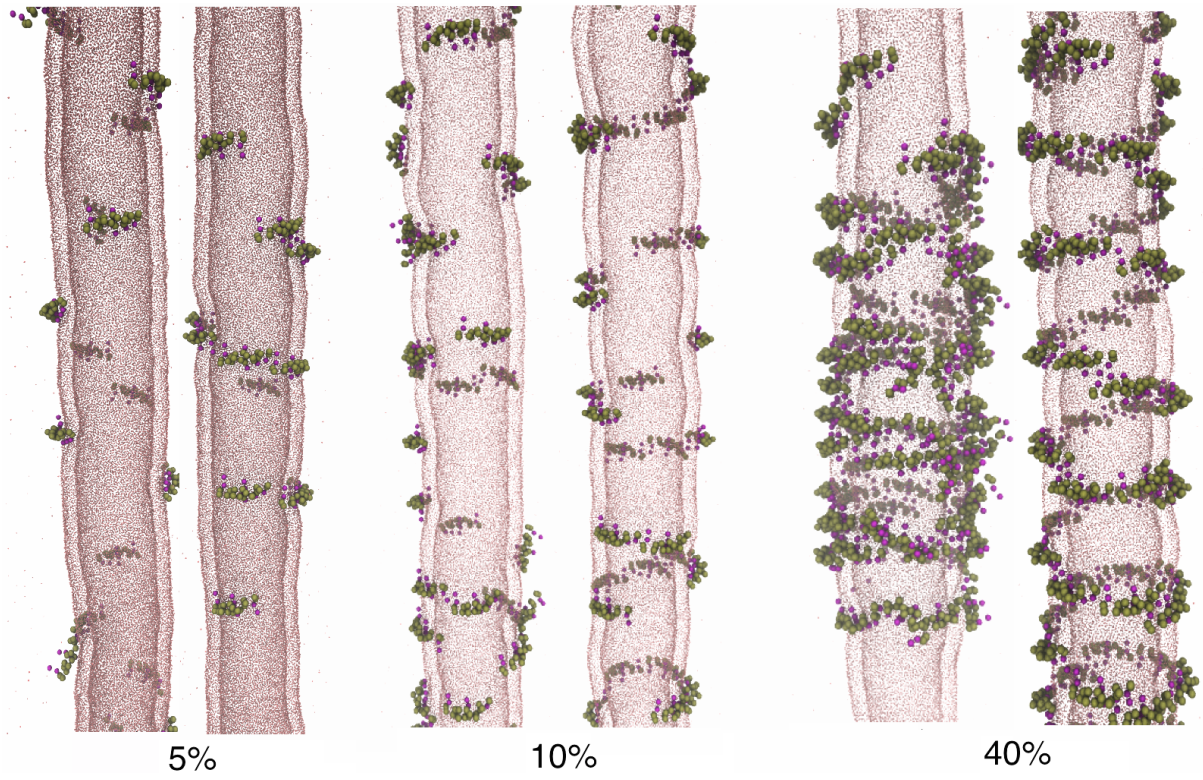

Figure 4.5.2: Assembly of N-BAR domains on membrane tubules. Shown are snapshots of CG MD simulations of lipid bilayer tubules coated with three different N-BAR densities (as indicated). Each density shows the starting (left) and final (right) configuration.

tubules, on the other hand, their assembly results in a **helix** (Fig. 4.5.2, right snapshot of each panel). From our simulations, we measure the angle of the helical turn with respect to the tubule axis to be 30°. We also count 7–8 N-BAR domains in a full helical turn, with the helix pitch averaged at 18.3 nm (Fig. 4.5.3, A).

At 35% density, the proteins form a continuous helix in which proteins remain with the same neighbors throughout the simulation. Figure 4.5.3 B plots a minimum distance between two N-BAR domains from neighboring helical turns, showing that the proteins gradually transform from a close assembly (as depicted in Fig. 4.5.2, penultimate panel) into a helix at ~ 15 million time steps, after which the helical pitch remains constant. We also measured the dimerization kinetics to show that the proteins do not exchange neighbors over the course of a simulation (Fig. 4.5.3, C).

What is particularly interesting is that, at low densities, the proteins still form helical assemblies with the same ~ 30° angle. An alternative assembly would be a continuous helix with a greater angle, however we never observed such structure. Instead, the proteins locally assemble. We note that the dimerization is more dynamic, evidenced by the breakage and reformation of local helices, as shown by the kymogram in Fig. 4.5.3, D.

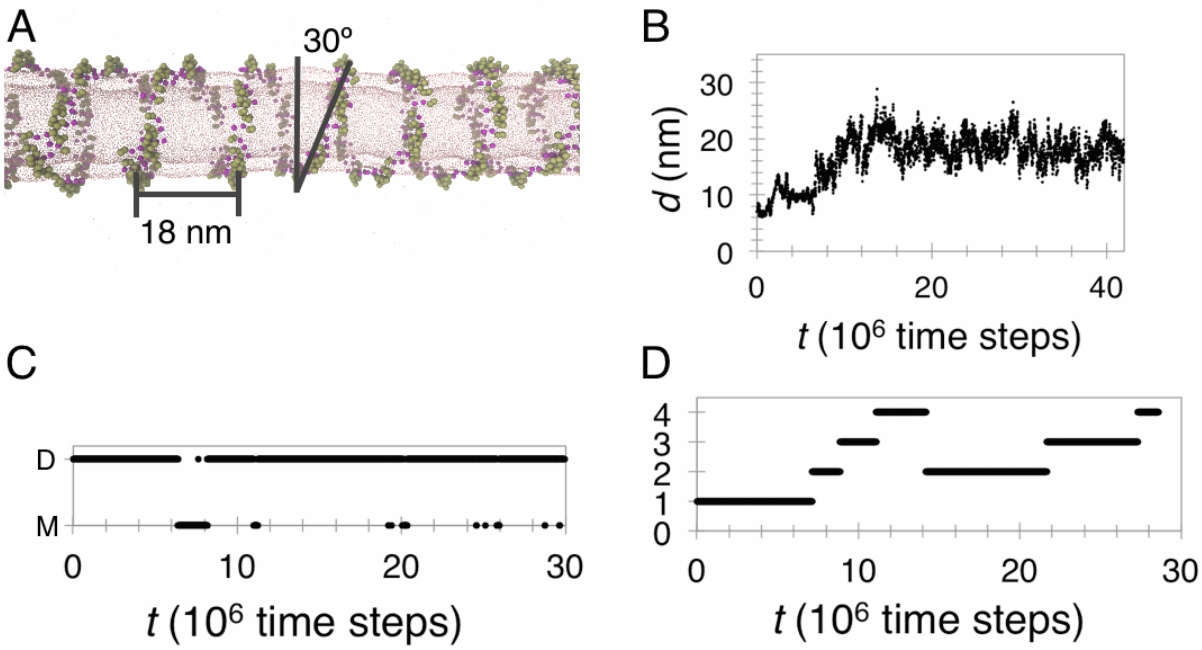

Figure 4.5.3: The formation of an N-BAR domain helix. (A) Structural properties of the helix from a CG simulation at 35% N-BAR density. (B) The distance between two representative N-BAR domains showing the convergence to the helical pitch distance. Taken from CG simulation at 35% density. (C) Dimerization kymogram showing the dimerization dynamics of two N-BAR domains as part of the helix at 35% density. M: monomer, D: dimer. (D) Polymerization kymogram, showing the dynamics of helix formation in a simulation at 12% density. Numbers on the *y*-axis represent the number of N-BAR domains in the helix.

In our study, we start with a radius of the tubule that has little mismatch with the scaffold radius, so to overcome computationally intractable timescales of the initial tubule constriction. Therefore, we simulated a steady-state configuration of the proteins on tubular membranes. A recent computational study has used rods of adjustable intrinsic curvature bound to a quasi-continuum membrane model to show the interaction of curved particles on wider tubules (Noguchi, 2014). They demonstrated that, if rods are highly curved, the tubule may undergo a phase separation marked by a condensation of the protein and a tubule constriction (Fig. 4.5.4). If starting from a vesicle, rods aggregate, leading to disc-like and tubular deformations, morphologically similar to another recent quasi-continuum simulation study (Noguchi, 2014; Ramakrishnan et al., 2013). Both works have shown that the anisotropy of bound particles is key in inducing membrane instabilities, in line with the CG MD simulations presented in the accompanying manuscript (Simunovic et al., 2013b).

However, in a quasi-continuum simulation, the harsh coarse-graining has taken away the molecularity of the system, therefore it is difficult to estimate the effective protein to lipid ratio in the equilibrated structures. It is also plausible that

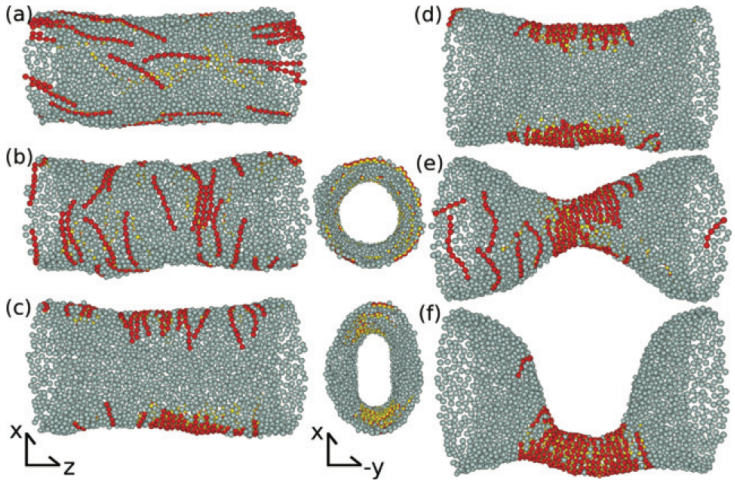

Figure 4.5.3: Phase separation of curved rods bound to a quasi-continuum membrane simulated by (Noguchi, 2014). Shown are snapshots from simulations at 17% surface coverage of rods with progressively increasing membrane spontaneous curvature and the actual intrinsic curvature of rods. Taken from (Noguchi, 2014).

their work, especially the results in Fig. 4.5.4 (Noguchi, 2014), show a metastable state after which the proteins will equilibrate into a much less dense structure.

Based on the striking similarity with the density of proteins measured in fluorescence microscopy experiments and our CG MD simulations, we propose that the equilibrated molecular structure of BAR proteins on the membrane is a helical arrangement, that follows a linear aggregation of proteins on the tubule. This structure clearly opposes highly densely packed (~ 100%) arrangements proposed based on cryo-electron microscopy imaging, however it seems much more likely considering that 1), it has been observed under more physiological protein concentrations and dynamic conditions (i.e., not frozen), and 2), our proposed structure permits the binding of other proteins on the tubule (such as dynamin), which is required for most types of endocytosis.

5. Fission of membrane tubules by BAR proteins and molecular motors

In the last step of endocytosis, the continuous surface of the lipid bilayer breaks, allowing the nascent bud to detach from the underlying membrane. This process, termed membrane fission, is less understood than other membrane-remodeling phenomena because it is fast and dynamic. We discussed in the Introduction (see Section 1.5) that in clathrin-mediated endocytosis, dynamin polymerizes on the neck of the endocytic bud, constricting it until it breaks. The constriction happens after a conformational change of dynamin, triggered by GTP hydrolysis (Roux et al., 2006). A recent work has demonstrated that membrane fission may be promoted in a nucleotide-independent manner, by shallow insertions of amphipathic helices into the bilayer (Boucrot et al., 2012). As part of this thesis, we show that endophilin can, in addition to generating curvature and stabilizing highly complex membrane structures, mediate a dynamic fission mechanism, likely as part of a fast clathrin-independent endocytosis (Boucrot et al., 2015; Renard et al., 2015). In this process, endophilin cooperates with actin and dynamin to efficiently internalize various cargo, such as signaling proteins and bacterial toxins. These results open routes for investigating novel ways to cut the membrane, i.e., an alternative pathway to what has extensively been ascribed to clathrin and dynamin. A most exciting implication is the relationship of curvature-inducing proteins and molecular motors, proteins that supply external pulling force in the cell. Our collaborators, Ludger Johannes, Harvey McMahon, and their coworkers, have investigated this mechanism in the cells, whereas our aim is to build a minimal model system, so to understand molecular mechanism and the underlying physics that drives this phenomenon.

5.1. Endophilin drives clathrin-independent endocytosis of bacterial toxins

In this section, I will present the results of cell biology experiments, carried out by Henri-François Renard in the lab of our collaborator Ludger Johannes (Institut Curie). These *in vivo* experiments are complementary to my *in vitro* work, presented in this chapter, and they were carried out at the same time. For the experimental details of *in vivo* experiments, I direct the reader to our joint publication (Renard et al., 2015).

It has been previously shown that bacterial toxins, namely Shiga toxin and, often, cholera toxin, get internalized into the cell in a clathrin-independent manner (Romer et al., 2007), however which protein machinery mediates this process was

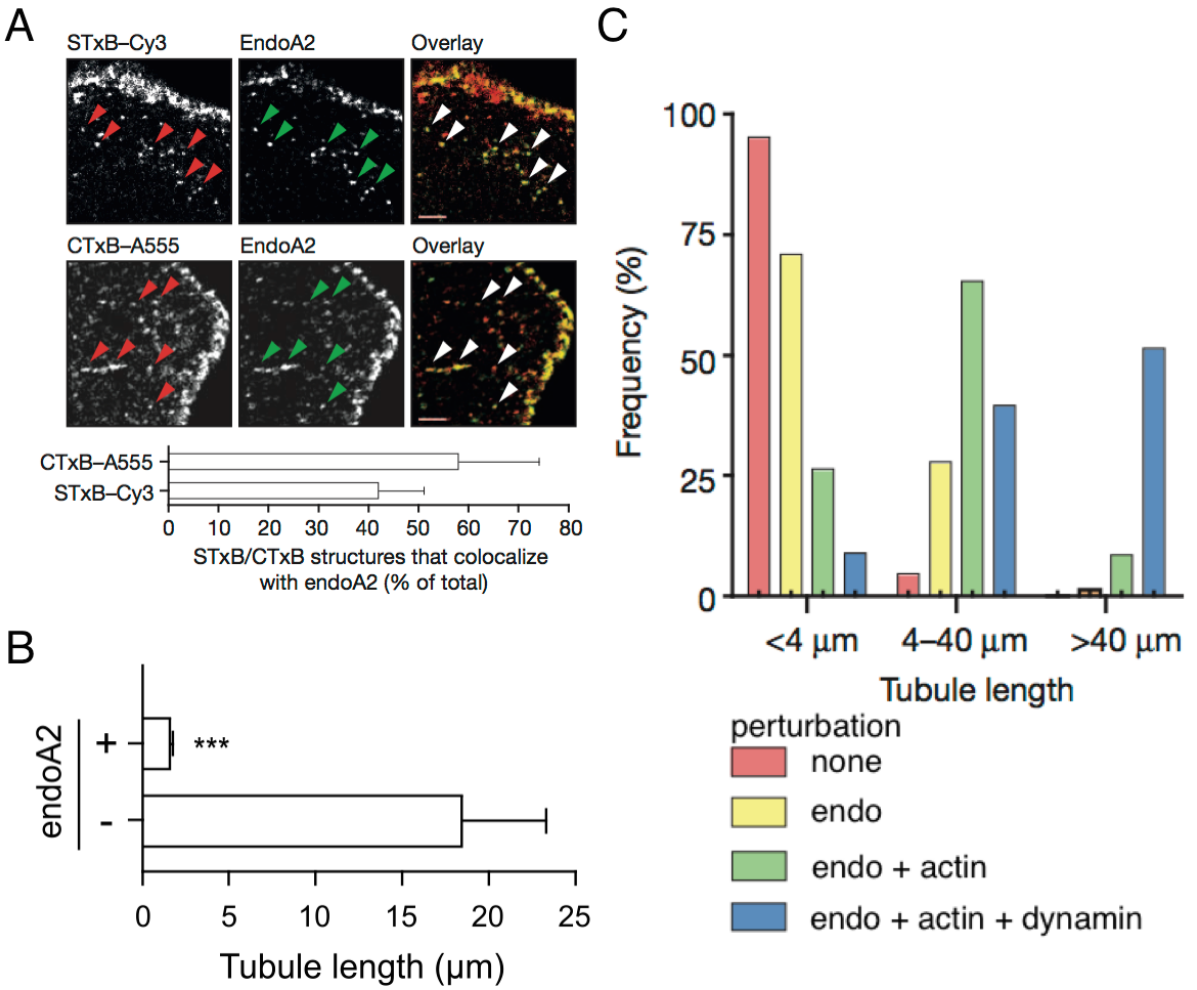

Figure 5.1.1: Endophilin-mediated endocytosis of bacterial toxins. (A) Co-localization of endophilin A2 (EndoA2) and Shiga toxin (STxB) or cholera toxin (CTxB) in cells. (B) STxB-induced tubule length in cells expressing and not expressing endoA2. (C) Frequency distribution of tubules according to length for four conditions shown in the legend. All panels adapted from (Renard et al, 2015).

not known. By studying the endocytosis of the two toxins in mammalian cells using confocal microscopy, our collaborators observed that endophilin A2 colocalizes with the very early invaginations of the plasma membrane induced by the toxin (Fig. 5.1.1, A). Moreover, upon depleting the cell of endophilin A2, Shiga toxin formed tubular and ten-fold longer invaginations in the cell membrane, measured by confocal and electron microscopies (Fig. 5.1.1, B). The frequency of these tubules was comparable to the amount of toxin-induced invaginations observed in the presence of endophilin A2, which implies that endophilin A2 could have a role in cutting toxin-containing tubules. They then measured the amount of internalized toxins as a function of endophilin A2 content. For this purpose, mutated versions of Shiga and cholera toxins, which become sulfated in in the Golgi apparatus, were used, because subsequently the sulfation level can be measured with radiography (Lauvrak et al., 2004; Mallard et al., 1998). They found that a stronger depletion of endophilin A2 re-

sulted in the lower amounts of trafficked toxins into the cell, which means that endophilin A2 is indeed key for the uptake of Shiga and cholera toxins.

Importantly, there was only weak colocalization of endophilin A2 with clathrin or its adaptor AP2. As mentioned in the Introduction, a study by McMahon and coworkers showed that endophilin drives its own very fast endocytic pathway, taking place at the leading edge of a cell (Boucrot et al., 2015). They found that many proteins take advantage of this endocytic route, especially several G-protein-coupled receptors, various receptor tyrosine kinases, and, as shown by the lab of Ludger Johannes, Shiga and cholera toxins.

Next, they investigated the interplay of endophilin A2 and other fission factors, which have been previously demonstrated to play roles in the uptake of Shiga toxin. It appears that actin also colocalized with the Shiga toxin invaginations, both in the presence and the absence of endophilin. Apparently, endophilin A2 is not required to recruit actin to the membrane. Depolymerization of actin by latrunculin-A resulted in a similar increase in the length of toxin-induced tubules, which indicates that actin contributes to the efficiency of endocytosis, independently of endophilin A2. Moreover, they found that dynamin behaves in the same manner and provides an additional independent contribution to the probability of fission of toxin-containing tubules. By binning the tubule lengths into short (< 4 μm), intermediate (4–40 μm), and long (> 40 μm), they found that depleting the cell of a), endophilin A2, b), endophilin A2 and actin, and c), endophilin A2, actin, and dynamin, progressively increases the length of tubules from a) to c) (Fig. 5.1.1, C). **This result shows that the three proteins act independently from one another in membrane fission, but their joint activity significantly enhances the efficiency of endocytosis.**

Another way to test the importance of individual components is by measuring protein biosynthesis after the infection by Shiga toxin. They found that cells depleted of one of the three key components showed a weak protection against Shiga intoxication. By contrast, shutting down the activity of all three components induced an appreciable defense against intoxication, so much that five-fold concentration of Shiga toxin was required to achieve the same inhibited level of protein biosynthesis as in control conditions. Taken together, endophilin A2 is key for clathrin-independent endocytosis of bacterial toxins, **however it does not seem to be sufficient for an efficient internalization of cargo into the cells**. We investigate the physical role of endophilin in endocytosis and how other protein modules may contribute to its mechanism in the following sections.

5.2. Membrane fission by insertion depends on membrane topology

We have already demonstrated in Chapter 4 that endophilin can induce the spontaneous tubulation of flat membranes and that it forms rigid scaffolds which dictate the radius of tubules. However, in light of the results obtained on the activity of endophilin in the endocytosis of bacterial toxins *in vivo*, the important question remains: **can endophilin induce fission?** As already mentioned in Section 1.5, a study showed that epsin and various N-BAR domain proteins induce the fragmentation of ~ 200-nm-wide liposomes, composed of the total brain extract and 5% PIP_2 (Boucrot et al., 2012), the same composition used here. The extent of fragmentation directly correlates with the number of amphipathic helices per protein and seems inhibited by the crescent BAR domain. At the same time, our combined computational simulations and electron microscopy imaging (see Chapter 3) showed that N-BAR domains, at high bound densities, induce a transformation of small lipid vesicles into a network of tubules. As this process requires breakage of the bilayer topology (Simunovic et al., 2013a), it is another evidence that N-BAR proteins may promote membrane fission.

However, in the great majority of experiments described in Chapter 4, we did not observe spontaneous fission of membrane tubules induced by endophilin A2 (only 3 fission events, $N = 72$), β2 centaurin (only 1 fission event, $N = 16$), or epsin 1 (no fission events, $N = 6$). These three proteins represent well the family of endocytic proteins as they display different structural characteristics. As a reminder, endophilin A2 contains both the scaffolding BAR domain and the amphipathic helices (two N-terminal and two small insertion motifs), β2 centaurin comprises only the scaffolding domain, while epsin 1 has an amphipathic helix, but no scaffolding domains.

Is it possible that we did not observe fission because of initial conditions of the membrane? In the described experiments we accessed a wide range of tubular radii (10–120 nm) and surface tensions (0.001–0.4 mN/m). We also tested the interaction of endophilin with tensionless membrane tubules, in case any non-vanishing membrane tension could preclude static fission. We created a tensionless membrane by rapidly hydrating a lipid film, a process which makes multilamellar sheets with emanating tubules[6] (see Section 2.1.5). We observed the edge of lipid sheets with differential interference contrast microscopy, in the same manner as it was used to observe tubules cut by dynamin (Roux et al., 2006). Again, we did not observe scission when adding endophilin A2 at bulk concentrations of ~ 5 μM, for up to 30 min (Fig. 5.2.1). Hence, it seems unlikely that membrane fission was precluded by not meeting the required geometric or mechanical conditions, namely the curvature of tubules and tension.

[6] Many thanks to Laura Picas for showing me how to make multilamellar lipid sheets.

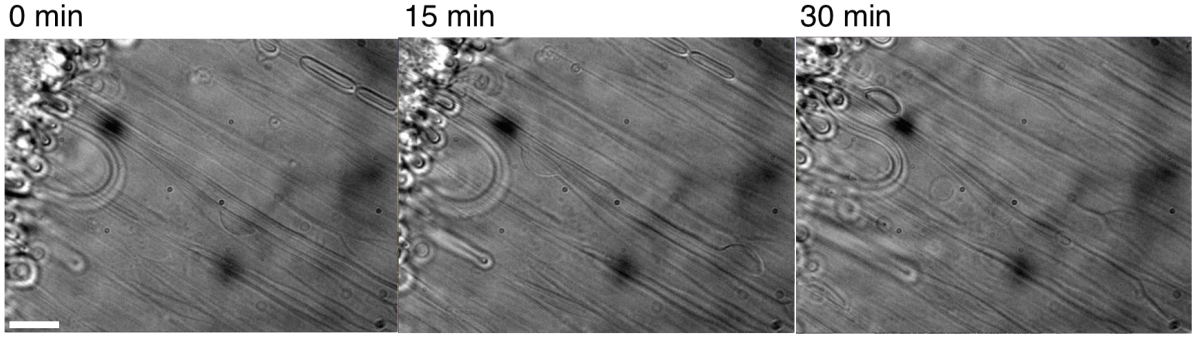

Figure 5.2.1: The absence of fission of tensionless tubules. Differential interference contrast microscopy images of multilamellar bilayer sheets (composed of the total brain extract + 5% PIP_2) incubated with 5 μM full length endophilin A2. No change in tubule length or amount observed in 30 min of imaging time. Scale bar approximately 5 μm.

What is the origin of this apparent discrepancy? Our hypothesis is that the initial topology of the membrane could be crucial in determining whether the insertion leads to membrane fission or the stabilization of curvature, at least on the time scale of minutes. The previously proposed model predicting vesiculation upon shallow insertion is valid at equilibrium (Boucrot et al., 2012), which may take a long time to achieve. Metastable states could also exist that were not previously considered. In other words, by having proteins interact with already formed membrane tubules, we may trap the system behind a very large energy barrier. Hence, the membrane stays in the cylindrical geometry for the time scale of our experiment (15–30 min), significantly longer than endocytosis (~ 1 s). Other factors could contribute to the metastability of the system, such as the influence of the protein scaffold on the mobility of lipids, which we explore below.

We also hypothesize that there could be a fundamental difference in the way proteins interact with the spherical than the cylindrical geometry. In fact, it has been shown using electron paramagnetic resonance that endophilin partitions deeper into the bilayer when bound on tubules, compared to small vesicles (Ambroso et al., 2014). Consequently, the tubules are additionally stabilized by the BAR domains, whereas the vesicles predominantly interact with the proteins via amphipathic helices (Fig. 5.2.2). Another way of looking at the problem is by considering that the cylindrical geometry of the tubules permits efficient packing of the crescent BAR domain. By contrast, packing of the BAR domain on spherical surface leaves defects (described in mathematics by the hairy ball theorem), which would have a destabilizing effect.

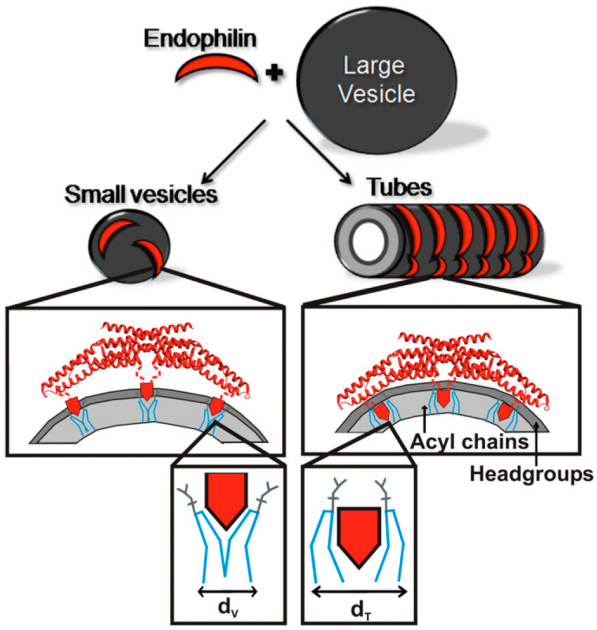

Figure 5.2.2: Binding of N-BAR proteins to tubules and vesicles illustrated by (Ambroso et al, 2014). N-BAR proteins predominantly bind to vesicles via amphipathic helices, which can induce vesiculation as shown in (Boucrot et al, 2012). Binding on tubules, however, is stabilized by protein scaffolds. Adapted from (Ambroso et al, 2014).

5.3. External pulling force induces fission of endophilin-scaffolded membrane tubules

We found that it is indeed possible to induce fission with endophilin, **but only after supplying external pulling force on the tubule**. We conducted the experiment by first, injecting the protein in the vicinity of a tubule at concentrations 1–5 μM in the pipette, as in Chapter 4. After the scaffold has formed, we remove the injection pipette. Then, using the piezo-electric actuator, we apply a pulling force opposite in direction of the trapped bead at constant velocity, thereby increasing the length of the tubule. In the case of endophilin A2, fission took place in the great majority of experiments (40 fission events, $N = 43$) when pulling at velocities of 50 to 8000 nm/s. In many experiments, just prior to fission, we observed the formation of domains, marked by significantly diminished fluorescence intensity in both the lipid and protein fluorophores (Fig. 5.3.1). The radius of the dim segments is difficult to quantify as the intensity in those regions is at the limit of detection, but we can assume that the radius is below the radius of the scaffolded tube (i.e., $\ll 10$ nm, see Chapter 4).

Based on confocal microscopy imaging, we believe that fission took place either at these narrow segments, either at the interface of the GUV and the tubule, or

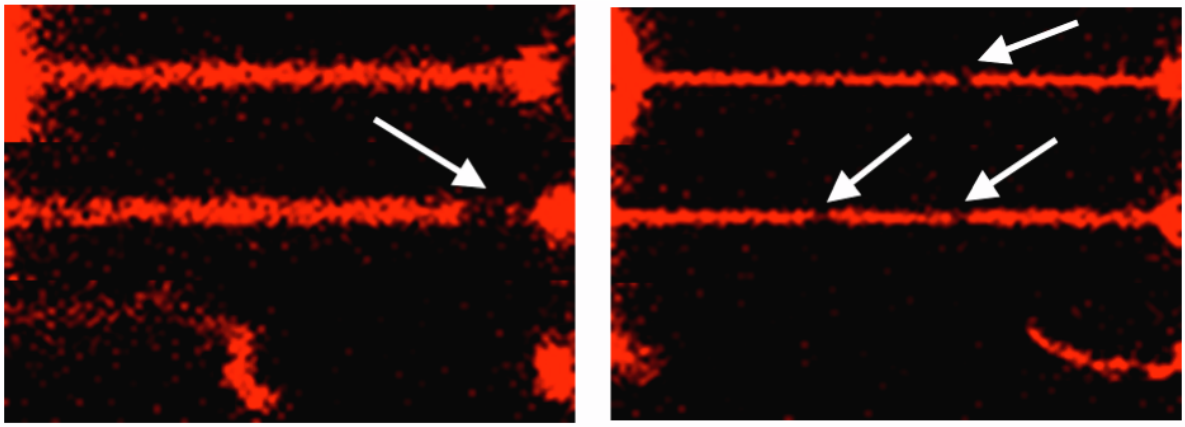

Figure 5.3.1: Fission of tubules scaffolded with endophilin A2 by external pulling force. Confocal images showing events just prior to fission on two different examples. The radius of the tubule (the measurable thick part) in both cases is ~10 nm (note, absolute fluorescent intensity between the two examples is different due to different imaging gains). The thin patch is too faint for quantitative fluorescence measurements.

at the interface between the tubule and the bead. We note that with our scanning confocal microscope we were imaging at a rate of no faster than ~ 3 images per second, limiting the precise determination of where the tubule broke.

We hypothesize two possible scenarios that would lead to a localized reduction in fluorescence with elongation: 1), the tubule gets squeezed in these segments or 2), a pore opens up and so we are imaging a single bilayer patch bridging the tubular structures. Both scenarios would hypothetically result in fission with further elongation. In the former case, considering the low radius of these domains (<< 10 nm), it is likely that continuous elongation would reduce the radius in those junctions down to ~ 3–5 nm, an estimated radius for crossing the fission barrier (Allain et al., 2004; Kozlovsky and Kozlov, 2003). In the latter case, proteins could lower the line tension of the formed pores, thus extending its lifetime. In a process of pore nucleation and with tubule elongation, pores could grow in size comparable to the tubule radius, hence induce fission. We do not attempt to resolve the molecular details of this mechanism as it is too dynamic for any high-resolution technique. Moreover, the multi-second timescale of this process makes it intractable for CG MD simulations. We focus on elucidating the steps leading to fission and understanding the mechanism from a macroscopic point of view.

To gain a quantitative insight into this fission mechanism, we monitored the tether-retraction force during elongation. First, we conduct several controls by pulling the tubule in the absence of the protein. First, we pulled the tether at a moderate rate of 0.3 μm/s, at different membrane tensions. The force was fairly constant even at high tension (Fig. 5.3.2, A, left). When pulling a higher rate of 1.3 μm/s, at a

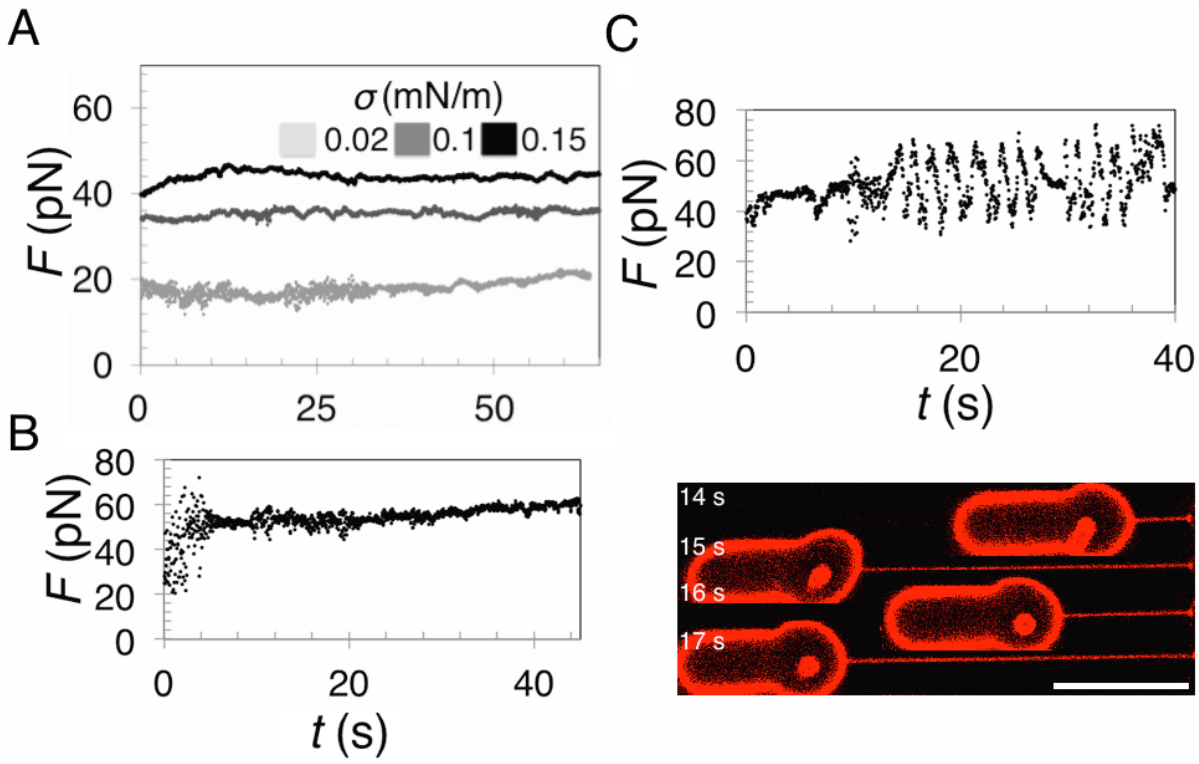

Figure 5.3.2: Control: elongating bare tethers at high rate. (A) Tubule retraction force , F, as a function of time, t, upon pulling of an already formed tether at 0.3 μm s^{-1}, at indicated membrane tension, σ. (B) Pulling at 1.3 μm s^{-1} (another example) at 0.08 mN/m. (C) Rapid and repeated elongations at ~ 20 μm s^{-1} at 0.08 mN/m, where the vesicle was brought back-and-forth (see below). The force reacts to pulses (as the lipids cannot equilibrate so fast) but rapidly equilibrates if ceasing to pull. The tether did not break after 12 such pulses. Time stamp in fluorescent images corresponds to the time in the plot above. Scale bar: 10 μm.

moderate tension of ~ 0.1 mN/m, we observed only a slight increase in the force of ~ 8 pN over 40 s (Fig. 5.3.2, B). Some increase in the force is expected due to friction between two membrane leaflets, which dominates lipid diffusion typically at high pulling rate (Evans and Yeung, 1994). Finally, to test the resilience of the bare tether, we subjected it to harsh pulses in which we repeatedly pulled the vesicle at a rate of ~ 20 μm/s then brought it back, immediately followed by another pull (see confocal images in Fig. 5.3.2, C). We repeated the pull-retract cycle 12 times and did not observe fission (Fig. 5.3.2, C). The force significantly fluctuated, likely 1), because the rapid elongation gives rise to a stick-slip mechanism (Ashok and Ananthakrishna, 2014), and 2), due to the aforementioned friction (Evans and Yeung, 1994).

By contrast, elongating tubules scaffolded by proteins significantly increased the retraction force up until the breakage point (Fig. 5.3.3, A). Moreover, the magnitude of the increase in force (i.e., $\Delta F = F_{break} - F_0$) scaled with the velocity of pulling (Fig. 5.3.3, B). A linear interpolation of the log-log plot of ΔF *versus* v reveals a slope of 0.43, indicating that the magnitude of force increase at breakage point scales as a

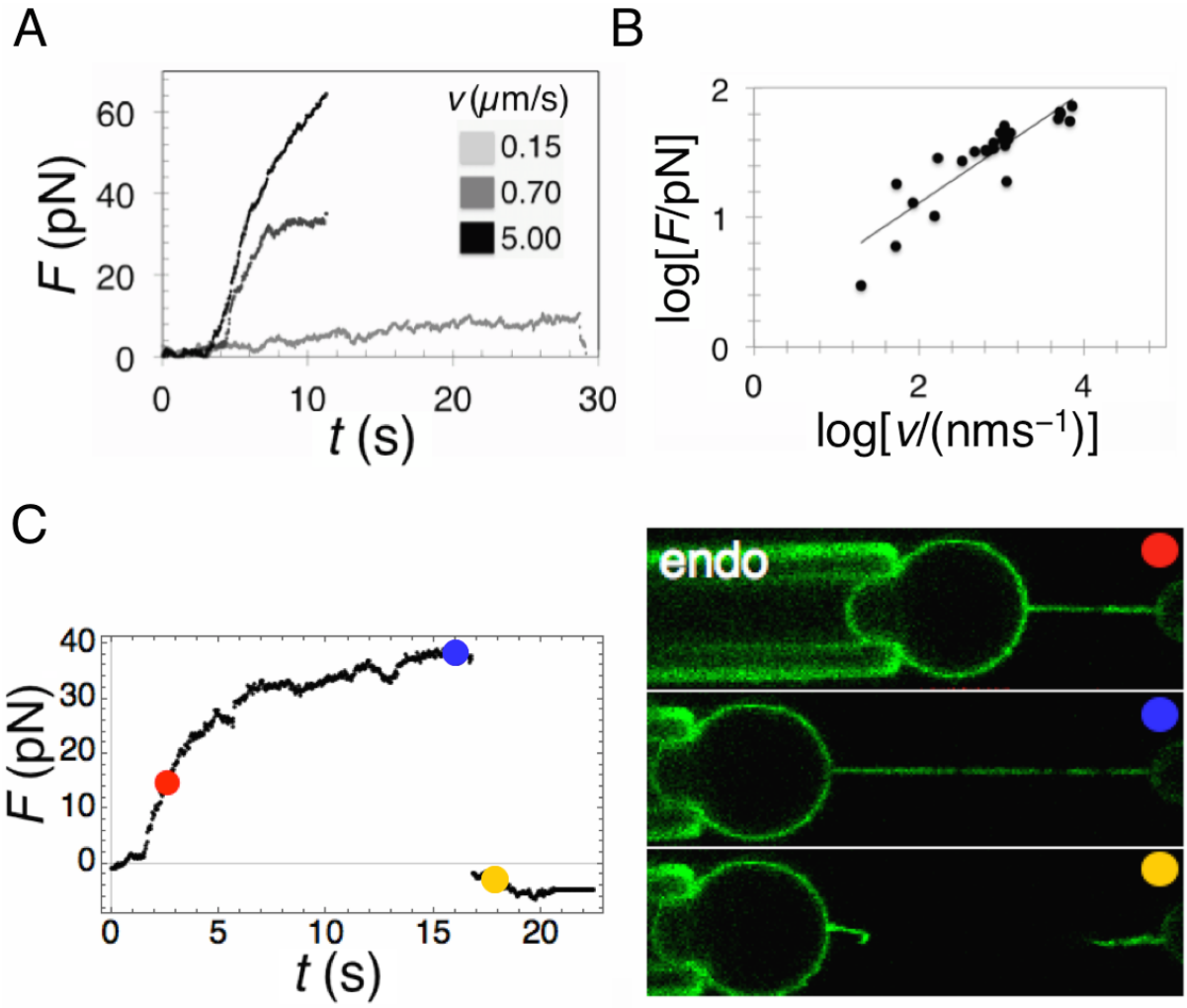

Figure 5.3.3: The increase in tether-retraction force during elongation of scaffolded tubules. (A) Tubule retraction force, F, as a function of time, t, upon pulling tubules scaffolded by endoA2 WT at different pulling rates, v. (B) Log-log plot of the magnitude of force increases at fission (F_f–F_0) versus v. The slope of the linear interpolation is 0.43. (C) An example of fission, showing confocal images of the protein channel and the corresponding force measurements. v = 0.8 μm/s, σ = 0.1 mN/m.

square root of the pulling velocity (Fig. 5.3.3, B). Figure 5.3.3, C shows the confocal images of the protein with the corresponding force measurements, in the course of pulling leading to membrane fission, revealing that the protein is generally present on the newly extruded segment of the tubule.

The positive correlation between the force and the pulling rate implies a type of **frictional force** may be at play, likely between the protein scaffold and the underlying lipids. This behavior is further evident by slow relaxation of the force (~ −0.5 pN/s) observed when ceasing to pull the tubule before the breakage (Fig. 5.3.4, A). Based on previous work, we speculate that the force relaxation comes from two sources. The slow time scale could be determined by the rate at which BAR proteins

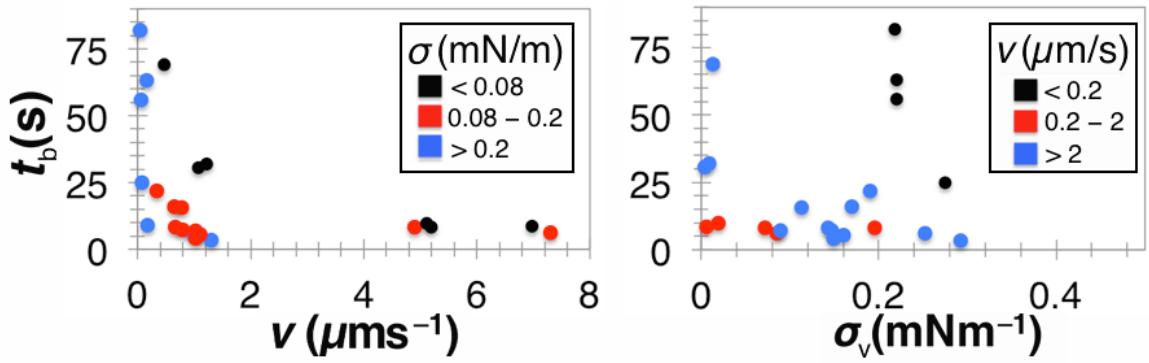

Figure 5.3.5: Timescale of fission. Fission time (t_b) inversely correlates with pulling rate, v (left) and weakly with vesicle tension, σ_v (right).

cross the barrier between the vesicle and the tether (Datar et al., 2015) and, possibly, additional similar time scale at which the scaffold forms. A fast relaxation time scale could directly come from friction, as was observed in GUVs doped with small amounts of oil (Campillo et al., 2013). In the work with interstitially inserted oil, the friction hypothetically comes from the interaction between the two leaflets, whereas in our case, the dissipative force is likely between the scaffold and the tubule.

The slowest elongation that led to fission in our case was 50 nm/s. Elongation at 20 nm/s resulted in a very slow increase in force and we could not observe fission in 150 s (Fig. 5.3.4, B). Likely, pulling at 20 nm/s is slow enough to allow for the proteins to cross the barrier and form a scaffold, thus continuously stabilize the tubule. Therefore, it is important to understand if forces generated in the cell are sufficient to create pulling velocities that overcome this threshold. We examine this issue in Section 5.6 below.

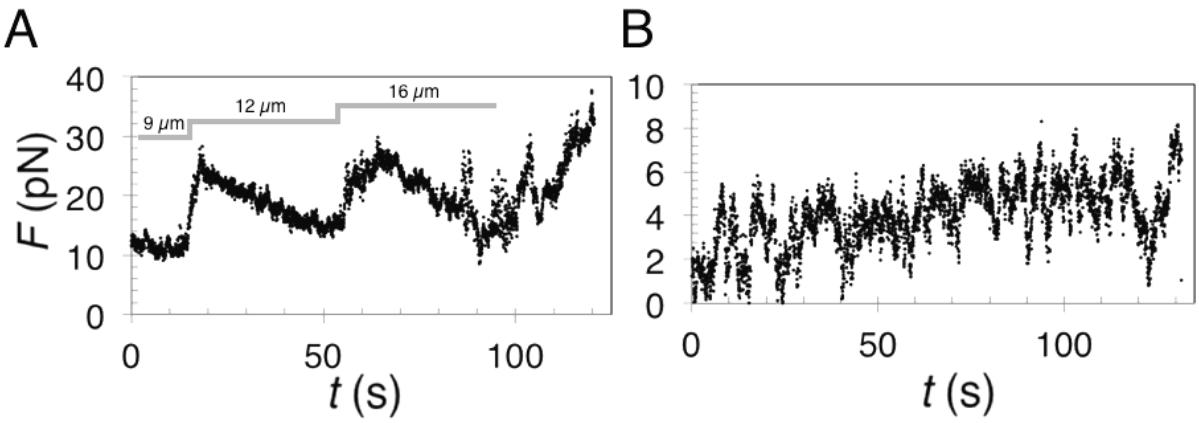

Figure 5.3.4: Force behavior during elongation of endophilin scaffolded tubule. (A) Slow recovery of the force after an elongation pulse at ~ 0.5 µm/s. Values above the plot indicate the corresponding tubule length. (B) Elongation at 20 nm/s, with no fission observed in 150 s.

We also observed that the time from activating the pulling force until fission inversely correlated with the pulling velocity (Fig. 5.3.5, left). Importantly, the magnitude in force increase at the breaking point did not seem to be greatly affected by tension in the vesicle (Fig. 5.3.5, right). We note that the time it takes for the membrane to break will also be affected by the way the tubule is pulled. If the external pulling force is briefly interrupted (as in Fig. 5.3.4, A), the time will most likely increase. It is possible that the weak correlation between tension and breakage time is due to the fact that tension in the vesicle is no longer connected to the tension in the tubule. We check the lipid diffusion behavior next.

5.4. Endophilin scaffold forms a lipid mobility barrier

To examine if the protein scaffold affects the dynamics of lipids, we measured the fluorescence recovery after photobleaching (FRAP). If the mobility of bleached component is unperturbed, then the fluorescence rapidly recovers due to mixing of the bleached and unbleached markers. In the experiment, the lipid fluorophores in the tubule ~ 10 μm in length were bleached by imaging only the tubule region at full laser power (generally, around ten images at a rate of 3 images s^{-1}; note that more than ten images runs the risk of photooxidation). Immediately after bleaching, the laser power was brought down and the system (vesicle + tubule) was imaged as described in Chapter 2.

We first checked the mobility of lipids in the reference membrane. We observed that the fluorescence recovery of bare tubules was indeed fast (< 5 s), hence demonstrating the free diffusivity of lipids in the absence of protein (Fig. 5.4.1, A). Conversely, in the presence of a scaffold formed by N-BAR domain of endophilin A2, the recovery was extremely slow. Precisely, the fluorescence intensity reached 50% of its reference value after ~ 90 s (Fig. 5.4.1, A).

We note that measuring photorecovery is in our case limited by the faint fluorescence signal of the lipid, as the tubule underneath the scaffold is strongly constricted. For this reason it is also impossible to quantitatively determine the diffusion coefficient, but our fluorescence measurement clearly shows that the mobility is significantly impeded. Another way to determine the diffusion dynamics is by observing the relaxation of the tubule radius after manually changing membrane tension. In case of freely diffusing lipids, the tubule radius will rapidly adjust to the membrane tension in the vesicle (as measured in Figs. 4.1.1 and 4.1.2). The most instructive cases for this analysis are those in which the scaffold only partially covered the tubule, as shown in Fig. 5.4.1, B (top). Considering that the tubular segment barely covered with the protein has a strong lipid fluorescence signal, it allows for a better quantification. We changed the tension in steps then measured the fluorescence in-

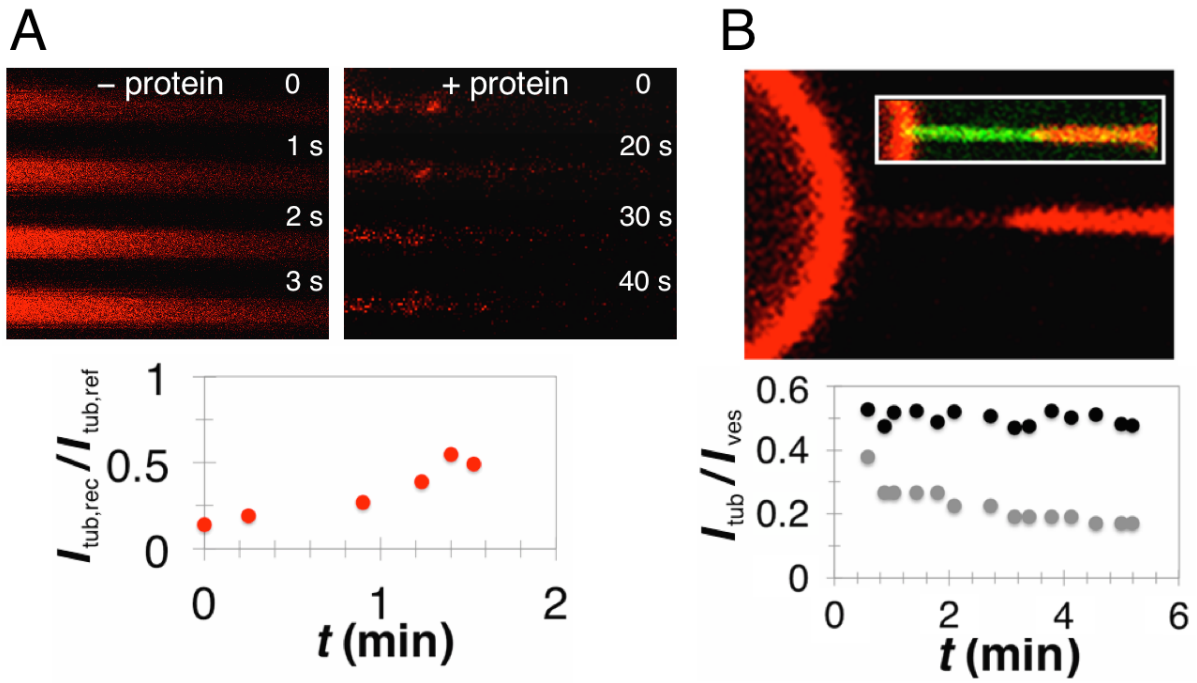

Figure 5.4.1: Protein scaffold forms an diffusion barrier. (A) Confocal images after bleaching the bare (left) and protein-scaffolded tubule (right). Bottom: fluorescence intensity (I_r) of the scaffolded tubule (normalized by the pre-bleaching value) as a function of time (t) of photo recovery. (B) Fluorescent image of a tube with coexisting scaffolded and non-scaffolded domains. Inset shows overlaid green (N-BAR domain) and red (lipid) channel. Graph shows the relative fluorescent intensity, normalized by the vesicle intensity, (I_r) on the non-scaffolded domain (black dots) and theoretically predicted for a bare membrane at the corresponding tension in the GUV (grey dots).

tensity along the tubule. As expected, the scaffolded part of the tubule had fixed lipid intensity, corresponding to ~ 10 nm in radius. However, over the course of minutes, the intensity of the non-scaffolded segment was also unchanged for all tested membrane tensions in the vesicle. For example, at high tension (0.16 mN/m), the fluorescence intensity was ~ 3 times higher than theoretically expected at this tension based on Eq. 4.2 (Fig. 5.4.1, B, black *versus* grey dots). This observation confirms that the scaffold sets a diffusion barrier preventing the lipids to freely flow between the vesicle and the non-scaffolded segment. In other words, BAR domain scaffolds decouple the lipids in the tubule from the vesicle reservoir, thus the tension in the tubule is likely different from the one in the vesicle. This observation can also explain the weak correlation of the tubule breakage time with the vesicle tension (Fig. 5.3.4, right).

5.5. Molecular motors have sufficient pulling force to drive fission mediated by endophilin scaffold

A recent work has shown that a molecular motor dynein supplies the force that forms very long tubular invaginations in the clathrin-independent endocytosis of bacterial toxins (Day et al., 2015). However, an important question still remains: **are forces supplied by motors sufficient to induce fission of membrane tubules covered by endophilin scaffolds?** To answer this question, we reconstitutes a minimal system composed of the membrane, endophilin A2, and a molecular motor. We chose to work with kinesin, as we have previously used this molecular motor in extruding membrane tethers from GUVs (Leduc et al., 2010; Leduc et al., 2004; Roux et al., 2002). In the assay (see Section 2.4 for experimental details), kinesin motors bind to GUVs via streptavidin-biotin bonds. Then, powered by ATP hydrolysis, they walk along microtubules, thus extruding a membrane tether from a GUV (schematized in Fig. 2.4.1, B and shown in Fig. 5.5.1, A).

This assay is technically challenging since it requires the precise timing of mixing the individual components and of imaging. The motors only work for up to 15 min after adding the motility buffer. However, not all vesicles are going to display motor activity, since some vesicles may get tethered by the motors and some could

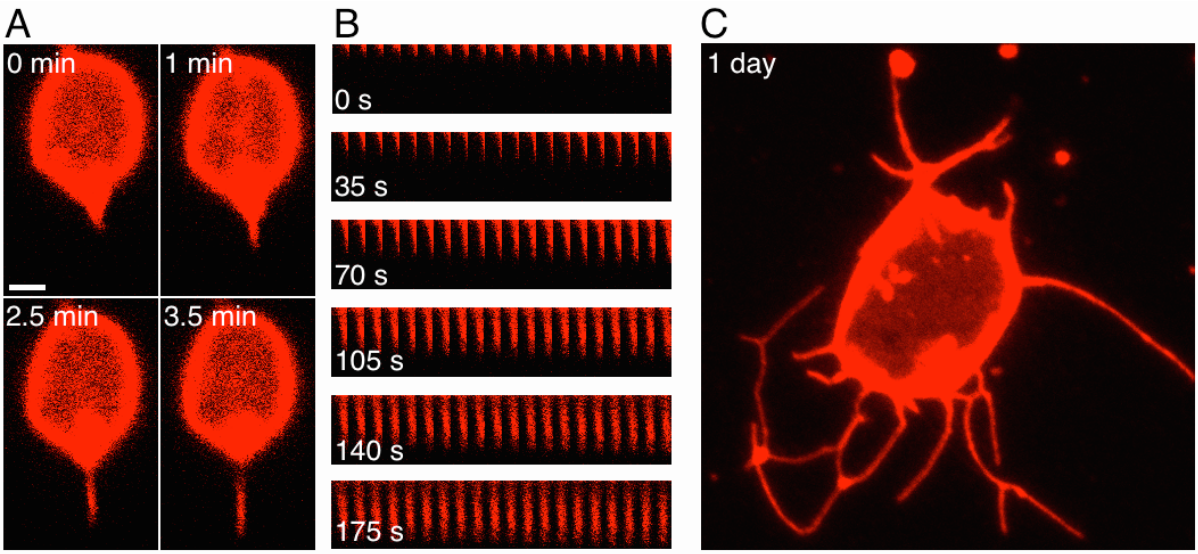

Figure 5.5.1: Kinesin motors pull tubules from brain extract GUVs. (A) Time lapse of tubule extrusion, with the start time taken within ten minutes of injecting GUVs. Scale bar: 2 μm. (B) Kymogram (split into six lines, with each line indicating the time of the first image), showing the growth of the tubule in the GUV in A. The total vertical length in each segment is 3.55 μm. (C) Another example with many extruded tubules, taken the day following the experiment. The chamber was sealed with putty sealant and kept in the fridge overnight. In all: fluorescence comes from labeled lipids.

be too tense. Furthermore, the oxidation of fluorescent labels induced by excessive fluorescence imaging inhibits kinesin, providing an additional technical constraint. From our experience, the most optimal conditions for observing tether extrusion by motors is to rapidly locate a vesicle deformed by pulling (usually shaped like a rugby ball) and conduct imaging at the lowest laser power that provides sufficient contrast. Then we start the experiment over in a different chamber.

First, we tested the viability of the assay in the absence of BAR proteins. We added the kinesin motors to the polymerized microtubules, introduced the motility buffer and, minutes after, we added the freshly collected GUVs (at ~ 20% total volume of the chamber). We let the vesicles sediment for a minute then started imaging. **We confirmed that kinesin successfully extract tubules from brain extract vesicles.** Figure 5.5.1, A and B shows the dynamics of tubule extrusion from a GUV within 10 minutes after injecting the vesicles into the chamber. In that example, the tubule ceased to grow after 3.5 minutes. We also confirmed the kinesin activity by imaging the chamber after ~ 30 min (up to the following day), where we observed many tubules extruded from many vesicles (such as represented in Fig. 5.5.1, C). Hence, our model membrane is viable for the molecular motor assay.

Next, we introduced endophilin A2 into the system. Again, the challenging part was timing the injection of the protein. In the experiments, we first mixed the kinesin with the microtubules and the motility buffer, as before, introduced GUVs minutes thereafter. After letting sediment for one minute, we injected endophilin A2 (20% of the total chamber volume, at concentration 8 μM, setting the total bulk concentration at ~ 3 μM). **As a result, we observed the fission of tubules mediated by kinesin.** Figure 5.5.2 shows three experiments where we observed fission after the binding of endophilin (indicated by the strong fluorescence signal) on motor-induced growing tubules. Due to technical challenges of the experiment, the fission events were not readily (and easily) observed, however they were reproducible.[7]

Working with Jean-Baptiste Manneville, we carried out further confirmation of fission of motor-pulled tubules by quantifying the frequency and morphological characteristics of tubules after 30 minutes of reaction time, in a similar way as we have done for *in vivo* experiments shown in Fig. 5.1.1. Similarly to cells in which the activity of endophilin A2 was perturbed, we observed an appreciable decrease in the the number of GUVs when endophilin was present (Fig. 5.5.3, top). In particular, approximately half the vesicles showed tubulation and each tubulated vesicle only had about half the number of tubules than the control (Fig. 5.5.3, bottom). Moreover, the length of pulled tubules was almost half the value in the absence of the protein. All

[7] I am grateful to Jean-Baptiste Manneville who taught me the motor assay and for collecting important data after my departure from Paris. In particular, he contributed to data shown in Fig. 5.5.2 (center and bottom) and Fig. 5.5.3.

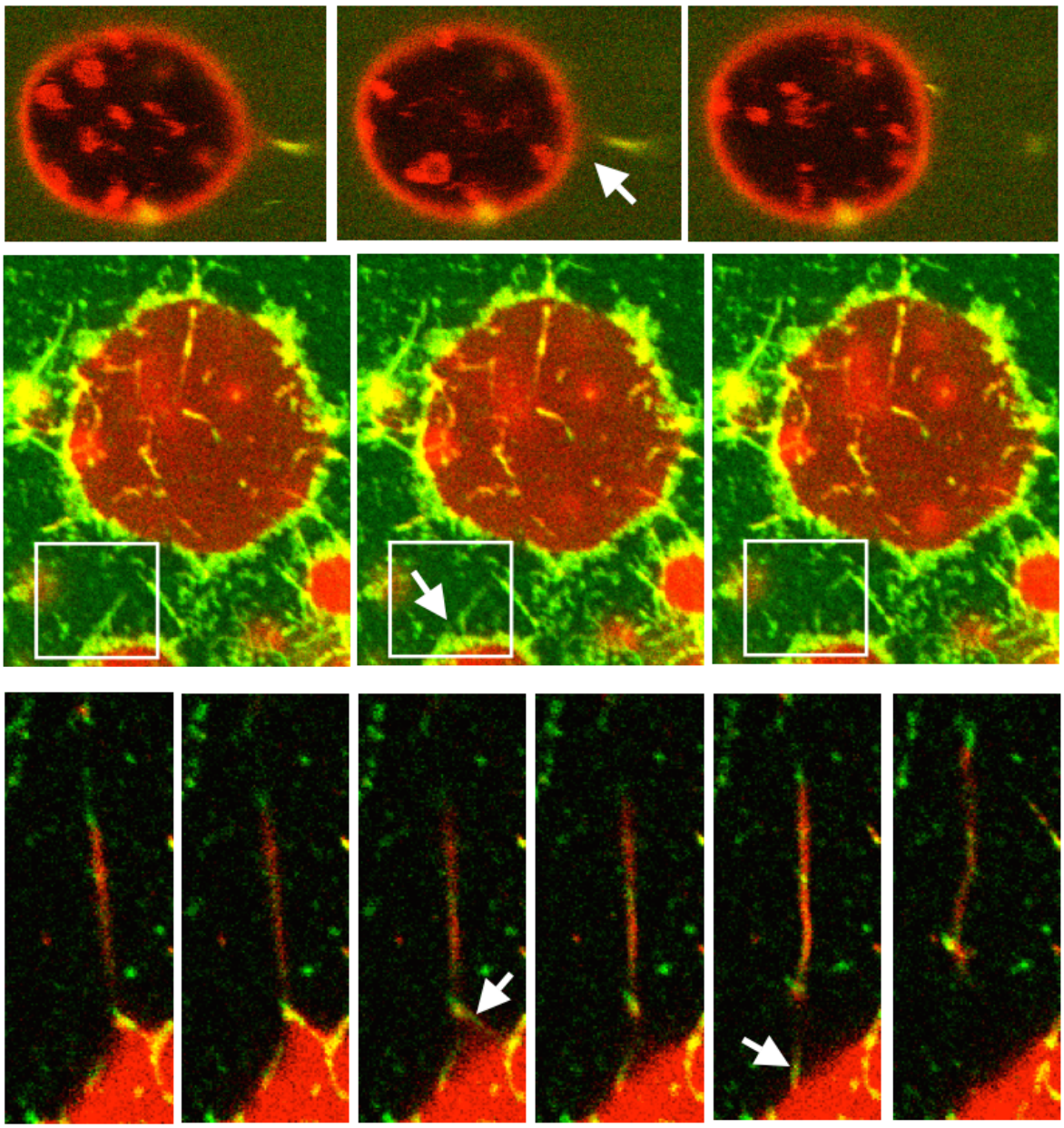

Figure 5.5.2: Fission of tubules mediated by kinesin observed in time. Shown are time lapse images of three different experiments. Arrows point to fission locations just prior to break. Third example shows two breakage events of a branched tubule. Overlaid fluorescence of lipid label (red) and protein label (green). Center and bottom images were contributed by Jean-Baptiste Manneville.

of these results indicate that endophilin induces membrane fission. Interestingly, we also observed fewer branches, likely indicating that tubules broke from networks and not just from the GUVs.

Let us clarify the apparent inconsistency in the observation that endophilin induces reduction of tubules, when BAR proteins are known and well demonstrated to induce spontaneous tubulation, including in this thesis. Note, tubules induced by endophilin, and other BAR proteins, are short, floppy and they usually cease to grow

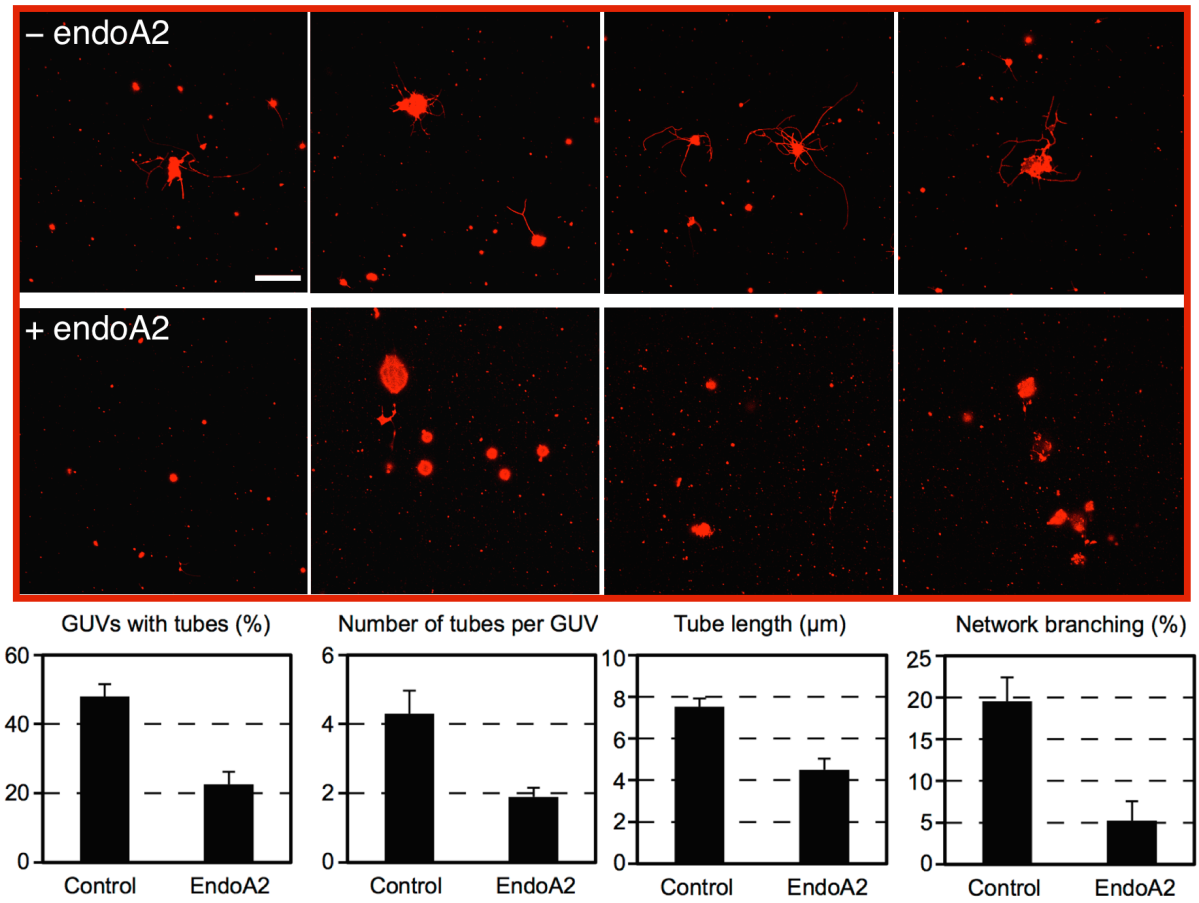

Figure 5.5.3: Steady-state observations of membrane fission mediated by kinesin and endophilin. Shown are representative images of vesicles in the presence of kinesin and ATP without endophilin A2 (− endoA2) and in the presence of 2.5 μm endophilin A2 (+ endoA2). Fluorescence comes from labeled lipids. Scale bar: 20 μm. Plots show quantification of the frequency and morphological characteristics of tubules in the control (kinesin + ATP) and in the presence of endophilin A2 (kinesin + ATP + endoA2). Observations taken after 30 min of reaction time. Contributed by Jean-Baptiste Manneville.

after about a minute (Fig. 4.2.1). By contrast, tubules pulled by kinesin are long, they follow the polymerized microtubules, thus usually crawl on the surface, and they appear tense since they are anchored to a moving motor (Fig. 5.5.1). Therefore, although endophilin spontaneously forms tubules, likely contributing to our measured residual tubulation (Fig. 5.5.3, bottom), such tubules do not preclude us to conclude that endophilin induced fission of kinesin-pulled tubules. Our steady-state quantification of membrane tubules, as done in Fig. 5.5.3, has been done in an equivalent way in cell experiments by our collaborators (Section 5.1).

We conclude that molecular motors have sufficient pulling force to induce fission of membrane tubules scaffolded by BAR proteins.

5.6. The role of protein subdomains in fission of scaffolded tubules

Are amphipathic helices crucial in fission mediated by protein scaffolds? We have already demonstrated that they are not key in forming scaffolds, although they are important for the binding and quantitatively influencing membrane remodeling (see Chapter 4). We tested the two endophilin mutants used in Chapter 4: 1), the N-terminal-helix-deletion mutant, and 2), the stronger binder via the BAR domain (i.e, E37K, D41K). Both mutants were able to mediate fission by external pulling force. To specify, we observed 6 fission events for the truncation mutant (N = 6) and 12 fission events for the stronger binder (N = 13, in the negative case, the bead was ejected). Moreover, the stronger binding mutant generated a higher force increase when pulled at the same rate as the wild type, whereas the truncation mutant induced a significantly lower force increase (Fig. 5.6.1, A). The data on the truncation mutant is limited as it was very difficult to recruit the protein to the membrane, especially in the scaffolding regime.

Likely, the adhesion strength of the protein scaffold on the tubule affected the friction coefficient and thus it increased the breakage force. Along the same lines, removing the insertion module, significantly decreased the force generated by pulling, as the friction between the scaffold and the underlying lipids is in that case much lower. An important conclusion from these experiments is that **amphipathic helices are not required to induce dynamic fission**, but they significantly contribute to the fission force. These experiments also demonstrate that the key prerequisite is the formation of a scaffold.

To test the specificity of endophilin in this mechanism, we tested two other proteins, as in Chapter 4, β2 centaurin and epsin 1. We observed five fission events for the scaffold formed by β2 centaurin (N = 8, in the three negative cases the bead was ejected from the trap) (Fig. 5.6.1, B, left). As a reminder from Chapter 4, we could not confirm that epsin 1 forms a rigid scaffold as the radius of the tubule—albeit affected—was not completely independent of the vesicle tension. Nevertheless, epsin-coated tubules also promoted fission by elongation. Specifically, we observed 4 fission events (N = 7, in two negative cases the bead was ejected). In the case of epsin, we only counted the cases where we observed the decrease in the force upon injection, as there was no fluorescent label on the protein. Interestingly, in some cases (for both proteins), we observed the formation of faint tubular segments prior to fission just like with endophilin (see Fig. 5.6.1, B, top right image).

In the tested range of pulling rates (~ 0.5 μm/s), β2 centaurin and epsin 1 had a comparable magnitude of force increase, which was somewhat lower than for endophilin A2. Precisely, the average ΔF for β2 centaurin and epsin 1, respectively, were 20±8 pN and 21±6 pN (at average pulling rates of 0.4±0.08 μm s^{-1} and 0.5±0.01 μm s^{-1}, N = 3 in both cases). Compare with a somewhat higher value of 31±1 pN for

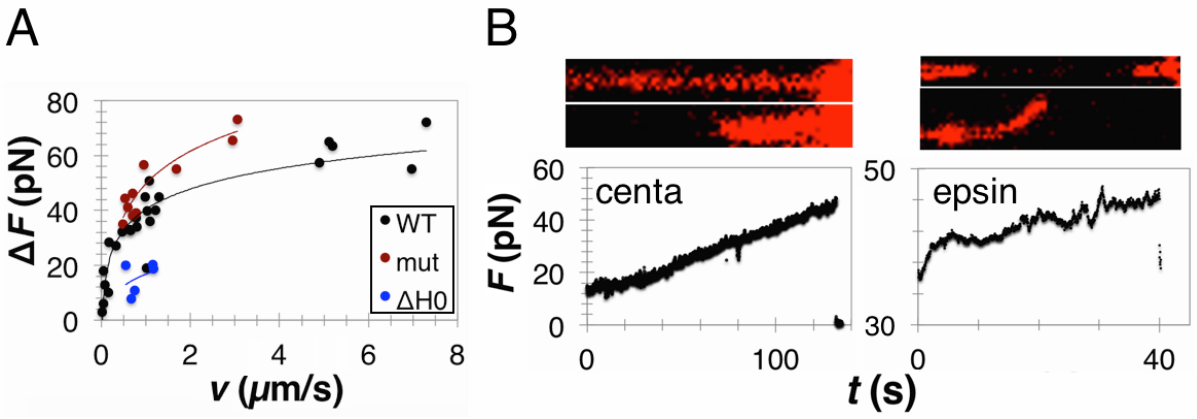

Figure 5.6.1: The influence of subdomains on membrane fission by BAR proteins. (A) Magnitude of force increase at fission at a given pulling rate is different for different endoA2 mutants. WT = wild type, mut = E37K, D41K (stronger binding to the membrane), ΔH0 = endoA2 with truncated N-terminal helices. The lines are added through the points to guide the eye. (B) Dynamic fission induced by left: β2 centaurin (centa), at v = 0.5 μm/s, σ = 0.04 mN/m, ΔF = 32 pN, and right: epsin 1, at v = 0.5 μm/s, σ = 0.01 mN/m, ΔF = 11 pN.

endophilin A2 in the same range of puling rates (0.5±0.1 μm/s, N = 5). Interestingly, the time required for fission (in the same range of pulling rates) is significantly longer for β2 centaurin (92±30 s) and epsin 1 (101±41 s), as compared to endophilin A2 (25±11 s). The shorter time of fission by endophilin is likely because in the case of endophilin the tubules start from a much lower radius.

5.7. The proposed mechanism and biological implications

We propose the following mechanism of pulling-force-induced fission. Once proteins form a scaffold, they impede the movement of lipids between the tubule and the membrane reservoir (GUV or, in the case of cells, the plasma membrane). This decoupling gives rise to local membrane tension in the tubule. Pulling the tubule results in the increase in force, as a consequence of friction between the scaffold and the underlying lipids. At the same time, there is an increase in tension of the tubule, leading to its constriction and, ultimately, fission. Fission could either be due to the formation of a hemifission state or, alternatively, pores that, stabilized by the proteins, nucleate until they become large enough to break the membrane.

Based on our experiments, the mechanism appears generic and the key prerequisite is the formation of a scaffold. However, endophilin seems especially tuned, as it generates very high spontaneous curvature, strongly constricts the tubule to a consistently low radius, and seems to very efficiently inhibit lipid diffusion. The combined effect is priming the membrane tubule for fission. Although we have observed fission with other proteins, such as the BAR protein centaurin and the ENTH

domain protein epsin, the timescales at which they operate are likely too slow to be relevant for the fast clathrin-independent endocytic pathways.

We are still tasked to devise a physical model that can quantitatively explain our data; namely, the square-root scaling of breakage force and pulling rate. In addition, we are left to understand the dependence of the breakage time on a), pulling rate and b), membrane tension. This work is currently underway by our collaborators Jacques Prost (Institut Curie) and Andrew-Callan Jones (Paris 7).

The most exciting prospect of our results is the discovery that molecular motors possess the sufficient pulling force to break a membrane tubule. This finding opens novel routes for future investigation, as there could be many unexplored mechanism in the cell that involve molecular motors and curvature-generating proteins. Moreover, the fast nature of endophilin-mediated endocytosis is most likely a result of the very generic mechanism of membrane fission, potentially caused by several different protein modules. By contrast, clathrin-mediated endocytosis heavily relies on the recruitment of dynamin to complete the process. We hope our results will inspire future work in this direction. For example, the next step is testing the influence of the lipid composition. We hypothesize that endophilin scaffold will impede the diffusion of some lipids less efficiently than of others. Recent work has shown that BAR proteins induce the clustering of PIP_2 on flat (Zhao et al., 2013) and tubular membranes (Picas et al., 2014). PIP_2 sequestration could have important dynamic consequences on the fission process. We also predict that, in the course of tubule elongation, there could be rearrangement of lipids. If the composition contains lipids of different tail lengths and saturation, a rearrangement can create domains with a mismatch in elastic properties, which, as theoretically predicted (Chen et al., 1997), would further promote tubule fission.

6. Sensing curved membranes at low protein densities

Previous two chapters discussed cases in which BAR proteins formed a rigid scaffold on membrane tubules, imparting a strong morphological and mechanical effect. We have also seen in Chapter 5 that in the course of scaffold formation, endophilin and β2 centaurin are enriched on membrane tubules compared to the quasi-flat surfaces of the vesicles, giving first indication that these proteins sense membrane curvature. By using the same tether-pulling assay, recent studies have demonstrated the curvature-sensing capability of several BAR proteins, which include: N-BAR proteins endophilin A1 (Zhu et al., 2012), amphiphysin (Heinrich et al., 2010; Sorre et al., 2012), and BIN1 (Wu et al., 2014); F-BAR protein syndapin 1 (Ramesh et al., 2013); and I-BAR protein IRSp53 (Prévost et al, unpublished results). A contradictory study hypothesized that the BAR domain itself is not responsible for sensing of curvature, despite its crescent shape (Bhatia et al., 2010; Bhatia et al., 2009). The assay of that study is based on imaging a large number of tethered small vesicles at the same time then correlating the size of each vesicle with the fluorescence intensity of bound proteins. The assay showed an enrichment in the bound protein for all tested BAR proteins that were either known to contain an amphipathic helix or the authors suspected might have insertion motifs. Curiously, they found no quantitative difference in the magnitude of enrichment between very different BAR proteins: endophilin (N-BAR), FCHo2 (F-BAR) and MIM (I-BAR), concluding that their BAR domain does not influence curvature sensing. Disrupting amphipathic helices seemed to have eliminated the curvature sensing power of BAR proteins. They also did not detect enrichment of IRSp53 (I-BAR without amphipathic helices) on positively curved vesicles (Bhatia et al., 2009).

However, they find β2 centaurin, a BAR protein without amphipathic helices, to be enriched on smaller vesicles, in contradiction to their own hypothesis. The authors attempt to reconcile this observation with a possibility that centaurin has a putative amphipathic helix. This prediction is inconsistent with a subsequent structural study of β1 centaurin where the only insertion motif was attributed to a very small loop belonging to the PH domain (Pang et al., 2014). Interestingly, the PH domain itself does not display curvature-sensing properties (Bhatia et al., 2009; Peter et al., 2004), keeping the mystery around this issue. The aim of this chapter is to quantify curvature sensing by β2 centaurin, as a member of the classical BAR domain family, and explore the mechanical effect of this protein under conditions where it does not form a scaffold.

6.1. BAR proteins sense tubular membrane curvature regardless of amphipathic helices

We tested the behavior of proteins under conditions where they do not form a rigid scaffold on the tubule, which is achieved by injecting the protein at lower bulk concentration (0.1–1 μM). According to a previous study, the formation of a scaffold by an N-BAR protein amphiphysin is triggered when its density on the vesicle exceeds ~ 1000 μm^{-2} (Sorre et al., 2012). We have demonstrated a similar density-dependent behavior for both endophilin A2 and β2 centaurin in Chapter 4, although recall there are cases in which very little density on the vesicle led to the formation of a rigid scaffold. Clearly, both proteins are potent sensors of membrane curvature.

First, let us test whether β2 centaurin displays curvature sensing power at low bound densities and if it gets sorted as observed with N-BAR, F-BAR, and I-BAR proteins. Figure 6.1.1. shows an example of β2 centaurin, along with an example of endophilin A2—which is expected to sort—demonstrating that centaurin indeed gets enriched on highly curved membranes. We quantified the enrichment as the relative ratio of the fluorescence intensities of the protein on the tubule compared to the

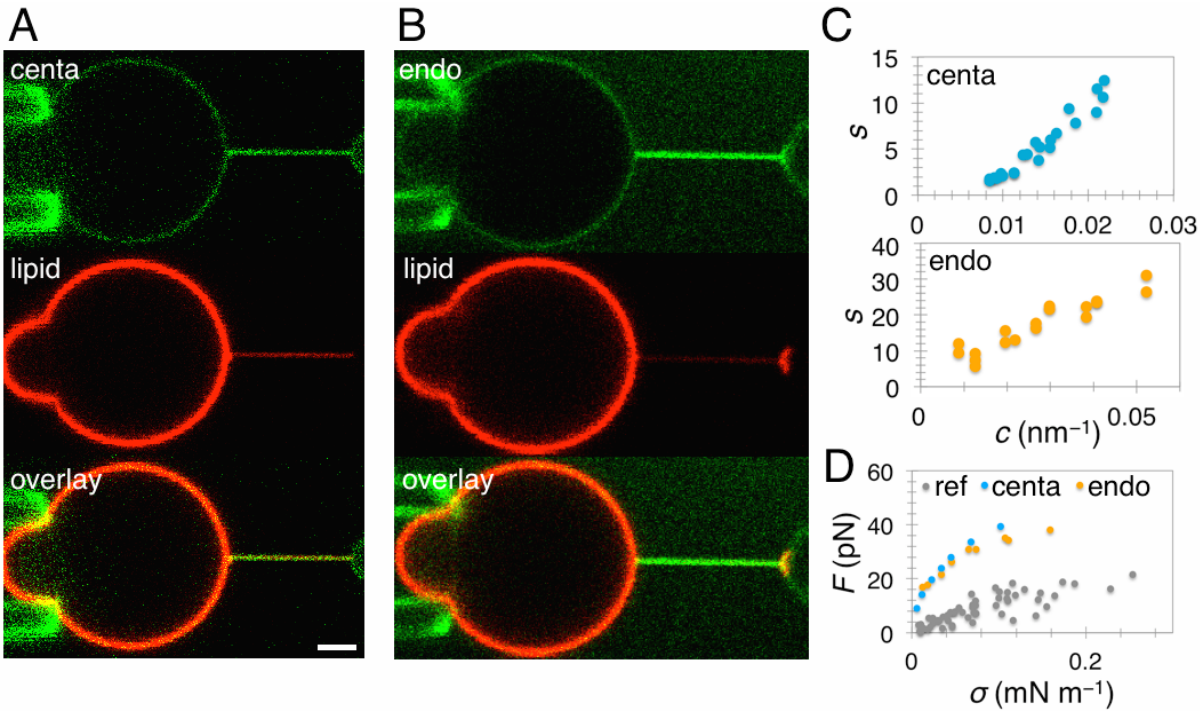

Figure 6.1.1: BAR proteins are sorted on curved membranes. An example with (A) β2 centaurin (centa) and (B) the N-BAR of endophilin A2 (endo) under the regime where they do not form a scaffold. Scale bar: 2 μm. (C) Sorting coefficient (s) as a function of membrane curvature (c), which is calculated from lipid fluorescence. (D) Tether-retraction force (F) as a function of membrane tension (σ), comparing the cases in A, B, and C to the measured force in the presence of the scaffold (ref). Reference shows scaffolds from both endophilin and centaurin.

vesicle, normalized by the fluorescence of lipids, otherwise known as the **sorting coefficient**:

$$s = \frac{I_{\mathrm{p,t}} / I_{\mathrm{p,ves}}}{I_{\mathrm{l,t}} / I_{\mathrm{l,ves}}}. \qquad \text{(Eq. 6.1.1)}$$

I is the fluorescence intensity while subscripts p, l, t, and ves represent, respectively, protein, lipid, tubule and vesicle. We observed that both proteins get progressively more enriched with increased curvature of the tubule (Fig. 6.6.1, C). To confirm that we are not observing a regime under which a scaffold forms, we compared the force at a given membrane tension for the two displayed cases and the scaffolding regime from Chapter 5 (grey dots). Evidently, the force is appreciably higher and it clearly has a different scaling with respect to membrane tension (Fig. 6.1.1, D). Recall from Chapter 4 that in the presence of a scaffold, the force becomes linearly dependent on tension.

Next, we quantified the sorting coefficient for all cases of low-density binding of β2 centaurin. Importantly, as we have mentioned previously, it is imprecise to compare experiments according to the concentration of the protein in the surrounding medium as not every vesicle will have identical composition, and hence the same amount of bound protein. The strength of our assay, compared to steady-state observations of many small vesicles at a time, is that we can compare our results based on the bound protein density. We binned the sorting coefficient data into different vesicle-bound regimes. We find that the magnitude of sorting is inversely proportional to the protein density on the vesicle, which is consistent with studies of other BAR proteins (Fig. 6.1.2, A).

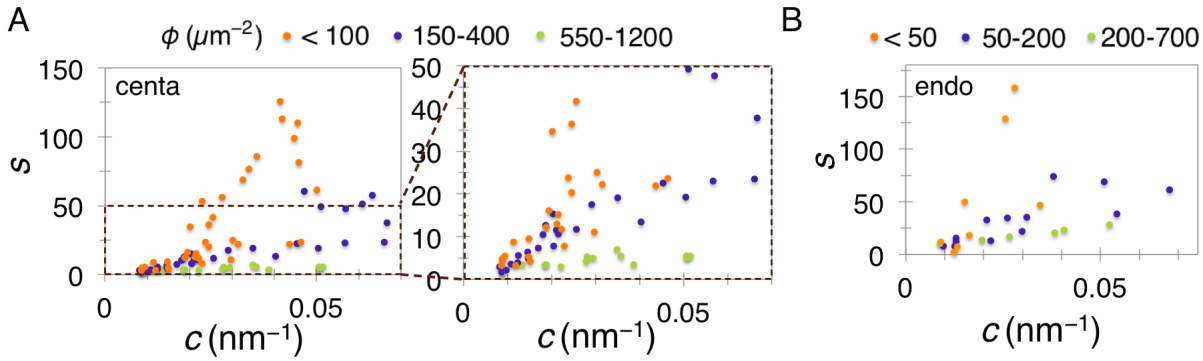

Figure 6.1.2: Magnitude of sorting depends inversely on protein bound density. Sorting coefficient of (A) β2 centaurin (centa) and (B) the N-BAR of endophilin A2 (endo) as a function of tubule curvature (measured from labeled lipid fluorescence). Data points are binned based on the protein density on the vesicle. Total number of independent experiments: $N = 16$ (A) and $N = 4$ (B).

Previously, two sorting regimes were found for endophilin A1 which differed based on the bulk protein concentration (Zhu et al., 2012). Recently, a quantitative relationship was established between the bound density of IRSp53 and its sorting on the tubule (Prévost et al, unpublished results), displaying similar qualitative dependence as we observe for centaurin. We repeated the same quantification of sorting for endophilin A2 and also found that the sorting coefficient inversely correlates with the bound density (Fig. 6.1.2, B). We warn the reader that for densities below 100 μm^{-2}, there is very low signal-to-noise ratio in the fluorescence intensity on the vesicle, hence the sorting coefficient may be highly uncertain.

Based on these results, it appears that proteins with a classical BAR domain, namely β2 centaurin, also get sorted on membrane curvature. This observation is in line with the observed sorting of centaurin on small vesicles (Bhatia et al., 2009). Considering that centaurin BAR domain does not have amphipathic helices, we conclude that **amphipathic helices are not required for sensing of membrane curvature nor for sorting**. That said, we point out that the work by Stamou and coworkers shows that endophilin with a mutation in the N-terminal helix does not get enriched on smaller vesicles (Bhatia et al., 2009). Unfortunately, despite laborious attempts, synthesizing endophilin A2 without the N-terminal helix was extremely challenging and we were ultimately unsuccessful in producing a fluorescently labeled protein. Nevertheless, we have shown in Chapter 4 that the deletion mutant still forms a scaffold on the membrane, strongly constricting the tubule underneath. We posit that such a formation would require the protein to first act as a curvature sensor, so to get strongly enriched on the tubule. Granted, endophilin still has small amphipathic helices at the center of the membrane-BAR interface, which could contribute to sensing. Therefore, we cannot make a strong conclusion based on experiments on endophilin alone.

We also note that it has been shown with electron paramagnetic resonance that the BAR domain in N-BAR proteins strongly interacts with tubular membranes (Ambroso et al., 2014), substantiating our hypothesis. Moreover, I-BAR protein IRSp53, that does not carry any amphipathic helices, gets sorted on (negative) membrane curvature (Prévost et al, unpublished results). The same study shows that an I-BAR protein ABBA, which contains an N-terminal amphipathic helix, may also sense positive in addition to negative curvature, albeit weakly (Coline Prévost, PhD thesis, Paris). Finally, we remind the reader that epsin, a protein that binds to the membrane solely via an amphipathic helix, also gets enriched on membrane tubules (Capraro et al., 2010).

The BAR domain binds stronger to tubular curvature likely as the shape of the protein permits more interaction with the curved membrane. Along the same lines, BAR domain should then sense spherical curvature much less than tubular, if

at all. Unlike BAR domains, amphipathic helices sense lipid packing defects, which are known to increase in curved membranes (Cui et al., 2011), both spherical and tubular. This hypothesis could explain the reason why mutating the N-terminal amphipathic helix in endophilin significantly diminishes its enrichment on small vesicles (Bhatia et al., 2009). We cannot rule out the possibility that single-point mutations in the helix may induce some other pathological behavior, such as aggregation, misfolding, protein docking geometry, or conformational change, which would alter its binding power to the membrane. **Taken together, we propose that the BAR domain and amphipathic helices both contribute to the curvature sensing power of BAR domain proteins. At least one of the two modules is required, but neither is essential.**

6.2. Membrane mechanics at low protein density

We saw in Chapter 4 that the scaling behavior of both endophilin and centaurin when forming a scaffold are consistent with previously developed model, however the quantitative discrepancy between the radius measurement and the model prediction demands a more rigorous approach. Before such model becomes available, let us test our data against two recent thermodynamic models, developed by Andrew Callan-Jones (Paris 7) for the study of IRSp53 (Prévost et al, unpublished results) and amphiphysin (Sorre et al., 2012). The full Hamiltonian of the tubule, F_t, can be written as:

$$F_t = 2\pi RL\left[\frac{1}{2}\kappa_m c^2 + \frac{1}{2}\bar{\kappa}\phi_t\left(c - \left|c_p\right|\right)^2 + f_s + f_m\right], \qquad \text{(Eq. 6.2.1)}$$

where L and R are the length and radius of the tubule, respectively, c is the curvature of the tubule, c_p is the intrinsic curvature of the protein, κ_m is the bending modulus of the bare membrane, $\bar{\kappa}$ is the elastic constant conjugate to the energy penalty of having a mismatch between membrane curvature and c_p, and ϕ_t is the protein density on the tubule. We warn the reader that we often report ϕ values in reciprocal square nanometers, however in all expressions they are used as areal fractions (taking the maximum coverage to be 20 000 μm^{-2}). Finally, f_s and f_m are free energy contributions due to, respectively, in-plane stretching and protein mixing entropy, whose expressions are detailed in (Prévost et al, unpublished results). These terms depend on the lipid and the protein density allowing us to relate protein bound density with membrane curvature. The solution to the full expression is too complex to be found analytically, but in the limit of low protein density on the vesicle, it simplifies to:

$$\frac{\phi_t}{\phi_{ves}} \approx \exp\left[\frac{\bar{\kappa} A_p}{k_B T}\left(c|c_p| - \frac{1}{2}c^2\right)\right]. \quad \text{(Eq. 6.2.2)}$$

ϕ_{ves} is the protein density on the vesicle, A_p is the area of the protein (~ 50 nm^2). The ratio of the protein on the tubule and the vesicle is essentially the sorting coefficient, experimentally determined by using Eq. 6.1.1. Interestingly, this equation predicts a non-monotonous dependence of sorting on membrane curvature. In other words, BAR proteins will become more and more enriched as curvature is increased, but up until a point. Beyond this optimal curvature (c_p), proteins desorb from the tubule. Indeed, experiments on IRSp53 clearly show this behavior (Prévost et al, unpublished results). In the case of centaurin, we also observed a reduction in the tubule concentration at tubule curvatures > 0.04 nm^{-1}. However, the sorting coefficient measured for centaurin is very high—approximately six times higher than for amphiphysin (Sorre et al., 2012) and four times higher than IRSp53 at the same density and tubule radius. Hence, it is possible that with increasing curvature, we cross into a higher density regime. We note that in the low-density cases where we reached high enough curvatures, the difference between the maximum and minimum protein density on the vesicle is ~ 25%. For this reason, we do not bin the results based on individual vesicles; rather, we separate the data based on the measured protein density on the vesicle. Interestingly, the earlier of the two models predicts a linear dependence of sorting on curvature and it fit very well in the case of amphiphysin. It turns out that in the case of protein scaffolds that constrict the tubule to a narrow radius, the left branch of the non-monotonous function (Gaussian) is almost linear. If we revisit Fig. 6.1.1, it indeed appears that the sorting for endophilin (panel C, bottom) may indeed be approximated with a linear function, whereas for centaurin it cannot. Therefore, for sorting data, we used the more recent model.

We binned the data, according to protein density on the vesicle, into four groups: 1), 65±18 μm^{-2} (~ 0.5%), 2), 165±40 μm^{-2} (~ 1%), 3), 450±90 μm^{-2} (~ 2.5%), and 4), 900±260 μm^{-2} (~ 5%). Fitting Eq. 6.2.2 to our sorting data yields values for the two free parameters: C_p and $\bar{\kappa}$. For C_p we obtain: 1), 0.043±0.003 nm^{-1}, 2), 0.054±0.004 nm^{-1}, 3), 0.048±0.017 nm^{-1}, 4) 0.042±0.003 nm^{-1}, while for $\bar{\kappa}$ fitting gives: 1), 21.8±2.9 k_BT, 2), 12.6±1.7 k_BT, 3), 12.4±7.6 k_BT, 4), 9.5±1.4 k_BT (Fig. 6.2.1). Finally, we average these parameters for the four different densities, yielding: c_p = 0.047±0.006 nm^{-1}, corresponding to the intrinsic radius of curvature of 21 nm. This radius is three times greater than the intrinsic radius of curvature measured for amphiphysin (Sorre et al., 2012), which is consistent with the four times larger radius of scaffolded tubules imposed by centaurin. Averaging $\bar{\kappa}$ over four different measurements gives 14.1±5.3 k_BT.

There is no clear way to simplify in analytical terms the dependence of force on the protein bound density from Eq. 6.2.1. Therefore, we use the expression de-

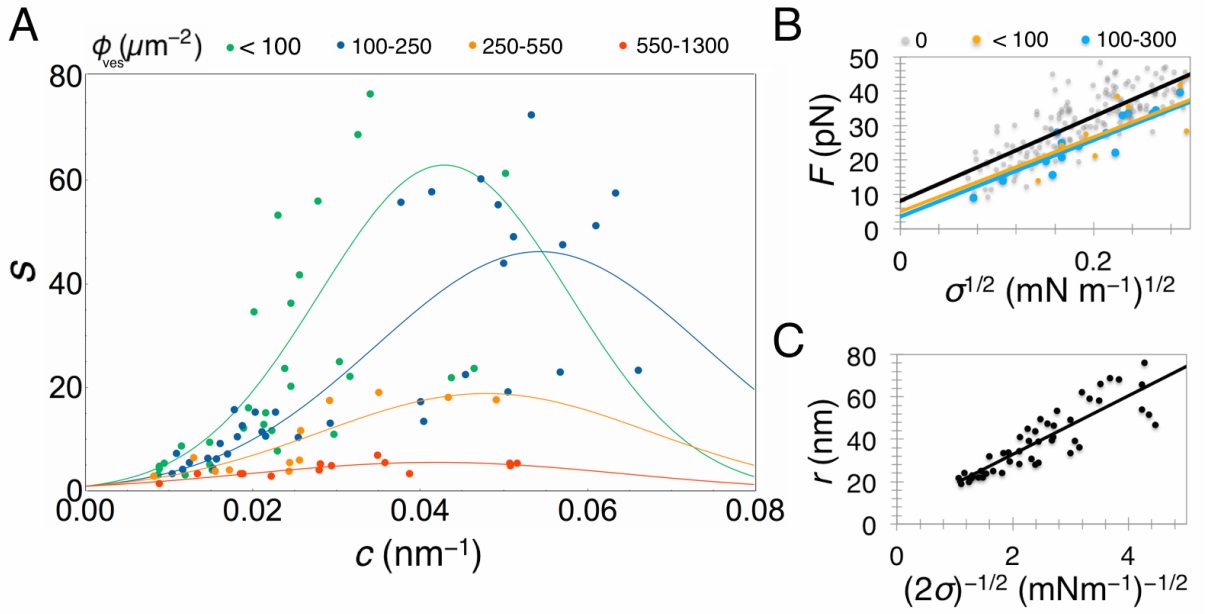

Figure 6.2.1: Mechanics of the membrane at low density of β2 centaurin. (A) Sorting coefficient, *s*, as a function of tubule curvature (*c*). Lines represent fitting of Eq. 6.2.2 to data from a total of 16 experiments. Fitting parameters are written in the text. (B) Low protein density induces a decrease in force (*F*) at the same membrane tension (σ), compared to the bare membrane. Lines represent fitting of Eq. 6.2.3 to data from a total of 10 experiments. (C) Fitting Eq. 6.2.5 to data derived from a total of 10 experiments with $\phi_{ves} < 300$ μm^{-2}. Tubule radius, *r*, measured from lipid label fluorescence.

rived in the study of amphiphysin (Sorre et al., 2012). There, it has been shown that under low protein density, the force depends on the square root of membrane tension, with an offset that increases with protein bound density, i.e.,

$$F = 2\pi\sqrt{2\kappa_{\text{eff}}\sigma} + F_0\,, \qquad \text{(Eq. 6.2.3)}$$

$$F_0 = F_{0,\text{b}} - 2\pi\kappa c_{\text{p}}\phi_{\text{ves}}\,. \qquad \text{(Eq. 6.2.4)}$$

Note, here we have manually inserted $F_{0,\text{b}}$ as the offset in force measured for the bare membrane (see Chapter 5), κ_{eff} is the effective bending modulus, not precisely the same measure as in Eq. 6.2.2. Clearly, even the low-density presence of the protein on the vesicle will change the offset in the force, and it should be linear with increased $\phi_{ves} > 0$. Indeed, plotting the force for the same cases as above reveals that the force decreases compared to the bare membrane (Fig. 6.2.1, B). Fitting Eq. 6.2.3 to our data yields the difference in the force offset (relative to the bare membrane offset) of $\Delta F_0 = -3.1$ pN ($\phi_{ves} < 100$ μm^{-2}) and $\Delta F_0 = -4.6$ pN ($\phi_{ves} < 100$–300 μm^{-2}). We now calculate the average intrinsic curvature by using κ_{m} of the bare membrane measured from force in Chapter 4 (average from two independent measurements = 51.5 $k_{\text{B}}T$) and the measured force offset reduction. Plugging in Eq. 6.2.4 and averag-

ing the two values yields 0.39±0.11 μm^{-2}, corresponding to a radius of curvature of 2.6 nm. Note, this value is significantly lower than obtained in sorting measurement and certainly lower than the radius of the centaurin scaffold (~ 40 nm), indicating that this model does not capture a more complex behavior of centaurin, such as protein-protein interactions. It is also highly plausible that $F_{0,b}$ also depends on ϕ_{ves}.

We can also determine the intrinsic curvature of the protein from the tubule radius, independently of the force, as those are measured from the fluorescence intensity of lipids. We remind the reader, we cannot use the force measurements as the force is affected by protein binding. Fitting Eq. 6.2.5, derived in (Sorre et al., 2012):

$$R = \sqrt{\frac{\kappa_{eff}}{2\sigma}} \approx \sqrt{\frac{\kappa_m}{2\sigma}}\left(1 - \frac{A_p \kappa c_p^{\,2}}{k_B T}\phi_{ves}\right), \qquad \text{(Eq. 6.2.5)}$$

to our measurements of the tubule radius (for all cases $\phi_{ves} < 300$ μm^{-2}), gets $c_p \approx 0.04$ nm^{-1}, corresponding to radius of intrinsic curvature of 25 nm (Fig. 6.2.1). This value is in excellent agreement with data obtained from sorting.

The results presented in this chapter demonstrate well that a classical BAR domain, is both a strong sensor and a strong inducer of membrane curvature, despite not having amphipathic helices. We have also seen in Chapter 5 that this protein forms rigid scaffolds at sufficiently high densities, equivalently to N-BAR proteins. To corroborate this conclusion, we measured the force imposed by an N-terminal helix deletion mutant of endophilin A2. Unfortunately, as the mutant does not contain a fluorescent label, we cannot determine its bound density and hence the spontaneous curvature. Nevertheless, the reduction in the force (Fig. 6.2.2, A) and the change of slope when fitting Eq. 6.2.5 (Fig. 6.2.2, B) clearly show that this mutant

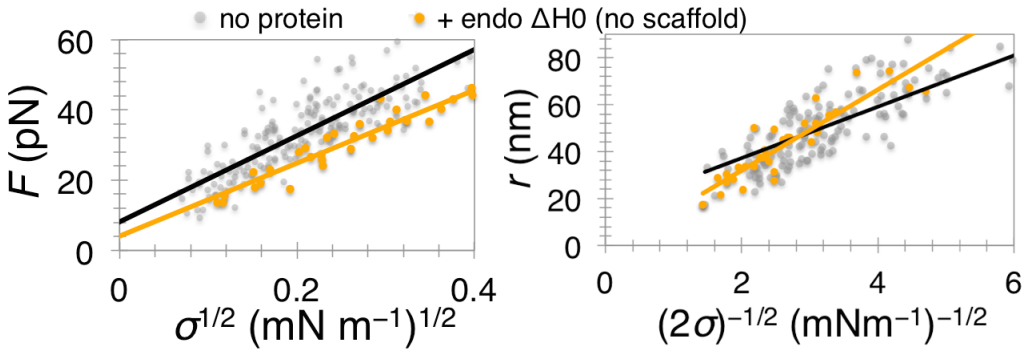

Figure 6.2.2: Endophilin A2 without amphipathic helices induces a mechanical effect at low density. Shown are measurements of the force (F) and tubule radius (r) as a function of membrane tension (σ) from six different experiments where we did not observe the formation of a scaffold based on clear tubule constriction. Fitting Eq. 6.2.3 yielded a −4.1 pN difference in offset from the bare membrane. Fitting Eq. 6.2.5 yields a slope of 17.2 nm (mN m^{-1})$^{1/2}$.

imposes (positive) spontaneous curvature, reaffirming the conclusions on the additive role of amphipathic helices made in Chapters 4 and 5.

7. Conclusions

Let us revisit the results of this thesis in its entirety and discuss the broader implications of our work. We will also propose directions for further research and methodology development. Considering that the two theses intertwine through a common biological problem, this chapter serves as a conclusion to both manuscripts.

The mechanism of membrane remodeling is deeply rooted in physics, which is why it equally fascinates biophysicists and biologists. The sheer scale of membrane-related phenomena demands a multiscale and a multidisciplinary approach. Why is that so? The protein-membrane interactions at the molecular scale usually have a profound and very long-range influence on the macroscopic morphology and the mechanics of the membrane. To access a fuller scope of protein-induced membrane remodeling, we combined various theoretical and experimental techniques.

The theoretical and simulation approach that I employed was based on the multiscale paradigm developed in the Voth group and specifically for studying protein-mediated membrane remodeling (Ayton and Voth, 2009). Figure 7.1.1 illustrates the modeling strategy in which the information from one resolution (level of theory) is passed into another. The model used in our CG MD simulations, the key simulation technique in this thesis, was derived from information obtained in atomic-level simulations (Fig. 7.1.1, left) (Ayton et al., 2010; Srivastava and Voth, 2013). Its high level of coarseness permits simulating very large systems, while keeping the quasi-molecular level of detail. This model significantly expanded the capabilities of MD techniques, allowing us to simulate vesicles big enough to be resolved by optical microscopy using reasonable computational power (Fig. 7.1.1, center). The information from CG simulations, combined with a variety of experimental observables (such as elastic constants), was used to parameterize the continuum-membrane model (Fig. 7.1.1, right). Such model, although operating at a similar length scale as the CG model, may access much larger time scales due to its less demanding computation.

The characteristic feature of our multiscale paradigm is the static passage of information from one resolution to another. That is, each level of theory is simulated on its own and the information obtained is used for a subsequent simulation at another level of theory. A more advanced approach envisioned for the future—and substantially more challenging—is to pass information on the fly. One possibility is to perform a multiresolution simulation, in which a small subset of the system is simulated at a higher resolution than the rest. This case is limited by the difficulty of correctly simulating the boundary between the two levels of resolution. Such approach has been very successful in connecting atomic with quantum-mechanical calculations (so-called QM-MM). Second approach is to carry out a number of time

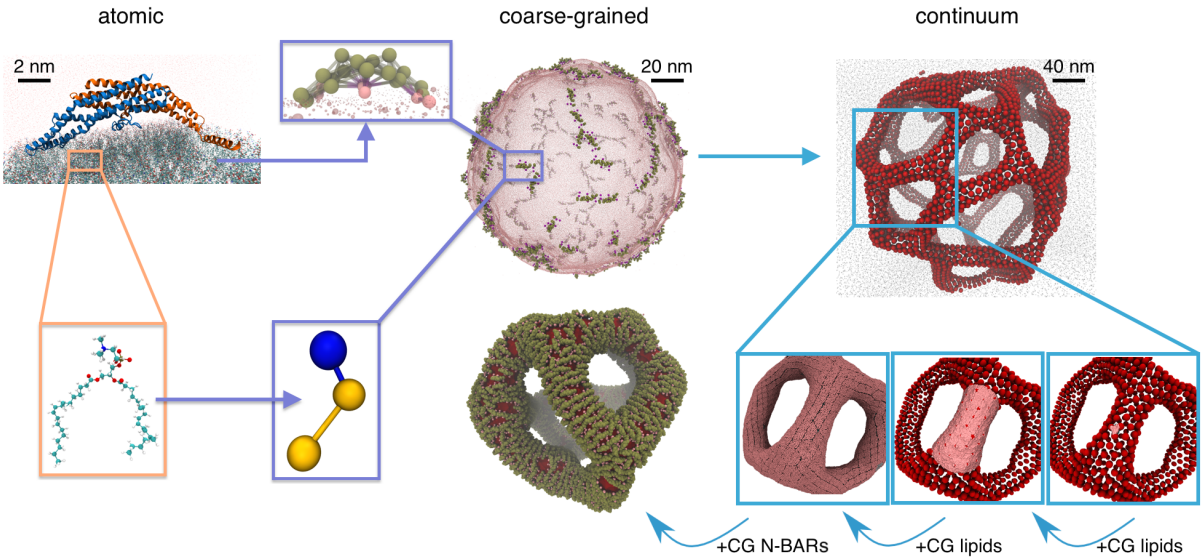

Figure 7.1.1: The multiscale simulation approach. Shown are three levels of resolution (theory): atomic (left), coarse-grained (center), and continuum (right), and the flow from one simulation to the other. Atomic simulations provide interaction parameters for the coarse-grained, which in turn help model the continuum model. Finally, via a reverse mapping procedure, the continuum simulation serves to create a starting configuration of a coarse-grained model.

steps at lower resolution, use the obtained information to build a higher-resolution system, simulate it for a number of steps then repeat. The difficulty here is in finding physical parameters that can correctly be passed between resolutions. In one project of this thesis, we used the latter approach by mapping the CG model onto a continuum model, essentially skipping the long time of equilibrating a reticular membrane (Fig. 7.1.1, right). We have only made one such pass across resolutions (from lower to higher). It would be highly valuable to devise a way to seamlessly switch between a CG and a continuum simulation.

BAR proteins control membrane-remodeling phenomena to ensure that they take place correctly and efficiently. An important issue in the field is understanding the underlying mechanism by which these proteins rapidly find one another on the membrane. Our CG MD simulations of large vesicles revealed that BAR proteins assemble into linear aggregates on the membrane. Such anisotropically ordered aggregation, as opposed to isotropic clustering, permits a much faster association of proteins from longer distances. Indeed, our free-energy calculations showed that the two BAR proteins see each other from a significant distance, ~ 10 times the distance of ionic interactions. Moreover, their membrane-mediated interaction strength is very high, on the order of 10 k_BT. Figure 7.1.2 demonstrates the self-assembly of N-BAR proteins and their coupling with membrane curvature.

Linear aggregation has been previously predicted using continuum and quasi-continuum models (Dommersnes and Fournier, 1999; Saric and Cacciuto, 2012),

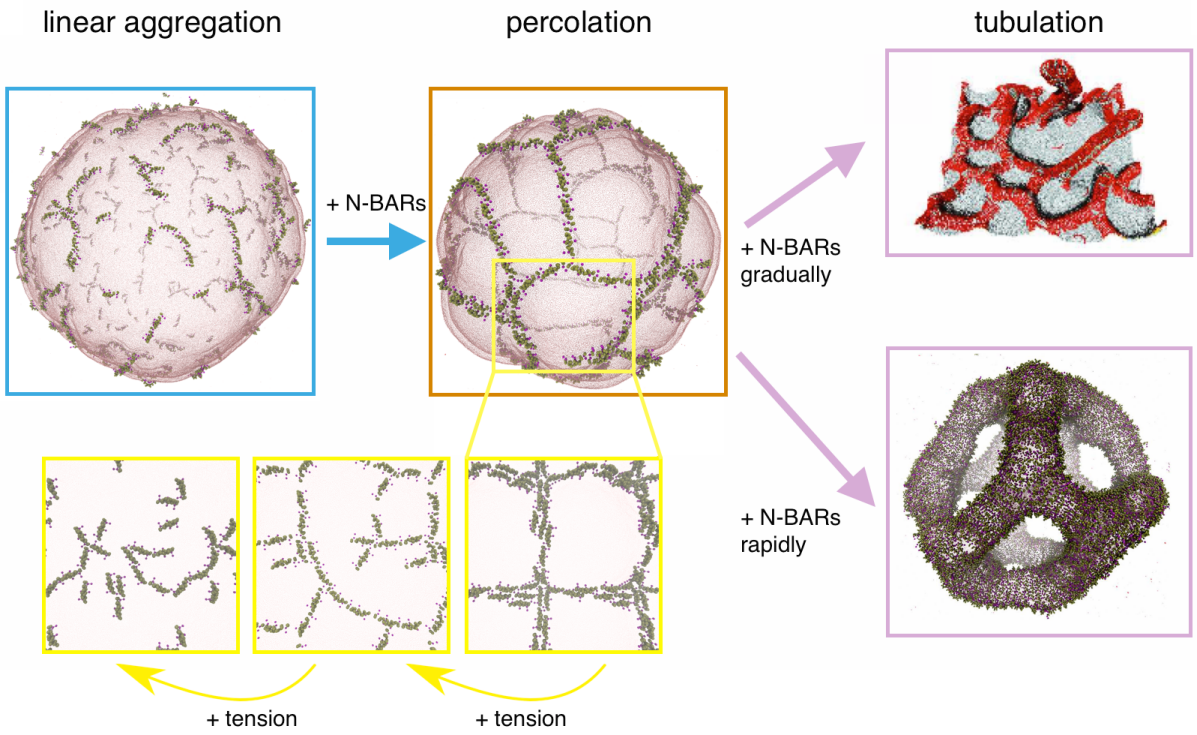

Figure 7.1.2: The assembly of N-BAR proteins and membrane reshaping. At low densities, proteins form linear aggregates (blue box). Further binding leads to meshing (green box). With further protein binding there is tubulation (purple boxes), either continuously and at long time scales (top, taken from (Noguchi, 2015)), or with breaking the bilayer topology with rapid adhesion of proteins to the membrane (bottom). Increasing membrane tension initially alters the mode of assembly then completely inhibits protein-protein interactions (yellow boxes).

where it was shown to be entirely driven by the underlying membrane as a consequence of anisotropic interactions. Our observations are in line with these predictions, as we see that the level of aggregation is dependent on the magnitude of imposed local curvature. Moreover, we measured a strong anisotropic curvature field near the protein. Interestingly, when starting from a flat membrane, we see proteins to readily aggregate in areas of negative curvature. On the first thought, this observation is contradictory with the well demonstrated fact that N-BAR proteins get enriched on areas of positive mean curvature. A closer inspection shows that N-BAR domains form a line of saddle-like (negative Gaussian) curvature, as is found at the neck of buds and tubules. Therefore, it seems that their alignment is well suited for the subsequent remodeling. In fact, our experiments, where we injected N-BAR proteins in the proximity of tubules extracted from GUVs, showed that in most cases the binding and scaffolding initiates from the neck of the tubule. Arguably, these findings indicate the curvature preference of N-BAR proteins.

We were never able to actually simulate the step in which tubules emerge from the surface for a simple reason — this process takes seconds, as confirmed by

experiments in this thesis. While it is difficult to calculate the actual time of a CG MD simulation, we estimate that the upper bound of our CG model is on the order of microseconds. A recent simulation study, using a quasi-continuum model, which can access much larger time scales, has demonstrated a mechanism by which the assembly of curved particles on the membrane can lead to tubule formation (Noguchi, 2015). Although there are some differences in the morphological transitions that they propose, it is exciting that they also observe linear aggregation and meshing as a common step prior to remodeling.

Self-association of N-BAR proteins largely depends on their bound density. We found that low protein densities (< 10%) will always lead to long strings of aggregates on tensionless membranes. Increasing protein density increases the distribution of dimerization angles and promotes the formation of meshes or networks. It turns out that the percolation density (i.e., the surface density of proteins at which a continuous network forms) is in the range of 10–15%. Curiously, in our experiments we find that the same vesicle-bound density of BAR proteins (3000 proteins μm^{-2}, or 15%) induces a change in the way membrane force scales with membrane tension. The change in scaling indicates that protein-protein interactions become significant at the macroscopic scale. We suspect that at percolating density, both protein and lipid mobility should be affected. Therefore, we propose an experiment of measuring lipid and protein diffusion with FRAP. To find the percolating density, BAR proteins would be gradually titrated on the supported lipid bilayer until, hypothetically, a change in mobility of one or both components would be observed. Again, a spherically or cylindrically curved surface may need to be crucial for the mesh formation.

Furthermore, we found that the protein association depends on membrane mechanics as well. Considering that the protein-protein interactions are driven by the underlying membrane, it is expected that increasing membrane tension will decrease the distance (λ) at which they see one another, simply based on the natural length scale of the membrane, $\lambda = \sqrt{\kappa_m / \sigma}$. This relation predicts very well the protein-protein interaction dependence on membrane tension, but only for two particles and usually at high tensions. Interactions at low non-vanishing tensions and when dealing with multiple proteins is more complex. First, at low, but non-vanishing, tension, the interaction length scale is much stronger than predicted, likely due to strong curvature coupling, but possibly also due to membrane fluctuations. Second, increasing tension, while decreasing the protein-protein interaction strength, also changes the geometry of their assembly. Our phase diagram has shown that linear aggregation can take place along the long axis of symmetry of N-BAR domains, but also along the short axis, as observed by (Noguchi, 2015). We show that the way proteins interact also depends on the bending modulus and the aspect ratio of the protein, which means that our calculations can roughly predict the assembly of other BAR proteins and their association on membranes of different composition.

Linear aggregation has not been yet experimentally found, except in one instance, where the authors observed one-dimensional ordering of spherical particles on vesicles (Koltover et al., 1999). We were successful in capturing lines of proteins on supported lipid bilayers using AFM. Initially, we were surprised to see extremely long lines (~ 5 μm) spaced by 100–500 nm, which is an order of magnitude larger than what we saw in CG MD simulations. Seeking out an explanation for this discrepancy, we found, using free energy simulations, that there is a very strong membrane-mediated repulsion between lines of protein aggregates. Moreover, two lines can sense each other at strikingly long distances, ~ 50 nm, and this length scale increases with increased length of protein aggregates. Therefore, it is expected that if proteins have sufficient space (which they do on supported bilayers), linear aggregates will align to be parallel to one another. Recall also that increased tension breaks meshes initially into linear aggregates (Fig. 7.1.2), therefore the non-vanishing tension of supported bilayers could give rise to the predominant linearization. Note that the magnitude of membrane tension of supported bilayers is non-vanishing due to the adhesion to the surface, however we created bilayers with a high excess of lipids which helps lower the tension as much as possible. We used a multimode AFM instrument that takes > 5 min to acquire an image, therefore limiting us to steady-state observations and lower imaging resolution, due to stage drift or advection of the protein assembly. A part of future research will be using much faster AFM instruments to capture the dynamics of protein assembly.

On geometrically confined membranes, such as on vesicles, the repulsion of protein lines should result in the formation of networks or meshes. We have shown such behavior with CG MD simulations, however we are yet to capture such an assembly *in vitro*. We have made preliminary experiments by using super-resolution imaging of BAR proteins incubated with small vesicles tethered on an inert flat surface. We have managed to resolve some images that indicate mesh formation, however the highly crowded field of fluorescent molecules makes it very difficult to conclusively determine their steady-state assembly. Moreover, our imaging method heavily relies on the fact that fluorophores remain in place for the entire length of imaging (i.e. 10 min), which makes it exceptionally difficult to resolve structures at the level of a single protein or even an aggregate, in case it is highly mobile. Nevertheless, our preliminary results are promising and hopefully will inspire further improvement in this direction.

In case of a rapid recruitment of N-BAR proteins on the membrane and at high densities (such as on highly charged membranes), we have demonstrated that an alternative mechanism of tubulation takes place. Here, the topology of the bilayer breaks, followed by the nematic assembly of proteins, which then drive the folding of tubules. As a result, a spherical vesicle transforms into a network of tubules, resembling reticular membranes found throughout the cell. Such mechanism is unlike-

ly relevant for endocytosis, however its elements could help explain the way anisotropic interactions cause the formation of reticular structures in endoplasmic reticulum (Shibata et al., 2010) or T-tubules, wherein the latter mechanism actually comprises an N-BAR protein amphiphysin (Lee et al., 2002). More importantly, this mechanism, together with experiments in the lab of Harvey McMahon (Boucrot et al., 2012) sets a precedent that N-BAR domains have membrane-fissiogenic capabilities.

The ability of N-BAR proteins to participate in fission is of key importance in understanding the mechanism of newly discovered endophilin-mediated endocytosis (Boucrot et al., 2015). Initially, we believed that endophilin could perform fission on its own, especially at high bound densities, however our experiments on membrane tubules showed just the opposite — BAR proteins stabilize tubules at sufficiently high densities (Renard et al., 2015). Our conclusion, inspired by recent electron paramagnetic resonance experiments (Ambroso et al., 2014), is that BAR proteins interact differently with tubules than with spherical membranes. We propose that at high densities BAR proteins assemble into a continuous network that ideally packs on a tubular configuration. CG MD simulations showed that BAR proteins form a helix, packing 7–8 domains per helical turn on 20-nm-wide tubules. Interestingly, the helix becomes continuous at 35% surface coverage, which is precisely the areal density of centaurin in the scaffold and a similar value has previously been found for amphiphysin (Sorre et al., 2012).

It turns out that endophilin requires external pulling force to mediate fission of membrane tubules. We have shown that during the course of external pulling of BAR-scaffolded tubules, membrane-remodeling force increases up until the tubule breaks, indicating a dissipative force between the protein scaffold and the underlying lipids. Moreover, protein scaffolds inhibit free flow of lipids between the tubule and the vesicle. Therefore, it seems that with pulling, the tension in the tubule rises, which can leads either to a diminished radius or to pore nucleation, both of which would eventually break the membrane. Importantly, the formation of a protein scaffold is the most important prerequisite for such fission mechanism. Our collaborators have seen that the endophilin-mediated endocytosis of bacterial toxins indeed largely relies on molecules that could provide external force, namely actin and dynein. These observations open many routes for future exploration. First, a theoretical model needs to be developed to show the dependence of force and the timing of fission on the pulling rate. This study is currently underway by our collaborators Jacques Prost and Andrew Callan-Jones. Further, we are interested in understanding how membrane composition affects this mechanism. It is conceivable that certain lipids from such a complex mixture could be recruited to certain interfaces (e.g. between the scaffold and the bare tubule or at the GUV-tubule interface) in the course

of pulling and thus contribute to fission. Varying the structure of lipid chains and its quantitative consequence on fission would elucidate this behavior.

While we were exploring the fissiogenic properties of endophilin, we also described the way BAR domains scaffold membrane tubules in a dynamic way. As we have already mentioned, endophilin strongly favors the neck of tubules, indicating its proclivity to negative Gaussian curvature. Interestingly, we also observed that as it binds and initially constricts membrane tubules, there is a very long-range repulsion between protein clusters, driving them to bind in an evenly spaced striated pattern. This phenomenon has so far only been observed for dynamin and it has been predicted in two theoretical papers. We did not observe such behavior with centaurin. We believe that a strong constriction is required to induce a sufficient pressure perturbation across the bilayer to induce long-range interaction along the tubule. As centaurin forms a scaffold four times larger in diameter than endophilin or dynamin, it does not give rise to such behavior. The energy gained by a growing scaffold overcomes the repulsion between clusters and so the scaffolds rapidly coarsen. Interestingly, as the scaffold elongates and continuously constricts the tubule underneath, it pushes the lipids, sometimes creating kinetic barriers, which are evident by the arrest of scaffold growth partway along the tubule. We did not observe this behavior with centaurin, again consistent with its much wider scaffold radius than endophilin. Curiously, this behavior has not been reported for amphiphysin, although previously in those experiments, the protein was typically added at high tension (i.e., low radius), therefore the pressure perturbation was weak. Furthermore, the bending modulus of our membrane model was significantly higher which serendipitously increased the timescale of membrane remodeling. Figure. 7.1.3 schematizes the proposed mechanism of endocytosis mediated by endophilin.

Finally, we addressed the importance of amphipathic helices *versus* BAR domains in curvature sensing and scaffolding. A previous study has concluded that amphipathic helices are solely responsible for sensing positive curvature. By contrast, this study, together with a recent study from our lab on IRSp53 (I-BAR protein without helices) (Prévost et al, unpublished results), show that centaurin and IRSp53 are sensors of curvature. In fact, we find that centaurin has a 3–5-fold higher sorting ratio than any BAR protein tested so far. We believe that both BAR domain and the amphipathic helix can sense membrane curvature, wherein BAR domain likely does not sense (or does not sense well) isotropically curved (i.e. spherical) surfaces (Bhatia et al., 2010). In continuation, both centaurin and endophilin with a truncated N-terminal helix readily form rigid scaffolds on membrane tubules. Although we did not have a fluorescent marker on the endophilin deletion mutant—precluding us from measuring the sorting coefficient—the fact that it formed a rigid scaffold likely indicates that the protein is also a curvature sensor. It seems infeasible that a protein that does not sense curvature could get sufficiently enriched on the tubule to form a scaf-

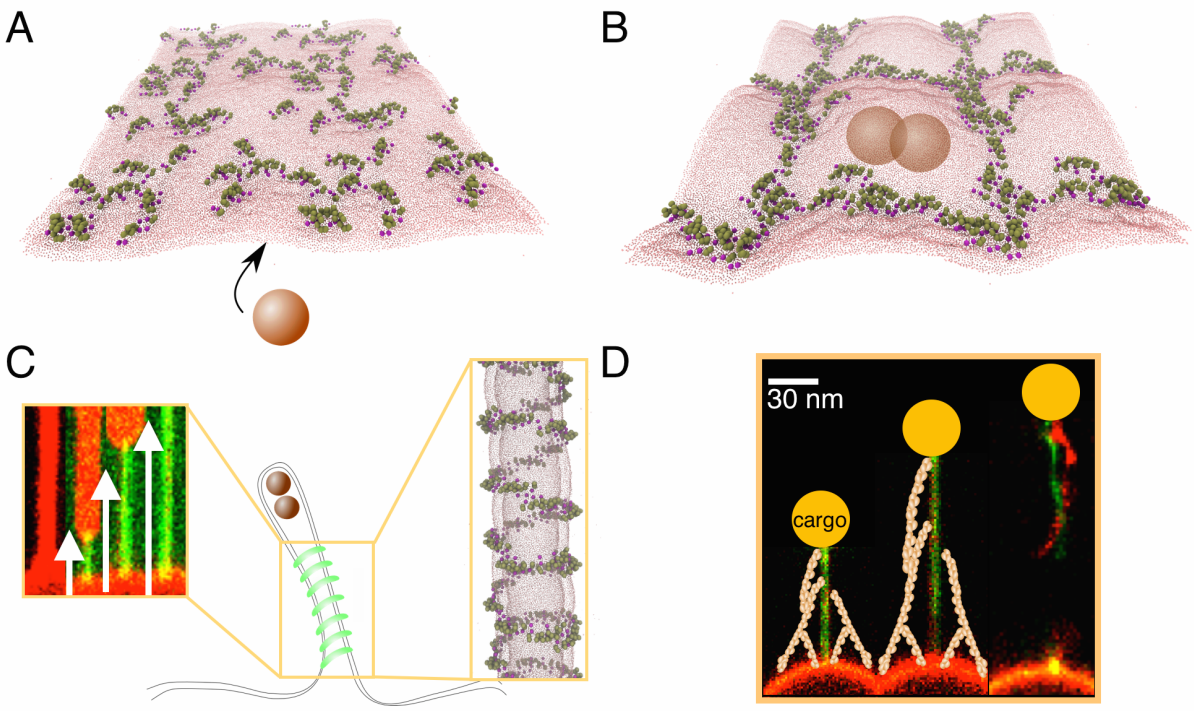

Figure 7.1.3: Scheme of endocytosis of cargo mediated by BAR proteins. (A) The binding of cargo. (B) The formation of an N-BAR protein network with concurrent recruitment of cargo (e.g. bacterial toxins) on the other side. (C) Tubulation and scaffolding by N-BAR domains. Elongation of the cargo-containing tubule (fluorescence: green - protein; red - lipid). (D). Activation of actin polymerization leading to fission and the release of encapsulated cargo into the cell lumen. In images, the cargo and actin are added by hand, they were not present in simulations or experiments.

fold. In conclusion, both protein domains (BAR and amphipathic helices) are sensors of cylindrical membrane curvature, wherein BAR domain is key for the formation of a rigid scaffold on membrane tubules. Amphipathic helices are a), key in helping recruit the protein to the membrane (especially spherical); b), they greatly enhance the curvature-generating power of the protein; and c), they rigidify the scaffold.

Continuing on this line of work, it is still necessary to demonstrate that there is a difference in binding of the BAR domain *versus* amphipathic helices to spherical and cylindrical membranes. CG MD simulations would be ideally suited for this task, however our current model is too coarse to simulate the insertion into the bilayer properly. In principle, we can apply our CG approach to model a molecule at any resolution, hence the next step is making a higher-resolution amphipathic helix model and, if needed, a higher-resolution lipid model. In addition, we need to separate the electrostatic contribution to properly model amphipathic interactions. This work is planned in the Voth group in the next few years.

In light of growing complexity of BAR protein interactions, it would be valuable to develop a curvature assay with a high throughput. For example, a bilayer supported over a microfabricated surface that features all types of curvature: cylindrical, spherical, saddle-like, would greatly help in elucidating the remaining unclear aspects of curvature coupling of a variety of proteins.

Another potential course of investigation is toward understanding an unresolved, albeit fascinating question: how do proteins find one another at the right place at the right time? The first step is studying the action of multiple proteins at a time, both *in vitro* and *in silico*. We have already performed several preliminary experiments with endophilin and centaurin injected at the same time at the same concentration ($N = 7$). In those experiments, the tubule became covered with either one or the other protein. In one experiment, we applied external pulling force for a short time then let go. This process triggered a segregation of large protein domains on the tubule followed by spontaneous fission. Future experiments and simulations could investigate if BAR proteins with different intrinsic curvatures help in regulating the timing and localization of recruitment. Take sorting nexins for instance, a family of proteins that participate in endosomal trafficking. The family comprises a dozen and possibly more proteins, all with differently curved BAR domains (van Weering et al., 2012). Building on this work, it would be very interesting to study the interaction of BAR proteins with other endocytic proteins, such as dynamin or actin to help understand equivalent *in vivo* experiments (Daumke et al., 2014; Meinecke et al., 2013). Moving toward systems that are more complex is the necessary next step in getting closer to understanding how proteins regulate membrane curvature in the cell. Nevertheless, minimal model systems are still irreplaceable as they abstract a biological problem to access its underlying physics.

Bibliography

(1) Aimon, S., Callan-Jones, A., Berthaud, A., Pinot, M., Toombes, G.E., and Bassereau, P. (2014). Membrane shape modulates transmembrane protein distribution. Dev Cell 28, 212-218.

(2) Alberts, B., Johnson, A., Lewis, J., Morgan, D., Raff, M., Roberts, K., and Walter, P. (2014). Molecular Biology of the Cell (Taylor & Francis).

(3) Allain, J.M., Storm, C., Roux, A., Ben Amar, M., and Joanny, J.F. (2004). Fission of a multiphase membrane tube. Phys Rev Lett 93, 158104.

(4) Ambroso, M.R., Hegde, B.G., and Langen, R. (2014). Endophilin A1 induces different membrane shapes using a conformational switch that is regulated by phosphorylation. Proc Natl Acad Sci U S A 111, 6982-6987.

(5) Angelova, M.I., Soléau, S., Méléard, P., Faucon, F., and Bothorel, P. (1992). Preparation of giant vesicles by external AC electric fields. Kinetics and applications. In Trends in Colloid and Interface Science VI, C. Helm, M. Lösche, and H. Möhwald, eds. (Steinkopff), pp. 127-131.

(6) Ashkin, A., Dziedzic, J.M., Bjorkholm, J.E., and Chu, S. (1986). Observation of a single-beam gradient force optical trap for dielectric particles. Opt Lett 11, 288.

(7) Ashok, B., and Ananthakrishna, G. (2014). Dynamics of intermittent force fluctuations in vesicular nanotubulation. J Chem Phys 141, 174905.

(8) Ashrafuzzaman, M., and Tuszynski, J.A. (2012). Membrane Biophysics (Springer).

(9) Atkins, P., and de Paula, J. (2010). Atkins' Physical Chemistry (OUP Oxford).

(10) Auth, T., Safran, S.A., and Gov, N.S. (2007). Fluctuations of coupled fluid and solid membranes with application to red blood cells. Phys Rev E Stat Nonlin Soft Matter Phys 76, 051910.

(11) Ayton, G.S., Lyman, E., and Voth, G.A. (2010). Hierarchical coarse-graining strategy for protein-membrane systems to access mesoscopic scales. Faraday Discuss 144, 347-357; discussion 445-381.

(12) Ayton, G.S., and Voth, G.A. (2009). Systematic multiscale simulation of membrane protein systems. Curr Opin Struct Biol 19, 138-144.

(13) Bai, J., Hu, Z., Dittman, J.S., Pym, E.C., and Kaplan, J.M. (2010). Endophilin functions as a membrane-bending molecule and is delivered to endocytic zones by exocytosis. Cell 143, 430-441.

(14) Bassereau, P., Sorre, B., and Levy, A. (2014). Bending lipid membranes: experiments after W. Helfrich's model. Adv Colloid Interface Sci 208, 47-57.

(15) Baumgart, T., Hess, S.T., and Webb, W.W. (2003). Imaging coexisting fluid domains in biomembrane models coupling curvature and line tension. Nature 425, 821-824.

(16) Berg, J.M., Tymoczko, J.L., and Stryer, L. (2002). Biochemistry, Fifth Edition (W.H. Freeman).

(17) Betzig, E., Patterson, G.H., Sougrat, R., Lindwasser, O.W., Olenych, S., Bonifacino, J.S., Davidson, M.W., Lippincott-Schwartz, J., and Hess, H.F. (2006). Imaging intracellular fluorescent proteins at nanometer resolution. Science 313, 1642-1645.

(18) Bhatia, V.K., Hatzakis, N.S., and Stamou, D. (2010). A unifying mechanism accounts for sensing of membrane curvature by BAR domains, amphipathic helices and membrane-anchored proteins. Semin Cell Dev Biol 21, 381-390.

(19) Bhatia, V.K., Madsen, K.L., Bolinger, P.Y., Kunding, A., Hedegard, P., Gether, U., and Stamou, D. (2009). Amphipathic motifs in BAR domains are essential for membrane curvature sensing. EMBO J 28, 3303-3314.

(20) Bickel, T., Jeppesen, C., and Marques, C.M. (2001). Local entropic effects of polymers grafted to soft interfaces. Eur Phys J E 4, 33-43.

(21) Bigay, J., Gounon, P., Robineau, S., and Antonny, B. (2003). Lipid packing sensed by ArfGAP1 couples COPI coat disassembly to membrane bilayer curvature. Nature 426, 563-566.

(22) Black, J.C., Cheney, P.P., Campbell, T., and Knowles, M.K. (2014). Membrane curvature based lipid sorting using a nanoparticle patterned substrate. Soft Matter 10, 2016-2023.

(23) Boucrot, E., Ferreira, A.P., Almeida-Souza, L., Debard, S., Vallis, Y., Howard, G., Bertot, L., Sauvonnet, N., and McMahon, H.T. (2015). Endophilin marks and controls a clathrin-independent endocytic pathway. Nature 517, 460-465.

(24) Boucrot, E., Pick, A., Camdere, G., Liska, N., Evergren, E., McMahon, H.T., and Kozlov, M.M. (2012). Membrane fission is promoted by insertion of amphipathic helices and is restricted by crescent BAR domains. Cell 149, 124-136.

(25) Boulant, S., Kural, C., Zeeh, J.C., Ubelmann, F., and Kirchhausen, T. (2011). Actin dynamics counteract membrane tension during clathrin-mediated endocytosis. Nat Cell Biol 13, 1124-1131.

(26) Breidenich, M., Netz, R.R., and Lipowsky, R. (2000). The shape of polymer-decorated membranes. Europhys Lett 49, 431-437.

(27) Brochard, F., and Lennon, J. (1975). Frequency spectrum of the flicker phenomenon in erythrocytes. J Phys-Paris 36, 1035-1047.

(28) Brogden, K.A. (2005). Antimicrobial peptides: pore formers or metabolic inhibitors in bacteria? Nat Rev Microbiol 3, 238-250.

(29) Brown, F.L. (2008). Elastic modeling of biomembranes and lipid bilayers. Annu Rev Phys Chem 59, 685-712.

(30) Callan-Jones, A., and Bassereau, P. (2013). Curvature-driven membrane lipid and protein distribution. Curr Opin Solid St M 17, 143-150.

(31) Campelo, F., McMahon, H.T., and Kozlov, M.M. (2008). The hydrophobic insertion mechanism of membrane curvature generation by proteins. Biophys J 95, 2325-2339.

(32) Campillo, C., Sens, P., Koster, D., Pontani, L.L., Levy, D., Bassereau, P., Nassoy, P., and Sykes, C. (2013). Unexpected membrane dynamics unveiled by membrane nanotube extrusion. Biophys J 104, 1248-1256.

(33) Canham, P.B. (1970). The minimum energy of bending as a possible explanation of the biconcave shape of the human red blood cell. J Theor Biol 26, 61-81.

(34) Capraro, B.R., Yoon, Y., Cho, W., and Baumgart, T. (2010). Curvature sensing by the epsin N-terminal homology domain measured on cylindrical lipid membrane tethers. J Am Chem Soc 132, 1200-1201.

(35) Chaikin, P.M., and Lubensky, T.C. (2000). Principles of Condensed Matter Physics (Cambridge University Press).

(36) Chen, C.M., Higgs, P.G., and MacKintosh, F.C. (1997). Theory of fission for two-component lipid vesicles. Phys Rev Lett 79, 1579-1582.

(37) Chen, H., and Antonarakis, S.E. (1997). The SH3D1A gene maps to human chromosome 21q22.1-->q22.2. Cytogenet Cell Genet 78, 213-215.

(38) Chen, H., Fre, S., Slepnev, V.I., Capua, M.R., Takei, K., Butler, M.H., Di Fiore, P.P., and De Camilli, P. (1998). Epsin is an EH-domain-binding protein implicated in clathrin-mediated endocytosis. Nature 394, 793-797.

(39) Cocucci, E., Gaudin, R., and Kirchhausen, T. (2014). Dynamin recruitment and membrane scission at the neck of a clathrin-coated pit. Mol Biol Cell 25, 3595-3609.

(40) Cooper, G. (2000). The Cell: A Molecular Approach (ASM Press).

(41) Cui, H., Lyman, E., and Voth, G.A. (2011). Mechanism of membrane curvature sensing by amphipathic helix containing proteins. Biophys J 100, 1271-1279.

(42) Cuvelier, D., Derenyi, I., Bassereau, P., and Nassoy, P. (2005). Coalescence of membrane tethers: experiments, theory, and applications. Biophys J 88, 2714-2726.

(43) Dai, J., and Sheetz, M.P. (1995). Regulation of endocytosis, exocytosis, and shape by membrane tension. Cold Spring Harb Symp Quant Biol 60, 567-571.

(44) Daillant, J., Bellet-Amalric, E., Braslau, A., Charitat, T., Fragneto, G., Graner, F., Mora, S., Rieutord, F., and Stidder, B. (2005). Structure and fluctuations of a single floating lipid bilayer. Proc Natl Acad Sci U S A 102, 11639-11644.

(45) Dannhauser, P.N., and Ungewickell, E.J. (2012). Reconstitution of clathrin-coated bud and vesicle formation with minimal components. Nat Cell Biol 14, 634-639.

(46) Datar, A., Bornschlogl, T., Bassereau, P., Prost, J., and Pullarkat, P.A. (2015). Dynamics of membrane tethers reveal novel aspects of cytoskeleton-membrane interactions in axons. Biophys J 108, 489-497.

(47) Daumke, O., Roux, A., and Haucke, V. (2014). BAR domain scaffolds in dynamin-mediated membrane fission. Cell 156, 882-892.

(48) Dawson, J.C., Legg, J.A., and Machesky, L.M. (2006). Bar domain proteins: a role in tubulation, scission and actin assembly in clathrin-mediated endocytosis. Trends Cell Biol 16, 493-498.

(49) Day, C.A., Baetz, N.W., Copeland, C.A., Kraft, L.J., Han, B., Tiwari, A., Drake, K.R., De Luca, H., Chinnapen, D.J., Davidson, M.W., et al. (2015). Microtubule motors power plasma membrane tubulation in clathrin-independent endocytosis. Traffic.

(50) den Otter, W.K., and Briels, W.J. (2003). The bending rigidity of an amphiphilic bilayer from equilibrium and nonequilibrium molecular dynamics. J Chem Phys 118, 4712-4720.

(51) den Otter, W.K., and Shkulipa, S.A. (2007). Intermonolayer friction and surface shear viscosity of lipid bilayer membranes. Biophys J 93, 423-433.

(52) Derenyi, I., Julicher, F., and Prost, J. (2002). Formation and interaction of membrane tubes. Phys Rev Lett 88, 238101.

(53) Derganc, J. (2007). Curvature-driven lateral segregation of membrane constituents in Golgi cisternae. Phys Biol 4, 317-324.

(54) Dietrich, C., Bagatolli, L.A., Volovyk, Z.N., Thompson, N.L., Levi, M., Jacobson, K., and Gratton, E. (2001). Lipid rafts reconstituted in model membranes. Biophys J 80, 1417-1428.

(55) Doherty, G.J., and McMahon, H.T. (2009). Mechanisms of endocytosis. Annu Rev Biochem 78, 857-902.

(56) Domanov, Y.A., Aimon, S., Toombes, G.E., Renner, M., Quemeneur, F., Triller, A., Turner, M.S., and Bassereau, P. (2011). Mobility in geometrically confined membranes. Proc Natl Acad Sci U S A 108, 12605-12610.

(57) Dommersnes, P.G., and Fournier, J.B. (1999). N-body study of anisotropic membrane inclusions: Membrane mediated interactions and ordered aggregation. Eur Phys J B 12, 9-12.

(58) Drin, G., and Antonny, B. (2010). Amphipathic helices and membrane curvature. FEBS Lett 584, 1840-1847.

(59) Evans, E., Heinrich, V., Ludwig, F., and Rawicz, W. (2003). Dynamic tension spectroscopy and strength of biomembranes. Biophys J 85, 2342-2350.

(60) Evans, E., and Rawicz, W. (1990). Entropy-driven tension and bending elasticity in condensed-fluid membranes. Phys Rev Lett 64, 2094-2097.

(61) Evans, E., and Smith, B.A. (2011). Kinetics of Hole Nucleation in Biomembrane Rupture. New J Phys 13.

(62) Evans, E., and Yeung, A. (1994). Hidden Dynamics in Rapid Changes of Bilayer Shape. Chem Phys Lipids 73, 39-56.

(63) Evans, E.A. (1983). Bending elastic modulus of red blood cell membrane derived from buckling instability in micropipet aspiration tests. Biophys J 43, 27-30.

(64) Feigenson, G.W. (2006). Phase behavior of lipid mixtures. Nat Chem Biol 2, 560-563.

(65) Fernandes, F., Loura, L.M., Chichon, F.J., Carrascosa, J.L., Fedorov, A., and Prieto, M. (2008). Role of helix 0 of the N-BAR domain in membrane curvature generation. Biophys J 94, 3065-3073.

(66) Filippov, A., Oradd, G., and Lindblom, G. (2003). The effect of cholesterol on the lateral diffusion of phospholipids in oriented bilayers. Biophys J 84, 3079-3086.

(67) Filippov, A., Oradd, G., and Lindblom, G. (2004). Lipid lateral diffusion in ordered and disordered phases in raft mixtures. Biophys J 86, 891-896.

(68) Ford, M.G., Mills, I.G., Peter, B.J., Vallis, Y., Praefcke, G.J., Evans, P.R., and McMahon, H.T. (2002). Curvature of clathrin-coated pits driven by epsin. Nature 419, 361-366.

(69) Fournier, J.B., Ajdari, A., and Peliti, L. (2001). Effective-area elasticity and tension of micromanipulated membranes. Phys Rev Lett 86, 4970-4973.

(70) Fournier, J.B., and Barbetta, C. (2008). Direct calculation from the stress tensor of the lateral surface tension of fluctuating fluid membranes. Phys Rev Lett 100, 078103.

(71) Fournier, J.B., Lacoste, D., and Raphael, E. (2004). Fluctuation spectrum of fluid membranes coupled to an elastic meshwork: jump of the effective surface tension at the mesh size. Phys Rev Lett 92, 018102.

(72) Frost, A., Perera, R., Roux, A., Spasov, K., Destaing, O., Egelman, E.H., De Camilli, P., and Unger, V.M. (2008). Structural basis of membrane invagination by F-BAR domains. Cell 132, 807-817.

(73) Funkhouser, C.M., Solis, F.J., and Thornton, K. (2010). Dynamics of two-phase lipid vesicles: effects of mechanical properties on morphology evolution. Soft Matter 6, 3462-3466.

(74) Gallop, J.L., Jao, C.C., Kent, H.M., Butler, P.J., Evans, P.R., Langen, R., and McMahon, H.T. (2006). Mechanism of endophilin N-BAR domain-mediated membrane curvature. EMBO J 25, 2898-2910.

(75) Galush, W.J., Nye, J.A., and Groves, J.T. (2008). Quantitative fluorescence microscopy using supported lipid bilayer standards. Biophys J 95, 2512-2519.

(76) Gauthier, N.C., Masters, T.A., and Sheetz, M.P. (2012). Mechanical feedback between membrane tension and dynamics. Trends Cell Biol 22, 527-535.

(77) Goetz, R., Gompper, G., and Lipowsky, R. (1999). Mobility and elasticity of self-assembled membranes. Phys Rev Lett 82, 221-224.

(78) Goni, F.M. (2014). The basic structure and dynamics of cell membranes: an update of the Singer-Nicolson model. Biochim Biophys Acta 1838, 1467-1476.

(79) Gould, T.J., and Hess, S.T. (2008). Chapter 12: Nanoscale biological fluorescence imaging: breaking the diffraction barrier. Methods Cell Biol 89, 329-358.

(80) Granger, E., McNee, G., Allan, V., and Woodman, P. (2014). The role of the cytoskeleton and molecular motors in endosomal dynamics. Semin Cell Dev Biol 31, 20-29.

(81) Guo, M., Ehrlicher, A.J., Jensen, M.H., Renz, M., Moore, J.R., Goldman, R.D., Lippincott-Schwartz, J., Mackintosh, F.C., and Weitz, D.A. (2014). Probing the stochastic, motor-driven properties of the cytoplasm using force spectrum microscopy. Cell 158, 822-832.

(82) Heinrich, M.C., Capraro, B.R., Tian, A., Isas, J.M., Langen, R., and Baumgart, T. (2010). Quantifying Membrane Curvature Generation of Amphiphysin N-BAR Domains. J Phys Chem Lett 1, 3401-3406.

(83) Heinrich, V., Svetina, S., and Zeks, B. (1993). Nonaxisymmetric Vesicle Shapes in a Generalized Bilayer-Couple Model and the Transition between Oblate and Prolate Axisymmetrical Shapes. Phys Rev E 48, 3112-3123.

(84) Helfrich, W. (1973). Elastic properties of lipid bilayers: theory and possible experiments. Z Naturforsch C 28, 693-703.

(85) Helfrich, W. (1998). Stiffening of fluid membranes and entropy loss of membrane closure: Two effects of thermal undulations. Eur Phys J B 1, 481-489.

(86) Hell, S.W., and Wichmann, J. (1994). Breaking the diffraction resolution limit by stimulated emission: stimulated-emission-depletion fluorescence microscopy. Opt Lett 19, 780-782.

(87) Henne, W.M., Boucrot, E., Meinecke, M., Evergren, E., Vallis, Y., Mittal, R., and McMahon, H.T. (2010). FCHo proteins are nucleators of clathrin-mediated endocytosis. Science 328, 1281-1284.

(88) Hess, S.T., Girirajan, T.P., and Mason, M.D. (2006). Ultra-high resolution imaging by fluorescence photoactivation localization microscopy. Biophys J 91, 4258-4272.

(89) Hochmuth, R.M., and Evans, E.A. (1982). Extensional Flow of Erythrocyte-Membrane from Cell Body to Elastic Tether .1. Analysis. Biophys J 39, 71-81.

(90) Holopainen, J.M., Angelova, M.I., and Kinnunen, P.K. (2000). Vectorial budding of vesicles by asymmetrical enzymatic formation of ceramide in giant liposomes. Biophys J 78, 830-838.

(91) Holthuis, J.C., and Levine, T.P. (2005). Lipid traffic: floppy drives and a superhighway. Nat Rev Mol Cell Biol 6, 209-220.

(92) Hu, J.L., Weikl, T.R., and Lipowsky, R. (2011). Vesicles with multiple membrane domains. Soft Matter 7, 6092-6102.

(93) Hu, M., Briguglio, J.J., and Deserno, M. (2012). Determining the Gaussian curvature modulus of lipid membranes in simulations. Biophys J 102, 1403-1410.

(94) Ipsen, J.H., Karlstrom, G., Mouritsen, O.G., Wennerstrom, H., and Zuckermann, M.J. (1987). Phase equilibria in the phosphatidylcholine-cholesterol system. Biochim Biophys Acta 905, 162-172.

(95) Israelachvili, J.N., Marcelja, S., and Horn, R.G. (1980). Physical principles of membrane organization. Q Rev Biophys 13, 121-200.

(96) Izvekov, S., and Voth, G.A. (2005). A multiscale coarse-graining method for biomolecular systems. J Phys Chem B 109, 2469-2473.

(97) Jackson, T.R., Kearns, B.G., and Theibert, A.B. (2000). Cytohesins and centaurins: mediators of PI 3-kinase-regulated Arf signaling. Trends Biochem Sci 25, 489-495.

(98) Jacobson, K., Mouritsen, O.G., and Anderson, R.G. (2007). Lipid rafts: at a crossroad between cell biology and physics. Nat Cell Biol 9, 7-14.

(99) Johannes, L., Wunder, C., and Bassereau, P. (2014). Bending "on the rocks"--a cocktail of biophysical modules to build endocytic pathways. Cold Spring Harb Perspect Biol 6.

(100) Kabaso, D., Bobrovska, N., Gozdz, W., Gov, N., Kralj-Iglic, V., Veranic, P., and Iglic, A. (2012). On the role of membrane anisotropy and BAR proteins in the stability of tubular membrane structures. J Biomech 45, 231-238.

(101) Karbowski, M., Jeong, S.Y., and Youle, R.J. (2004). Endophilin B1 is required for the maintenance of mitochondrial morphology. J Cell Biol 166, 1027-1039.

(102) Kirchhausen, T. (2000). Clathrin. Annu Rev Biochem 69, 699-727.

(103) Kirchhausen, T. (2009). Imaging endocytic clathrin structures in living cells. Trends Cell Biol 19, 596-605.

(104) Kirchhausen, T. (2012). Bending membranes. Nat Cell Biol 14, 906-908.

(105) Kishimoto, T., Sun, Y., Buser, C., Liu, J., Michelot, A., and Drubin, D.G. (2011). Determinants of endocytic membrane geometry, stability, and scission. Proc Natl Acad Sci U S A 108, E979-988.

(106) Kjaerulff, O., Brodin, L., and Jung, A. (2011). The structure and function of endophilin proteins. Cell Biochem Biophys 60, 137-154.

(107) Kobayashi, H., and Fukuda, M. (2012). Rab35 regulates Arf6 activity through centaurin-beta2 (ACAP2) during neurite outgrowth. J Cell Sci 125, 2235-2243.

(108) Koltover, I., Radler, J.O., and Safinya, C.R. (1999). Membrane mediated attraction and ordered aggregation of colloidal particles bound to giant phospholipid vesicles. Phys Rev Lett 82, 1991-1994.

(109) Koster, G., VanDuijn, M., Hofs, B., and Dogterom, M. (2003). Membrane tube formation from giant vesicles by dynamic association of motor proteins. Proc Natl Acad Sci U S A 100, 15583-15588.

(110) Kozlov, M.M., Campelo, F., Liska, N., Chernomordik, L.V., Marrink, S.J., and McMahon, H.T. (2014). Mechanisms shaping cell membranes. Curr Opin Cell Biol 29, 53-60.

(111) Kozlov, M.M., McMahon, H.T., and Chernomordik, L.V. (2010). Protein-driven membrane stresses in fusion and fission. Trends Biochem Sci 35, 699-706.

(112) Kozlovsky, Y., and Kozlov, M.M. (2003). Membrane fission: model for intermediate structures. Biophys J 85, 85-96.

(113) Kralj-Iglic, V., Svetina, S., and Zeks, B. (1996). Shapes of bilayer vesicles with membrane embedded molecules. Eur Biophys J 24, 311-321.

(114) Kühnel, W. (2002). Differential Geometry: Curves - Surfaces - Manifolds (American Mathematical Society).

(115) Kukulski, W., Schorb, M., Kaksonen, M., and Briggs, J.A. (2012). Plasma membrane reshaping during endocytosis is revealed by time-resolved electron tomography. Cell 150, 508-520.

(116) Kummrow, M., and Helfrich, W. (1991). Deformation of giant lipid vesicles by electric fields. Phys Rev A 44, 8356-8360.

(117) Kwok, R., and Evans, E. (1981). Thermoelasticity of large lecithin bilayer vesicles. Biophys J 35, 637-652.

(118) Lauvrak, S.U., Torgersen, M.L., and Sandvig, K. (2004). Efficient endosome-to-Golgi transport of Shiga toxin is dependent on dynamin and clathrin. J Cell Sci 117, 2321-2331.

(119) Leduc, C., Campas, O., Joanny, J.F., Prost, J., and Bassereau, P. (2010). Mechanism of membrane nanotube formation by molecular motors. Biochim Biophys Acta 1798, 1418-1426.

(120) Leduc, C., Campas, O., Zeldovich, K.B., Roux, A., Jolimaitre, P., Bourel-Bonnet, L., Goud, B., Joanny, J.F., Bassereau, P., and Prost, J. (2004). Cooperative extraction of membrane nanotubes by molecular motors. Proc Natl Acad Sci U S A 101, 17096-17101.

(121) Lee, E., Marcucci, M., Daniell, L., Pypaert, M., Weisz, O.A., Ochoa, G.C., Farsad, K., Wenk, M.R., and De Camilli, P. (2002). Amphiphysin 2 (Bin1) and T-tubule biogenesis in muscle. Science 297, 1193-1196.

(122) Leibler, S. (1986). Curvature Instability in Membranes. J Phys-Paris 47, 507-516.

(123) Li, J., Peters, P.J., Bai, M., Dai, J., Bos, E., Kirchhausen, T., Kandror, K.V., and Hsu, V.W. (2007). An ACAP1-containing clathrin coat complex for endocytic recycling. J Cell Biol 178, 453-464.

(124) Li, J., Zhang, H., and Qiu, F. (2013). Budding behavior of multi-component vesicles. J Phys Chem B 117, 843-849.

(125) Li, Z., Anvari, B., Takashima, M., Brecht, P., Torres, J.H., and Brownell, W.E. (2002). Membrane tether formation from outer hair cells with optical tweezers. Biophys J 82, 1386-1395.

(126) Lieber, A.D., Yehudai-Resheff, S., Barnhart, E.L., Theriot, J.A., and Keren, K. (2013). Membrane tension in rapidly moving cells is determined by cytoskeletal forces. Curr Biol 23, 1409-1417.

(127) Lindahl, E., and Edholm, O. (2000). Mesoscopic undulations and thickness fluctuations in lipid bilayers from molecular dynamics simulations. Biophys J 79, 426-433.

(128) Lingwood, D., and Simons, K. (2010). Lipid rafts as a membrane-organizing principle. Science 327, 46-50.

(129) Lipowsky, R. (1991). The conformation of membranes. Nature 349, 475-481.

(130) Lipowsky, R. (2013). Spontaneous tubulation of membranes and vesicles reveals membrane tension generated by spontaneous curvature. Faraday Discussions 161, 305-331.

(131) Lipowsky, R. (2014). Coupling of bending and stretching deformations in vesicle membranes. Adv Colloid Interface Sci 208, 14-24.

(132) Lipowsky, R., and Dobereiner, H.G. (1998). Vesicles in contact with nanoparticles and colloids. Europhys Lett 43, 219-225.

(133) Lodish, H. (2008). Molecular Cell Biology (W. H. Freeman).

(134) Lorenzen, S., Servuss, R.M., and Helfrich, W. (1986). Elastic Torques about Membrane Edges: A Study of Pierced Egg Lecithin Vesicles. Biophys J 50, 565-572.

(135) Lundmark, R., and Carlsson, S.R. (2010). Driving membrane curvature in clathrin-dependent and clathrin-independent endocytosis. Semin Cell Dev Biol 21, 363-370.

(136) Lyman, E., Cui, H., and Voth, G.A. (2011). Reconstructing protein remodeled membranes in molecular detail from mesoscopic models. Phys Chem Chem Phys 13, 10430-10436.

(137) Mackinnon, R. (2004). Structural biology. Voltage sensor meets lipid membrane. Science 306, 1304-1305.

(138) Mallard, F., Antony, C., Tenza, D., Salamero, J., Goud, B., and Johannes, L. (1998). Direct pathway from early/recycling endosomes to the Golgi apparatus revealed through the study of shiga toxin B-fragment transport. J Cell Biol 143, 973-990.

(139) Manneville, J.B., Bassereau, P., Levy, D., and Prost, J. (1999). Activity of transmembrane proteins induces magnification of shape fluctuations of lipid membranes. Phys Rev Lett 82, 4356-4359.

(140) Marsh, D. (2006). Elastic curvature constants of lipid monolayers and bilayers. Chem Phys Lipids 144, 146-159.

(141) Masuda, M., Takeda, S., Sone, M., Ohki, T., Mori, H., Kamioka, Y., and Mochizuki, N. (2006). Endophilin BAR domain drives membrane curvature by two newly identified structure-based mechanisms. EMBO J 25, 2889-2897.

(142) Mathivet, L., Cribier, S., and Devaux, P.F. (1996). Shape change and physical properties of giant phospholipid vesicles prepared in the presence of an AC electric field. Biophys J 70, 1112-1121.

(143) Mattila, P.K., Pykalainen, A., Saarikangas, J., Paavilainen, V.O., Vihinen, H., Jokitalo, E., and Lappalainen, P. (2007). Missing-in-metastasis and IRSp53 deform PI(4,5)P2-rich membranes by an inverse BAR domain-like mechanism. J Cell Biol 176, 953-964.

(144) Mayor, S., Parton, R.G., and Donaldson, J.G. (2014). Clathrin-independent pathways of endocytosis. Cold Spring Harb Perspect Biol 6.

(145) McLaughlin, S., and Murray, D. (2005). Plasma membrane phosphoinositide organization by protein electrostatics. Nature 438, 605-611.

(146) McMahon, H.T., and Boucrot, E. (2011). Molecular mechanism and physiological functions of clathrin-mediated endocytosis. Nat Rev Mol Cell Biol 12, 517-533.

(147) McMahon, H.T., and Gallop, J.L. (2005). Membrane curvature and mechanisms of dynamic cell membrane remodelling. Nature 438, 590-596.

(148) Meinecke, M., Boucrot, E., Camdere, G., Hon, W.C., Mittal, R., and McMahon, H.T. (2013). Cooperative recruitment of dynamin and BIN/amphiphysin/Rvs (BAR) domain-containing proteins leads to GTP-dependent membrane scission. J Biol Chem 288, 6651-6661.

(149) Meleard, P., Bagatolli, L.A., and Pott, T. (2009). Giant unilamellar vesicle electroformation from lipid mixtures to native membranes under physiological conditions. Methods Enzymol 465, 161-176.

(150) Mertz, J. (2010). Introduction to Optical Microscopy (Roberts).

(151) Messa, M., Fernandez-Busnadiego, R., Sun, E.W., Chen, H., Czapla, H., Wrasman, K., Wu, Y., Ko, G., Ross, T., Wendland, B., et al. (2014). Epsin deficiency impairs endocytosis by stalling the actin-dependent invagination of endocytic clathrin-coated pits. Elife 3, e03311.

(152) Miao, L., Seifert, U., Wortis, M., and Dobereiner, H.G. (1994). Budding transitions of fluid-bilayer vesicles: The effect of area-difference elasticity. Phys Rev E Stat Phys Plasmas Fluids Relat Interdiscip Topics 49, 5389-5407.

(153) Micheva, K.D., Kay, B.K., and McPherson, P.S. (1997). Synaptojanin forms two separate complexes in the nerve terminal. Interactions with endophilin and amphiphysin. J Biol Chem 272, 27239-27245.

(154) Mim, C., Cui, H., Gawronski-Salerno, J.A., Frost, A., Lyman, E., Voth, G.A., and Unger, V.M. (2012). Structural basis of membrane bending by the N-BAR protein endophilin. Cell 149, 137-145.

(155) Mim, C., and Unger, V.M. (2012). Membrane curvature and its generation by BAR proteins. Trends Biochem Sci 37, 526-533.

(156) Monnier, S., Rochal, S.B., Parmeggiani, A., and Lorman, V.L. (2010). Long-range protein coupling mediated by critical low-energy modes of tubular lipid membranes. Phys Rev Lett 105, 028102.

(157) Montes, L.R., Alonso, A., Goni, F.M., and Bagatolli, L.A. (2007). Giant unilamellar vesicles electroformed from native membranes and organic lipid mixtures under physiological conditions. Biophys J 93, 3548-3554.

(158) Morlot, S., Galli, V., Klein, M., Chiaruttini, N., Manzi, J., Humbert, F., Dinis, L., Lenz, M., Cappello, G., and Roux, A. (2012). Membrane shape at the edge of the dynamin helix sets location and duration of the fission reaction. Cell 151, 619-629.

(159) Morlot, S., and Roux, A. (2013). Mechanics of dynamin-mediated membrane fission. Annu Rev Biophys 42, 629-649.

(160) Munro, S. (2003). Lipid rafts: elusive or illusive? Cell 115, 377-388.

(161) Neuman, K.C., and Block, S.M. (2004). Optical trapping. Rev Sci Instrum 75, 2787-2809.

(162) Neuman, K.C., and Nagy, A. (2008). Single-molecule force spectroscopy: optical tweezers, magnetic tweezers and atomic force microscopy. Nat Methods 5, 491-505.

(163) Nikolov, V., Lipowsky, R., and Dimova, R. (2007). Behavior of giant vesicles with anchored DNA molecules. Biophys J 92, 4356-4368.

(164) Noguchi, H. (2014). Two- or three-step assembly of banana-shaped proteins coupled with shape transformation of lipid membranes. Epl-Europhys Lett 108.

(165) Noguchi, H. (2015). Membrane tubule formation by banana-shaped proteins with or without intermediate network structure. arXiv.

(166) Nuscher, B., Kamp, F., Mehnert, T., Odoy, S., Haass, C., Kahle, P.J., and Beyer, K. (2004). Alpha-synuclein has a high affinity for packing defects in a bilayer membrane: a thermodynamics study. J Biol Chem 279, 21966-21975.

(167) Olbrich, K., Rawicz, W., Needham, D., and Evans, E. (2000). Water permeability and mechanical strength of polyunsaturated lipid bilayers. Biophys J 79, 321-327.

(168) Pan, J., Mills, T.T., Tristram-Nagle, S., and Nagle, J.F. (2008). Cholesterol perturbs lipid bilayers nonuniversally. Phys Rev Lett 100, 198103.

(169) Pang, X., Fan, J., Zhang, Y., Zhang, K., Gao, B., Ma, J., Li, J., Deng, Y., Zhou, Q., Egelman, E.H., et al. (2014). A PH domain in ACAP1 possesses key features of the BAR domain in promoting membrane curvature. Dev Cell 31, 73-86.

(170) Pecreaux, J., Dobereiner, H.G., Prost, J., Joanny, J.F., and Bassereau, P. (2004). Refined contour analysis of giant unilamellar vesicles. Eur Phys J E Soft Matter 13, 277-290.

(171) Peliti, L., and Leibler, S. (1985). Effects of thermal fluctuations on systems with small surface tension. Phys Rev Lett 54, 1690-1693.

(172) Peter, B.J., Kent, H.M., Mills, I.G., Vallis, Y., Butler, P.J., Evans, P.R., and McMahon, H.T. (2004). BAR domains as sensors of membrane curvature: the amphiphysin BAR structure. Science 303, 495-499.

(173) Picas, L., Viaud, J., Schauer, K., Vanni, S., Hnia, K., Fraisier, V., Roux, A., Bassereau, P., Gaits-Iacovoni, F., Payrastre, B., et al. (2014). BIN1/M-Amphiphysin2 induces clustering of phosphoinositides to recruit its downstream partner dynamin. Nat Commun 5, 5647.

(174) Pranke, I.M., Morello, V., Bigay, J., Gibson, K., Verbavatz, J.M., Antonny, B., and Jackson, C.L. (2011). alpha-Synuclein and ALPS motifs are membrane curvature sensors whose contrasting chemistry mediates selective vesicle binding. J Cell Biol 194, 89-103.

(175) Prost, J., and Bruinsma, R. (1996). Shape fluctuations of active membranes. Europhys Lett 33, 321-326.

(176) Qiu, H., and Caffrey, M. (2000). The phase diagram of the monoolein/water system: metastability and equilibrium aspects. Biomaterials 21, 223-234.

(177) Qualmann, B., Koch, D., and Kessels, M.M. (2011). Let's go bananas: revisiting the endocytic BAR code. EMBO J 30, 3501-3515.

(178) Ramachandran, R., Pucadyil, T.J., Liu, Y.W., Acharya, S., Leonard, M., Lukiyanchuk, V., and Schmid, S.L. (2009). Membrane insertion of the pleckstrin homology domain variable loop 1 is critical for dynamin-catalyzed vesicle scission. Mol Biol Cell 20, 4630-4639.

(179) Ramakrishnan, N., Sunil Kumar, P.B., and Ipsen, J.H. (2013). Membrane-mediated aggregation of curvature-inducing nematogens and membrane tubulation. Biophys J 104, 1018-1028.

(180) Ramamurthi, K.S., Lecuyer, S., Stone, H.A., and Losick, R. (2009). Geometric cue for protein localization in a bacterium. Science 323, 1354-1357.

(181) Ramesh, P., Baroji, Y.F., Reihani, S.N., Stamou, D., Oddershede, L.B., and Bendix, P.M. (2013). FBAR syndapin 1 recognizes and stabilizes highly curved tubular membranes in a concentration dependent manner. Sci Rep 3, 1565.

(182) Randazzo, P.A., Andrade, J., Miura, K., Brown, M.T., Long, Y.Q., Stauffer, S., Roller, P., and Cooper, J.A. (2000). The Arf GTPase-activating protein ASAP1 regulates the actin cytoskeleton. Proc Natl Acad Sci U S A 97, 4011-4016.

(183) Rao, M., and Sarasij, R.C. (2001). Active fusion and fission processes on a fluid membrane. Phys Rev Lett 87, 128101.

(184) Rao, Y., and Haucke, V. (2011). Membrane shaping by the Bin/amphiphysin/Rvs (BAR) domain protein superfamily. Cell Mol Life Sci 68, 3983-3993.

(185) Raucher, D., and Sheetz, M.P. (1999). Characteristics of a membrane reservoir buffering membrane tension. Biophys J 77, 1992-2002.

(186) Rawicz, W., Olbrich, K.C., McIntosh, T., Needham, D., and Evans, E. (2000). Effect of chain length and unsaturation on elasticity of lipid bilayers. Biophys J 79, 328-339.

(187) Rawicz, W., Smith, B.A., McIntosh, T.J., Simon, S.A., and Evans, E. (2008). Elasticity, strength, and water permeability of bilayers that contain raft microdomain-forming lipids. Biophys J 94, 4725-4736.

(188) Reeves, J.P., and Dowben, R.M. (1969). Formation and properties of thin-walled phospholipid vesicles. J Cell Physiol 73, 49-60.

(189) Renard, H.F., Simunovic, M., Lemiere, J., Boucrot, E., Garcia-Castillo, M.D., Arumugam, S., Chambon, V., Lamaze, C., Wunder, C., Kenworthy, A.K., et al. (2015). Endophilin-A2 functions in membrane scission in clathrin-independent endocytosis. Nature 517, 493-496.

(190) Renner, L.D., and Weibel, D.B. (2011). Cardiolipin microdomains localize to negatively curved regions of Escherichia coli membranes. Proc Natl Acad Sci U S A 108, 6264-6269.

(191) Rim, J.E., Ursell, T.S., Phillips, R., and Klug, W.S. (2011). Morphological phase diagram for lipid membrane domains with entropic tension. Phys Rev Lett 106, 057801.

(192) Romer, W., Berland, L., Chambon, V., Gaus, K., Windschiegl, B., Tenza, D., Aly, M.R.E., Fraisier, V., Florent, J.C., Perrais, D., et al. (2007). Shiga toxin induces tubular membrane invaginations for its uptake into cells. Nature 450, 670-U673.

(193) Roux, A., Cappello, G., Cartaud, J., Prost, J., Goud, B., and Bassereau, P. (2002). A minimal system allowing tubulation with molecular motors pulling on giant liposomes. Proc Natl Acad Sci U S A 99, 5394-5399.

(194) Roux, A., Cuvelier, D., Nassoy, P., Prost, J., Bassereau, P., and Goud, B. (2005). Role of curvature and phase transition in lipid sorting and fission of membrane tubules. EMBO J 24, 1537-1545.

(195) Roux, A., Koster, G., Lenz, M., Sorre, B., Manneville, J.B., Nassoy, P., and Bassereau, P. (2010). Membrane curvature controls dynamin polymerization. Proc Natl Acad Sci U S A 107, 4141-4146.

(196) Roux, A., Uyhazi, K., Frost, A., and De Camilli, P. (2006). GTP-dependent twisting of dynamin implicates constriction and tension in membrane fission. Nature 441, 528-531.

(197) Rust, M.J., Bates, M., and Zhuang, X. (2006). Sub-diffraction-limit imaging by stochastic optical reconstruction microscopy (STORM). Nat Methods 3, 793-795.

(198) Saarikangas, J., Zhao, H., Pykalainen, A., Laurinmaki, P., Mattila, P.K., Kinnunen, P.K., Butcher, S.J., and Lappalainen, P. (2009). Molecular mechanisms of membrane deformation by I-BAR domain proteins. Curr Biol 19, 95-107.

(199) Sackmann, E. (1994). The seventh Datta Lecture. Membrane bending energy concept of vesicle- and cell-shapes and shape-transitions. FEBS Lett 346, 3-16.

(200) Saheki, Y., and De Camilli, P. (2012). Synaptic vesicle endocytosis. Cold Spring Harb Perspect Biol 4, a005645.

(201) Saric, A., and Cacciuto, A. (2012). Fluid Membranes Can Drive Linear Aggregation of Adsorbed Spherical Nanoparticles. Phys Rev Lett 108.

(202) Saric, A., and Cacciuto, A. (2013). Self-assembly of nanoparticles adsorbed on fluid and elastic membranes. Soft Matter 9, 6677-6695.

(203) Seddon, J.M. (1990). Structure of the inverted hexagonal (HII) phase, and non-lamellar phase transitions of lipids. Biochim Biophys Acta 1031, 1-69.

(204) Semrau, S., Idema, T., Schmidt, T., and Storm, C. (2009). Membrane-mediated interactions measured using membrane domains. Biophys J 96, 4906-4915.

(205) Sens, P., and Turner, M.S. (2006). Budded membrane microdomains as tension regulators. Phys Rev E Stat Nonlin Soft Matter Phys 73, 031918.

(206) Sens, P., and Turner, M.S. (2011). Microphase separation in nonequilibrium biomembranes. Phys Rev Lett 106, 238101.

(207) Sheetz, M.P. (2001). Cell control by membrane-cytoskeleton adhesion. Nat Rev Mol Cell Biol 2, 392-396.

(208) Sheetz, M.P., Sable, J.E., and Dobereiner, H.G. (2006). Continuous membrane-cytoskeleton adhesion requires continuous accommodation to lipid and cytoskeleton dynamics. Annu Rev Biophys Biomol Struct 35, 417-434.

(209) Shi, Z., and Baumgart, T. (2015). Membrane tension and peripheral protein density mediate membrane shape transitions. Nat Commun 6, 5974.

(210) Shibata, Y., Shemesh, T., Prinz, W.A., Palazzo, A.F., Kozlov, M.M., and Rapoport, T.A. (2010). Mechanisms determining the morphology of the peripheral ER. Cell 143, 774-788.

(211) Shlomovitz, R., Gov, N.S., and Roux, A. (2011). Membrane-mediated interactions and the dynamics of dynamin oligomers on membrane tubes. New J Phys 13.

(212) Simons, K., and Ikonen, E. (1997). Functional rafts in cell membranes. Nature 387, 569-572.

(213) Simons, K., and Sampaio, J.L. (2011). Membrane organization and lipid rafts. Cold Spring Harb Perspect Biol 3, a004697.

(214) Simons, K., and van Meer, G. (1988). Lipid sorting in epithelial cells. Biochemistry 27, 6197-6202.

(215) Simunovic, M., and Bassereau, P. (2014). Reshaping biological membranes in endocytosis: crossing the configurational space of membrane-protein interactions. Biol Chem 395, 275-283.

(216) Simunovic, M., Lee, K.Y., and Bassereau, P. (2015). Screening calcium-induced spontaneous curvature of lipid membranes. Submitted.

(217) Simunovic, M., Mim, C., Marlovits, T.C., Resch, G., Unger, V.M., and Voth, G.A. (2013a). Protein-mediated transformation of lipid vesicles into tubular networks. Biophys J 105, 711-719.

(218) Simunovic, M., Srivastava, A., and Voth, G.A. (2013b). Linear aggregation of proteins on the membrane as a prelude to membrane remodeling. Proc Natl Acad Sci U S A 110, 20396-20401.

(219) Simunovic, M., and Voth, G.A. (2012). Molecular and thermodynamic insights into the conformational transitions of Hsp90. Biophys J 103, 284-292.

(220) Simunovic, M., and Voth, G.A. (2015). Membrane tension controls the assembly of curvature-generating proteins. Nat Commun.

(221) Singer, S.J., and Nicolson, G.L. (1972). The fluid mosaic model of the structure of cell membranes. Science 175, 720-731.

(222) Sinha, B., Koster, D., Ruez, R., Gonnord, P., Bastiani, M., Abankwa, D., Stan, R.V., Butler-Browne, G., Vedie, B., Johannes, L., et al. (2011). Cells respond to mechanical stress by rapid disassembly of caveolae. Cell 144, 402-413.

(223) Solon, J., Pecreaux, J., Girard, P., Faure, M.C., Prost, J., and Bassereau, P. (2006). Negative tension induced by lipid uptake. Phys Rev Lett 97, 098103.

(224) Sorre, B., Callan-Jones, A., Manneville, J.B., Nassoy, P., Joanny, J.F., Prost, J., Goud, B., and Bassereau, P. (2009). Curvature-driven lipid sorting needs proximity to a demixing point and is aided by proteins. Proc Natl Acad Sci U S A 106, 5622-5626.

(225) Sorre, B., Callan-Jones, A., Manzi, J., Goud, B., Prost, J., Bassereau, P., and Roux, A. (2012). Nature of curvature coupling of amphiphysin with membranes depends on its bound density. Proc Natl Acad Sci U S A 109, 173-178.

(226) Srivastava, A., and Voth, G.A. (2013). A Hybrid Approach for Highly Coarse-grained Lipid Bilayer Models. J Chem Theory Comput 9, 750-765.

(227) Stachowiak, J.C., Schmid, E.M., Ryan, C.J., Ann, H.S., Sasaki, D.Y., Sherman, M.B., Geissler, P.L., Fletcher, D.A., and Hayden, C.C. (2012). Membrane bending by protein-protein crowding. Nat Cell Biol 14, 944-949.

(228) Suarez, A., Ueno, T., Huebner, R., McCaffery, J.M., and Inoue, T. (2014). Bin/Amphiphysin/Rvs (BAR) family members bend membranes in cells. Sci Rep 4, 4693.

(229) Svetina, S., and Zeks, B. (1989). Membrane bending energy and shape determination of phospholipid vesicles and red blood cells. Eur Biophys J 17, 101-111.

(230) Sweitzer, S.M., and Hinshaw, J.E. (1998). Dynamin undergoes a GTP-dependent conformational change causing vesiculation. Cell 93, 1021-1029.

(231) Takei, K., Slepnev, V.I., Haucke, V., and De Camilli, P. (1999). Functional partnership between amphiphysin and dynamin in clathrin-mediated endocytosis. Nat Cell Biol 1, 33-39.

(232) Taniguchi, T. (1996). Shape deformation and phase separation dynamics of two-component vesicles. Phys Rev Lett 76, 4444-4447.

(233) Taniguchi, T., Yanagisawa, M., and Imai, M. (2011). Numerical investigations of the dynamics of two-component vesicles. J Phys-Condens Mat 23.

(234) Taylor, M.J., Perrais, D., and Merrifield, C.J. (2011). A high precision survey of the molecular dynamics of mammalian clathrin-mediated endocytosis. PLoS Biol 9, e1000604.

(235) Teasdale, R.D., and Collins, B.M. (2012). Insights into the PX (phox-homology) domain and SNX (sorting nexin) protein families: structures, functions and roles in disease. Biochem J 441, 39-59.

(236) Tian, A., Capraro, B.R., Esposito, C., and Baumgart, T. (2009). Bending stiffness depends on curvature of ternary lipid mixture tubular membranes. Biophys J 97, 1636-1646.

(237) Turner, M.S., Sens, P., and Socci, N.D. (2005). Nonequilibrium raftlike membrane domains under continuous recycling. Phys Rev Lett 95, 168301.

(238) Unwin, N. (2005). Refined structure of the nicotinic acetylcholine receptor at 4A resolution. J Mol Biol 346, 967-989.

(239) Ursell, T.S., Klug, W.S., and Phillips, R. (2009). Morphology and interaction between lipid domains. Proc Natl Acad Sci U S A 106, 13301-13306.

(240) van Gunsteren, W.F., Bakowies, D., Baron, R., Chandrasekhar, I., Christen, M., Daura, X., Gee, P., Geerke, D.P., Glattli, A., Hunenberger, P.H., et al. (2006). Biomolecular modeling: Goals, problems, perspectives. Angew Chem Int Ed Engl 45, 4064-4092.

(241) van Meer, G., Voelker, D.R., and Feigenson, G.W. (2008). Membrane lipids: where they are and how they behave. Nat Rev Mol Cell Biol 9, 112-124.

(242) van Weering, J.R., Sessions, R.B., Traer, C.J., Kloer, D.P., Bhatia, V.K., Stamou, D., Carlsson, S.R., Hurley, J.H., and Cullen, P.J. (2012). Molecular basis for SNX-BAR-mediated assembly of distinct endosomal sorting tubules. EMBO J 31, 4466-4480.

(243) Vanni, S., Hirose, H., Barelli, H., Antonny, B., and Gautier, R. (2014). A sub-nanometre view of how membrane curvature and composition modulate lipid packing and protein recruitment. Nat Commun 5, 4916.

(244) Vanni, S., Vamparys, L., Gautier, R., Drin, G., Etchebest, C., Fuchs, P.F., and Antonny, B. (2013). Amphipathic lipid packing sensor motifs: probing bilayer defects with hydrophobic residues. Biophys J 104, 575-584.

(245) Verstreken, P., Kjaerulff, O., Lloyd, T.E., Atkinson, R., Zhou, Y., Meinertzhagen, I.A., and Bellen, H.J. (2002). Endophilin mutations block clathrin-mediated endocytosis but not neurotransmitter release. Cell 109, 101-112.

(246) Walther, T.C., and Farese, R.V., Jr. (2009). The life of lipid droplets. Biochim Biophys Acta 1791, 459-466.

(247) Weissenhorn, W. (2005). Crystal structure of the endophilin-A1 BAR domain. J Mol Biol 351, 653-661.

(248) Wieprecht, T., Apostolov, O., and Seelig, J. (2000). Binding of the antibacterial peptide magainin 2 amide to small and large unilamellar vesicles. Biophys Chem 85, 187-198.

(249) Wilson, C., Wardell, M.R., Weisgraber, K.H., Mahley, R.W., and Agard, D.A. (1991). Three-dimensional structure of the LDL receptor-binding domain of human apolipoprotein E. Science 252, 1817-1822.

(250) Wu, T., Shi, Z., and Baumgart, T. (2014). Mutations in BIN1 associated with centronuclear myopathy disrupt membrane remodeling by affecting protein density and oligomerization. PLoS One 9, e93060.

(251) Yoon, Y., Tong, J., Lee, P.J., Albanese, A., Bhardwaj, N., Kallberg, M., Digman, M.A., Lu, H., Gratton, E., Shin, Y.K., et al. (2010). Molecular basis of the potent membrane-remodeling activity of the epsin 1 N-terminal homology domain. J Biol Chem 285, 531-540.

(252) Yu, S., Cho, K., Kim, Y.H., Park, S., Kim, J., and Oh, H.B. (2006). Identification of phospholipid molecular species in porcine brain extracts using high mass accuracy of 4.7 Tesla Fourier transform ion cyclotron resonance mass spectrometry. B Kor Chem Soc 27, 793-796.

(253) Zemel, A., Ben-Shaul, A., and May, S. (2008). Modulation of the spontaneous curvature and bending rigidity of lipid membranes by interfacially adsorbed amphipathic peptides. J Phys Chem B 112, 6988-6996.

(254) Zhang, P., and Hinshaw, J.E. (2001). Three-dimensional reconstruction of dynamin in the constricted state. Nat Cell Biol 3, 922-926.

(255) Zhao, H., Michelot, A., Koskela, E.V., Tkach, V., Stamou, D., Drubin, D.G., and Lappalainen, P. (2013). Membrane-sculpting BAR domains generate stable lipid microdomains. Cell Rep 4, 1213-1223.

(256) Zhu, C., Das, S.L., and Baumgart, T. (2012). Nonlinear sorting, curvature generation, and crowding of endophilin N-BAR on tubular membranes. Biophys J 102, 1837-1845.

Annexe (Appendix) I
Screening calcium-induced spontaneous curvature of lipid membranes

Mijo Simunovic,[a,b] Ka Yee C. Lee[b] and Patricia Bassereau[a]

Lipid membranes are key regulators of cellular function. An important step in membrane-related phenomena is the reshaping of the lipid bilayer, often induced by binding of macromolecules. Numerous experimental and simulation efforts have revealed that calcium, a ubiquitous cellular messenger, has a strong impact on the phase behavior, structural properties, and the stability of membranes. Yet, it is still unknown the way interactions of calcium with lipids affect their macroscopic mechanical properties. In this work, we studied the interaction of calcium ions with membrane tethers pulled from giant unilamellar vesicles, to quantify the mechanical effect on the membrane. We found that calcium imposes a positive spontaneous curvature in negatively charged membranes, contrary to predictions we made based on the proposed atomic structure. Surprisingly, this effect vanishes in the presence of physiologically relevant concentrations of sodium chloride. Our work implies that calcium may be a trigger of membrane reshaping only at high concentrations, in a process that is robustly screened by sodium ions.

Notes and references

a Institut Curie, Centre National de la Recherche Scientifique, Unité Mixte de Recherche 168, Université Pierre et Marie Curie, F-75248 Paris, France.
b Department of Chemistry, Institute for Biophysical Dynamics, and James Franck Institute, The University of Chicago, 60637 Illinois, USA.
Correspondence: patricia.bassereau@curie.fr

Introduction

Calcium ion is a major signaling species that takes part in numerous cellular processes[1]. It significantly alters the local electrostatics of macromolecules and, by doing so, it can trigger a conformational change in some proteins[2, 3]. Being a powerful cellular messenger, its equilibrium cytosolic concentration is kept four orders of magnitude lower than outside the cell, at ~ 100 nM[1]. Calcium also interacts with lipid membranes, which may drive large-scale morphological transformations, such as membrane fusion[4].

The effect of calcium on lipid membranes has been studied for decades. Early on, it was shown that calcium couples with the phase behavior, structural properties, and the stability of bilayers[5-7]. More lately, tremendous experimental and simulation efforts have been taken to elucidate the interactions of calcium with lipid bilayers, in light of significantly varying views on the precise atomic aspects of this phenomenon[8, 9]. This variation is often attributed to the measuring methodology or experimental conditions, such as the concentration of calcium or other ions[8].

Studies on monolayers composed of phosphatidylinositol 4,5-bisphosphate (PIP_2) revealed that ions have a marked effect on the organization of lipids. Specifically, monovalent cations induce the expansion of PIP_2 monolayers, while divalent cations compress them[10]. The same authors did not observe an appreciable effect of Na^+ on phosphatidylserine (PS) monolayers, although others have reported a reduction of lipid area upon Ca^{2+} binding to PS-containing bilayers[9, 11]. Simulations have shown that Na^+ penetrates deep into the bilayer[12-14]. Calcium ions, on the other hand, seem to be coordinated at the level of the phosphate group in both PS and PIP_2 membranes[15, 16]. This structural arrangement and the reported dehydration of the bilayer upon calcium binding[8, 17] most likely results in the tighter packing of lipids leading to a reduction in the lipid area.

Binding of calcium may even drive the formation of heterogeneities in the lateral composition of the membrane. In particular, studies have shown calcium-induced clustering of PIP_2 in monolayers and bilayers composed of phosphatidylcholine (PC) and PIP_2[10, 16]. Moreover, calcium causes demixing of PS-containing monolayers at lower lateral pressure[11].

In light of the numerous effects calcium can impart on the membrane, it is expected that its binding leads to macroscopic changes in the structure of the bilayer. However, it is still unclear whether Ca^{2+} affects the mechanical and morphological properties of the membrane, such as bending rigidity or the spontaneous curvature. Cell membranes in great part comprise PC and PS lipids, especially in the cytosolic leaflet[18], therefore it is of key importance to understand all aspects of how this ubiquitous signaling ion interacts with PS-containing membranes. Our aim in this work is to investigate and quantify the mechanical effect of Ca^{2+} ions on mixed PC/PS model membranes.

Results and Discussion

A membrane at equilibrium will take a shape that corresponds to its spontaneous curvature. If a bilayer has homogeneously distributed lipids and equal composition in both layers, its spontaneous curvature is zero. Binding of particles may impose an asymmetry in the bilayer that leads to a nonzero spontaneous curvature[19]. We define positive curvature when the membrane curves toward the binding leaflet and negative otherwise (Fig. A1A).

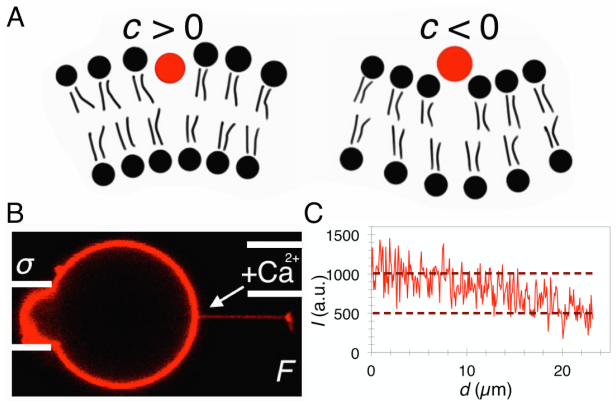

Fig A1 (A) A scheme of a lipid bilayer with positive (left) and negative (right) spontaneous curvature (c). Na^+ dilates the lipid leaflet and is expected to induce positive curvature, while Ca^{2+} compresses lipids and so it should induce negative curvature. **(B)** A scheme of a tether-pulling experiment. Aspiration pipette controls membrane tension (σ), while the remodeling force (F) is measured from the displacement of the bead in the optical trap. We use another pipette to inject Ca^{2+}. **(C)** Dilution of the injected solution from the injection pipette exit to the base of the membrane tether, measured from fluorescence intensity of a labeled molecule. The plot shows one out of three measurements.

Based on experimental and simulation evidence, monovalent cations insert between the lipids and dilate the membrane. Considering that, this way, lipids prefer to be further apart from one another, we expect this process to induce a positive spontaneous curvature (Fig. A1A, left). Conversely, as calcium contracts the lipid bilayer, it could lead to negative spontaneous curvature where lipids in the calcium-binding leaflet are closer to one another (Fig. A1A, right).

To study this effect, we used a giant unilamellar vesicle (GUV) as a model membrane. By changing the pressure in the aspiration micropipette holding the GUV, we control its surface tension. We used a micron-sized bead, trapped with optical tweezers, to pull a tether from the GUV. Based on the movement of the bead, we track, in time, the retraction force of the tether. This force effectively represents the remodeling force of the membrane. Finally, with another pipette, we inject a Ca^{2+} solution in the vicinity of the system (Fig. A1B). We refer the reader to our previous work where we have shown that this method is very sensitive to detecting spontaneous curvature, evidenced by a sudden change in the tether-retraction force upon the injection of curvature-inducing molecules[20, 21].

An important advantage of injecting calcium solution directly onto the GUV and not pre-incubating the GUV is that we can compare the behavior in the absence and the presence of the ion on the same vesicle. Additionally, high bulk Ca^{2+} concentrations would induce undesirable fusion between vesicles. However, the concentration inside the pipette is not the same as the concentration in the vicinity of the membrane tether due to dilution. Therefore, we first determined how much of the injected solution is diluted. We injected a fluorescent marker linked to a membrane-binding protein and measured the fluorescence intensity from the exit of the injection pipette to the GUV (see Materials and Methods). We found that the concentration of the injected solution is on average halved at the tether-GUV interface (Fig. A1C) and so, in the following calculations, we corrected the bulk calcium concentrations accordingly.

We carried out experiments on three different lipid compositions: 1) DOPC; 2) DOPC:DOPS (9:1); and 3) DOPC:DOPS (8:2). We did not test membranes with higher net charge, as physiologically relevant concentration of PS lipids is in the 10–20% range[22]. Unexpectedly, the tether retraction force did not deviate when injecting 10 mM Ca^{2+} on a 20% DOPS GUV (Fig. A2A). In addition, we could not observe a difference in the retraction force compared to a bare membrane at a wide range of surface tensions, up to 0.2 mN/m (Fig. A2B). To ensure that Ca^{2+} binding is not dependent on the direction of change of membrane tension, we confirmed that the forces superimpose whether stepwise increasing or decreasing tension (Fig. A2B, red and maroon dots). If binding of Ca^{2+} would induce negative curvature, the bilayer would tend to curve away from the binding leaflet and thus oppose the positive curvature of the membrane tether. Hence, we would expect an increase in the tether retraction force.

Moreover, nonzero spontaneous curvature would affect the equilibrium radius of the pulled tether, compared to a reference membrane at the same membrane tension. We computed the radius of the tether from the measured lipid fluorescence intensity (see Materials and Methods) and found no difference in the presence or absence of Ca^{2+} on 20% PS membranes (Fig. A2B).

Before discussing the implications of these results, we quantify the mechanical properties of the membrane. First, we derive the relationship between force, radius, and tension from the Helfrich Hamiltonian[19]:

$$H_t = \frac{\kappa}{2}\left(\frac{1}{r}-\frac{1}{R_0}\right)^2 A + \sigma A - fL \qquad \text{(A1)}$$

H_t is the total free energy of the tether, κ is the membrane bending rigidity, r and R_0 are respectively the mean and the spontaneous radii of curvature, A and L are respectively the

area and the length of the tether, and f is the pulling force on the membrane. At equilibrium, r becomes the tether radius (R) and the force becomes the aforementioned tether retraction force (F). To compute R and F, we minimize H_t with respect to L and R[23], i.e. $\partial H_t / \partial R = 0$ and $\partial H_t / \partial L = 0$, yielding,

$$F \approx 2\pi\sqrt{2\kappa\sigma} - 2\pi\kappa\frac{1}{R_0} \qquad \text{(A2)}$$

$$\frac{1}{R^2} = \frac{2\sigma}{\kappa} + \frac{1}{R_0^{\,2}} \qquad \text{(A3)}$$

The equations reveal that the tether curvature and the tether-retraction force scale as square root of membrane tension. Fitting the model to our data gives κ and R_0. Considering that we measured the radius from the fluorescence intensity, we have two independent measurements of κ and R_0. We note that we cannot predict the direction of curvature from Eq. A3 since R_0 appears as a square.

Just like in the two GUVs presented in Figure 2 (A and B), we did not detect an appreciable difference in the radius or the force in the presence of up to 50 mM Ca^{2+} for any of the three membrane compositions, at a relatively wide range of membrane tensions, up to ~0.3 mN/m (Fig. A2C).

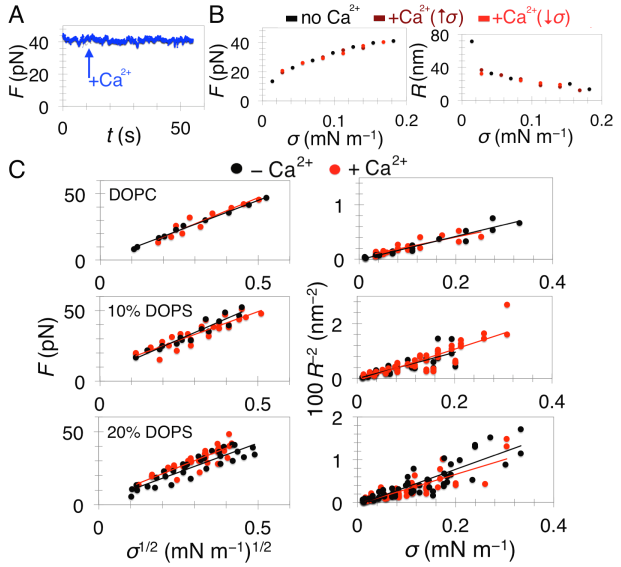

Fig A2 The mechanics of DOPC and DOPC/DOPS membranes in the presence of NaCl and Ca^{2+}. (**A**) F as a function of time (t) during injection of 10 mM Ca^{2+} to a DOPC:DOPS = 8:2 GUV in 100 mM NaCl buffer. **(B)** F and R as a function of σ for a DOPC:DOPS = 8:2 GUV in 100 mM NaCl buffer (different example from A). First, the measurement was done in the absence of Ca^{2+} (black dots) by stepwise increasing σ. Then, σ was reduced to a minimum and the measurement was repeated with 10 mM Ca^{2+} (maroon dots). Finally, continuing to inject, the measurement was repeated, but the tension was stepwise reduced (red dots). (**C**) Uncharged membrane displays no spontaneous curvature (top), while charged membranes show weak negative spontaneous curvature (centre and bottom). The injection of 5, 10, or 50 mM Ca^{2+} does not have any detectable mechanical effect (due to the absence of effect, we combine data points from all three Ca^{2+} concentrations for each composition). Top: 100% DOPC (N = 3), centre: DOPC:DOPS = 9:1 (N = 3), bottom: DOPC:DOPS = 8:2 (N = 10). Refer to Table A1 for fitting parameters.

Interestingly, even in the absence of Ca^{2+}, charged membranes displayed low negative spontaneous curvature. Precisely, R_0, obtained from force measurements (Eq. A2) for reference 10% and 20% DOPS membranes, measured to be −120 nm and −200 nm, respectively (Table A1). We hypothesize two possible sources of the spontaneous curvature of charged membranes. First, the internal solution of vesicles is composed of pure sucrose, whereas the vesicles are immersed into a 100 mM NaCl buffer. Therefore, the repulsions of charged PS head groups are much less screened on the inner than the outer leaflet. As a result, the membrane tends to curve inward to alleviate this effect, hence generating negative curvature. Another possible contribution to spontaneous curvature is the insertion of Na^+ into the bilayer. A shallow insertion (just below the phosphate, Fig. A1A) would induce positive curvature, similar to the effect amphipathic protein helices have on the membrane[24]. Deeper penetration into the hydrocarbon core may, however, reverse the sign of curvature, as predicted by theory[24]. Considering that the effect is quite weak and is not affected by Ca^{2+}, we did not pursue its precise source.

It is still puzzling that Ca^{2+}, even at 50 mM does not impart any effect on 20% DOPS membranes. All experiments so far were performed in a 100 mM NaCl solution. If Na^+ indeed inserted deeply into the bilayer, as predicted by spontaneous curvature, it would be difficult to displace it with other ions.

We therefore repeated the experiment with 20% DOPS in the absence of NaCl. In this case, we observed a significant effect at 50 mM Ca^{2+} to both the retraction force and the tether radius. Surprisingly, however, both force and radius decreased compared to the reference membrane (Fig. A3). It appears, contrary to our predictions based on the atomic structure, Ca^{2+} generates positive membrane curvature, i.e. bends the bilayer toward the binding leaflet. Fitting Eq. A2 to the data yields reverse and approximately twice the magnitude of spontaneous curvature (R_0 = +110 nm) than the reference membrane in NaCl (Table A1).

It is generally assumed that the spontaneous curvature scales with the surface coverage of curvature-inducing particles[25, 26]. We can write this expression as:

$$\frac{1}{R_0} = \frac{1}{\tilde{R}_0}x \ , \qquad \text{(A4)}$$

where $\tilde{R}_0$ is the effective spontaneous curvature (intrinsic to the binding particle) and x is the molar area fraction of bound Ca^{2+}. To calculate x, we use the Langmuir adsorption isotherm:

$$\frac{x}{1-x} = KC \quad , \tag{A5}$$

where C is the bulk ion concentration and K the equilibrium binding constant. Taking K = 650 M^{-1}, as previously measured on 20% DOPS membrane[8], we obtain $x_{c=50mM}$ = 0.97. Therefore, $\tilde{R}_0$ for Ca^{2+} binding to 20% PS membranes is 107 nm, or 29 nm if calculated from fluorescence (the corresponding effective spontaneous curvatures are 0.009±0.009 nm^{-1}, or 0.035±0.0005 nm^{-1} if calculated from fluorescence).

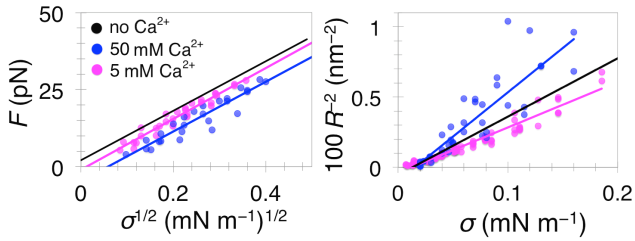

Fig A3 Ca^{2+} induces spontaneous curvature in the absence of NaCl. Fitting Eq. A2 (left) and Eq. A3 (right) to data obtained from DOPC:DOPS = 8:2 membrane in the presence of Ca^{2+} at 5 mM (N = 3) and 50 mM (N = 4). Refer to Table A1 for fitting parameters.

Lower concentration of Ca^{2+} (5 mM) induces five times lower, albeit still positive, curvature (R_0 = +540 nm). Compared to the size of the membrane, this value of spontaneous curvature is negligible and unlikely affects the morphology of the membrane. We list R_0 and κ from all experiments in Table A1.

The observed positive spontaneous curvature is incompatible with our initial predictions based on lipid area contraction induced by Ca^{2+} and with the proposed atomic coordination of Ca^{2+} with the phosphodiester group[9, 15, 27, 28]. It seems that drawing an analogy with amphipathic protein helices, which insert below the phosphate, may be inaccurate. Instead, it is more likely that the strong repulsion between Ca^{2+} ions, brought by their high charge density, becomes even stronger upon lipid area contraction. The perturbation is alleviated by generating positive curvature which will push Ca^{2+} ions apart.

Taken together, we learn that NaCl strongly screens any mechanical effect on the membrane, even at 50 mM Ca^{2+}. It has been reported that Na^+ competes with divalent cations for the binding on PS-containing membranes[8] and, even on 100% PS membranes, it can replace Ca^{2+} to a great extent[29]. To test the extent of electrostatic screening by NaCl, we performed ζ-potential measurements on small liposomes composed of 20% DOPS. We offset the concentration of salts with glucose to prevent the osmotic shock. We find, in the absence of NaCl and Ca^{2+}, the potential to be −57.6±2.4 mV (mean±SD), however note that in the absence of electrolytes, this measurement is uncertain. In the presence of NaCl, due to electrostatic screening, there is a decrease in magnitude with increased NaCl concentrations (Fig. A4), measuring −69.6±3.6 mV (0.075 mM NaCl), −62.5±2.1 mV (0.75 mM NaCl), −59.4±1.9 mV (10 mM NaCl), and −52.4±1.9 mV (20 mM NaCl), in good agreement with previously reported values[8, 30]. In the absence of NaCl, the ζ-potential continuously rises with the concentration of Ca^{2+}, measuring −30.4±0.9 mV (0.05 mM Ca^{2+}), −22.5±1.4 mV (0.5 mM Ca^{2+}), −10.9±0.5 mV (5 mM Ca^{2+}), and 0.7±0.7 mV (20 mM Ca^{2+}) (Fig. A4).

Finally, we measured the ζ-potential in the presence of both ions. At 0.05 mM Ca^{2+}, we measured −46.6±3.4 mV (10 mM NaCl) and −49.6±3.2 mV (20 mM NaCl), whereas at 5 mM Ca^{2+} the values were −13.4±0.8 mV (20 mM NaCl) and −16.7±3.5 mV (40 mM NaCl) (Fig. A4). It therefore appears that NaCl screens Ca^{2+} relatively well at low concentrations (200–400 NaCl/Ca^{2+} molar ratio). At high Ca^{2+} concentrations (4–8 NaCl/Ca^{2+} molar ratio) the ζ-potential is also lower compared to NaCl-free conditions, however the screening effect is much weaker.

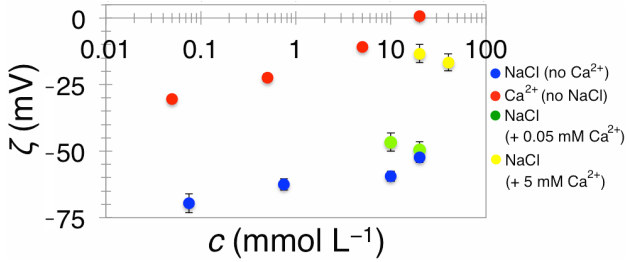

Fig A4 ζ-potential measurements of small liposomes (DOPC:DOPS = 8:2), as a function of salt concentration. Blue and red dots are measured in NaCl or Ca^{2+}, respectively. Green and yellow dots are measured in NaCl at a concentration indicated on the x-axis and it additionally contains, respectively, 0.05 or 5 mM Ca^{2+}.

Table A1 Fitting parameters obtained from all experiments (mean±SD). Top values were obtained from force measurements using Eq. A2, whereas parenthetic values were obtained from fluorescence measurements using Eq. A3 and, in case of the radius, have an ambiguous sign.

	DOPC		10% DOPS		20% DOPS		20% DOPS, no NaCl	
	no Ca	+ Ca^{2+}	no Ca	+ Ca^{2+}	no Ca	+ Ca^{2+}	+5 mM Ca^{2+}	+50 mM Ca^{2+}
$1/R_0$ (1/nm)	1/3600±6E-5 (1/100±1E-3)	1/350±2E-3 (1/50±2E-3)	−1/120±4E-3 (1/160±7E-4)	−1/60±8E-3 (1/90±6E-4)	−1/200±5E-3 (1/50±4E-4)	−1/160±6E-3 (1/60±4E-4)	1/540±2E-3 (1/50±9E-5)	1/110±9E-3 (1/30±5E-4)
κ (k_BT)	25.1±1.4 (22.2±1.5)	29.9±7.0 (26.3±3.4)	27.1±5.1 (9.7±0.7)	20.0±3.9 (9.9±1.2)	18.9±3.4 (12.4±1.1)	23.4±4.5 (13.0±1.2)	20.8±1.9 (15.0±0.5)	19.9±2.9 (7.7±0.7)

Conclusions

Our single-vesicle essay shows that Ca^{2+} ions induce positive spontaneous curvature on negatively charged membranes. We propose that the repulsion between Ca^{2+} ions drives the membrane to curve outward, as to minimize their interactions. We also speculate that if Ca^{2+} potentially drives the formation of PS domains, locally concentrating explicit charge would additionally result in positive spontaneous curvature. Our simple model predicts that Ca^{2+} induces a positive radius of curvature on membranes with 20% net charge, with the magnitude of ~110 nm. This magnitude of curvature scales linearly with the bound coverage of Ca^{2+}, which depends on the bulk concentration and the amount of charged lipids in the bilayer. We note that there is a quantitative discrepancy between the calculated spontaneous curvature from independent force and fluorescence measurements. Both of these measurements have limitations, especially at high tension, where the radius is very thin and the force is very high, so it is difficult to predict which measurement provides a more accurate estimate of spontaneous curvature. Nevertheless, both measurements show qualitatively the same behavior in the presence and absence of NaCl, although fluorescence measurements systematically predict a lower radius of curvature.

What could be the consequences for a cell membrane? In cells, the concentration of Ca^{2+} is very tightly controlled. While extracellular solution contains ~2.5 mM Ca^{2+}, the cytosolic concentration of Ca^{2+} is normally kept at only nanomolar. It seems unlikely that Ca^{2+} would induce a mechanical effect on a membrane of a quiescent cell. However, during various signaling events, its concentration may jump orders of magnitude and, combined with lipid clustering and area contraction, Ca^{2+} could sufficiently locally cover the membrane to induce budding and tubulation. Such consequences would be undesirable in signal transduction phenomena. Na^+ ions completely inhibit the curvature effect of Ca^{2+}. Considering that our electrokinetic measurements revealed that Ca^{2+} still alters the electrostatic environment of the membrane, curvature screening is not a consequence of electrostatic screening. Instead, we propose that the tight binding and deep insertion of Na^+ into the bilayer may serve as a very robust protection mechanism against nonspecific remodelling. Specialized proteins, such as those containing scaffolding domains, take the role of membrane sculptors, as they are specifically targeted to membrane remodeling sites[31, 32].

We hope our work will provide a better understanding of the extent of Ca^{2+} ions affecting membrane mechanical properties at relevant concentrations of charge in the membrane and in the presence of physiological ionic strength.

Materials and Methods

Reagents. 1,2-Dioleoyl-sn-glycero-3-phosphatidylcholine (DOPC), 1,2-dioleoyl-sn-glycero-3-phosphatidylserine (DOPS), and 1,2-distearoyl-sn-glycero-3-phosphoethanolamine-N-[biotinyl(polyethyleneglycol)-2000] (DSPE-PEG(2000)-biotin) were purchased from Avanti Polar Lipids. BODIPY-TR-C5-ceramide was purchased from Molecular Probes. All reagents used to make buffers and β-casein from bovine milk (>99%) were purchased from Sigma-Aldrich.

Preparation of GUVs. GUVs were prepared by electroformation on indium tin oxide glass[33]. DOPC and DOPS were mixed at desired molar ratio (see Results & Discussion) to which we added 0.5% BODIPY-TR-C5-ceramide and 0.03% DSPE-PEG(2000)-biotin (both molar percent). We smeared 10 μL of the mix (at 3 g/L) on each of the two slides of indium tin oxide glass, dried the film under vacuum for at least 1 h, then hydrated with sucrose. GUVs were grown under a sine voltage (1 V, 10 Hz) for approximately 1 h. The sucrose concentration was adjusted for each experiment so that the molalities of solutions inside and outside GUVs match.

Tether-pulling experiment. We followed the procedure described elsewhere[20, 21]. The experimental chamber and the aspiration pipette (~ 5 μm in diameter at the tip) were immersed for 30 min. in a solution of β-casein (5 g/L, dissolved in 100 mM NaCl, 10 mM HEPES) to minimize the adhesion of lipids to the glass surface. The chamber was then filled with the experimental solution (for experiments containing NaCl: 100 mM NaCl and 10 mM HEPES at pH = 7.4, and glucose to offset the molality inside GUVs; for saltless experiments: glucose with equal molality as the sucrose inside GUVs). Another pipette was filled with 10, 20, or 100 mM $CaCl_2$ (see Text) and offset if necessary with glucose to match the molality of the experimental solution. The chamber was sealed with oil after ~ 10 min. to prevent evaporation. GUVs with enough excess area to form an aspiration tongue[34, 35] were aspired in a micropipette. Membrane tension was controlled via the aspiration pressure,

using the Laplace relation: $\sigma = 0.5\Delta p r_p / (1 - r_p / r_v)$, where Δp is the hydrostatic pressure, r_p and r_v are radii of pipette and the vesicle, respectively[34]. A tether was created by bringing in contact the GUV with a streptavidin-coated polystyrene bead, ~ 3 μm in diameter (Spherotec), trapped with optical tweezers. We measure the tether retraction force as: $F = k(a - a_0)$, where a is the actual and a_0 the equilibrium position of the bead, tracked with bright field microscopy, k is the stiffness of the trap, calibrated using the viscous drag method[36]. Typical measurement was performed by stepwise increasing the aspiration pressure and measuring the force and fluorescence for several minutes at each pressure. The measurement was then repeated by approaching the injection pipette and injecting Ca^{2+}, by either starting over from low pressure or reducing stepwise from high pressure. The direction of pressure did not affect the results (see Text). In experiments with no NaCl, we could only measure the steps after injecting Ca^{2+}, as the streptavidin-biotin interactions require the presence of ions. We conducted experiments by injecting 100 mM Ca^{2+} (in the pipette, see above for the dilution factor) and incubating the vesicles with 5 mM Ca^{2+}. We measured the radius of the tether using the following relationship: $R = C_f I_t / I_v$, where I_t and I_v are the lipid fluorescence intensities of the tether and vesicle, respectively, and $C_f = 200 \pm 50$ is the calibration factor deduced previously[20].

We determined the dilution of the injected solution by injecting ~2 μM Alexa488 from a similar distance and injection pressure (10–20 Pa) as in all experiments with calcium. Alexa488 was bound to a membrane-binding protein, β2 centaurin, kindly provided by Harvey McMahon. We then measured the decrease in fluorescence intensity as a function of the distance from the pipette (three measurements). Keep in mind that assuming the same dilution factor for Ca^{2+} as for the marker likely overestimates the near-vesicle concentration, considering that Ca^{2+} has a lower hydrodynamic radius and it would diffuse out faster than the fluorescence marker. Taking the upper-limiting case ensures we do not overestimate the effect we quantify.

Preparation of small liposomes. The lipid mix composed of DOPC:DOPS (4:1, molar ratios), was dried under nitrogen to obtain 1 mg of dry mass. The mix was hydrated in 1 mL sucrose then freeze-thawed five times, followed by extrusion through a polycarbonate filter with pores 100 nm in diameter. We confirmed the final size of liposomes to be 106±7 nm ($N = 4$) with dynamic light scattering.

***ζ*-potential measurements.** We used a Malvern Zetaseizer NanoZS (Malvern Instruments Ltd.) to measure the electrophoretic mobility, which was converted to *ζ*-potential using Henry's equation $\zeta = 3u\eta / (2\varepsilon f)$ [37], where u is the electrophoretic mobility, η viscosity of the solution, ε the dielectric constant, and f Henry's function, calculated as [38]: $f = 1 + 0.5\left[1 + \left(2.5 / \lambda a\left[1 + 2e^{-\lambda a}\right]\right)\right]^{-3}$, where a = 100 nm was taken as the particle radius of curvature and λ is the inverse Debye length, calculated as: $\lambda = \sqrt{\sum_{i=1}^{N} e^2 z_i^2 n_i / \varepsilon_r \varepsilon_0 k_B T}$. N is the number of ionic species, e is the elementary charge, z_i and n_i are charge number and amount of ion i, respectively, ε_r and ε_0 are the relative and vacuum electric permittivity, k_B is the Boltzmann constant, and T the thermodynamic temperature[37]. For the case of pure glucose f = 1.0 was approximated. All measurements were taken three times.

Acknowledgements

We acknowledge the support of the Chateaubriand Fellowship (MS) and the France and Chicago Collaborating in the Sciences fund (MS). The Bassereau team is a member of the Labex CelTisPhyBio (ANR-11-LABX0038), of Paris Sciences et Lettres (ANR-10-IDEX-0001_02) and of the French research consortium *CellTiss*. We thank Coline Prévost, Tom Rapoport and Misha Kozlov for insightful discussions.

Bibliography

1. D. E. Clapham, *Cell*, 2007, **131**, 1047-1058.
2. M. E. Monteiro, M. J. Sarmento and F. Fernandes, *Biochem Soc Trans*, 2014, **42**, 1441-1446.
3. O. H. Petersen, M. Michalak and A. Verkhratsky, *Cell Calcium*, 2005, **38**, 161-169.
4. P. K. Tarafdar, H. Chakraborty, S. M. Dennison and B. R. Lentz, *Biophys J*, 2012, **103**, 1880-1889.
5. R. Ekerdt and D. Papahadjopoulos, *Proc Natl Acad Sci U S A*, 1982, **79**, 2273-2277.
6. T. Ito and S. I. Ohnishi, *Biochim Biophys Acta*, 1974, **352**, 29-37.
7. D. Papahadjopoulos, S. Nir and N. Duzgunes, *J Bioenerg Biomembr*, 1990, **22**, 157-179.
8. C. G. Sinn, M. Antonietti and R. Dimova, *Colloid Surface A*, 2006, **282**, 410-419.
9. P. T. Vernier, M. J. Ziegler and R. Dimova, *Langmuir*, 2009, **25**, 1020-1027.
10. I. Levental, A. Cebers and P. A. Janmey, *J Am Chem Soc*, 2008, **130**, 9025-9030.
11. M. Sovago, G. W. Wurpel, M. Smits, M. Muller and M. Bonn, *J Am Chem Soc*, 2007, **129**, 11079-11084.
12. R. A. Bockmann, A. Hac, T. Heimburg and H. Grubmuller, *Biophys J*, 2003, **85**, 1647-1655.
13. P. Mukhopadhyay, L. Monticelli and D. P. Tieleman, *Biophys J*, 2004, **86**, 1601-1609.
14. S. A. Pandit and M. L. Berkowitz, *Biophys J*, 2002, **82**, 1818-1827.
15. U. R. Pedersen, C. Leidy, P. Westh and G. H. Peters, *Biochim Biophys Acta*, 2006, **1758**, 573-582.
16. Y. H. Wang, A. Collins, L. Guo, K. B. Smith-Dupont, F. Gai, T. Svitkina and P. A. Janmey, *J Am Chem Soc*, 2012, **134**, 3387-3395.
17. H. Binder and O. Zschornig, *Chem Phys Lipids*, 2002, **115**, 39-61.
18. G. van Meer, D. R. Voelker and G. W. Feigenson, *Nat Rev Mol Cell Biol*, 2008, **9**, 112-124.
19. W. Helfrich, *Z Naturforsch C*, 1973, **28**, 693-703.
20. B. Sorre, A. Callan-Jones, J. Manzi, B. Goud, J. Prost, P. Bassereau and A. Roux, *Proc Natl Acad Sci USA*, 2012, **109**, 173-178.
21. H. F. Renard, M. Simunovic, J. Lemiere, E. Boucrot, M. D. Garcia-Castillo, S. Arumugam, V. Chambon, C. Lamaze, C. Wunder, A. K. Kenworthy, A. A. Schmidt, H. T. McMahon, C. Sykes, P. Bassereau and L. Johannes, *Nature*, 2015, **517**, 493-496.
22. K. Boesze-Battaglia and R. Schimmel, *J Exp Biol*, 1997, **200**, 2927-2936.
23. I. Derenyi, F. Julicher and J. Prost, *Phys Rev Lett*, 2002, **88**, 238101.

24. A. Zemel, A. Ben-Shaul and S. May, *J Phys Chem B*, 2008, **112**, 6988-6996.
25. S. Leibler, *J Phys-Paris*, 1986, **47**, 507-516.
26. R. Lipowsky, *Faraday Discuss*, 2013, **161**, 305-331; discussion 419-359.
27. J. M. Boettcher, R. L. Davis-Harrison, M. C. Clay, A. J. Nieuwkoop, Y. Z. Ohkubo, E. Tajkhorshid, J. H. Morrissey and C. M. Rienstra, *Biochemistry*, 2011, **50**, 2264-2273.
28. J. Seelig, *Cell Biol Int Rep*, 1990, **14**, 353-360.
29. R. Kurland, C. Newton, S. Nir and D. Papahadjopoulos, *Biochimica Et Biophysica Acta*, 1979, **551**, 137-147.
30. F. J. Carrion, A. Delamaza and J. L. Parra, *J Colloid Interf Sci*, 1994, **164**, 78-87.
31. H. T. McMahon and J. L. Gallop, *Nature*, 2005, **438**, 590-596.
32. M. Simunovic and P. Bassereau, *Biol Chem*, 2014, **395**, 275-283.
33. M. I. Angelova, S. Soléau, P. Méléard, F. Faucon and P. Bothorel, in *Trends in Colloid and Interface Science VI*, eds. C. Helm, M. Lösche and H. Möhwald, Steinkopff, 1992, vol. 89, pp. 127-131.
34. R. Kwok and E. Evans, *Biophys J*, 1981, **35**, 637-652.
35. D. Cuvelier, I. Derenyi, P. Bassereau and P. Nassoy, *Biophys J*, 2005, **88**, 2714-2726.
36. K. C. Neuman and S. M. Block, *Rev Sci Instrum*, 2004, **75**, 2787-2809.
37. A. V. Delgado, F. Gonzalez-Caballero, R. J. Hunter, L. K. Koopal and J. Lyklema, *J Colloid Interf Sci*, 2007, **309**, 194-224.
38. H. Ohshima, *J Colloid Interf Sci*, 1994, **164**, 510-513.

ABSTRACT

Many biological phenomena are accompanied by the change in shape of the cell membrane. This process is often mediated by curvature-generating proteins, most notably by those containing one of many BAR domains. At the same time, membrane curvature controls the way proteins interact with one another and so it acts as a vital signaling mechanism in the cell. In our work, presented in two theses, we combine theoretical modeling, high-resolution imaging, and quantitative microscopy techniques to study the assembly of BAR proteins on the membrane and its influence on membrane shape and mechanics. Our simulations elucidate the molecular mechanism underlying the self-assembly of BAR proteins on the membrane and the way their collective behavior affects the large-scale membrane reshaping. Experimental biophysical methods demonstrate a novel mechanism of membrane fission mediated by BAR proteins and molecular motors. It also quantifies how the formation of protein scaffolds alters the mechanical behavior of the membrane. These results are essential for understanding a newly discovered pathway of endocytosis, mediated by a BAR protein endophilin. Our combined theoretical and experimental approach gives vital clues on how the mechanical properties of the membrane may regulate protein dynamics in living cells.

RESUME

De nombreux phénomènes biologiques s'accompagnent de déformations de la membrane cellulaire. Ce processus est souvent induit par des protéines, tout particulièrement par des protéines possédant un des différents domaines BAR. Dans le même temps, la courbure membranaire contrôle l'interaction entre protéines, donc elle représente un mécanisme essentiel de signalisation dans la cellule. Dans mon travail, présenté en deux thèses, je combine la modélisation théorique, l'imagerie à haute résolution, et la microscopie quantitative pour étudier l'assemblage des protéines à domaine BAR sur les membranes et leur influence sur la forme et la mécanique membranaire. Mes simulations expliquent le mécanisme moléculaire sous-jacent de l'auto-assemblage des protéines BAR et la façon dont leur comportement collectif affecte le remodelage de la membrane à grande échelle. Grâce à des expériences de biophysique, j'ai pu mettre en évidence un nouveau mécanisme de fission des tubules membranaires induit par des protéines BAR et des moteurs moléculaires. J'ai également étudié la formation de structures en "scaffold" par ces protéines et comment elles modifient le comportement mécanique de la membrane. Ces résultats sont essentiels pour comprendre la voie d'endocytose, découverte récemment, qui est contrôlées par une protéine BAR, l'endophiline. Mon travail qui combine théorie et expériences propose des explications sur la manière dont les propriétés mécaniques de la membrane peuvent réguler la dynamique des protéines dans la cellule.